frontiers | Research Topics

Optobiomechanics of the eye

Edited by
Sabine Kling, Jos J. Rozema, Anna Marina Pandolfi and Norberto López Gil

Published in
Frontiers in Bioengineering and Biotechnology
Frontiers in Medicine

ISSN 1664-8714
ISBN 978-2-8325-7164-4
DOI 10.3389/978-2-8325-7164-4

Generative AI statement
Any alternative text (Alt text) provided alongside figures in the articles in this ebook has been generated by Frontiers with the support of artificial intelligence and reasonable efforts have been made to ensure accuracy, including review by the authors wherever possible. If you identify any issues, please contact us.

About Frontiers

Frontiers is more than just an open access publisher of scholarly articles: it is a pioneering approach to the world of academia, radically improving the way scholarly research is managed. The grand vision of Frontiers is a world where all people have an equal opportunity to seek, share and generate knowledge. Frontiers provides immediate and permanent online open access to all its publications, but this alone is not enough to realize our grand goals.

Frontiers journal series

The Frontiers journal series is a multi-tier and interdisciplinary set of open-access, online journals, promising a paradigm shift from the current review, selection and dissemination processes in academic publishing. All Frontiers journals are driven by researchers for researchers; therefore, they constitute a service to the scholarly community. At the same time, the *Frontiers journal series* operates on a revolutionary invention, the tiered publishing system, initially addressing specific communities of scholars, and gradually climbing up to broader public understanding, thus serving the interests of the lay society, too.

Dedication to quality

Each Frontiers article is a landmark of the highest quality, thanks to genuinely collaborative interactions between authors and review editors, who include some of the world's best academicians. Research must be certified by peers before entering a stream of knowledge that may eventually reach the public - and shape society; therefore, Frontiers only applies the most rigorous and unbiased reviews. Frontiers revolutionizes research publishing by freely delivering the most outstanding research, evaluated with no bias from both the academic and social point of view. By applying the most advanced information technologies, Frontiers is catapulting scholarly publishing into a new generation.

What are Frontiers Research Topics?

Frontiers Research Topics are very popular trademarks of the *Frontiers journals series*: they are collections of at least ten articles, all centered on a particular subject. With their unique mix of varied contributions from Original Research to Review Articles, Frontiers Research Topics unify the most influential researchers, the latest key findings and historical advances in a hot research area.

Find out more on how to host your own Frontiers Research Topic or contribute to one as an author by contacting the Frontiers editorial office: frontiersin.org/about/contact

Optobiomechanics of the eye

Topic editors
Sabine Kling — University of Bern, Switzerland
Jos J. Rozema — University of Antwerp, Belgium
Anna Marina Pandolfi — Polytechnic University of Milan, Italy
Norberto López Gil — University of Murcia, Spain

Citation
Kling, S., Rozema, J. J., Pandolfi, A. M., López Gil, N., eds. (2025). *Optobiomechanics of the eye*. Lausanne: Frontiers Media SA. doi: 10.3389/978-2-8325-7164-4

Table of contents

frontiers | Frontiers in Bioengineering and Biotechnology

TYPE Editorial
PUBLISHED 07 November 2025
DOI 10.3389/fbioe.2025.1727136

OPEN ACCESS

EDITED AND REVIEWED BY
Markus O. Heller,
University of Southampton, United Kingdom

*CORRESPONDENCE
Sabine Kling,
kling.sabine@gmail.com

RECEIVED 17 October 2025
ACCEPTED 22 October 2025
PUBLISHED 07 November 2025

CITATION
Kling S, Pandolfi A, Lopez-Gil N and Rozema J (2025) Editorial: Optobiomechanics of the eye. *Front. Bioeng. Biotechnol.* 13:1727136. doi: 10.3389/fbioe.2025.1727136

Editorial: Optobiomechanics of the eye

Sabine Kling[1]*, Anna Pandolfi[2], Norberto Lopez-Gil[3] and Jos Rozema[4]

[1]University of Bern, Bern, Switzerland, [2]Politecnico di Milano, Milan, Italy, [3]Universidad de Murcia, Murcia, Spain, [4]Visual Optics Lab Antwerp (VOLANTIS), Faculty of Medicine and Health Sciences, Universiteit Antwerpen, Antwerp, Belgium

KEYWORDS

corneal biomechanics, intraocular pressure, lens biomechanics, imaging, modelling

Editorial on the Research Topic
Optobiomechanics of the eye

Introduction

Opto-biomechanics is an interdisciplinary field that focuses on the coupling between optical and mechanical properties in biological systems and on the use of optical approaches to non-invasively study biomechanical behavior. The eye is a complex organ where structural mechanics and optical performance are inherently connected. Understanding this optobiomechanical interplay has become increasingly important in both fundamental research and clinical translation, in particular in the context of corneal cross-linking, refractive surgery, intraocular pressure (IOP) regulation, or lens dynamics.

The eleven contributions featured in this Research Topic span the cornea, sclera, lens, and optic nerve head, presenting new models, novel diagnostic techniques and experimental studies that push forward our ability to diagnose, predict, and potentially treat ocular diseases. This editorial summarizes and synthesizes their insights, highlighting areas of convergence and opportunities for future research.

Corneal biomechanics

Several studies investigated corneal biomechanics using novel experimental techniques or finite element modeling, particularly in the context of riboflavin/ultraviolet A (UVA) cross-linking (CXL) and laser refractive surgery.

Bell et al. combined synchrotron X-ray scattering, biomechanical testing, and analytical modeling to probe how riboflavin/UVA crosslinking alters the corneal stroma. Interestingly, while cross-linking stiffened the cornea by about 60%, the stiffening was not attributable to changes in individual fibril stiffness. Instead, enhanced fibril interconnectivity and reorientation under load emerged as the dominant mechanism. This better mechanistic understanding demonstrates that therapeutic stiffening relies on mesoscale organization rather than microscale material alterations.

Rix et al. examined Brillouin spectroscopy and polarization sensitive Optical Coherence Tomography (OCT) as a non-invasive measure of corneal biomechanics. By carefully

controlling hydration in porcine eyes, the authors demonstrated that Brillouin measurements after CXL are largely confounded by water uptake, in contrast to polarization-sensitive OCT, which more directly captures changes in collagen fiber alignment. Raman spectroscopy further revealed no detectable formation of new molecular cross-links. Together, these results caution against simplistic interpretations of Brillouin data and point toward multimodal approaches for robuster assessments of cross-linking efficacy.

A broader perspective on corneal biomechanics is provided by Pang et al. in a review about finite element (FE) modeling. The authors survey geometrical and constitutive models of the cornea, discuss critical factors influencing numerical outcomes, and highlight validation challenges given the scarcity of human tissue. They underscore FE modeling as an economical and flexible framework for exploring corneal biomechanics and stress the need for more realistic constitutive descriptions.

Refractive surgery and ectasia risk represent another dimension of corneal biomechanics. Zhang et al. trained a random forest model on over 2,600 patients to predict the suitability for Small Incision Lenticule Extraction (SMILE) surgery. With high accuracy (Aread Under the Curve (AUC) = 0.976), the model identified tomographic and biomechanical indices as key discriminators, providing a powerful tool for clinical decision-making. Complementarily, Fantaci et al. used finite-element simulations to investigate whether Photorefractive Keratotomy (PRK), Laser Assisted in-situ Keratomeleusis (LASIK), or SMILE could induce ectasia. Their simulations suggested that surgeries alone are unlikely to *cause* ectasia but may accelerate pre-existing weaknesses, with SMILE having the greatest biomechanical impact on the posterior cornea. Together, these studies highlight how computational models and data-driven tools are valuable for pre-surgical screening and risk assessment.

Intraocular pressure and biomechanics

The relationship between IOP and ocular biomechanics has been investigated at multiple levels, from tissue-specific alterations to whole-eye deformation responses.

Ma et al. explored how chronic high IOP alters the mechanical properties of the lamina cribrosa (LC) and retinal ganglion cell (RGC) axons. Using atomic force microscopy on a rat glaucoma model, the authors documented a time-dependent reduction in stiffness of both LC glial tissue and RGC axons, with up to 80% loss in modulus over 12 weeks. This weakening likely contributes to axonal vulnerability and progressive glaucomatous damage, emphasizing the need for therapies that preserve or restore LC integrity.

Extending the focus from local tissue mechanics to global ocular responses, two other studies applied air-puff tonometry to connect corneal and scleral responses to IOP. Redaelli et al. developed a computational model to simulate corneal deformation under air-puff tonometry, addressing the fact that traditional measures are confounded by corneal thickness and the tissue's mechanical properties. By shifting the analysis toward the timing of maximum apex velocity, the authors propose a more reliable IOP estimator less dependent on corneal properties. Using the same air-puff tonometry, De La Hoz et al. examined scleral biomechanics in rabbits in combination with computational modeling. Their findings showed scleral stiffness strongly influences deformation responses, suggesting that this non-invasive tool could provide valuable biomechanical markers for myopia and glaucoma risk evaluation.

Lens biomechanics

Although crucial to the process of accommodation, the biomechanical behavior of the crystalline lens is not yet entirely understood. Dahaghin et al. introduced a biomechanical model of lens "wobbling," the oscillatory motion that occurs after rapid eye movement. By combining Purkinje image analysis with optobiomechanical simulations, the authors reproduced oscillation frequencies and damping factors observed *in vivo*, while also revealing subject-specific variability. This work sets the stage for personalized lens models that could deepen our understanding of ocular biomechanical mechanisms.

Tahsini et al. examined how preservation methods alter the mechanical properties of *ex vivo* porcine lenses. Using optical coherence elastography and inverse finite-element analysis, the authors showed that freezing significantly alters cortical and nuclear strains, while refrigeration preserves the lens' mechanical properites best. Removal of the capsule changed the strain distribution across lens nucleus and cortex. These findings are essential for interpreting *ex vivo* experiments and designing standardized protocols for lens biomechanics research.

Conclusion

Taken together, these eleven contributions provide a rich insight in the evolving field of optobiomechanics.

From synchrotron scattering to, air-puff tonometry, OCT elastography, machine learning and numerical simulations, diverse methods are converging to give a more complete picture of ocular biomechanics. Studies on corneal cross-linking, scleral stiffness, and lamina cribrosa degradation deepen our understanding of disease and treatment mechanisms. Computational models and predictive algorithms are directly informing refractive surgery screening and IOP measurement, while non-invasive imaging modalities offer prospects for routine biomechanical monitoring.

The continued growth of optobiomechanics will rely on interdisciplinary collaborations across physics, biology, engineering, and clinical sciences, ultimately driving innovations that improve patient care and visual performance.

Author contributions

SK: Writing – original draft. AP: Writing – review and editing. NL-G: Writing – review and editing. JR: Writing – review and editing.

Funding

The author(s) declare that no financial support was received for the research and/or publication of this article.

Conflict of interest

The authors declare that the research was conducted in the absence of any commercial or financial relationships that could be construed as a potential conflict of interest.

The author(s) declared that they were an editorial board member of Frontiers, at the time of submission. This had no impact on the peer review process and the final decision.

Generative AI statement

The author(s) declare that Generative AI was used in the creation of this manuscript. To assist with summarisation and rephrasing. The output was thoroughly reviewed and corrected where necessary.

Any alternative text (alt text) provided alongside figures in this article has been generated by Frontiers with the support of artificial intelligence and reasonable efforts have been made to ensure accuracy, including review by the authors wherever possible. If you identify any issues, please contact us.

Publisher's note

frontiers | Frontiers in Bioengineering and Biotechnology

TYPE Original Research
PUBLISHED 13 June 2024
DOI 10.3389/fbioe.2024.1398659

OPEN ACCESS

EDITED BY
Anna Marina Pandolfi,
Polytechnic University of Milan, Italy

REVIEWED BY
Bjørn Skallerud,
NTNU, Norway
Matthew A. Reilly,
The Ohio State University, United States

*CORRESPONDENCE
Sabine Kling,
sabine.kling@unibe.ch

RECEIVED 10 March 2024
ACCEPTED 27 May 2024
PUBLISHED 13 June 2024

CITATION
Tahsini V, Gil IC and Kling S (2024), Storage-induced mechanical changes of porcine lenses assessed with optical coherence elastography and inverse finite element modeling.
Front. Bioeng. Biotechnol. 12:1398659.
doi: 10.3389/fbioe.2024.1398659

Storage-induced mechanical changes of porcine lenses assessed with optical coherence elastography and inverse finite element modeling

Vahoura Tahsini[1], Iulen Cabeza Gil[2] and Sabine Kling[1]*

[1]ARTORG Center for Biomedical Engineering Research, University of Bern, Bern, Switzerland, [2]Aragón Institute of Engineering Research (i3A), University of Zaragoza, Zaragoza, Spain

Introduction: In an effort of gaining a better understanding of the lens mechanics, *ex vivo* lenses samples are often used. Yet, *ex vivo* tissue might undergo important postmortem changes depending on the unavoidable preservation method employed. The purpose of this study was to assess how various storage conditions and the removal of the lens capsule affect the mechanical properties of *ex vivo* porcine lens samples.

Methods: A total of 81 freshly enucleated porcine eyes were obtained and divided into six groups and preserved differently. In the first three groups, the lens within the intact eye was preserved for 24 h by: (i) freezing at −80°C (n = 12), (ii) freezing at −20°C (n = 12), and (iii) refrigeration at +8°C (n = 12). In the remaining groups, the lenses were immediately extracted and treated as follows: (iv) kept intact, no storage (n = 12), (v) decapsulated, no storage (n = 21), and (vi) immersed in Minimum Essential Medium (MEM) at +8°C (n = 12) for 24 h. Frozen lenses were thawed at room temperature. Each lens was compressed between two glass lamella and subjected, first to a period of relaxation during which the compression force was recorded and second to an oscillating micro-compression while the deformation was recorded with a total of 256 subsequent B-scans via optical coherence tomography. The corresponding axial strain was retrieved via phase-sensitive image processing and subsequently used as input for an inverse finite element analysis (iFEA) to retrieve the visco-hyperelastic material properties of the lenses.

Results: After freezing at temperatures of −80°C and −20°C, the cortical strains increased by 14% ($p = 0.01$) and 34% ($p < 0.001$), and the nuclear strains decreased by 17% ($p = 0.014$) and 36% ($p < 0.001$), compared to the lenses tested immediately after postmortem, respectively. According to iFEA, this resulted from an increased ratio of the nuclear: cortical E-modulus (4.06 and 7.06) in −80°C and −20°C frozen lenses compared to fresh lenses (3.3). Decapsulation had the largest effect on the material constant C_{10}, showing an

increase both in the nucleus and cortex. Preservation of the intact eye in the refrigerator induced the least mechanical alterations in the lens, compared to the intact fresh condition.

Discussion: Combining iFEA with optical coherence elastography allowed us to identify important changes in the lens mechanics induced after different preserving *ex vivo* methods.

KEYWORDS

optical coherence elastography, inverse finite element analysis, crystalline lens, hyperelastic material, preservation condition

1 Introduction

The most important refractive components of the eye are the cornea and the crystalline lens. The latter provides approximately one-third of the refractive power and has the unique characteristic to change its shape and adjust the focal length of the eye to different distances, which is referred to as accommodation. During accommodation, the diameter of the lens changes by contracting the ciliary muscles and relaxing the tension on the zonular fibers. This goes along with a large mechanical deformation that heavily depends on the inherent material properties of the lens. In terms of its mechanical properties, the lens capsule has previously been reported to play an important role in the lenticular deformation behavior (Reilly and Cleaver, 2017), particularly with respect to the lens' viscoelastic properties (Mekonnen et al., 2023). In an effort to get a better understanding of accommodation, the deformation behavior of the crystalline lens during accommodation has mostly been investigated by means of macroscopic changes in the lens thickness, diameter, and curvature assessed with diverse imaging techniques, including ultrasound (Yoon et al., 2012; Zhang et al., 2018) and magnetic resonance (Sheppard et al., 2011), but predominantly via optical imaging techniques (Purkinje, Scheimpflug, Optical Coherence Tomography). Other studies have examined the mechanical deformation behavior of the *ex vivo* crystalline lens under controlled loading conditions, such as during spinning (Wilde et al., 2012; Reilly et al., 2016) or while mounted in a lens stretcher (Marussich et al., 2015; Heilman et al., 2018; Martinez-Enriquez et al., 2020). Due to their *ex vivo* nature, most of these mechanical characterization studies on crystalline lenses have been conducted in human donor tissues. It is critical that the *ex vivo* lens is adequately preserved after harvesting to prevent degradation and maintain its physiological characteristics. While low temperature helps maintain cell viability for long periods, its effect on the tissue's mechanical characteristics has hardly been addressed. The difference in mechanical properties due to storage of the intact eye in the refrigerator has previously been assessed with spinning tests (Fisher, 1971), and of extracted lenses in saline solution in the refrigerator with indentation tests (Czygan and Hartung, 1996), where no relevant differences were reported. Freezing is another common preservation technique, but it had previously been demonstrated to affect the viscoelastic behavior of the lens (Weeber et al., 2005). Another study has reported a minor softening effect of the lens capsule in response to freezing (Krag and Andreassen, 1998). Yet, it remains unclear whether cortical and nuclear regions are similarly affected by storage and which is the most suitable preservation method in terms of not altering the mechanical properties. Another common preservation for the crystalline lens (Jones et al., 2005) is minimum essential medium (MEM), which provides cells with essential components necessary for survival, growth, and proliferation. To our knowledge, the effects of preservation in MEM on the lens mechanics have not been studied before.

So far, all of these studies have in common that internal lenticular deformations could only be indirectly retrieved by inverse modeling (Weeber et al., 2007; Weeber and Van Der Heijde, 2008). In this context, inverse Finite Element Analysis (iFEA) is a valuable technique to identify mechanical parameters either from non-invasive geometrical measurements, or in materials with complex mechanical properties, and with patient-specific geometries (Lanchares et al., 2012). Applied to the lens, iFEA previously allowed to quantify the change in material properties underlying presbyopia (Lanchares et al., 2012) by considering the accommodation amplitude at different ages. However, due to the highly nonlinear properties of the lens, material model selection and material parameter identification remains challenging.

Recently, Brillouin microscopy has provided the first highly-resolved stiffness maps (Besner et al., 2016) of the aging human lens measured *in vivo*. Yet Brillouin scattering depends on the refractive index and the tissue's hydration state, which could be severely affected by the gradient distribution within the lens. This would explain the discrepancy of the retrieved stiffness distribution with Brillouin compared to those expected from earlier studies. Optical coherence elastography (OCE) is an emerging technique for characterizing tissue mechanics (Kling, 2020) with high spatial resolution. In the past, air-puff based OCE has shown promising results to identify differences in lens stiffness both, at different intraocular pressures (Wu et al., 2018) and with age (Li et al., 2019; Zhang et al., 2022). Previously, we applied phase-sensitive quasi-static OCE in combination with iFEA to quantify the visco-hyperelastic mechanical properties of the porcine lens under an oscillating compression. Due to the higher resolution compared to earlier macroscopic relaxation measurements (Sharma et al., 2011; Alzoubi et al., 2024), we were able to quantify nuclear and cortical regions separately, and to find out that viscoelasticity was only present in the nucleus.

In the current study, we apply the same technique to study the effect of the lens capsule and different preservation conditions on the mechanical properties of the lens. Importantly, we perform a mechanical comparison of different regions within the lens. This investigation is particularly relevant, as many *ex vivo* studies on accommodation have been performed in donor eyes that have been preserved for different durations before the measurement was

TABLE 1 Summary of the experimental conditions assessed in this study.

Group	Name	Sample size	Storage	Preservation time (h)	Lens extraction	Decapsulation
1	fresh	12	tested immediately	0	immediately	no
2	de-cap	21	tested immediately	0	immediately	yes
3	fridge8	12	+8°C intact	24	after 24 h	no
4	MEM8	12	+8°C in MEM	24	immediately	no
5	frozen20	12	−20°C intact	24	after 24 h	no
6	frozen80	12	−80°C intact	24	after 24 h	no

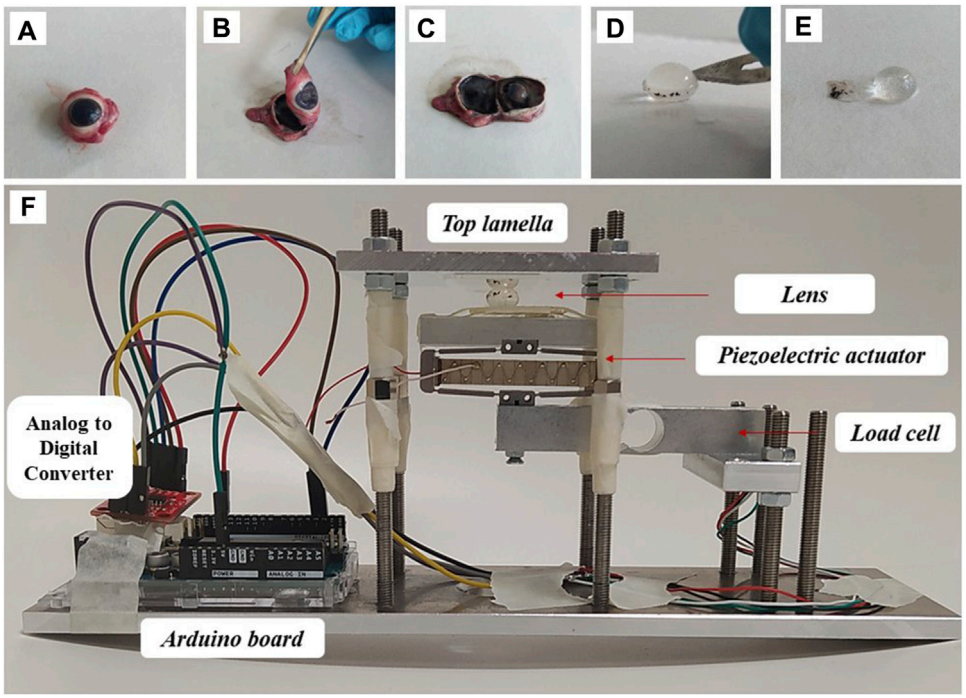

FIGURE 1
Sample preparation and experimental set-up. **(A–C)** Individual steps of lens separation, **(D,E)** lens decapsulation, **(F)** mounting in the compression setup.

conducted. As such, the current study will enable a better comparison of earlier works using different preservation techniques.

2 Materials and methods

Optical Coherence Elastography (OCE) and inverse Finite Element Analysis (iFEA) were combined in the current study to quantify the axial strain of the crystalline lens during an oscillating compression and inversely retrieve its biomechanical properties.

2.1 Samples and preservation conditions

A total of 81 porcine lenses were obtained from the local slaughterhouse and prepared as follows, see also Table 1: Crystalline lenses of eyes in group 1 were excised in the freshly enucleated eye and tested immediately. Lenses of group 2 were excised in the freshly enucleated eye, subsequently decapsulated and tested immediately. Eyes in group 3 were stored intact at +8°C for 24 h before the crystalline lenses were excised and tested. Crystalline lenses of eyes in group 4 were excised in the fresh eyes and subsequently stored in Minimum Essential Medium (MEM) for 24 h at 8°C before the measurement. Eyes in group 5 were stored intact at −20°C for approx. 24 h before the eyes were allowed to thaw at room temperature. Subsequently the crystalline lenses were excised and tested. Eyes in group 6 were stored intact at −80°C for approx. 24 h before the eyes were allowed to thaw at room temperature, similar as in previous studies (Weeber et al., 2007).

For crystalline lens extraction (Figures 1A–E), a scalpel was used to place an incision at the scleral equator. Then the anterior part of the eyeball was separated by micro-dissection scissors. After removing the aqueous humor, the lens was dissected from the

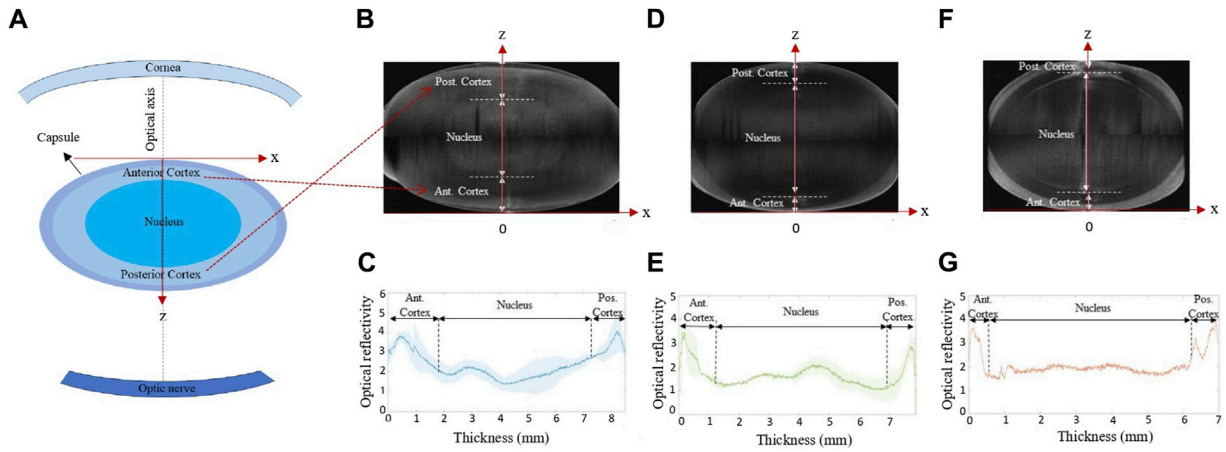

FIGURE 2
(A) Sketch of the lens position within eye. **(B,D,F)** Representative cross-sectional OCT images and **(C,E,G)** mean intensity profile of the lenses before compression, respectively, averaged for the conditions **(B,C)** frozen at −20°C, −80°C and MEM, **(D,E)** fresh and refrigerator, and **(F,G)** after decapsulation.

ciliary muscle. For group 2 lenses, the capsule was dissected by carefully cutting along the lens equator before peeling the capsule off with a set of tweezers.

2.2 Geometrical assessment

Before the actual mechanical characterization was conducted, the intact lens geometry was recorded. All geometric assessments and mechanical measurements were conducted at room temperature. For this purpose, a commercial optical coherence tomography device (Anterion, Heidelberg Engineering, Germany) was used, with an axial and lateral resolution of 9.5 µm (in air) and 35 µm, respectively. Two structural OCT scans were conducted: one with the anterior side of the lens facing towards the OCT, and one with the posterior side facing towards the OCT. The two scans were then merged into a single scan with extended depth. Subsequently, the corresponding reflectivity profiles were retrieved and used to identify the lens nucleus and cortical regions, see Figure 2.

2.3 Mechanical stimulation

Two separate measurements were performed to fully determine the mechanical properties of the lens:

(i) Stress relaxation. For this purpose, the distance between the two glass lamellas was reduced to 5.4 mm for lenses with capsule, and to 4.4 mm for the decapsulated group, to induce an engineering pre-strain of the lens of 33%. The distance between the two lamella and thus of the compressed lens thickness was measured by OCT (Figure 1F). A load cell weight sensor (HX711, max. load 1 kg) positioned under the piezo electric actuator was used to record the force relaxation for a duration of 2 min (short) and 30 min (long). Force was measured in gram-force (1 gf = 9.8 mN). The relatively high initial pre-strain was necessary to achieve (a) a reliable force measurement and (b) a compression over a larger proportion of the lens.

(ii) Oscillating compression. For this purpose, the pre-compressed lens was subjected to a sinusoidal compression/relaxation cycle by means of a piezoelectric actuator (APF705, Thorlabs, USA), which displaced the bottom lamella with a stroke length of −32–36 µm. The latter was quantified previously (Cabeza-Gil et al., 2023). Simultaneously to the oscillating displacement, the dynamic strain distribution within the lens was quantified.

2.4 Optical coherence elastography

For dynamic strain assessment during the oscillating compression, a total of 256 subsequent OCT B-scans were acquired at the same location with a frame rate of 33 Hz, resulting in an overall measurement duration of 7.6 s. The displacement that occurred between two subsequent B-scans was determined by phase-sensitive processing of the complex-valued OCT signal as described recently (Zaitsev et al., 2016; Kling, 2020). Briefly, the axial displacement is calculated from Eq. 1:

$$\Delta z = \frac{\lambda . \angle R}{4\pi . n(z)}, \tag{1}$$

where λ = 1200 nm is the central wavelength of the OCT, n(z) is the gradient refractive index of the porcine lens and $\angle R$ is the angle of the complex cross-correlation which is retrieved from Eq. 2:

$$R = \sum_{j=-w_z}^{w_z} \sum_{k=-w_x}^{w_x} B_S(z+j, x+k) \cdot B^*_{S+1}(z+j, x+k), \tag{2}$$

where B represents an OCT B-scan, B* its complex conjugate, and s = {1, 256} is the number of B-scans. Phase-processing windows with a size of w_z = 10 and w_x = 1 pixels were applied. Strain was approximated as the axial gradient and computed by applying a second cross-correlation with the by one pixel axially shifted first complex cross-correlation, according to Eq. 3:

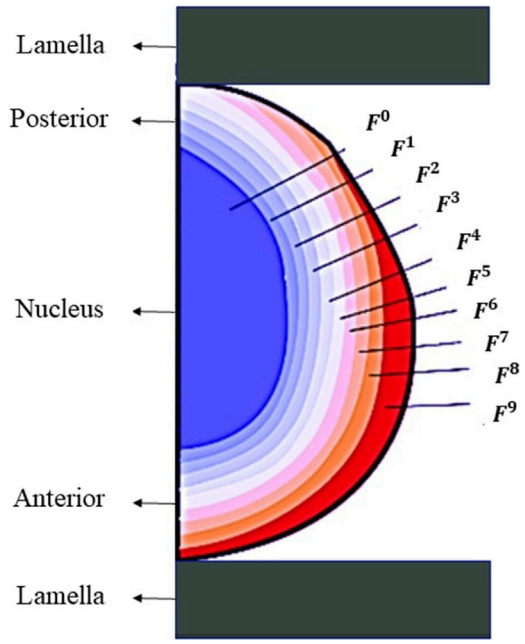

FIGURE 3
Geometry used for finite element modeling.

$$\varepsilon_z = \frac{\Delta z \cdot \boldsymbol{n}(\mathbf{z})}{\mathbf{asu}} = \frac{\boldsymbol{\lambda} \cdot \angle \sum_{l=-v_z}^{v_z} \sum_{m=-v_x}^{v_x} \left(\boldsymbol{R}_s(\boldsymbol{z}+\boldsymbol{l},\boldsymbol{x}+\boldsymbol{m}) \cdot \boldsymbol{R}_s^*(\boldsymbol{z}+\mathbf{1}+\boldsymbol{l},\boldsymbol{x}+\boldsymbol{m})\right)}{\boldsymbol{4\pi} \cdot \mathbf{asu}}, \quad (3)$$

being asu = 9.5 μm the axial sampling unit (in air), which means the axial dimension of a pixel. v_z = 15 and v_x = 1 pixels were the applied strain processing windows. Note that in contrast to displacement, axial strain measured with OCE is independent of the refractive index. Also, due to the compression between two flat glass lamella, no optical distortions due to the lens geometry are expected.

Cross-sectional axial strain was recorded. In order to improve signal quality, strains were averaged across a lateral zone of 2.3 mm. Subsequently, the average strain within three distinct regions(anterior cortex, posterior cortex and the nucleus) was computed for comparison among the groups. The corresponding regions were identified from the structural OCT image (see Figure 2). For validation, the average OCE strain across the full lens thickness was computed and a homogenous refractive index (Regal et al., 2019) of 1.49 was assumed to determine the corresponding lamella distance in order to compare the OCE-measured compression with the macroscopic compression applied by the piezoelectric actuator.

2.5 Finite element modeling

In order to retrieve the mechanical properties of the lenses tested experimentally under different conditions, inverse finite element analysis (iFEA) was performed in Abaqus (version 6.14, Dassault Systèmes). For this purpose, a 2D axisymmetric finite element (FE) model was developed to simulate the experiment. The glass lamella were modeled as rigid bodies, whilst the lens shapes were obtained from structural OCT scans of the lens without any zonular anchoring taken before any mechanical tests were performed. A representative geometry was determined for every condition.

The lens geometry was composed of the nucleus, the cortex and the capsule. To simulate the previously reported stiffness (Weeber et al., 2007) gradient within the lens and to account for the anatomical layered structure of the lens fiber cells (Kuszak, 1995; Taylor et al., 1996), the anterior part was divided into nine layers of cortex whilst the posterior was divided into 6, see Figure 3. This division was made to describe the difference in stiffness observed in the experimental tests between the anterior and posterior cortex of the lens. The stiffness of every layer of the cortex was defined by Eq. 4:

$$\mathbf{Cortex}(\boldsymbol{n}) = \boldsymbol{N}_{\mathbf{stiffness}} \cdot \boldsymbol{F}^{\boldsymbol{n}} \cdot \boldsymbol{C}_{\mathbf{10-N}}^{\infty}, \quad (4)$$

where n in the exponent is the number of the respective cortical layer, being n = 1 the cortical layer closest to the nucleus. F is a form factor to differentiate the stiffness across the cortical layers. N is used to increase the relative stiffness of the nucleus with the cortex, and $C_{10-(N)}^{\infty}$ is the long-term Neo-Hookean modulus of the nucleus. Because the thickness of the posterior cortex is thinner than the anterior one, it contains only six layers. The anterior cortex contains all nine layers. To better describe the elasticity of the anterior and posterior cortex in the results section, the $C_{10-(n)}^{\infty}$ modulus was averaged as the stiffness of the layers that compose the anterior or posterior cortex, respectively, giving an average $\bar{C}_{10-ANT}$ and $\bar{C}_{10-POST}$.

Initially, the top lamella axially compressed the lens to a thickness of $LT_{test} = LT_0 - \Delta$. This step was performed to assure the lens stability in the setup. The undeformed thickness LT_0 of the decapsulated lenses was notably lower (6.6 mm) compared to all lenses with an intact capsule (8.06 mm). Therefore, $LT_{test} = 4.40\,mm$ was used for decapsulated lenses and $LT_{test} = 5.40\,mm$ for the other conditions, such that a similar compression of 33% was achieved. After the initial compression, an experimental sinusoidal micro-displacement was performed by the bottom lamella. The strains were calculated with the compressed lens configuration as a reference.

Large strains and nonlinearity were considered in this dynamic simulation. The axisymmetric conditions were imposed in the model about the *y*-axis. A "hard contact" behavior, strictly prohibiting penetration between the lamella and lens surfaces, was applied to maximize the realism of the simulation. No friction was applied.

The lens can be described as a visco-hyperelastic material consisting of the nucleus, cortex and capsule. The importance of accounting for the lens capsule has recently been demonstrated in a simulation study (Reilly and Cleaver, 2017) under a similar compressive loading. Therefore, following the approach of our recent study (Cabeza-Gil et al., 2023), the lens capsule was modeled with a homogeneous thickness of 60 μm and a Neo-Hookean coefficient of 0.166 MPa (equivalent to a Young's modulus of 1 MPa). Due to the substantial strain induced during the pre-compression step, the lens nucleus was characterized by an

TABLE 2 Parameters and their ranges used for the response surface.

	Thickness	Tau	F	N
fresh, fridge8	[7.1, 7.4, 7.55, 7.8]	[0.25, 0.5, 1, 1.5, 3, 5, 7.5]	Ranging from 1.0 to 3.0 in increments of 0.25	Ranging from 0.65 to 1.05 in increments of 0.05
de-cap	[5.7, 6.3, 6.8, 7.3]	[0.25, 0.5, 1, 1.5, 3, 5, 7.5]	Ranging from 1.0 to 4.0 in increments of 0.4	[0.85 in 0.03 increments up to 1.03] Ranging from 0.85 to 1.03 in increments of 0.03
MEM8	[8.1, 8.4 8.8]	[0.25, 0.5, 1, 1.5, 3, 5, 7.5]	Ranging from 1.0 to 3.0 in increments of 0.25	Ranging from 0.65 to 1.05 in increments of 0.05
frozen20, frozen80	[8.3, 8.8, 9.2]	[0.25, 0.5, 1, 1.5, 3, 5, 7.5]	Ranging from 2.0 to 6.0 in increments of 0.25	Ranging from 0.85 to 1.15 in increments of 0.05

incompressible visco-hyperelastic Neo-Hookean material model with a strain energy density function of Eq. 5:

$$\psi(\boldsymbol{C},t) = \boldsymbol{C}^{R}_{10-N}(t)\,(\boldsymbol{I}_1 - 3), \tag{5}$$

being $\boldsymbol{C}^{R}_{10-N}(t)$ the hyperelastic Neo-Hookean coefficient and $\boldsymbol{I}_1$ the first invariant of the right Cauchy-Green deformation tensor. The time dependence of $\boldsymbol{C}^{\infty}_{10-N}(t)$ is defined by a one term ($N = 1$) Prony series according to Eqs 6 and 7:

$$\boldsymbol{C}^{R}_{10-N}(t) = \boldsymbol{C}^{0}_{10}\left(1 - \sum_{i=1}^{N} g_i\left(1 - e^{-\frac{t}{\tau_i}}\right)\right), \tag{6}$$

$$\boldsymbol{C}^{\infty}_{10} = \boldsymbol{C}^{0}_{10}\left(1 - \sum_{i=1}^{N} g_i\right), \tag{7}$$

where C^{0}_{10} is the instantaneous modulus and C^{∞}_{10} the long-term modulus. The Prony series parameters are defined by the pre-exponential factor g_1 and the relaxation time τ_1.

For consistency with linear elasticity in small deformations and for comparison across studies, the incompressible Neo-Hookean model can be converted to a linear elastic model according to Eqs 8 and 9 with the following relationship:

$$\mu = 2C_{10}, \tag{8}$$

$$E = 3\mu, \tag{9}$$

which μ is the first Lamé parameter, and E, the Young's modulus.

The lens cortex was modeled with a hyperelastic Neo-Hookean material model, without effect of any viscous behavior as we did not observe this previously. (Cabeza-Gil et al., 2023).

2.5.1 Inverse finite element analysis

A response surface was generated to inversely retrieve the mechanical properties for all the lenses under investigation. A response surface was generated with a full factorial design for every lens preserving condition, involving the thickness of the lens, the Prony series terms of the lens nucleus (τ_1), and the stiffness ratio $\frac{C^{\infty}_{10-N}}{\bar{C}_{10-ANT}}$, $\frac{C^{\infty}_{10-N}}{\bar{C}_{10-POST}}$. The Prony term, g_1 (−), was set to 0.25 for all preserving conditions in order to reduce overfitting and consequently allow a better comparison across all samples (Cabeza-Gil et al., 2023).

Three to four levels of thickness, seven levels of τ_1, and 10 levels of the parameter F and N (100 combinations) were varied for every preserving lens condition to do the inverse fitting. Each range parameter was chosen based on screening analysis trying to cover the behavior of all samples of one condition. There was no geometrical difference between short and long-term relaxation measurements, therefore the same lens geometries and response surfaces were used to retrieve the mechanical properties. Table 2 summarizes the full factorial design used to characterize each preserving lens condition. This resulted in approximately 2000 simulations for every lens conditions.

After generating the response surface with the full factorial design, an optimization process was carried out in Minitab to inversely retrieve the mechanical properties of each lens ($\frac{C^{\infty}_{10-N}}{\bar{C}_{10-ANT}}$; $\frac{C^{\infty}_{10-N}}{\bar{C}_{10-POST}}$, τ_1, F, $N_{stiffness}$) from the experimental values. The optimization was performed by minimizing an error metric (SSE) see eq. 10 defined as the relative average sum of the maximum and minimum strains in the anterior cortex, posterior cortex, and nucleus, along with the viscoelastic delay. All outputs had the same weight.

$$SSE = \sum_{i=1}^{n}(\alpha_i - \kappa(x_i))^2 + (\beta_i - \lambda(x_i))^2 + (\gamma_i - \mu(x_i))^2 + (\delta_i - \nu(x_i))^2, \tag{10}$$

where $\alpha_i, \beta_i, \gamma_i$ are the measured strain amplitudes at the i^{th} data point of the anterior cortex, posterior cortex, and nucleus, respectively, and $\kappa(x_i), \lambda(x_i), \mu(x_i)$ the corresponding predicted values from the square function at the ith data point. δ corresponds to the nucleus delay and $\nu(x_i)$ to the predicted delay at the ith data point. This error metric served as a measure of how well the numerical results match the experimental ones. The response surface optimizer was employed to iteratively adjust the input parameters, optimizing them with respect to all these outputs simultaneously. This way, we aimed to find the optimal set of mechanical properties for every lens that best matched the experimental strain results. Due to the strain-controlled design of the experimental setting, these three derived mechanical properties were independent of the absolute mechanical properties ($C^{\infty}_{10-N}, \bar{C}_{10-ANT}, \bar{C}_{10-POST}$). Therefore, in order to approximate the latter, the minimal force measured after the initial relaxation period was taken into account in a second optimization round. Given that the force measurements were affected by substantial experimental noise, force measurements were averaged across each condition, rather than considered individually for each sample.

2.6 Statistical analysis

Statistical analysis was conducted with IBM SPSS Statistics (Version 28.0.1.1(14)). Normality of the data was assessed with

10.3389/fbioe.2024.1398659

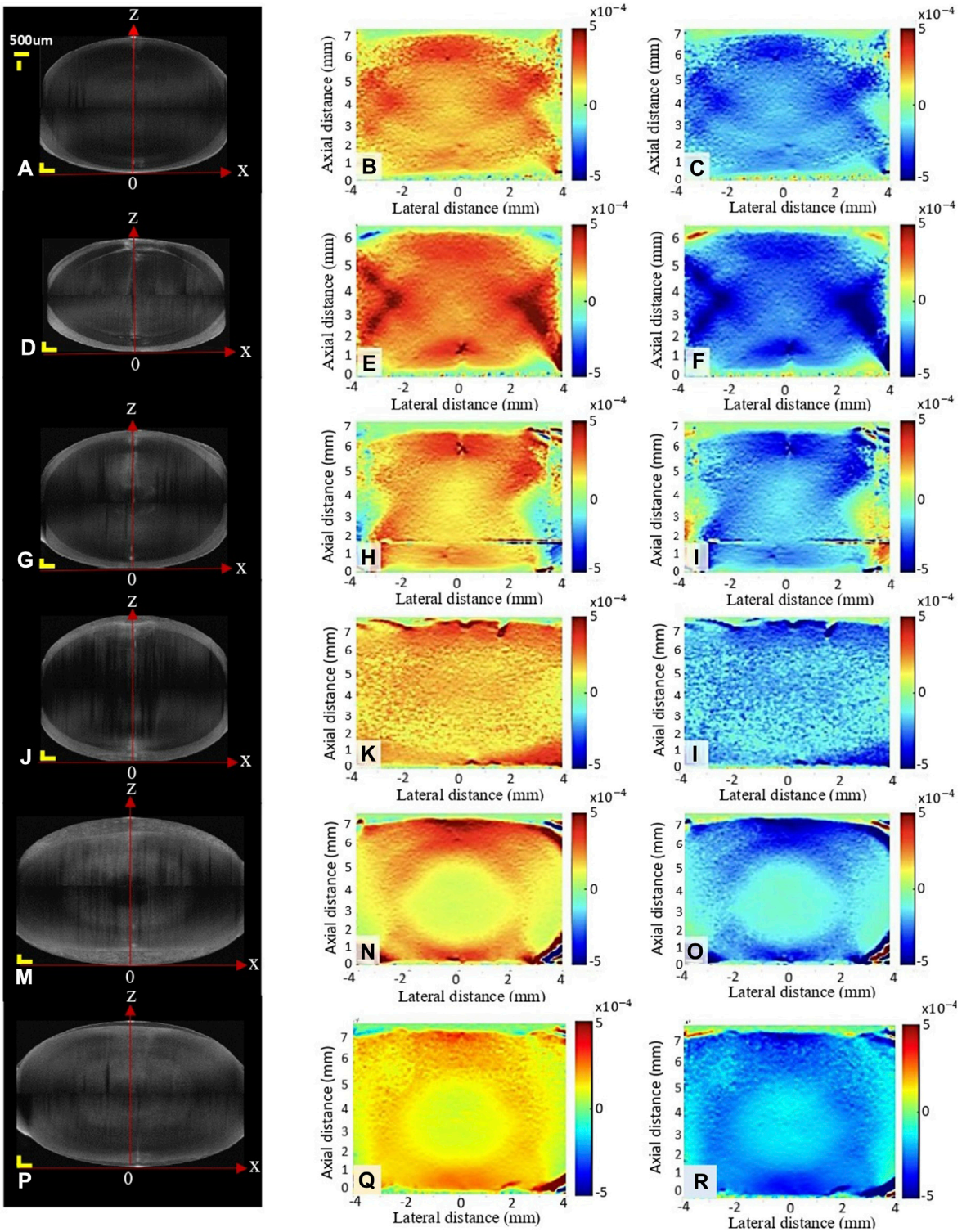

FIGURE 4
Structural image **(A,D,G,J,M,P)** and axial strain map during relaxation **(B,E,H,K,N,Q)** and compression **(C,F,I,L,O,R)** under different conditions: fresh **(A–C)**, decapsulated **(D–F)**, refrigerator **(G–I)**, MEM **(J–L)**, frozen at −20°C **(M–O)** and frozen at −80°C **(P–R)**. Scale bars in the structural image correspond to 500 μm each.

the Shapiro-Wilk test and accordingly parametric (ANOVA, Student's t-test) and non-parametric (Independent-Samples Kruskal–Wallis test) tests were applied to compare parameters with normal and skewed distributions, respectively. Bonferroni correction was applied to account for multiple testing. A *p*-value of 0.05 was considered to indicate statistical significance.

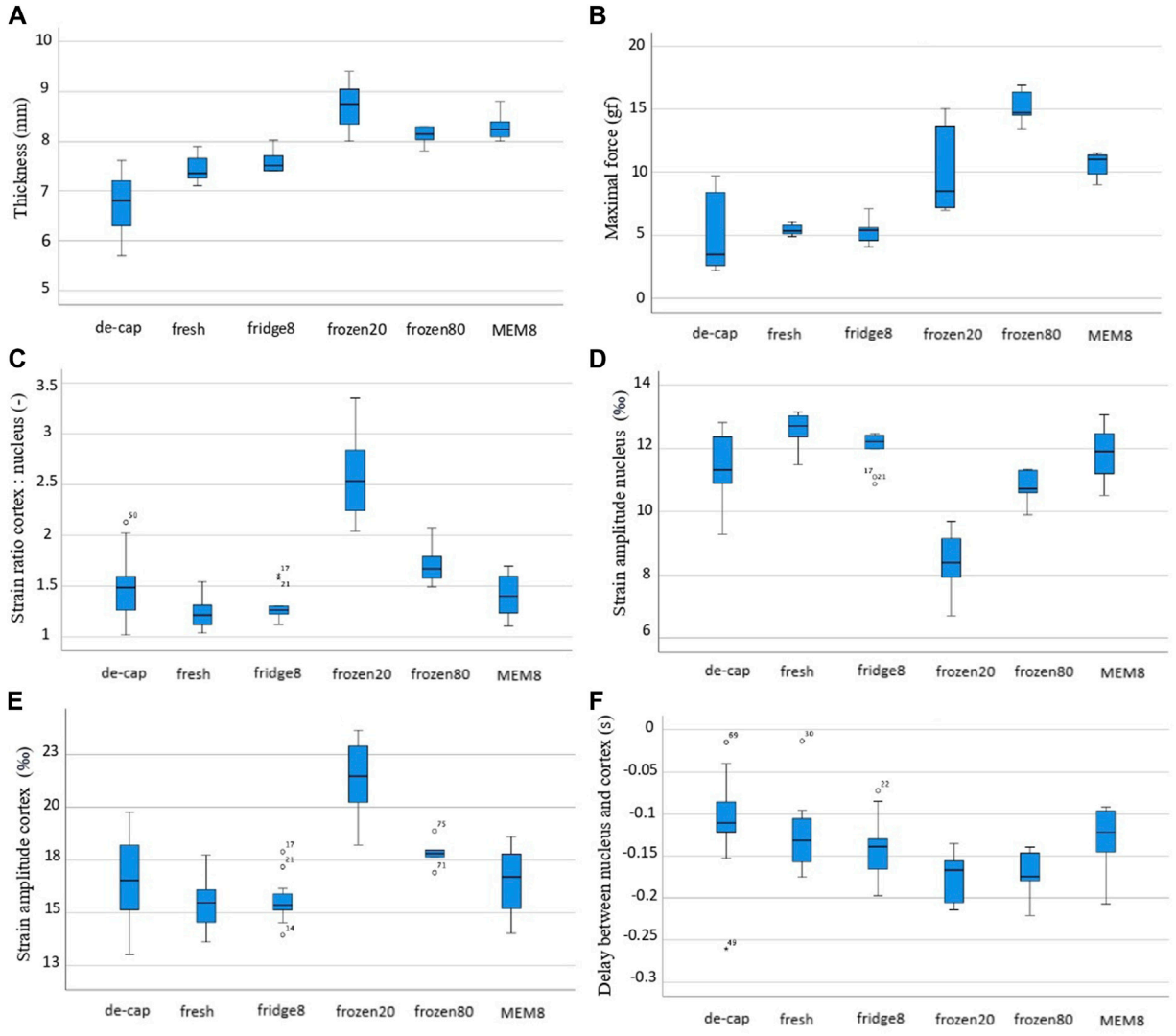

FIGURE 5
Box and whiskers plot for different experimentally derived parameters: **(A)** lens thickness, **(B)** maximal initial force, **(C)** ratio of cortical to nuclear strain amplitude, **(D)** strain amplitude in the nucleus, **(E)** strain amplitude in the cortex, **(F)** time delay between nucleus and cortex.

3 Results

3.1 Experimental results

The first column of Figure 4 shows the structural scan of the lens of the different groups before compression. As can be noticed, storage in MEM and freezing at both, −20 and −80°C, resulted in a significantly increased lens thickness by +0.85 mm ($p < 0.001$), +1.27 mm ($p < 0.001$) and +0.69 mm ($p < 0.001$), compared to the fresh condition, see also Figure 5A. In contrast, a significant decrease in lens thickness by −0.76 mm ($p < 0.001$) was observed after decapsulation, compared to the fresh group.

In agreement with the thickness changes, a higher initial maximal force applied (Figure 5B) in the relaxation test was measured for MEM (11.0 gf, $p = 0.001$) and frozen groups at −20°C and −80°C (8.49 gf, $p = 0.013$ and 9.66 gf, $p = 0.005$), compared to fresh lenses (5.35 gf). The correlation of the maximal force with the lens thickness was statistically significant (r = 0.775, $p < 0.001$). As expected, the minimal force measured at the end of the relaxation was significantly ($p < 0.001$) higher for short relaxation times compared to the longer one (on average 7.52 vs. 2.30 gf). There was also a significant correlation between lens thickness and the min force after relaxation, both at short ($c_{sp} = 1.0$, $p < 0.01$) and long ($c_{sp} = 0.98$, $p < 0.001$) relaxation times. Figure 6 presents the strongest correlations observed among the experimental parameters.

The second and third columns in Figure 4 show representative axial strain maps obtained during the oscillating relaxation and compression test. The strain distribution refers to the mean amplitude during relaxation (second column) and compression (third column). Notice that this corresponds to a dynamic strain distribution superposed on top of the pre-strain, which was applied during the initial compression. For better visibility, the pre-strain is omitted here. After freezing at −20°C, the lenses showed the highest strain ratio between the cortex: nucleus with a factor of 2.59 versus the fresh condition with a factor of 1.23 ($p < 0.001$), Figure 5C. Freezing at −80°C induced changes in the same direction but of

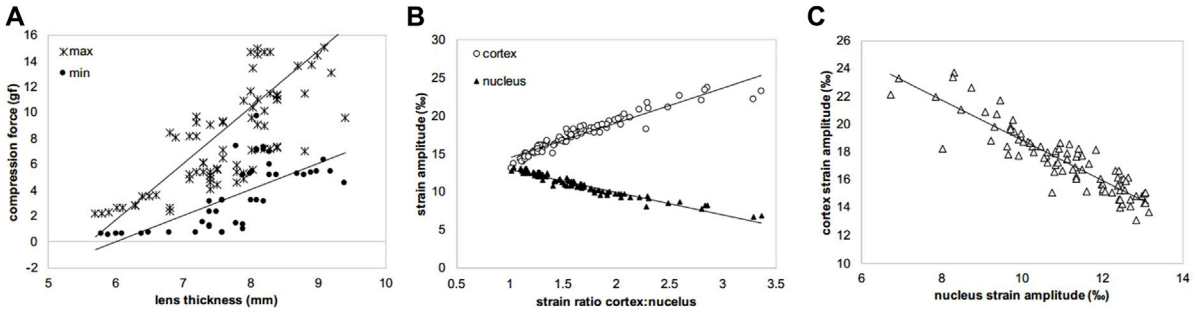

FIGURE 6
Scatter plots showing the three strongest correlations observed among the experimental variables. **(A)** max and min compression forces versus lens thickness (c_{sp} = 0.775 and c_{sp} = 0.359, $p < 0.001$ and $p = 0.002$), **(B)** strain amplitudes in cortex and nucleus versus strain ratio (c_{sp} = 0.972 and c_{sp} = 0.962, both $p < 0.001$), **(C)** cortical versus nuclear strain amplitudes (c_{sp} = 0.883, $p < 0.001$). c_{sp} means Spearman correlation coefficient.

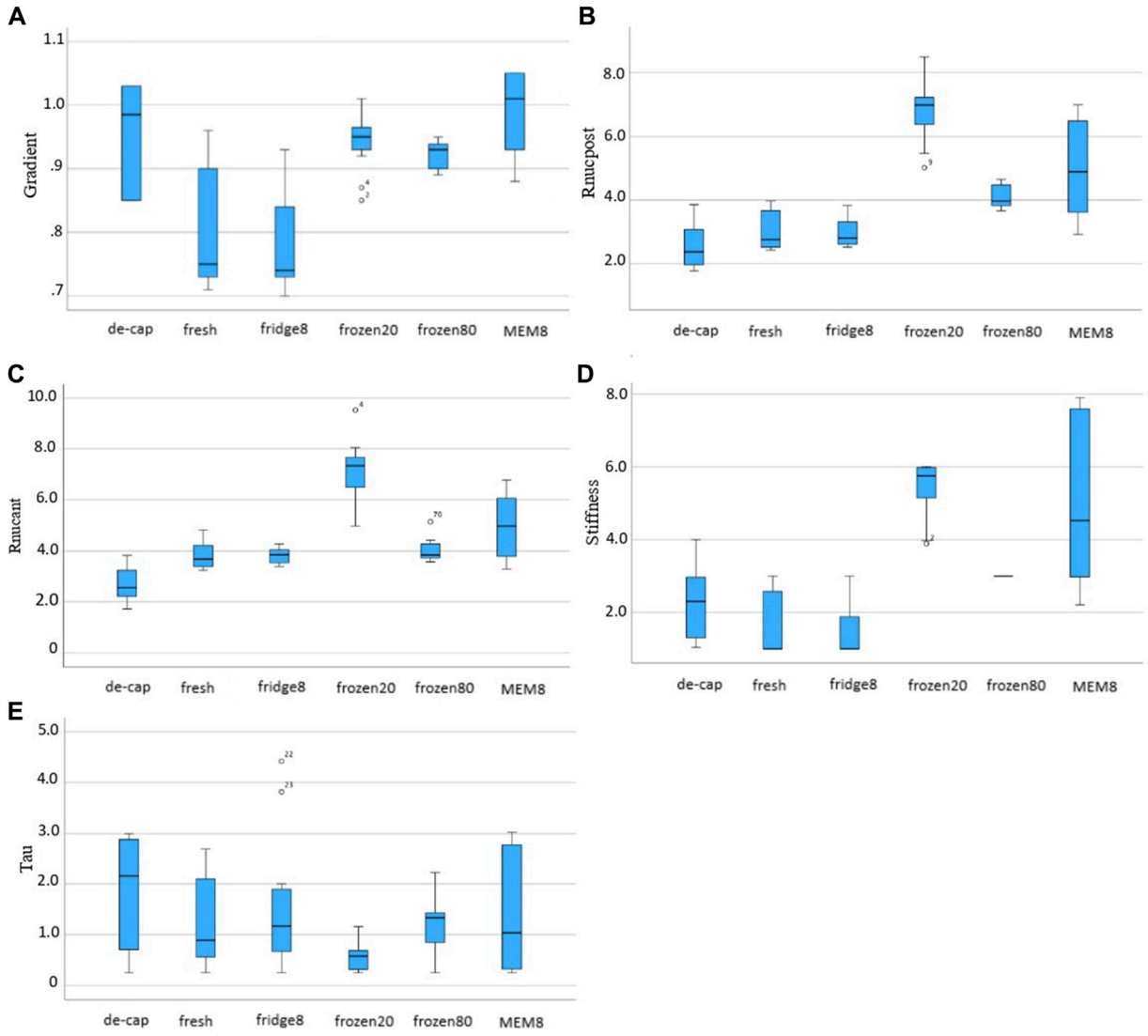

FIGURE 7
Box and whiskers plots for the inversely derived mechanical parameters: **(A)** form factor F, **(B)** ratio $\frac{C^{\infty}_{10-N}}{C_{10-POST}}$, **(C)** ratio $\frac{C^{\infty}_{10-N}}{C_{10-ANT}}$, **(D)** stiffness $N_{stiffness}$, **(E)** τ_1.

lower amplitude (1.70, $p = 0.005$). No significant differences were observed between short and long relaxation times. When comparing the absolute strain amplitudes in the nucleus (Figure 5E) and cortex (Figure 5E), freezing at −20°C induced both, a significant decrease in the nuclear strain amplitude by −4.23‰ ($p < 0.001$) and an increase in the cortical strain amplitude by +6.43‰ ($p < 0.001$). Freezing at −80°C induced more subtle changes in nuclear (−1.74‰, $p < 0.001$) and cortical strains (+2.40‰, $p = 0.005$). Decapsulation resulted in a reduced nuclear strain amplitude of −1.30‰ ($p = 0.010$) and an increased cortical strain amplitude by +1.19‰ ($p = 0.041$), compared to the fresh group.

When comparing the different lens conditions in terms of the time delay between nucleus and cortex (Figure 5F), freezing at −20°C and −80°C demonstrated a significantly higher delay than the fresh group (−132 ms vs. −176 ms and −173 ms, $p \leq 0.015$). No differences were found between short and long relaxation times. Supplementary Figure S1 show the average oscillation pattern in different regions of the lens (cortex and nucleus) for the different conditions.

3.2 Numerical results

Figure 7 presents the mechanical parameters retrieved from iFEA. The inverse fitting was best in the refrigerator condition (91.6%, 91.8%)—with short and long relaxation times, respectively –, followed by MEM (89.8%, 91.6%), decapsulated (88.8%, 86.8%), fresh (87.0%, 82.0%), frozen80 (85.2%, 88.0%) and frozen20 (89.0%, 80.0%) conditions, as determined by the R^2 (R square) value.

Over all conditions, τ_1 (1.43 ± 2.07 s vs. 0.82 ± 1.17 s, $p = 0.023$) and the form factor F (0.94 ± 0.16 gf vs. 0.92 ± 0.10 gf, $p = 0.039$) were significantly higher with short compared to long relaxation times. Yet, no significant differences between short and long relaxation times were observed at the level of an individual group.

$N_{stiffness}$ was significantly higher in frozen, both at −20°C and −80°C, and MEM conditions compared to fresh lenses (5.76 ± 0.89, 3.00 ± 0.00 and 4.53 ± 4.67 vs. 1.00 ± 1.69, both $p < 0.01$). Form factor F was significantly higher in decapsulated (0.985 ± 0.18, $p = 0.005$), frozen20 (0.943 ± 0.05, $p = 0.005$) and MEM (1.01 ± 0.13, $p < 0.001$) conditions compared to intact fresh lenses. The ratio between nuclear and cortical strains $\frac{C^{\infty}_{10-N}}{C_{10-ANT}}$ (7.18 ± 1.17 vs. 3.79 ± 0.51, $p = .004$) and $\frac{C^{\infty}_{10-N}}{C_{10-POST}}$ (6.78 ± 0.92 vs. 3.04 ± 0.62, $p < 0.001$) were both increased after freezing at −20°C (but not at −80°C), compared to the fresh condition.

4 Discussion

Storage of the lens tissue between the time of enucleation and the time when experimental testing is performed is unavoidable when working with human donor eyes. The more important is that an adequate type of storage is chosen that does not alter the lens optical and mechanical properties. While the impact of lens storage was addressed in selected studies[11(p71),12,14], a spatially-resolved assessment of different interior regions within the lens has not been studied before. Here, we propose OCE in combination with iFEA as a novel tool to assess the internal lens deformations under a controlled compression stimulus for a mechanical characterization at a much higher resolution as before. This study is a further extension of our recent article (Cabeza-Gil et al., 2023), in which we described the combination of compression based OCE with iFEA for the inverse mechanical characterization of fresh *ex vivo* porcine lenses.

The highest impact on the strain distribution within the lens was observed after freezing at −20°C and to a lesser extent after freezing at −80°C. It had been hypothesized earlier that freezing could be associated with structural damage to the lens capsule and this way affect its mechanical behavior. However, despite an increased hydration (thickness) of the lens capsule after freezing was found, its mechanical properties were previously reported to be hardly affected with a 20% decrease in elastic modulus at 0.4 of strain. (Krag and Andreassen, 1998). In contrast, the observations of the current study suggest a substantial change of the internal lens mechanics after freezing, particularly at −20°C. Interestingly, the stiffness in the cortex (weakening) and nucleus (stiffening) experienced changes in opposite directions, which might explain why earlier studies assessing the macroscopic stiffness of the whole lens hardly found a difference. Compared to the preservation in MEM, which experienced a similar increase in lens thickness as the freezing condition, the modified strain distribution across cortex and nucleus appears to be specifically associated with freezing and not related to the lens geometry. The freezing process in porous media such as soil (Talamucci, 2003) has been described to similarly induce a volumetric increase as we observed in the current study, but only if the freezing rate was slow and the overburden pressure was low. We did not observe this effect in the lens. Even though the freezing-induced changes were smaller at −80°C (with a faster freezing rate) compared to −20°C, they were not completely absent. Further increasing the freezing rate to −190°C by immersing the eye globe into liquid nitrogen did burst the eye and thus was not feasible, at least for intact eye globe preservation. The current study is in agreement with earlier findings that suggest storage in the refrigerator (Fisher, 1971) does not significantly affect the lens mechanics.

Overall, our results agree with earlier literature (Ambekar et al., 2020) that the porcine lens has a stiffer nucleus than cortex. (1.98 kPa anterior, 2.93 kPa posterior cortex, 11.9 kPa nucleus). A recent OCE study (Mekonnen et al., 2023) on ARF-stimulated wave propagation concluded that both, the elastic modulus and the shear viscosity coefficient decreased after lens decapsulation (E = 8.14 kPa and $\eta = 0.89$ Pa s versus E = 3.10 kPa and $\eta = 0.28$ Pa·s). Interestingly, in the current study we observed the opposite behavior suggesting an increase in the lens stiffness after decapsulation. This discrepancy might originate from a pre-stress in the lens and capsule due to the presence of the latter, which was not considered in any of these experimental assessments.

The main limitation of the current study is the relatively small sample size and the precision of the load cell to measure force relaxation. Also, it might be perceived that an experimental limitation of the current study was that the maximal forces applied in MEM and frozen groups were higher, because the same lamella distance was used for compression as in the fresh condition. Nevertheless, the fact that no differences were observed in the strain-related measures among short and long relaxation times suggests that the degree of pre-compression had a minor effect on the elastographic assessment. On the other hand, in terms of the inverse FEM, the different degree of pre-strain was adequately

considered such that it did not have any negative impact on the numerical results. The primary limitation of the numerical model lies in its own lack of robustness, which is constrained by the potential variability in lens responses under different preservation methods. While the model facilitates the replication of various experimental tests, it necessitates multiple parameters to fully comprehend the crystalline behavior. Advanced material models incorporating features such as porosity and nonlinear viscoelasticity will be explored in forthcoming analyses to potentially yield a more robust depiction of crystalline behavior. In some samples the average (macroscopic strain across the entire lens thickness) differed more than 10% from the theoretically-expected value. Another limitation is that g1 was fixed for all conditions. While this reduced the probability of overfitting, at the same time our methodology was ignorant to any changes in g1 the preservation condition might have caused. Another limitation is that experiments were performed at room temperature instead of body temperature, which reportedly has a measurable effect on the absolute stiffness of the lens (Heilman et al., 2022). However, the primary goal of this study was to assess the impact of different preservation conditions on the lens biomechanics. As all groups were tested at the same temperature and furthermore, we restricted our analyses to relative stiffness ratios, we do not expect any temperature-related bias on the conclusions retrieved in here.

In conclusion, OCT elastography in combination with iFEA is a powerful tool to investigate the mechanical properties of the *ex vivo* lens with high spatial resolution. Our approach was able to detect mechanical changes induced by different preservation techniques, which is critical for a correct interpretation of previous experimental studies on *ex vivo* lenses. At the same time, we could reveal subtle differences in the overall lens' mechanical behavior due to decapsulation.

Data availability statement

The original contributions presented in the study are included in the article/Supplementary Material, further inquiries can be directed to the corresponding author.

Ethics statement

Ethical approval was not required for the study involving animals in accordance with the local legislation and institutional requirements because experiments on *ex vivo* porcine tissue do not require prior ethical approval in Switzerland.

Author contributions

VT: Data curation, Writing–review and editing, Writing–original draft. IG: Writing–review and editing, Writing–original draft, Visualization, Software, Methodology, Investigation, Data curation. SK: Writing–review and editing, Writing–original draft, Supervision, Software, Project administration, Methodology, Investigation, Conceptualization.

Funding

The author(s) declare that financial support was received for the research, authorship, and/or publication of this article. This work received funding from the European Union's HORIZON 2020 research and innovation programme under grant agreement No. 956720.

Conflict of interest

The authors declare that the research was conducted in the absence of any commercial or financial relationships that could be construed as a potential conflict of interest.

Publisher's note

Supplementary material

The Supplementary Material for this article can be found online at: https://www.frontiersin.org/articles/10.3389/fbioe.2024.1398659/full#supplementary-material

References

Alzoubi, D., Rich, W., and Reilly, M. A. (2024). Automated compression testing of the ocular lens. *J. Vis. Exp.* 206. doi:10.3791/66040

Ambekar, Y. S., Singh, M., Zhang, J., Nair, A., Aglyamov, S. R., Scarcelli, G., et al. (2020). Multimodal quantitative optical elastography of the crystalline lens with optical coherence elastography and Brillouin microscopy. *Biomed. Opt. express* 11 (4), 2041–2051. doi:10.1364/boe.387361

Besner, S., Scarcelli, G., Pineda, R., and Yun, S. H. (2016). *In vivo* Brillouin analysis of the aging crystalline lens. *Investigative Ophthalmol. Vis. Sci.* 57 (13), 5093–5100. doi:10.1167/iovs.16-20143

Cabeza-Gil, I., Tahsini, V., and Kling, S. (2023). Viscoelastic properties of porcine lenses using optical coherence elastography and inverse finite element analysis. *Exp. eye Res.* 233, 109558. doi:10.1016/j.exer.2023.109558

Czygan, G., and Hartung, C. (1996). Mechanical testing of isolated senile human eye lens nuclei. *Med. Eng. Phys.* 18 (5), 345–349. doi:10.1016/1350-4533(95)00076-3

Fisher, R. (1971). The elastic constants of the human lens. *J. physiology* 212 (1), 147–180. doi:10.1113/jphysiol.1971.sp009315

Heilman, B. M., Durkee, H., Rowaan, C. J., Arrieta, E., Kelly, S. P., Ehrmann, K., et al. (2022). Temperature affects the biomechanical response of *in vitro* non-human primate lenses during lens stretching. *Exp. eye Res.* 216, 108951. doi:10.1016/j.exer.2022.108951

Heilman, B. M., Manns, F., Ruggeri, M., Ho, A., Gonzalez, A., Rowaan, C., et al. (2018). Peripheral defocus of the monkey crystalline lens with accommodation in a lens stretcher. *Investigative Ophthalmol. Vis. Sci.* 59 (5), 2177–2186. doi:10.1167/iovs.17-23273

Jones, C. E., Atchison, D. A., Meder, R., and Pope, J. M. (2005). Refractive index distribution and optical properties of the isolated human lens measured using magnetic resonance imaging (MRI). *Vis. Res.* 45 (18), 2352–2366. doi:10.1016/j.visres.2005.03.008

Kling, S. (2020). Optical coherence elastography by ambient pressure modulation for high-resolution strain mapping applied to patterned cross-linking. *J. R. Soc. Interface* 17 (162), 20190786. doi:10.1098/rsif.2019.0786

Krag, S., and Andreassen, T. T. (1998). Effect of freezing on lens capsule mechanical behavior. *Ophthalmic Res.* 30 (5), 280–285. doi:10.1159/000055485

Kuszak, J. (1995). The ultrastructure of epithelial and fiber cells in the crystalline lens. *Int. Rev. Cytol.* 163, 305–350. doi:10.1016/s0074-7696(08)62213-5

Lanchares, E., Navarro, R., and Calvo, B. (2012). Hyperelastic modelling of the crystalline lens: accommodation and presbyopia. *J. Optometry* 5 (3), 110–120. doi:10.1016/j.optom.2012.05.006

Li, Y., Zhu, J., Chen, J. J., Yu, J., Jin, Z., Miao, Y., et al. (2019). Simultaneously imaging and quantifying *in vivo* mechanical properties of crystalline lens and cornea using optical coherence elastography with acoustic radiation force excitation. *Apl. photonics* 4 (10), 106104. doi:10.1063/1.5118258

Martinez-Enriquez, E., De Castro, A., Mohamed, A., Maceo Heilman, B., Williams, S., Nandyala, S., et al. (2020). 3D OCT-based geometrical changes of human crystalline lenses during simulated accommodation in a lens stretcher. *Investigative Ophthalmol. Vis. Sci.* 61 (7), 1713.

Marussich, L., Manns, F., Nankivil, D., Maceo Heilman, B., Yao, Y., Arrieta-Quintero, E., et al. (2015). Measurement of crystalline lens volume during accommodation in a lens stretcher. *Investigative Ophthalmol. Vis. Sci.* 56 (8), 4239–4248. doi:10.1167/iovs.15-17050

Mekonnen, T., Zevallos-Delgado, C., Zhang, H., Singh, M., Aglyamov, S. R., and Larin, K. V. (2023). The lens capsule significantly affects the viscoelastic properties of the lens as quantified by optical coherence elastography. *Front. Bioeng. Biotechnol.* 11, 1134086. doi:10.3389/fbioe.2023.1134086

Regal, S., O'Connor, D., Brige, P., Delattre, R., Djenizian, T., and Ramuz, M. (2019). Determination of optical parameters of the porcine eye and development of a simulated model. *J. Biophot.* 12 (11), e201800398. doi:10.1002/jbio.201800398

Reilly, M. A., and Cleaver, A. (2017). Inverse elastographic method for analyzing the ocular lens compression test. *J. Innovative Opt. Health Sci.* 10 (06), 1742009. doi:10.1142/s1793545817420093

Reilly, M. A., Martius, P., Kumar, S., Burd, H. J., and Stachs, O. (2016). The mechanical response of the porcine lens to a spinning test. *Z. für Med. Phys.* 26 (2), 127–135. doi:10.1016/j.zemedi.2015.12.009

Sharma, P., Busscher, H., Terwee, T., Koopmans, S., and van Kooten, T. (2011). A comparative study on the viscoelastic properties of human and animal lenses. *Exp. eye Res.* 93 (5), 681–688. doi:10.1016/j.exer.2011.08.009

Sheppard, A. L., Evans, C. J., Singh, K. D., Wolffsohn, J. S., Dunne, M. C., and Davies, L. N. (2011). Three-dimensional magnetic resonance imaging of the phakic crystalline lens during accommodation. *Investigative Ophthalmol. Vis. Sci.* 52 (6), 3689–3697. doi:10.1167/iovs.10-6805

Talamucci, F. (2003). Freezing processes in porous media: formation of ice lenses, swelling of the soil. *Math. Comput. Model.* 37 (5-6), 595–602. doi:10.1016/s0895-7177(03)00053-0

Taylor, V. L., Al-Ghoul, K. J., Lane, C. W., Davis, V. A., Kuszak, J. R., and Costello, M. J. (1996). Morphology of the normal human lens. *Investigative Ophthalmol. Vis. Sci.* 37 (7), 1396–1410.

Weeber, H. A., Eckert, G., Pechhold, W., and van der Heijde, R. G. (2007). Stiffness gradient in the crystalline lens. *Graefe's Archive Clin. Exp. Ophthalmol.* 245 (9), 1357–1366. doi:10.1007/s00417-007-0537-1

Weeber, H. A., Eckert, G., Soergel, F., Meyer, C. H., Pechhold, W., and van der Heijde, R. G. (2005). Dynamic mechanical properties of human lenses. *Exp. eye Res.* 80 (3), 425–434. doi:10.1016/j.exer.2004.10.010

Weeber, H. A., and Van Der Heijde, R. G. (2008). Internal deformation of the human crystalline lens during accommodation. *Acta Ophthalmol.* 86 (6), 642–647. doi:10.1111/j.1600-0420.2007.01116.x

Wilde, G., Burd, H., and Judge, S. (2012). Shear modulus data for the human lens determined from a spinning lens test. *Exp. eye Res.* 97 (1), 36–48. doi:10.1016/j.exer.2012.01.011

Wu, C., Aglyamov, S. R., Han, Z., Singh, M., Liu, C. H., and Larin, K. V. (2018). Assessing the biomechanical properties of the porcine crystalline lens as a function of intraocular pressure with optical coherence elastography. *Biomed. Opt. express* 9 (12), 6455–6466. doi:10.1364/boe.9.006455

Yoon, S., Aglyamov, S., Karpiouk, A., and Emelianov, S. (2012). A high pulse repetition frequency ultrasound system for the *ex vivo* measurement of mechanical properties of crystalline lenses with laser-induced microbubbles interrogated by acoustic radiation force. *Phys. Med. Biol.* 57 (15), 4871–4884. doi:10.1088/0031-9155/57/15/4871

Zaitsev, V. Y., Matveyev, A. L., Matveev, L. A., Gelikonov, G. V., Sovetsky, A. A., and Vitkin, A. (2016). Optimized phase gradient measurements and phase-amplitude interplay in optical coherence elastography. *J. Biomed. Opt.* 21 (11), 116005. doi:10.1117/1.jbo.21.11.116005

Zhang, H., Singh, M., Zvietcovich, F., Larin, K., and Aglyamov, S. (2022). Age-related changes in the viscoelasticity of rabbit lens characterised by surface wave dispersion analysis. *Quantum Electron.* 52 (1), 42–47. doi:10.1070/qel17964

Zhang, X., Wang, Q., Lyu, Z., Gao, X., Zhang, P., Lin, H., et al. (2018). Noninvasive assessment of age-related stiffness of crystalline lenses in a rabbit model using ultrasound elastography. *Biomed. Eng. online* 17 (1), 75–11. doi:10.1186/s12938-018-0509-1

frontiers | Frontiers in Bioengineering and Biotechnology

TYPE Original Research
PUBLISHED 25 July 2024
DOI 10.3389/fbioe.2024.1406870

OPEN ACCESS

EDITED BY
C. Ross Ethier,
Georgia Institute of Technology, United States

REVIEWED BY
Marco Parente,
University of Porto, Portugal
Osama Maklad,
University of Greenwich, United Kingdom

*CORRESPONDENCE
Elena Redaelli,
elena.redaelli@unizar.es

RECEIVED 25 March 2024
ACCEPTED 17 June 2024
PUBLISHED 25 July 2024

CITATION
Redaelli E, Calvo B, Rodriguez Matas JF, Luraghi G and Grasa J (2024), Non-contact tonometry: predicting intraocular pressure using a material—corneal thickness—independent methodology. *Front. Bioeng. Biotechnol.* 12:1406870. doi: 10.3389/fbioe.2024.1406870

Non-contact tonometry: predicting intraocular pressure using a material—corneal thickness—independent methodology

Elena Redaelli[1]*, Begoña Calvo[1,2], Jose Felix Rodriguez Matas[3], Giulia Luraghi[3] and Jorge Grasa[1,2]

[1]Aragón Institute of Engineering Research (I3A), Universidad de Zaragoza, Zaragoza, Spain, [2]Centro de Investigación Biomecánica en Red en Bioingeniería, Biomateriales y Nanomedicina (CIBER-BBN), Zaragoza, Spain, [3]LaBS, Department of Chemistry, Materials and Chemical Engineering "Giulio Natta", Politecnico di Milano, Milan, Italy

Introduction: Glaucoma, a leading cause of blindness worldwide, is primarily caused by elevated intraocular pressure (IOP). Accurate and reliable IOP measurements are the key to diagnose the pathology in time and to provide for effective treatment strategies. The currently available methods for measuring IOP include contact and non contact tonometers (NCT), which estimate IOP based on the corneal deformation caused by an external load, that in the case of NCT is an air pulse. The deformation of the cornea during the tonometry is the result of the coupling between the IOP, the mechanical properties of the corneal tissue, the corneal thickness, and the external force applied. Therefore, there is the need to decouple the four contributions to estimate the IOP more reliably.

Methods: This paper aims to propose a new methodology to estimate the IOP based on the analysis of the mechanical work performed by the air jet and by the IOP during the NCT test. A numerical eye model is presented, initially deformed by the action of a falling mass to study the energy balance. Subsequently, Fluid-Structure Interaction (FSI) simulations are conducted to simulate the action of Corvis ST.

Results and discussion: The new IOP estimation procedure is proposed based on the results of the simulations. The methodology is centred on the analysis of the time of maximum apex velocity rather than the point of first applanation leading to a new IOP estimation not influenced by the geometrical and mechanical corneal factors.

KEYWORDS

intraocular pressure, fluid structure interaction simulation, central corneal thickness, corneal mechanical properties, energetic balance, Corvis ST

1 Introduction

One of the objectives of the human eye is the convergence of incoming light rays from the external environment onto the retina, situated on the posterior segment of the eye. The retina establishes a connection with the brain through the optic nerve, which transmits visual signals. The aqueous humor, a clear fluid that fills the ocular chamber, maintains the eye's structural integrity and is pressurized within a range of 8–20 mmHg in healthy conditions, referred to as intraocular pressure (IOP) (Wang et al., 2018). The equilibrium between the production and drainage of aqueous humor governs the IOP, which, when

elevated, poses a substantial risk factor for the development of glaucoma, a collective term for a group of eye disorders that can lead to irreversible vision loss (Jordanova et al., 2022). The vision impairment associated with glaucoma is primarily attributed to the degeneration of the optic nerve, which is a consequence of elevated IOP. Glaucoma is a leading cause of blindness worldwide, after cataracts in underdeveloped countries and after senile degeneration of the macula in developed countries (Jordanova et al., 2022). In 2020, the disease affected about 80 million people globally, and this figure is projected to rise to 111 million by 2040 (Brusini et al., 2022). Because glaucoma has a gradual onset and lacks noticeable symptoms until late stages, it is often referred to as a "silent disease" (Brusini et al., 2022). In this context, reducing IOP is the primary option available for managing the pathology and preventing blindness (Sharma et al., 2020; Eliasy et al., 2022).

Accurate and repeatable IOP measurements are the key to diagnose the pathology in time and to provide for effective treatment strategies. However, currently available methods are indirect, they only provide an estimation of IOP (Brusini et al., 2021; Brusini et al., 2022; Silva and Lira, 2022), and the evaluation of their precision and accuracy is a critical field of research.

Ophthalmologists use a variety of techniques to measure IOP, including Goldmann applanation tonometry (GAT) (Goldmann and Schmidt, 1957) and Non Contact Tonometry (NCT) such as Corvis ST and Ocular Response Analyzer (ORA). The gold standard is GAT: it involves the use of a probe that is gently pressed against the cornea to flatten a small area, creating a uniform surface of known size. A calibrated force is then applied to the probe, and the amount of force required to flatten the cornea is measured. The estimation of IOP in GAT is based on the Imbert-Fick law (Imbert, 1885): it is a modification of the Maklakoff law (Maklakoff, 1885), and states that an external force against a sphere equals the pressure in the sphere multiplied by the area applanated by the external force. The validity of the law requires that the sphere should be perfectly spherical, dry, perfectly flexible and infinitely thin (Sharma et al., 2020), conditions that are not fulfilled in the cornea (Wu et al., 2020; Brusini et al., 2021). Other methods to measure the IOP are the ORA and the Corvis ST, which are NCTs. Their purpose is to obtain IOP measurements with minimal invasion of the eye (Silva and Lira, 2022); the idea is the same as GAT but the deformation of the cornea is obtained by a high-velocity air jet, without the need of contact. The difference between ORA and Corvis ST is that in the former, the air pressure at the outlet of the device varies among patients, while in the latter it is always the same; however, both of them provide an estimation of the IOP based on the first applanation time of the cornea during the air jet. In addition, Corvis ST is equipped with a Scheimpflug camera which gives 140 images of the central section of the cornea over the 30 ms of the air jet.

Although GAT and NCT are the most widely used instruments to estimate the IOP (Silva and Lira, 2022), their accuracy is significantly affected by the thickness of the cornea and the mechanical properties of corneal tissue (Ariza-Gracia et al., 2015; Asaoka et al., 2015; Greene et al., 2016). It has been proved (Ajazaj et al., 2018), for instance, that IOP measurements following LASIK refractive surgeries for the correction of myopia may be unreliable due to changes in central corneal thickness (CCT) and due to the applanation of the corneal surface after surgery. To mitigate the risk of obtaining falsely low IOP applanation readings after LASIK, adjustments should be made to the measured IOP, as highlighted in studies such as (Kohlhaas et al., 2006; Ajazaj et al., 2018; Helmy and Hashem, 2020). Other studies demonstrated that the biomechanical properties of the eye affect the measurement of IOP (Liu and Roberts, 2005; Kaushik et al., 2012; Aoki et al., 2023). The corneal deformation during tonometry is the result of the coupling between four factors: the IOP, the mechanical properties of the corneal tissue, the corneal geometry (in particular, its thickness), and the external force applied (Ariza-Gracia et al., 2015). The first applanation time used to estimate the IOP in NCT, could be different in patients with the same IOP because those patients can have different corneal mechanical properties or different corneal geometries.

Corvis ST provides a corneal-corrected IOP measurement, the bIOP, designed to exclude the influence of central corneal thickness and age (Joda et al., 2016; Eliasy et al., 2022). There is still a need to reduce its dependence on corneal mechanical properties. bIOP derives from an algorithm correlating various dynamic corneal response parameters obtained through structural numerical simulations of Corvis ST (Eliasy et al., 2022). However, the simulations assume a constant air pressure over the corneal apex which does not depend on corneal deformation like in the real scenario. Furthermore, the numerical model assumes the mechanical properties of the corneal tissue solely age-dependent. While age is a factor, individuals of the same age may exhibit different mechanical properties in their corneal tissue (Ariza-Gracia et al., 2015). As a consequence of this simplification, the algorithm proposed can be improved. A methodology to reliably estimate the IOP not influenced by the mechanical properties and geometry of the cornea is still missing.

This paper aims to propose a new methodology to estimate the IOP. The methodology is based on the analysis of the internal and external energies impacting the anterior corneal surface during the first 10 ms of the corneal deformation during the air puff.

The paper is organized as follows. In the materials and methods section, the numerical model of the eye is presented. Two different loading conditions are proposed: a simplified model of a mass falling under the gravity effect - which allows for a easier examination of the external energy exerted on the eye - and a Fluid-Structure Interaction (FSI) simulation simulating the air puff of Corvis ST. In the same section, the energetic analysis is outlined highlighting the region of interest (the anterior corneal surface) and the energies playing a role in the deformation of the eye. In the following section, the results of the energetic analysis are presented for both the loading cases. Then, the new methodology to estimate the IOP is proposed. The paper concludes with a discussion of the obtained results.

2 Materials and methods

2.1 Numerical model

The structural model of the eye used in the simulations is depicted in Figure 1A. It comprises cornea, limbus, sclera and humors. The humors are modelled as an incompressible fluid pressurized at IOP. The cornea and the limbus are described as anisotropic, nearly incompressible, hyperelastic materials, to

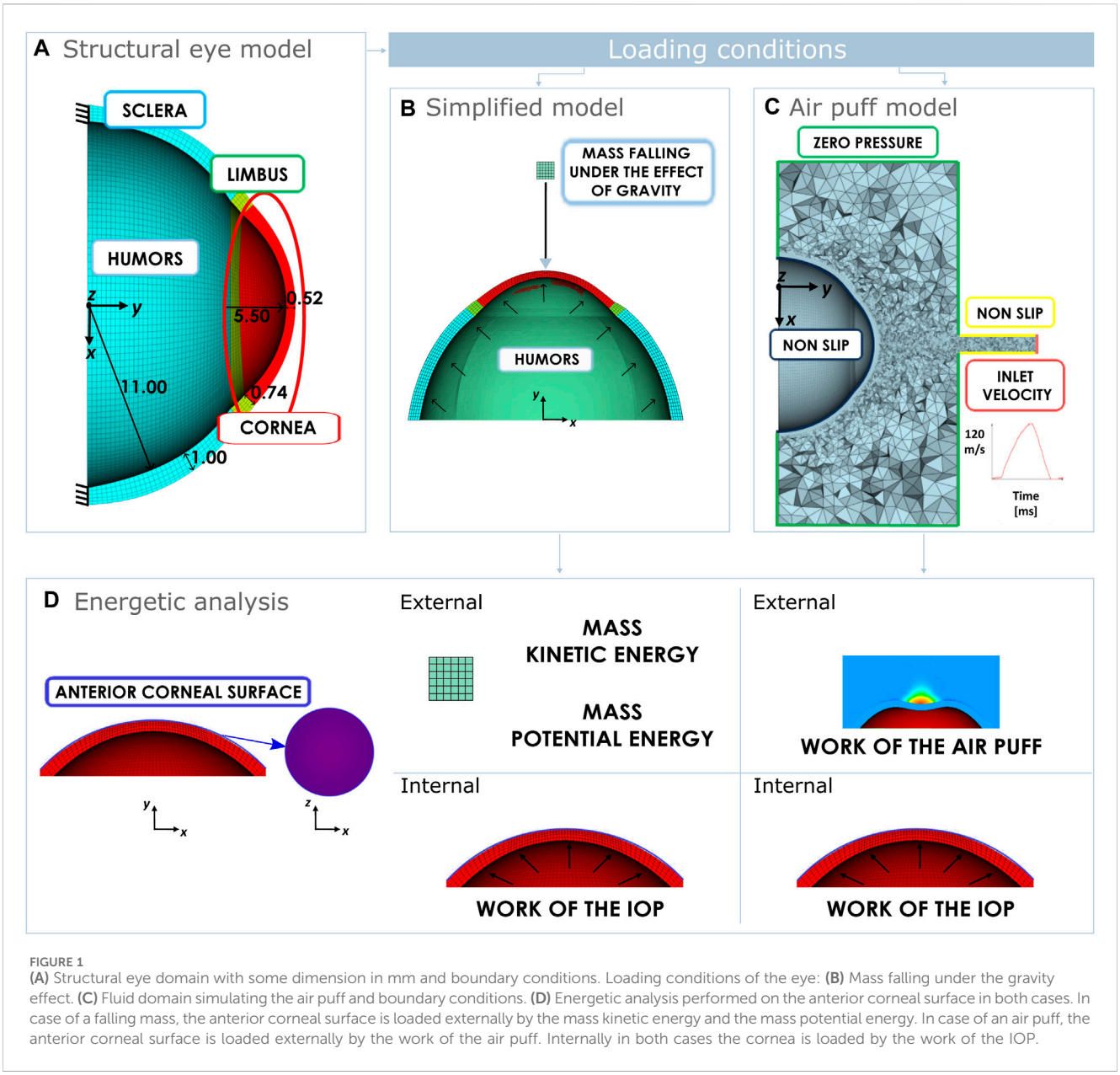

FIGURE 1
(A) Structural eye domain with some dimension in mm and boundary conditions. Loading conditions of the eye: **(B)** Mass falling under the gravity effect. **(C)** Fluid domain simulating the air puff and boundary conditions. **(D)** Energetic analysis performed on the anterior corneal surface in both cases. In case of a falling mass, the anterior corneal surface is loaded externally by the mass kinetic energy and the mass potential energy. In case of an air puff, the anterior corneal surface is loaded externally by the work of the air puff. Internally in both cases the cornea is loaded by the work of the IOP.

account for the influence given by the network of collagen fibres. The cornea is described with two families of mutually orthogonal collagen fibres assumed perfectly aligned with the nasal-temporal (NT) and superior-inferior (SI) direction and the limbus is described with one circumferential family of fibres. In both cases, the Holzapfel-Gasser-Ogden (Holzapfel et al., 2000) constitutive model is used. Eq. (1) shows the isochoric contribution of this model to the free energy.

$$\bar{\Psi} = C_{10}\left(\bar{I}_1 - 3\right) + \frac{k_1}{2k_2}\sum_{i=4,6} e^{k_2\left(\bar{I}_i - 1\right)^2} \tag{1}$$

where C_{10}[MPa] is a material parameter related to the extracellular matrix behaviour, k_1[MPa] refers to the stiffness of the fibres and k_2[-] models their non-linearity. I_1 is the first invariant of the right isochoric Cauchy-Green stress tensor, while I_4 and I_6 are respectively the fourth and the sixth pseudo-invariants related to the fibres stretch. The sclera is modelled as a nearly incompressible hyperelastic isotropic material with a Neo-Hookean formulation Eq. (2).

$$\bar{\Psi} = C_{10}\left(\bar{I}_1 - 3\right) \tag{2}$$

More details on the geometry and materials functions used in the structural model can be found in our previous work (Redaelli et al., 2024). The geometry is meshed using software ANSA Pre Processor v23.01 (BETA CAE Systems, Switzerland) with hexahedral solid elements. The structural eye model presented corresponds to a pressurized configuration, therefore, in the first step of each simulation, the zero pressure configuration of the eye is computed following the iterative algorithm presented previously (Ariza-Gracia et al., 2016). Once the zero-pressure configuration is found, the incompressible fluid of the humors is pressurized to obtain the reference configuration of the eye.

10.3389/fbioe.2024.1406870

To study the energetic balance of the eye during NCT, we preliminary investigated the behaviour of a mass falling under the effect of gravity as presented in Figure 1B. A mass of 2.02 g modelled as a rigid cube with a side length of 1.5 mm, falls onto the cornea from a height of 8 mm with respect to the apex of the cornea. This simplified model is useful to comprehend the energetic balance of the eye when subjected to an external load. In this case, the total mechanical energy of the mass transmitted to the cornea during the impact is easy to calculate (corresponding to the sum of potential and kinetic energy of the mass).

Once the simplified model was analyzed, 3D FSI simulations were run to reproduce *in silico* the NCT. Since during the NCT, an air puff hit a cornea causing its deformation, FSI simulations are the best numerical approach to model the phenomenon (Ariza-Gracia et al., 2018); where the structure (the eye) and the fluids (the air sorrounding the eye and the humors) are coupled. The fluid domain of the FSI, along with the boundary conditions are depicted in Figure 1C. The inlet velocity corresponds to the velocity of the air puff at the outlet of the nozzle of Corvis ST.

In both cases, after the pressurization, a deformation of the eye occurs caused by the action of an external agent. In the first phase of the impact, small deformations occurs, then after the corneal applanation, the cornea continues to deform through bending, resulting in larger deformations.

The simulations were implemented in the finite-element solver LS-Dyna R14.0 (ANSYS, 71 Inc., Canonsburg, PA, United States) (Dev, 2024) and performed using an Intel i9-10940X (3.30 GHz) on 14 CPUs. The average computational time of the falling mass simulation was 10 min; while the average computational time of the FSI simulation was 48 h.

2.2 Energetic analysis

All mechanical motion is the result of some form of energy transformation. Work is a measure of the energy transfer that occurs when an object is moved over a distance by an external force. The sign of the work done on an object determines if energy is transferred in or out of the object. A force applied to an object in the opposite direction to its motion will tend to slow it down, and thus it would drew kinetic energy off the object. With energy leaving the object, the work done should be negative and *vice versa*.

In this study, we conducted an analysis of the mechanical work exchange occurring on the anterior corneal surface, as illustrated in Figure 1D, under the loading conditions detailed in Section 2.1. As explained earlier in the introduction, Corvis ST records by means of a Scheimpflug camera 140 images of the central section of the cornea over the 30 ms of the air jet. While the anterior corneal surface is visible at all times, the posterior corneal surface may experience distortion during corneal deformation, and cannot be acurately identified. Results of previous studies indicated statistically significant differences among the thickness values obtained from Pentacam and Corvis ST (Rajabi et al., 2022). Consequently, to make our energetic analysis more reliable, we focused on the anterior corneal surface rather than the posterior surface.

The work of external forces is computed in the y-direction due to the axi-symmetric nature of the eye model, rendering the total work along the x and z-axes zero.

In both the simulations, the cornea is loaded internally by the IOP. The work of the IOP in direction y on the anterior corneal surface can be calculated with Eq. (3).

$$\begin{aligned} \mathrm{Work}_{\mathrm{IOP}} &= \sum_{j=1}^{\mathrm{increments}} \mathrm{Work}_{\mathrm{IOP}}^{j} \\ \mathrm{Work}_{\mathrm{IOP}}^{j} &= \sum_{i=1}^{\mathrm{nodes}} \frac{\left(\mathrm{F}_{\mathrm{IOP_i}}^{j} + \mathrm{F}_{\mathrm{IOP_i}}^{j-1}\right) \cdot \left(\mathrm{u}_{\mathrm{i}}^{j} - \mathrm{u}_{\mathrm{i}}^{j-1}\right)}{2} \\ \mathrm{F}_{\mathrm{IOP_i}}^{j} &= \mathrm{IOP}\left(\Delta t^{j}\right) \cdot \mathrm{area_i}\left(\Delta t^{j}\right) \end{aligned} \tag{3}$$

where at increment j of the simulation: $\mathrm{area_i}(\Delta t^j)$ is the area associated to the node i and $\mathrm{u_i^j}$ is its displacement in direction y. Since the IOP exerted by the humors is modelled as homogenous in space, it has the same interpolated value over the nodes.

On the external side of the anterior surface, the region of interest is loaded by different conditions. In case of the mass falling under the effect of gravity, the external work transmitted to the cornea corresponds to the total mechanical energy of the mass, which is the sum of its kinetic and potential energies.

In case of the air puff, the external work due to the air is given by:

$$\begin{aligned} \mathrm{Work}_{\mathrm{AIR}} &= \sum_{j=1}^{\mathrm{increments}} \mathrm{Work}_{\mathrm{AIR}}^{j} \\ \mathrm{Work}_{\mathrm{AIR}}^{j} &= \sum_{i=1}^{\mathrm{nodes}} \frac{\left(\mathrm{F}_{\mathrm{AIR_i}}^{j} + \mathrm{F}_{\mathrm{AIR_i}}^{j-1}\right) \cdot \left(\mathrm{u}_{\mathrm{i}}^{j} - \mathrm{u}_{\mathrm{i}}^{j-1}\right)}{2} \\ \mathrm{F}_{\mathrm{AIR_i}}^{j} &= \mathrm{P}_{\mathrm{AIR_i}}\left(\Delta t^{j}\right) \cdot \mathrm{area_i}\left(\Delta t^{j}\right) \end{aligned} \tag{4}$$

where at increment j of the simulation: $\mathrm{P_{AIR_i}}(\Delta t^j)$ is the equivalent air pressure on the node i on the corneal anterior surface obtained by the software; $\mathrm{area_i}(\Delta t^j)$ is the area associated to that node and $\mathrm{u_i^j}$ is its displacement in direction y. The air pressure is calculated by the software on the center of the cell and then projected to the nodes of the mesh. The air pressure over the corneal anterior surface is not constant neither homogeneous; it depends on the corneal deformation as depicted in Figure 1D.

3 Results

3.1 Energetic analysis of the deformation of the eye under the effect of a falling mass

In this section, the results of the energy analysis of the mass falling onto the eye are presented.

Initially, the mass is at a certain height with respect to the eye and starts falling under the force of gravity. As it falls, its kinetic energy increases due to its increasing speed while its potential energy decreases. In the initial part of the plot in Figure 2, the curves are depicted with dashed lines, because numerically it is not possible to impose to the mass a sudden acceleration equal to the gravitational acceleration. Numerically, the mass begins with zero acceleration, and in the initial instants, it dynamically reaches the gravitational acceleration. For this reason, when the gravitational acceleration is reached (at 4 ms), the velocity (and therefore the kinetic energy of the mass) is not zero. When the system stabilizes, the sum of the potential and kinetic energies is constant as depicted with the red line in Figure 2.

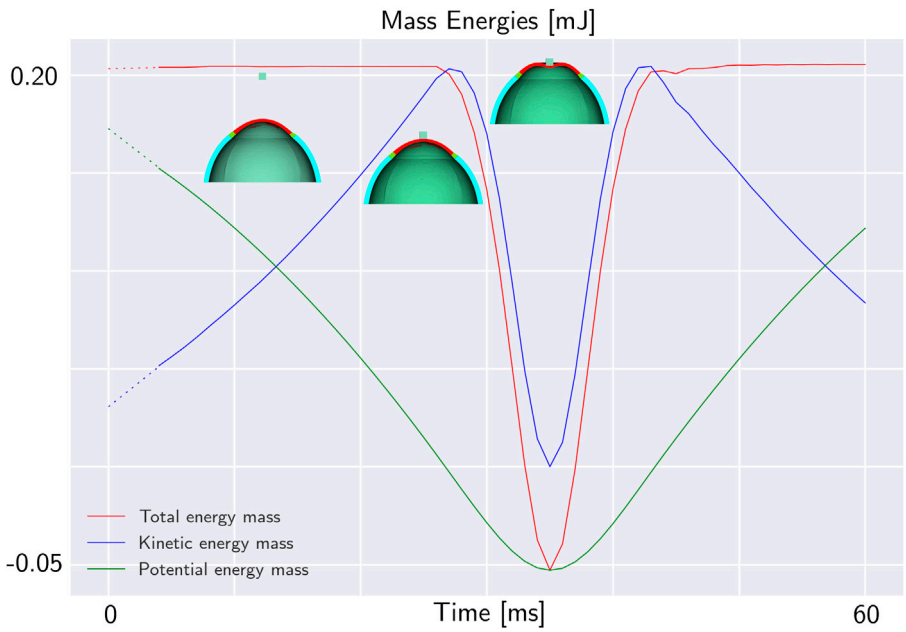

FIGURE 2
Total mechanical energy of a mass falling under the effect of gravity on the eye. The potential energy is in green, the kinetic energy in blue and the total mechanical energy in red. In the first 25 ms, the mass is falling without impacting the eyeball. Until the impact, the total mechanical energy of the mass is constant. When the mass impacts the eye, its mechanical energy decreases. At 35 ms, the maximum deformation of the eye occurs, then the structure returns to its original configuration.

When the mass contacts the external surface of the eye-globe, it starts to deform the object. For this reason, the total energy of the mass decreases. The total mechanical energy of the mass along with its potential and kinetic energy during the impact are depicted in Figure 2. At the point of impact, the energy of the mass is transmitted to the eye where it is stored in the form of elastic energy. Figure 3A. Plots both the total energy of the mass and the total internal energy of the eye. The total internal energy of the eye increases in the first 5 ms corresponding to the eye pressurization. Then, it remains constant before experiencing an important increase during the impact. Since there is no energy dissipation, the absolute decrease of the energy of the mass is equal to the increase of the internal energy of the eye as shown in Figure 3B.

Meanwhile, as the mass falls onto eye-ball, the pressure inside the chamber of the eye increases uniformly in all directions, following the principles of hydrostatic pressure (Figure 3C). This pressure acts on the surrounding walls of the container, causing it to expand to accommodate the increased pressure. The pressure in the fluid exerts a mechanical work on the anterior surface of the cornea calculated with Eq. 3. The work of the IOP increases as the pressure rises during the pressurization phase. In the pressurization phase, the work is positive because it is done by the fluid expanding the surrounding walls. After the impact with the mass, the work done by the fluid starts to decrease (Figure 3D). This decrease occurs because the displacement of the cornea is in the opposite direction to the IOP force.

On the other hand, during the impact of the mass with the eye, the internal energy of the cornea increases. Since the cornea is much more compliant than the sclera, the variation in the internal energy of the cornea during the impact is very close to the work exerted by the IOP as shown in Figure 3E. In the first phase of the impact, all the corneal deformation is converted into an increase of IOP. Moreover, even if the variation in the elastic energy of the cornea during the impact generally is an unknown fraction of the variation of the elastic energy of the eye-ball, depending on the compliance of the sclera and on the diameter of the cornea relative to the diameter of the sclera, in the first phase of the simulation this fraction is close to 1. For this reason, since the corneal deformation energy fully transmits energy to the internal fluid, we can analyze the energy balance only by considering the work done by the IOP and the external energy.

When the work of the IOP becomes equal to the total mechanical energy acting on the mass, the net force on the mass becomes zero and the mass stops accelerating. We will concentrate our analysis on the time at which the works acting on the corneal anterior surface are equal. The intersection point between the work of the IOP and the decrease in the total energy of the mass is the point of maximum kinetic energy and, therefore the point of maximum velocity of the mass as depicted in Figure 3F. The maximum velocity of the mass is equal to the maximum velocity of the corneal apex because the mass falls over the corneal apex; therefore when the works acting on the anterior corneal surface are equal, the apex velocity is maximum.

Remark 1. *The mechanical energy of the mass (kinetic and potential) is converted in deformation of the eyeball, in particular, in the first phase of the deformation it is converted in deformation energy of the cornea.*

Remark 2. *The deformation of the cornea during the impact is converted in increase of IOP.*

Remark 3. *The time when the works acting on the anterior corneal surface are equal occurs when the velocity of the apex is maximum.*

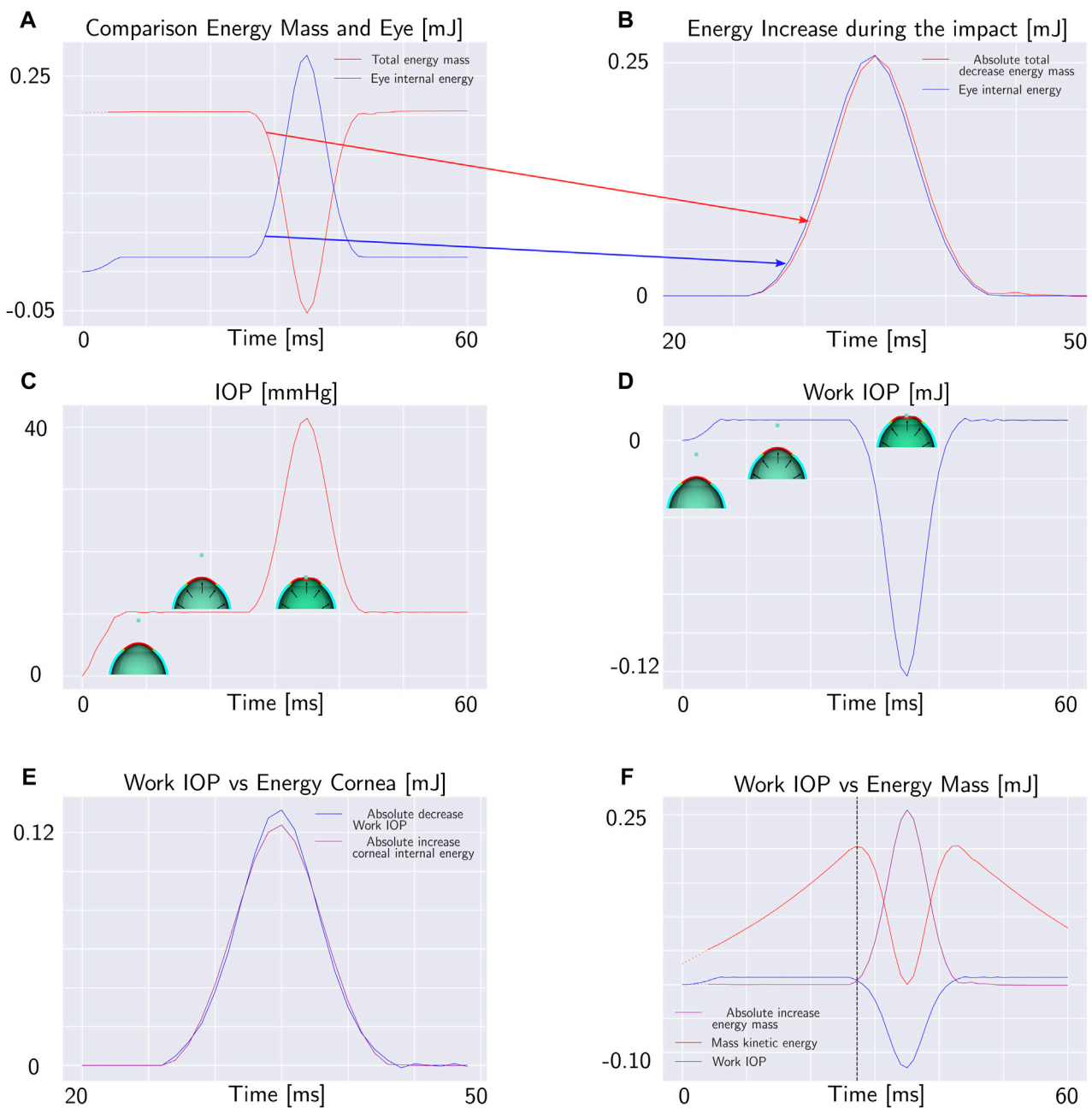

FIGURE 3
Mass falling under the effect of gravity on the eye: **(A)** Total energy of the mass and total internal energy of the eye. **(B)** Increase of the internal energy of the eye and absolute value of the decrease of the total energy of the mass during the impact. **(C)** Pressure of the fluid cavity during the impact. **(D)** Work of the internal fluid on the anterior corneal surface. **(E)** Internal energy of the cornea and work of the internal fluid (with opposite sign). **(F)** Work of the internal fluid, total energy of the mass and kinetic energy of the mass. In the intersection point between the total energy of the mass and work of the internal fluid, the kinetic energy is maximum.

3.2 Energetic analysis of the deformation of the eye under the effect of an air jet of corvis ST

According to the results obtained by the mass falling model, we propose to study the cornea subjected to the air puff of Corvis ST at the time when the works acting on the anterior corneal surface are equal. Based on those previous results, all the external energy is converted in increasing the IOP, therefore during the first part of the deformation, the energy transfer only depends on the IOP. In this section, the balance between the work of the air puff and the work of the IOP on the corneal anterior surface is calculated, to verify that the air puff effect on the eye is the same as the mass. To achieve this aim, the outline of the FSI simulation described in Section 2.1 is used with multiple combinations of mechanical properties of corneal tissue, IOP and thickness as presented in Table 1. Actually, the displacement field, strain and stress states of the FSI depend on the IOP, the mechanical properties of the corneal tissue and corneal geometry as demonstrated in our previous work (Redaelli

10.3389/fbioe.2024.1406870

TABLE 1 Parameters of the mechanical model of the corneal tissue, intraocular pressure (IOP) and central corneal thickness (CCT) for each simulation. C_{10} represents the collagen matrix stiffness in MPa, k_1 the fibers stiffness in MPa and k_2 the fibers non linearity [–].

Simulation	C_{10} [MPa]	k_1 [MPa]	k_2 [-]	IOP [mmHg]	CCT [μm]
1	0.045	0.027	180	10	558
2	0.045	0.027	180	15	558
3	0.045	0.027	180	20	558
4	0.045	0.027	180	25	558
5	0.045	0.027	180	30	558
6	0.0675	0.027	180	15	558
7	0.0225	0.027	180	15	558
8	0.045	0.0405	180	15	558
9	0.045	0.0135	180	15	558
10	0.045	0.027	270	15	558
11	0.045	0.027	90	15	558
12	0.035	0.13	1,000	15	558
13	0.01	0.015	100	15	558
14	0.045	0.027	180	15	484
15	0.045	0.027	180	15	525
16	0.045	0.027	180	15	600

et al., 2022) because it is a strongly coupled problem. In the simple problem with the mass, the energy of the mass does not depend on the eye deformation, while in this case, the air pressure over the corneal apex depends on the corneal deformation as presented in Figure 1D. We performed the same FSI simulation sixteen times, with each repetition involving a variation in one parameter in order to reproduce the NCT test for different patients. In the first thirteen simulations, the corneal geometry was the same with a Central Corneal Thickness (CCT) of 558 μm, the varying parameters of these simulations were the parameters describing the mechanical properties of the corneal tissue and the IOP. In the last three simulations, also the corneal geometry changed, with different corneal thickness. The parameters used in the simulations are listed in Table 1. For each simulation, the air pressure over the corneal anterior surface, the corneal displacement and the IOP were measured as output during the air puff. These quantities were used to calculate the work of the IOP and the work of the air pressure over the corneal anterior surface with Eqs 3, 4.

3.2.1 Pressurization phase

Initially, we analyzed the first five simulations characterized by the same CCT and mechanical properties and different IOP (ranging between 10 and 30 mmHg). The zero-pressure configuration of the eye varies in each simulation since we started from the same pressurized configuration. For this reason, the displacement of the anterior surface of the cornea from the zero pressure configuration to the end of pressurization is different in each case. The displacement contour at the end of the pressurization is depicted in Figure 4.

The deformation state of the cornea at the end of pressurization is different in each case since the displacement at the end of pressurization depends on the IOP. In particular, the maximum displacement in each case has a linear relationship with the IOP as depicted in Figure 4. The work of the IOP at the end of pressurization depends on the IOP of the patient and on the displacement of the anterior surface of the cornea. For this reason, the IOP has a quadratic relationship with the work of the IOP at the end of pressurization as depicted in Figures 5A,B.

In particular, under the mechanical properties of the corneal tissue analysed, the relationship between the IOP and the work of the IOP at the end of pressurization is defined by Eq. 5:

$$\begin{aligned} \text{IOP} = &\left(-1.69 \cdot 10^3\right) \cdot \text{Initial work IOP}^2 + \left(4.21 \cdot 10^2\right) \\ &\cdot \text{Initial work IOP} + 6.18 \\ R^2 = &\ 0.98 \end{aligned} \tag{5}$$

3.2.2 Air jet phase

In Figure 6 the evolution of the work of the air puff and the work of the IOP during the impact are represented for one of the sixteen cases from the sensitivity analysis (Table 1).

As illustrated in Figure 6A, the IOP's work increases in the first 10 ms as the eye undergoes pressurization from its initial zero-pressure state. In the subsequent stabilization step, both the work of the air puff and the work of the IOP remain constant. At 50 ms, the corneal surface is impacted by the air puff, resulting in deformation in the direction opposite to that of the IOP but in the same direction as the air puff pressure. Additionally, the IOP increases during the air puff, as depicted in Figure 6B and reported in our previous work (Redaelli et al., 2022) because the fluid is incompressible. Conversely, the work of the air puff increases during the impact (Figure 6A), while the work of the

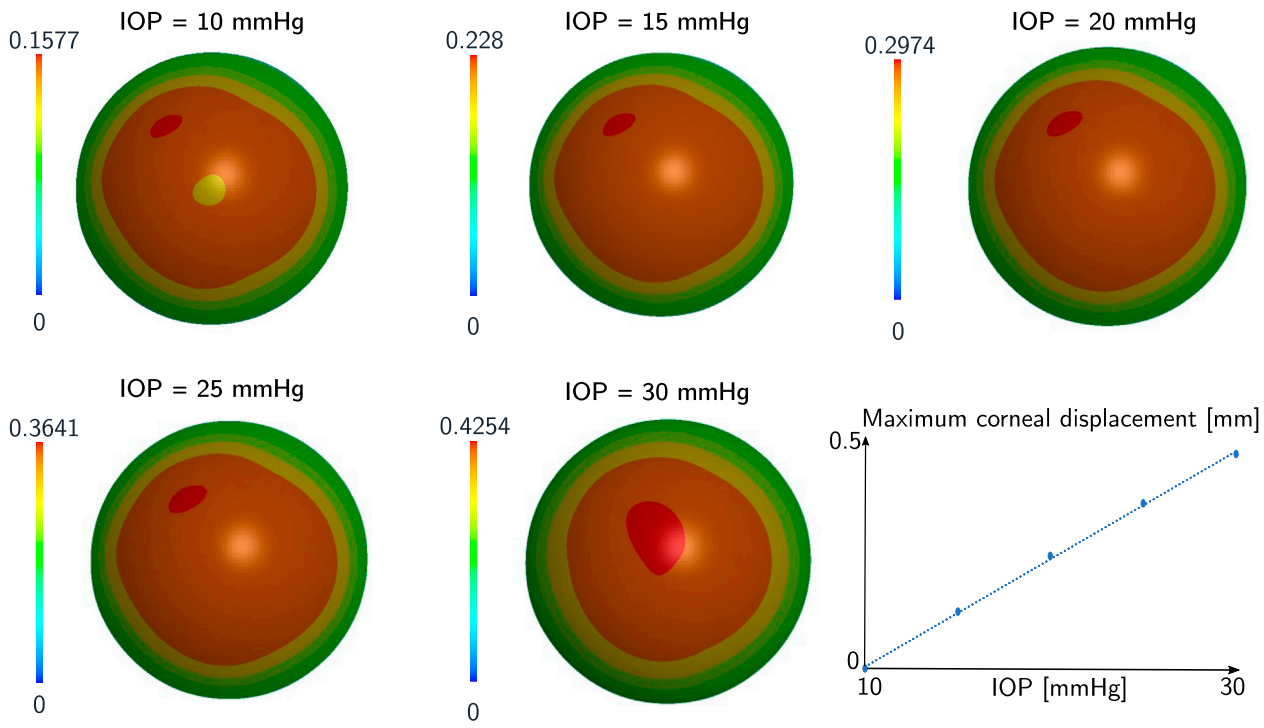

FIGURE 4
Displacement in mm of the anterior corneal surface at the end of pressurization for the first five cases of the sensitivity analysis. The mechanical properties and the geometry of the cornea are the same in each case, the IOP varies. The corneal displacement at the end of pressurization had a linear relationship with the IOP.

IOP decreases. There are two intersection points of the curves, which correspond to the time of maximum velocity of the apex. This time is different from the time of the first applanation, as shown in Figures 6C,D. The time difference is not always the same since it depends on the corneal structural properties, the range of difference is between 1 and 5 ms.

Analyzing the first five simulations characterized by the same central corneal thickness (CCT) and mechanical properties but different IOP, we observe that the work of the IOP and the work of the air puff during the impact differ in each simulation, as shown in Figure 7A. Figure 7B demonstrates that, for the considered mechanical properties and thickness, the relationship between the initial work of the IOP and the work at the intersection is linear. Specifically, the work at the intersection is approximately half of the initial work. In particular, a quadratic relationship exists between the time of maximum velocity and the initial work of the IOP, as shown in Figure 7C and reported in Eq. 6.

$$\begin{aligned}\text{Initial work IOP } [\text{mJ}] = &\left(1.09 \cdot 10^{-3}\right) \cdot \text{time}^2_{\text{max-vel}} + \left(-8.28 \cdot 10^{-3}\right) \\ &\cdot \text{time}_{\text{max-vel}} + 1.19 \cdot 10^{-2} \\ R^2 = &\ 0.98\end{aligned} \tag{6}$$

But what happens when we change the mechanical properties of the corneal tissue and the thickness of the cornea? (simulations 6–16 in Table 1). Changing both the mechanical properties of the corneal tissue and the thickness of the eye, the time of intersection between the work of the air puff and the work of the IOP does not change as demonstrated by the plots in Figures 7D,E. Therefore, this point does not depend on the geometry and mechanical proprierties of the cornea. The work of the air puff and the work of the IOP during the air puff for each simulation are reported in Figure 8.

Remark 4. *There exist a relationship between the maximum velocity time and the initial IOP.*

Remark 5. *The mechanical properties of the corneal tissue and the corneal thickness does not influence the energetic balance at the beginning of the deformation.*

4 IOP estimation with corvis ST

4.1 Clinical analysis of the first applanation time and highest velocity time

We presented in the previous sections, the results of numerical simulations of the Corvis ST test, to analyse the energy balance of the system. The outcomes of these simulations can be extrapolated to the clinical scenario, as the equipment captures the temporal evolution of apex velocity for each patient. In this section, we will delve into a detailed analysis of the apex velocity. The Corvis ST results of six healthy and six keratoconic corneas are presented in this section as an example. These data were used to evaluate if the first applanation

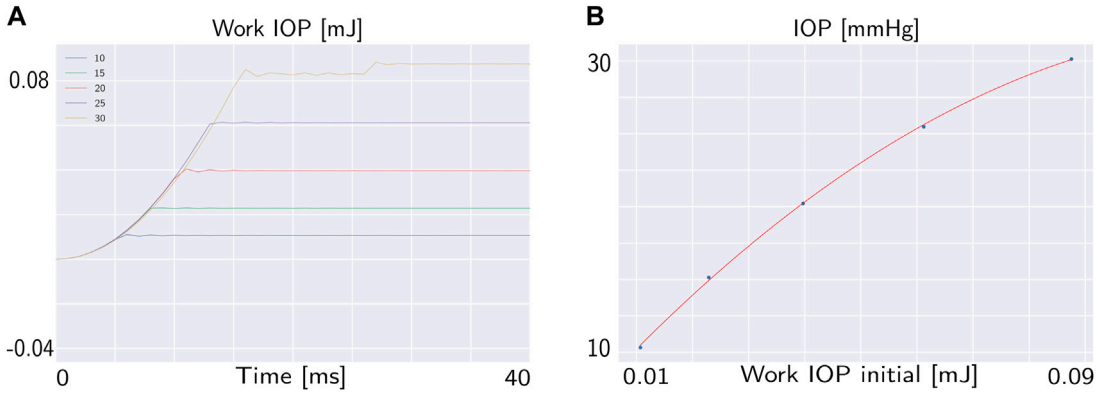

FIGURE 5
(A) Work of the IOP during the pressurization phase for different IOP. **(B)** Relationship between the work of the IOP at the end of pressurization and the IOP.

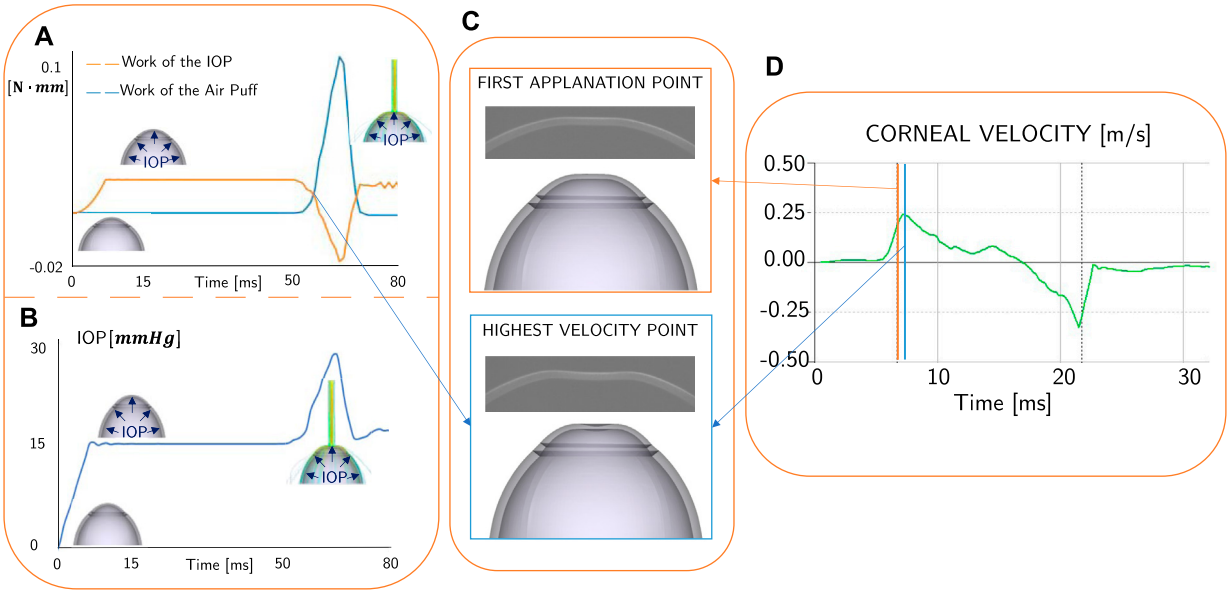

FIGURE 6
(A) Work of the air puff (in blue) and work of the IOP (in orange) calculated from the FSI simulation: the intersection point of the curves is the interest of this analysis. **(B)** Evolution of the IOP during the simulation: when the air puff impact the eye, the IOP increases. **(C)** Clinical and numerical comparison between the first applanation point and the highest velocity point. **(D)** Clinical result: apex velocity as output of Corvis ST: the first applanation time (orange line) does not coincide with the highest velocity time (blue line).

time of the cornea and the point of maximum velocity are coincident. The data used were randomly selected from a previous study conducted at Antwerp University Hospital. The study was conducted according to the tenets of the Declaration of Helsinki and participants gave signed informed consent prior to measurement (reference number of the Antwerp University Hospital Ethical Committee: 17/12/136). The analysis of the apex velocity during Corvis ST examination from both healthy and keratoconic patients, revealed that the first applanation point, typically used as reference to measure the IOP *in-vivo*, does not correspond to the instant of highest velocity of the corneal apex as shown in Figure 9. Additionally, the time difference between the maximum velocity instant and the first applanation time varies among patients. After the first applanation point, the corneal velocity continues to increase, revealing that the cornea is subjected to a positive acceleration and force. The corneal velocity reaches its maximum value when the corneal acceleration is zero, therefore the force acting on the cornea is zero. After that, the corneal velocity decreases, reaching zero velocity at the highest concavity.

4.2 Methodology proposal

Given the results of Section 3, it is possible to propose a new procedure to estimate the IOP of a patient based on the time of maximum velocity of the corneal apex provided by Corvis ST.

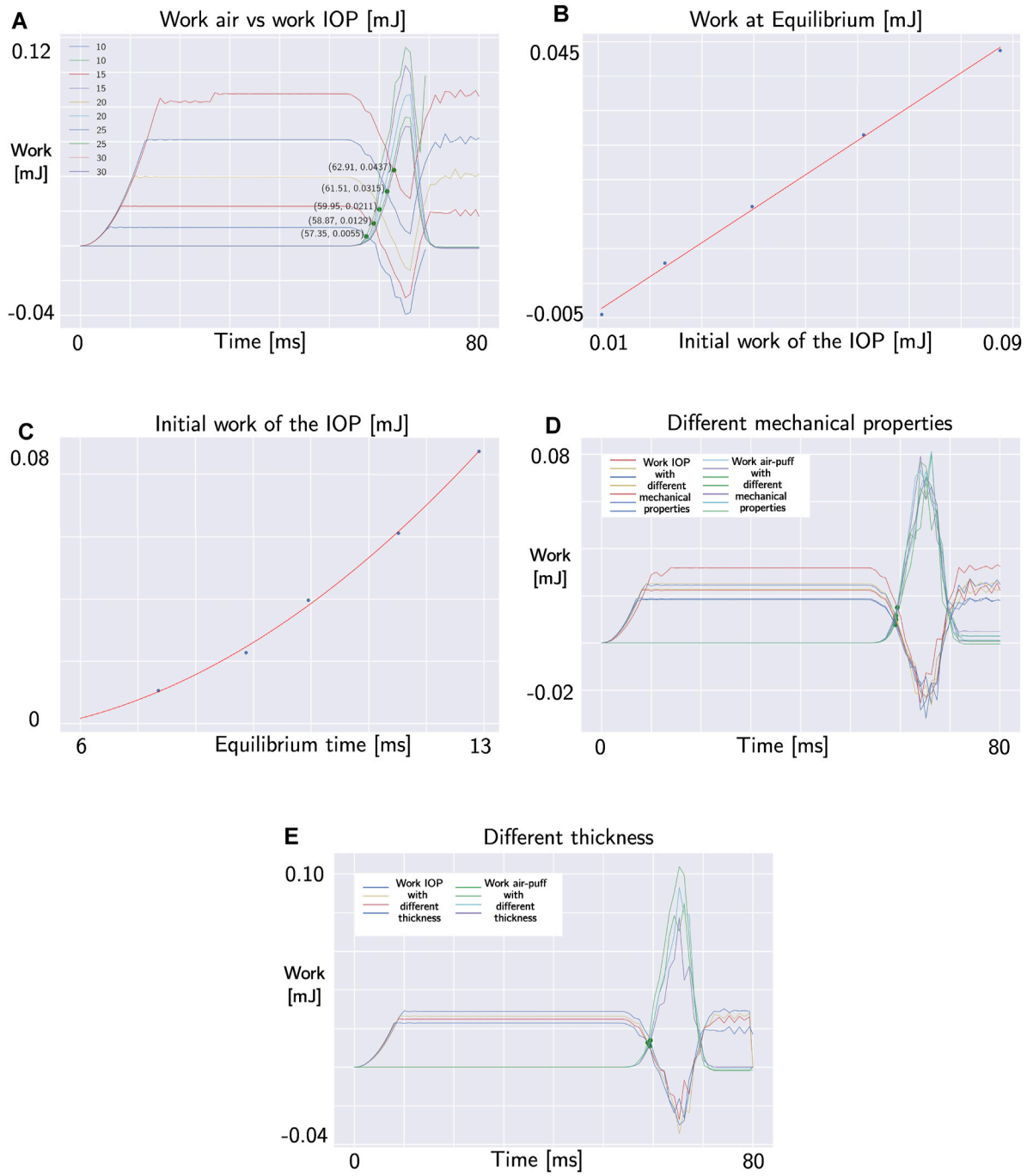

FIGURE 7
(A) Intersection points between internal and external work in the simulations with different IOP. **(B)** Linear relationship between the initial work of the IOP and the work at intersection (both in mJ). **(C)** Quadratic relationship between the time of maximum velocity (in ms) and the initial work of the IOP (in mJ). **(D)** Intersection points between internal and external work in the simulations with different mechanical properties of the corneal tissue. **(E)** Intersection points between internal and external work in the simulations with different thickness.

The new IOP will be called *wIOP* because it is based on the analysis of the works acting on the corneal anterior surface. Since the time at which the works acting on the corneal surface are equal does not depend on the mechanical properties of the corneal tissue and on the corneal thickness, this time can be used to estimate the wIOP. From the output data of Corvis ST, the velocity of the apex is known. The time of maximum velocity of the apex corresponds to the intersection time of the works and it is used to calculate the wIOP by means of Eq. 7 which is given by the combination of Eqs 5, 6.

$$\text{wIOP}\ [\text{mmHg}] = \left(-2.01 \cdot 10^{-3}\right) \cdot \text{time}_{\text{max-vel}}{}^{4} + \left(3.05 \cdot 10^{-2}\right) \cdot \text{time}_{\text{max-vel}}{}^{3} + \left(2.99 \cdot 10^{-1}\right) \cdot \text{time}_{\text{max-vel}}{}^{2} - 3.15 \cdot \text{time}_{\text{max-vel}} + 10.95 \quad (7)$$

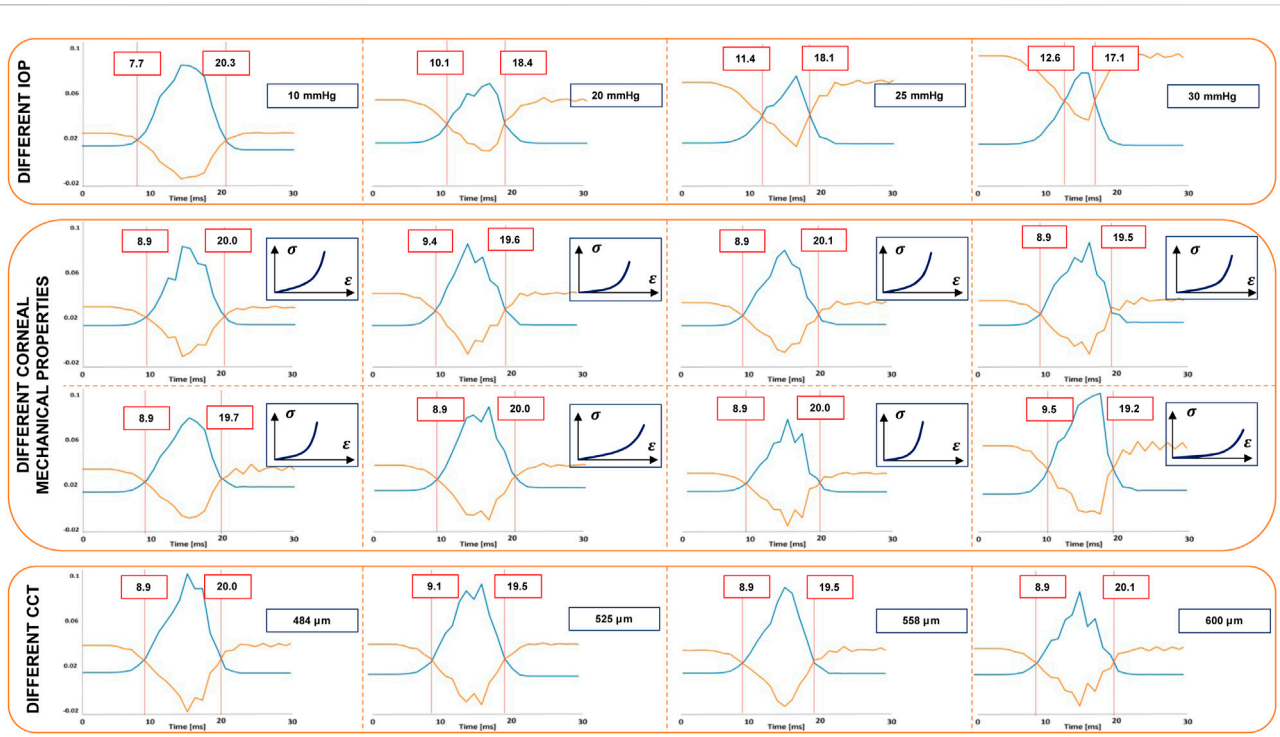

FIGURE 8
Time of intersection point between the work of the air puff (in blue) and the work of the IOP (in orange) in different FSI simulations (Table 1). This point of the cornea changes when the IOP changes. However, it does not depend on the mechanical properties of the corneal tissue and the central corneal thickness.

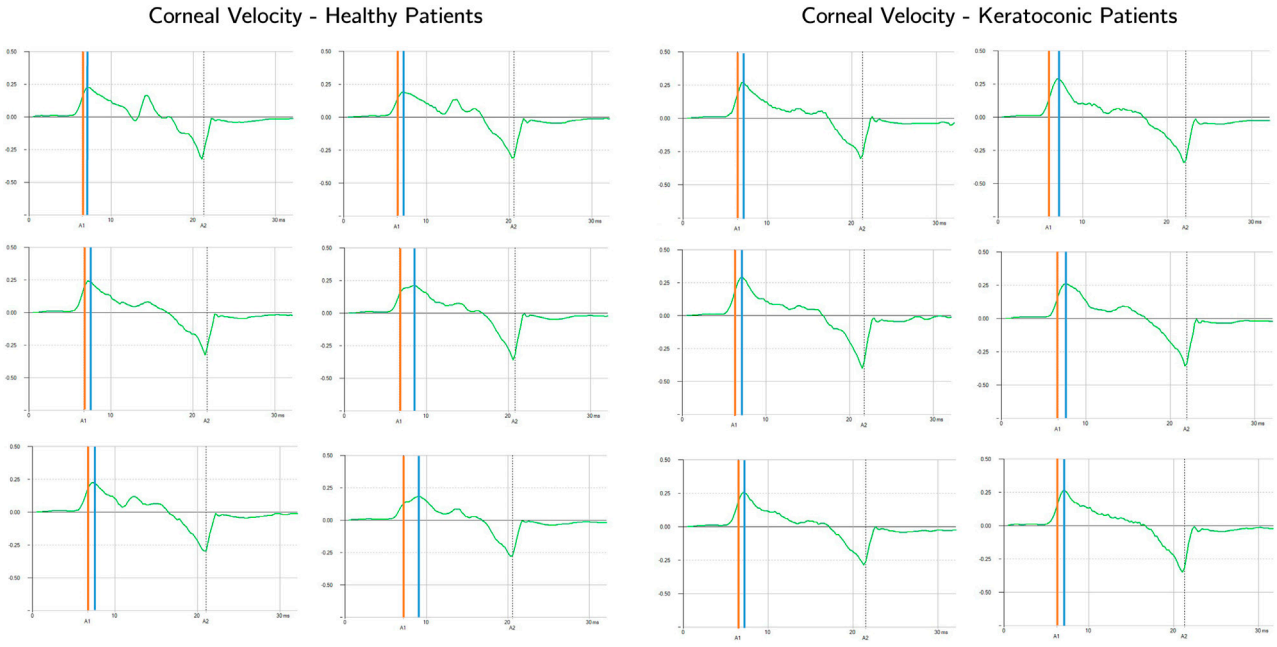

FIGURE 9
Apex velocity in time for six healthy and six keratoconic patients during Corvis ST. The first applanation time is highlighted with the orange vertical line while the highest velocity time is highlighted with the blue vertical line.

5 Discussion

The point in which the external and internal forces are equal in NCT of Corvis ST was previously believed to be equal to first applanation point of the cornea (Sharma et al., 2020; Brusini et al., 2021; Silva and Lira, 2022). However, a closer inspection of the clinical results revealed that the first applanation point does not coincide with the point of highest velocity. The cornea's deformation depends on the coupled effect of the IOP, the corneal thickness, the mechanical properties of the corneal tissue and the air pressure on the cornea (Ariza-Gracia et al., 2015; Redaelli et al., 2022). Consequently, the equilibrium point may not necessarily coincide with an applanated cornea. However, in the instant of highest velocity, the acceleration of the cornea is zero, indicating that the total force acting on the cornea is also zero. The FSI simulation presented in our previous work (Redaelli et al., 2022) predicts the air pressure on the corneal surface during the puff; in contrast with the output of the Corvis ST, which only provides the air pressure at the outlet of the device nozzle's (Simonini and Pandolfi, 2016). Previous numerical works attempted to estimate the IOP removing the influence of corneal structural parameters. *Joda et al.* (Joda et al., 2016) and more recently *Eliasy et al.* (Eliasy et al., 2022) proposed an algorithm to correct the IOP estimated by Corvis ST trying to exclude the influence of CCT and age. However, their algorithm is based on structural numerical simulations in which the air pressure on the cornea does not vary depending on the mechanical properties and thickness of the patient. *Simonini et al.* (Simonini and Pandolfi, 2016) studied the influence of a varying air jet pressure on the output of the NCT, revealing that different air pressures on the cornea can lead to changes in the estimation of IOP. That work considered different pressure values on the cornea as a defined function of a structural simulation, independent on the corneal deformation. The Corvis ST tonometer nozzle consists of a tube with an inner diameter of 1–2 mm, and a distance of 11 mm between the nozzle and the eye is required, which affects the cross-sectional profile of the pressure applied to the eye. Due to the nozzle to eye distance and subsequent change in the pressure profile, the spatial and temporal profile of the airflow pressure on the cornea differs significantly from that of the internal device pressure (Oehring et al., 2021). *Oehring at al* (Oehring et al., 2021). investigated the spatial distribution of the Corvis ST airflow pressure using mapping grids. However, the pressure on the corneal surface was supposed to be only dependent on the distance, not on the corneal deformation. The novelty of our FSI is the evaluation of the air pressure on the corneal surface in each case with the possibility to calculate the work of the air puff in different scenarios. To the best of our knowledge, only *Zhang et al.* (Zhang et al., 2021) have investigated the NCT by means of an energetic approach but they considered a constant pressure on the corneal surface. The work of the air puff in *Zhang et al.* (Zhang et al., 2021) is assumed to be equal to the corneal internal energy. Our energetic analysis considers the energy balance of the anterior corneal surface at the intersection point between the work of the air puff and the work of the IOP. Both works are calculated on the anterior corneal surface, so the thickness of the eye is not considered and does not influence the results, as supported by the analysis of different CCT shown in Section 3.2. We conducted an analysis of the energy balance in the *y* direction, since the thickness of the structure is negligible with respect to its surface, the mechanical properties of the cornea do not play a role in the results. Our analysis of various mechanical properties in Section 3.2 supports this non-dependency. Figure 10 depicts the stress-strain curves of the corneal materials we tested which are consistent with other previous experimental studies (Elsheikh et al., 2008; Xiang et al., 2018; Liu et al., 2020). *Xue et al.* (Xue et al., 2018) found that under physiological IOP, the corneal stress is about 0.02 MPa, which is consistent with the stress strain curves we tested in our simulations.

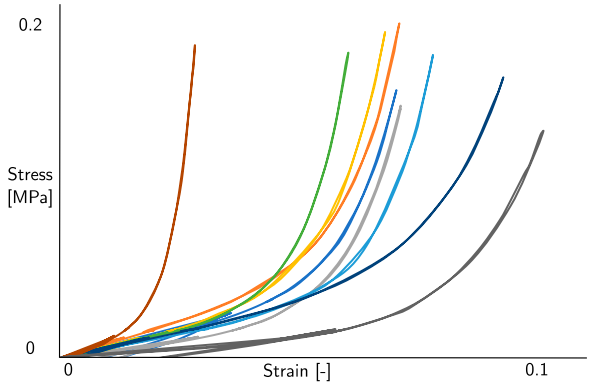

FIGURE 10
Stress strain curves of the corneal material tested in our simulations.

We are aware that our research has some limitations. First of all, the FSI simulations conducted and the clinical evaluation was conducted for patients with a regular geometry. Further studies should be conducted with the aim to study the air pressure distribution on the corneal surface in case of non-symmetric corneal geometries, for example, in keratoconic patients, where the bulging of a region of the cornea has the consequence of an non symmetric geometry. Or other studies should be conducted in analyzig the nergy balance in case the air jet does not impact exactly the apex of the cornea. Furthermore, an *in vitro* validation of the procedure should be conducted. The problem with *in vitro* validation is that we should have a very sensitive sensor (with a sampling similar to the one of the camera) capable of measuring the IOP changes in the experimental set up during the air puff. To the best of author knowledge, some experimental set-up with Corvis ST have been proposed to estimate the influence of the IOP on corneal deformation during the air puff (Kling and Marcos, 2013; Bekesi et al., 2016a; Bekesi et al., 2016b; Bekesi et al., 2017; Eliasy et al., 2018). However, the pressure transducers used in these experiments does not capture the IOP change which occurs during the air puff.

In conclusion, the significance of our novel pressure estimation lies in two key aspects. Firstly, the method provides a more realistic and real-time assessment of a patient's intraocular pressure (IOP) based on the results of Corvis ST, decoupling it from the mechanical properties of the cornea. This real-time capability enhances the dynamic monitoring of IOP, allowing for prompt and responsive adjustments in clinical interventions.

Secondly, once an accurate estimate of IOP is obtained, it can serve as a foundational parameter for further investigations. Specifically, this IOP data can be leveraged in conjunction with other methodologies to estimate the mechanical properties of the cornea. This dual-pronged

approach addresses an emerging challenge in ophthalmology, offering a comprehensive understanding of both IOP and corneal biomechanics. By advancing our ability to assess these interconnected factors in real-time, our methodology contributes to a more nuanced and comprehensive approach to ocular health diagnostics.

6 Conclusion

The corneal deformation induced by the air puff is influenced by IOP, CCT, mechanical properties of the corneal tissue and the force exerted by the air puff. Our proposed methodology in this study focuses on isolating and accurately estimating the IOP, excluding the effects of the aforementioned factors. By decoupling the contribution of these variables, our approach provides a more reliable assessment of IOP. The new wIOP can be useful in advancing our understanding of ocular biomechanics and establishing a more accurate foundation for diagnostic and therapeutic interventions.

Data availability statement

The original contributions presented in the study are included in the article/Supplementary Material, further inquiries can be directed to the corresponding author.

Ethics statement

The studies involving humans were approved by Antwerp University Hospital Ethical Committee with reference number 17/12/136. The studies were conducted in accordance with the local legislation and institutional requirements. Written informed consent for participation was not required from the participants or the participants' legal guardians/next of kin in accordance with the national legislation and institutional requirements.

Author contributions

ER: Conceptualization, Investigation, Methodology, Writing–original draft. BC: Methodology, Supervision, Writing–review and editing. JR: Writing–review and editing. GL: Supervision, Writing–review and editing. JG: Conceptualization, Methodology, Supervision, Writing–review and editing.

Funding

The author(s) declare that financial support was received for the research, authorship, and/or publication of this article. This project has received funding from the European Union's Horizon 2020 research and innovation program under the Marie Skłodowska-Curie grant agreement No 956720 and the Department of Industry and Innovation (Government of Aragon) through the research group Grant T24–20R (cofinanced with Feder 2014-2020: Construyendo Europa desde Aragon). Part of the work was performed by the ICTS "NANBIOSIS" specifically by the High Performance Computing Unit (U27), of the CIBER in Bioengineering, Biomaterials and Nanomedicne (CIBER-BBN at the University of Zaragoza).

Acknowledgments

We thank prof Jos Rozema from Antwerp university for providing clinical data.

Conflict of interest

The authors declare that the research was conducted in the absence of any commercial or financial relationships that could be construed as a potential conflict of interest.

Publisher's note

References

Ajazaj, V., Kaçaniku, G., Asani, M., Shabani, A., and Dida, E. (2018). Intraocular pressure after corneal refractive surgery. *Med. Arch.* 72, 341. doi:10.5455/medarh.2018.72.341-343

Aoki, S., Asaoka, R., Fujino, Y., Nakakura, S., Murata, H., and Kiuchi, Y. (2023). Comparing corneal biomechanic changes among solo cataract surgery, microhook ab interno trabeculotomy and istent implantation. *Sci. Rep.* 13, 19148. doi:10.1038/s41598-023-46709-5

Ariza-Gracia, M. Á., Wu, W., Calvo, B., Malvè, M., Büchler, P., and Matas, J. F. R. (2018). Fluid–structure simulation of a general non-contact tonometry. a required complexity? *Comput. methods Appl. Mech. Eng.* 340, 202–215. doi:10.1016/j.cma.2018.05.031

Ariza-Gracia, M. Á., Zurita, J., Piñero, D. P., Calvo, B., and Rodríguez-Matas, J. F. (2016). Automatized patient-specific methodology for numerical determination of biomechanical corneal response. *Ann. Biomed. Eng.* 44, 1753–1772. doi:10.1007/s10439-015-1426-0

Ariza-Gracia, M. Á., Zurita, J. F., Piñero, D. P., Rodriguez-Matas, J. F., and Calvo, B. (2015). Coupled biomechanical response of the cornea assessed by non-contact tonometry. a simulation study. *PloS one* 10, e0121486. doi:10.1371/journal.pone.0121486

Asaoka, R., Nakakura, S., Tabuchi, H., Murata, H., Nakao, Y., Ihara, N., et al. (2015). The relationship between corvis st tonometry measured corneal parameters and intraocular pressure, corneal thickness and corneal curvature. *PloS one* 10, e0140385. doi:10.1371/journal.pone.0140385

Bekesi, N., Dorronsoro, C., de la Hoz, A., and Marcos, S. (2016a). Material properties from air puff corneal deformation by numerical simulations on model corneas. *PLoS One* 11, e0165669. doi:10.1371/journal.pone.0165669

Bekesi, N., Gallego-Munoz, P., Ibarés-Frías, L., Perez-Merino, P., Martinez-Garcia, M. C., Kochevar, I. E., et al. (2017). Biomechanical changes after *in vivo* collagen cross-linking with rose bengal–green light and riboflavin-uva. *Investigative Ophthalmol. Vis. Sci.* 58, 1612–1620. doi:10.1167/iovs.17-21475

Bekesi, N., Kochevar, I. E., and Marcos, S. (2016b). Corneal biomechanical response following collagen cross-linking with rose bengal–green light and riboflavin-uva. *Investigative Ophthalmol. Vis. Sci.* 57, 992–1001. doi:10.1167/iovs.15-18689

Brusini, P., Salvetat, M. L., and Zeppieri, M. (2021). How to measure intraocular pressure: an updated review of various tonometers. *J. Clin. Med.* 10, 3860. doi:10.3390/jcm10173860

Brusini, P., Salvetat, M. L., and Zeppieri, M. (2022). Intraocular Pressure and ocular hypertension (MDPI books).

Dev, L.-D. (2024). *LS-DYNA theory manual 3*.

Eliasy, A., Chen, K.-J., Vinciguerra, R., Maklad, O., Vinciguerra, P., Ambrósio, R., et al. (2018). *Ex-vivo* experimental validation of biomechanically-corrected intraocular pressure measurements on human eyes using the corvis st. *Exp. eye Res.* 175, 98–102. doi:10.1016/j.exer.2018.06.013

Eliasy, A., Lopes, B. T., Wang, J., Abass, A., Vinciguerra, R., Vinciguerra, P., et al. (2022). Introduction and clinical validation of an updated biomechanically corrected intraocular pressure biop (v2). *Curr. eye Res.* 48, 382–391. doi:10.1080/02713683.2022.2162087

Elsheikh, A., Brown, M., Alhasso, D., Rama, P., Campanelli, M., Garway-Heath, D., et al. (2008). Experimental assessment of corneal anisotropy. *J. Refract. Surg.* 24, 178–187. doi:10.3928/1081597X-20080201-09

Goldmann, H., and Schmidt, T. (1957). Über applanationstonometrie. *Ophthalmologica* 134, 221–242. doi:10.1159/000303213

Greene, P., Sergienko, N., and Wang, S. (2016). Review: measurement techniques for intraocular pressure. *Optom. Open Access* 1, 2476–2075. doi:10.4172/2476-2075.1000120

Helmy, H., and Hashem, O. (2020). Intraocular pressure calculation in myopic patients after laser-assisted *in situ* keratomileusis. *Clin. Ophthalmol.* 14, 509–516. doi:10.2147/opth.s239329

Holzapfel, G. A., Gasser, T. C., and Ogden, R. W. (2000). A new constitutive framework for arterial wall mechanics and a comparative study of material models. *J. Elast.* 61, 1–48. doi:10.1023/A:1010835316564

Imbert, D. A. (1885). *Théorie des ophtalmotonomètres,... (A. Davy)*.

Joda, A. A., Shervin, M. M. S., Kook, D., and Elsheikh, A. (2016). Development and validation of a correction equation for corvis tonometry. *Comput. methods biomechanics Biomed. Eng.* 19, 943–953. doi:10.1080/10255842.2015.1077515

Jordanova, E., Hentova-Sencanic, P., Marjanović, I., Senčanin, I., Stefanović, I., and Baralić, M. (2022). The cornea and methods for measuring intraocular pressure. *Sanamed* 17, 167–173. doi:10.5937/sanamed0-41040

Kaushik, S., Pandav, S. S., Banger, A., Aggarwal, K., and Gupta, A. (2012). Relationship between corneal biomechanical properties, central corneal thickness, and intraocular pressure across the spectrum of glaucoma. *Am. J. Ophthalmol.* 153, 840–849.e2. doi:10.1016/j.ajo.2011.10.032

Kling, S., and Marcos, S. (2013). Contributing factors to corneal deformation in air puff measurements. *Investigative Ophthalmol. Vis. Sci.* 54, 5078–5085. doi:10.1167/iovs.13-12509

Kohlhaas, M., Spoerl, E., Boehm, A. G., and Pollack, K. (2006). *A correction formula for the real intraocular pressure after lasik for the correction of myopic astigmatism*.

Liu, J., and Roberts, C. J. (2005). Influence of corneal biomechanical properties on intraocular pressure measurement: quantitative analysis. *J. Cataract Refract. Surg.* 31, 146–155. doi:10.1016/j.jcrs.2004.09.031

Liu, T., Shen, M., Huang, L., Xiang, Y., Li, H., Zhang, Y., et al. (2020). Characterization of hyperelastic mechanical properties for youth corneal anterior central stroma based on collagen fibril crimping constitutive model. *J. Mech. Behav. Biomed. Mater.* 103, 103575. doi:10.1016/j.jmbbm.2019.103575

Maklakoff, C. L. (1885). Ophthalmotonometrie. *Arch. Ophthalmol. Paris.* 5, 159.

Oehring, D., Jenkins, D., Buckhurst, P. J., and Buckhurst, H. (2021). Experimental assessment of the spatial and temporal distribution of non-contact tonometer airflows. *Appl. Sci.* 11, 2499. doi:10.3390/app11062499

Rajabi, S., Asharlous, A., Riazi, A., Khabazkhoob, M., and Moalej, A. (2022). Differences and limits of agreement among pentacam, corvis-st, and iol-master 700 optical biometric devices regarding central corneal thickness measurements. *J. Curr. Ophthalmol.* 34, 44. doi:10.4103/joco.joco_96_21

Redaelli, E., Grasa, J., Calvo, B., Rodriguez Matas, J. F., and Luraghi, G. (2022). A detailed methodology to model the non contact tonometry: a fluid structure interaction study. *Front. Bioeng. Biotechnol.* 10, 981665. doi:10.3389/fbioe.2022.981665

Redaelli, E., Nana, M., Calvo, B., Matas, J. F. R., Luraghi, G., Rozema, J., et al. (2024). Improving early detection of keratoconus by non contact tonometry. a computational study and new biomarkers proposal. *J. Mech. Behav. Biomed. Mater.* 152, 106413. doi:10.1016/j.jmbbm.2024.106413

Sharma, H., Nainiwal, S. K., Sarraf, A., Porwal, R., and Sharma, V. (2020). Intraocular pressure measurement techniques: current concepts and a review. *Indian J. Clin. Exp. Ophthalmol.* 6, 315–323. doi:10.18231/j.ijceo.2020.069

Silva, F., and Lira, M. (2022). Intraocular pressure measurement: a review. *Surv. Ophthalmol.* 67, 1319–1331. doi:10.1016/j.survophthal.2022.03.001

Simonini, I., and Pandolfi, A. (2016). The influence of intraocular pressure and air jet pressure on corneal contactless tonometry tests. *J. Mech. Behav. Biomed. Mater.* 58, 75–89. doi:10.1016/j.jmbbm.2015.07.030

Wang, Y. X., Xu, L., Wei, W. B., and Jonas, J. B. (2018). Intraocular pressure and its normal range adjusted for ocular and systemic parameters. the beijing eye study 2011. *PLoS One* 13, e0196926. doi:10.1371/journal.pone.0196926

Wu, Y., Luttrell, I., Feng, S., Chen, P. P., Spaide, T., Lee, A. Y., et al. (2020). Development and validation of a machine learning, smartphone-based tonometer. *Br. J. Ophthalmol.* 104, 1394–1398. doi:10.1136/bjophthalmol-2019-315446

Xiang, Y., Shen, M., Xue, C., Wu, D., and Wang, Y. (2018). Tensile biomechanical properties and constitutive parameters of human corneal stroma extracted by smile procedure. *J. Mech. Behav. Biomed. Mater.* 85, 102–108. doi:10.1016/j.jmbbm.2018.05.042

Xue, C., Xiang, Y., Shen, M., Wu, D., Wang, Y., et al. (2018). Preliminary investigation of the mechanical anisotropy of the normal human corneal stroma. *J. Ophthalmol.* 2018, 1–7. doi:10.1155/2018/5392041

Zhang, D., Zhang, H., Tian, L., Zheng, Y., Fu, C., Zhai, C., et al. (2021). Exploring the biomechanical properties of the human cornea *in vivo* based on corvis st. *Front. Bioeng. Biotechnol.* 9, 771763. doi:10.3389/fbioe.2021.771763

frontiers | Frontiers in Bioengineering and Biotechnology

TYPE Original Research
PUBLISHED 30 July 2024
DOI 10.3389/fbioe.2024.1426060

OPEN ACCESS

EDITED BY
Anna Marina Pandolfi,
Polytechnic University of Milan, Italy

REVIEWED BY
Hamed Hatami-Marbini,
The University of Chicago, United States
Osama Maklad,
University of Greenwich, United Kingdom

*CORRESPONDENCE
Andres De La Hoz,
andres.delahoz@csic.es

RECEIVED 30 April 2024
ACCEPTED 16 July 2024
PUBLISHED 30 July 2024

CITATION
De La Hoz A, Villegas L, Marcos S and Birkenfeld JS (2024), A simple computational model for scleral stiffness assessments via air-puff deformation OCT.
Front. Bioeng. Biotechnol. 12:1426060.
doi: 10.3389/fbioe.2024.1426060

A simple computational model for scleral stiffness assessments via air-puff deformation OCT

Andres De La Hoz[1]*, Lupe Villegas[1], Susana Marcos[2] and Judith S. Birkenfeld[1]

[1]Instituto de Óptica "Daza de Valdés", Consejo Superior de Investigaciones Científicas (IO-CSIC), Madrid, Spain, [2]Center for Visual Science, The Institute of Optics, Flaum Eye Institute, University of Rochester, Rochester, NY, United States

Introduction: The mechanical properties of the sclera are related to its structural function, and changes to these properties are believed to contribute to pathologies such as myopia. Air-puff deformation imaging is a tool that uses an imaging system coupled with an air-puff excitation source to induce and measure deformation in a tissue *in vivo*. Typically used for the study of the cornea's mechanical properties and IOP, this tool has been proposed as a method to evaluate scleral stiffness.

Methods: In this work, we present a computational model of the rabbit eye to assess scleral deformation under air-puff. Parametric studies were conducted to evaluate the effects of material properties, intraocular pressure, and other parameters on the deformation response. Output from the model was also compared to experimental measurements of air-puff deformation in rabbit eyes under varying IOP.

Results: Central deformation response was found to be most influenced by material properties of the sclera (at site of air-puff and posterior), thickness, and IOP, whereas deformation profile was most influenced by material properties. Experimental and simulated IOP dependence were found to be similar (RMSE = 0.13 mm).

Discussion: Scleral APDI could be a useful tool for quick *in vivo* assessment of scleral stiffness.

KEYWORDS

OCT, sclera, finite element, air-puff, myopia

1 Introduction

The sclera is the eye's principal load-bearing tissue and determines the size and shape of the eye. It consists of bundled collagen fibers (Keeley et al., 1984), irregular in thickness and density, with preferential orientation and high stiffness (Coudrillier et al., 2013) embedded in an extracellular matrix composed of proteoglycans, glycosaminoglycans, water, and other molecules. The sclera's properties are of particular interest in the study of pathologies that involve the sclera's structural function. Myopia (near-sightedness) is one such pathology, typically caused by an excessive ocular axial elongation. Myopia has been associated with scleral thinning (Curtin and Teng, 1958), changes in collagen fibril diameter (McBrien et al., 2001) and orientation (Markov et al., 2018) and extracellular matrix composition (McBrien et al., 2000; Rada et al., 2000). Changes in mechanical

behavior of myopic scleral tissue have been observed, such as differences in elastic (Phillips and McBrien, 1995) and viscoelastic (Phillips et al., 2000) properties. Cross-linking has been proposed as a method to slow down the progression of the disease (Wollensak and Spoerl, 2004) by stiffening the tissue and reducing axial growth (Dotan et al., 2014; Liu et al., 2016).

The study of the sclera's mechanical properties can be approached with standard mechanical testing tools (such as uniaxial tensile testing). A number of more complex techniques have been proposed. Examples include inflation (sometimes combined with wide-angle X-ray scattering (Coudrillier et al., 2012; Grytz et al., 2014; Coudrillier et al., 2015), Brillouin microscopy (Shao et al., 2016), and Optical Coherence Elastography (Zvietcovich et al., 2020; Ramier et al., 2020; Villegas et al., 2024). These methods have been used to characterize isotropic and anisotropic properties of the sclera.

Air-puff deformation imaging (APDI) is a technique that involves the use of a rapid, controlled pulse of air (or "air-puff") that induces deformation of the ocular tissue over few milliseconds and which is coupled to an imaging system that images the resulting deformation. Commercially used corneal APDI, typically coupled with a Scheimpflug camera, is mainly used to measure intraocular pressure (Corvis ST, Oculus, Wetzlar, Germany). Laboratory-based APDI systems using high-speed OCT for corneal imaging have been demonstrated for the study of the cornea's (Dorronsoro et al., 2012; Bronte-Ciriza et al., 2021) mechanical response, and recently in the sclera (Bronte-Ciriza et al., 2021). The estimation of the material parameters is based on the quantified changes of the recorded tissue deformation images, and is often aided by the use of finite element (FE) modelling, a widely used numerical simulation method for the study of the mechanical behavior of structures under load. In this procedure, an FE model of the tissue (or the entire ocular globe) is subjected to a defined air-puff pressure load, and the resulting deformation is calculated. This approach has been used to estimate the effect of the corneal elastic modulus, intraocular pressure (IOP), and central corneal thickness (CCT) on the corneal deformation under air-puff (Kling et al., 2014; Ariza-Gracia et al., 2015). The insights obtained from such models can be used to estimate material properties based on easily-quantifiable APDI outputs (Joda et al., 2016; Chen et al., 2019; Eliasy et al., 2019). FE models can also be used to estimate material parameters by matching the output of a simulation with experimental results, a procedure known as inverse analysis. This approach has been used to estimate material properties using APDI (Bekesi et al., 2016; Bekesi et al., 2017) and other techniques such as inflation (Grytz et al., 2014; Coudrillier et al., 2015).

FE-aided approaches require making choices about the type of material model used, and thus the type of information that can be retrieved. For the sclera, the simplest approach has been the use of an isotropic material model (Asejczyk-Widlicka et al., 2007; Norman et al., 2011; Nguyen et al., 2019; Geragthy et al., 2020). Anisotropic models that treat the extracellular matrix as isotropic and the collagen fibers as having preferential direction have also been used in various inverse modeling approaches (Coudrillier et al., 2012; Grytz et al., 2014; Coudrillier et al., 2015; Jia et al., 2017; Schwaner et al., 2020), sometimes requiring additional experimental input to define this preferential direction (Coudrillier et al., 2015). An additional consideration is whether to implement spatial variation in the sclera, which can be done in various ways, e.g., modeling the sclera in discrete segments (Geragthy et al., 2020). The more complex approaches, e.g., anisotropic models, provide detailed information on the sclera, at the expense of higher computation times and limiting the application to *ex vivo* experimental work. APDI has traditionally used an isotropic model, allowing for an assessment of macro stiffness that is more easily transferable to study of live subjects and medical practice, at the expense of detail.

We have previously presented the use of APDI on the sclera (Bronte-Ciriza et al., 2021). In the current work we analyzed the differences between air-puff deformation behavior in scleral and corneal tissues, and estimated material parameters using an FE model with fixed dimensions and IOP. The extensive literature on corneal APDI indicates that the interplay between dimensions, IOP, and material affects the deformation response. Uncoupling these effects is the main challenge in assessing material properties for multiple subjects.

This current study attempts to account for the effects of expected differences across eyes, such thickness, IOP, materials, and dimensions of the ocular globe, to estimate the relative impact of these on the estimates of the scleral air-puff deformation response. These effects are studied in an FE model of the New Zealand rabbit eye subjected to a defined air-puff pressure. Two parametric studies were conducted using this FE model. In the first, a sensitivity study, a single model parameter is set as a variable and the remaining parameters are held constant. This allows the influence of each parameter on the deformation to be assessed. In the second, a random sampling study was conducted, all model parameters are set as variables and each is assigned a random value. This allows an assessment of the interplay between the input parameters and the relative strength of each in determining the scleral deformation response. Finally, the FE model was compared to experimental data of scleral air-puff deformation of *ex vivo* rabbit eyes.

2 Methods

2.1 Finite element model

2.1.1 Geometry

A FE model of a New Zealand rabbit eye globe was developed in ANSYS Mechanical, v.2020 (Canonsburg, Pennsylvania). The eye was modelled on one side of the sagittal plane (assuming symmetry on the plane) and one side of the axial plane, in order to reduce computational demand. The sclera was assumed to vary in thickness across the eye, with the posterior end being the thickest part. The dimensions of the model, described in Table 1, are selected on the basis of measurements of *ex vivo* rabbit eyes in our laboratory. The exterior of the ocular globe is modelled as an ellipse with two diameters, the vertical corresponding to equatorial length (EL) and the horizontal one corresponding to axial length (AL), and the interior of the ocular globe is modelled with another ellipse using the variable of Thickness (at equator) and a fixed horizontal thickness of 0.6 mm. The cornea is modelled at an angle of 120° from the optic nerve, with a fixed thickness of 0.4 mm, and its apex extends 1 mm from the exterior ellipse such that the axial length equals the horizontal diameter of the ellipse +1.

10.3389/fbioe.2024.1426060

TABLE 1 Direct and indirect model input parameters evaluated in the parametric study.

Model input parameters	Abbreviation	Initial	Interval
"Direct" parameters			
Material coefficient (MPa)	μ	0.083	0.06–0.10
Scleral thickness at air-puff location (mm)	THK	0.35	0.34–0.40
Intraocular pressure (mmHg)	IOP	18	10–25
"Indirect" parameters			
Posterior material coefficient (MPa)	μ_{post}	0.083	0.02–0.10
Axial length (mm)	AL	18	17–19
Equatorial length (mm)	EL	19	18.4–19.6

2.1.2 Material model

The material model used in this FE model is the first-order Ogden hyperelastic isotropic model. Assuming incompressibility, the stress-strain relationship under uniaxial tension for this model reduces to:

$$\sigma_1 = \mu\left(\lambda^{\alpha} - \lambda^{-\frac{1}{2}\alpha}\right) \quad (1)$$

where σ is the stress, λ is the stretch ratio (strain+1), and α and μ are the models' coefficients. In this model, parameter α is an exponent which influences the shape of the stress-strain curve and parameter μ influences its magnitude. The shape of the stress-strain is associated with the shape of the time profile of the air-puff deformation (displacement as a function of time). In our previous work (Bronte-Ciriza et al., 2021), the normalized time profile of various scleral regions under air-puff was found to be largely constant, suggesting a similar shape for the stress-strain curves. Based on this finding, the value of parameter α is fixed in this model, and parameter μ is treated as the variable, describing the magnitude of the stress response. Parameter α was assigned a value of 40 on the basis of approximating the shape of experimental stress-strain scleral rabbit curves and displacement time profiles.

The sclera's material properties are known to vary spatially, which has been implemented in the model. The stiffness of the sclera is affected by physiological factors such as GAGs content (Pachenari and Hatami-Marbini, 2021) and is known to decrease from the anterior to the posterior regions (Elsheikh et al., 2010). However, fully mapping the gradient of this change is limited by technical challenges (such as sample size for uniaxial testing). In this model we have assumed the spatial variations are linear, and implemented them by setting the material coefficient of the scleral elements as a function of their position, using the following formula:

$$\mu(x) = \mu - (\Delta\mu) \times \frac{x}{x_f} \quad (2)$$

In this formula (Eq. 2), x = central position of the element, x_f = distance from equator (x = 0) to the most posterior distance of the sclera, and $\Delta\mu = \mu - \mu_{post}$, where μ is the material coefficient at the equator, and μ_{post} is the material coefficient at x_f.

2.1.3 Boundary conditions, loads, and solution

The model is meshed with SOLID186 elements for the sclera and cornea and HSFLD16 for a total of 5,188 elements. Several boundary conditions and loads are required to complete the model: displacement constraints, intraocular pressure (IOP), and pressure load. Displacement constraints are as follows: symmetry on XY plane, fixed Y-displacement at XZ plane, and fixed displacements at node corresponding to most posterior point of the ocular globe.

The IOP is applied in the first loading step using HSFLD16 hydrostatic fluid elements which fill the interior of the eye. The applied pressure deforms the entire ocular structure, with the extent of the deformation depending on the magnitude of the pressure and the material properties. To account for the effect of this pressure on the initial geometry, an iterative "stress-free" procedure was introduced, adapted from the work by Elsheikh et al. (2013). The procedure begins with a predetermined geometry X_0. IOP and scleral material properties are applied to the model, and the deformation resulting from applied IOP is extracted (u_0). This deformation u_0 is then subtracted from X_0 to create a new geometry X_i. This new geometry is used as the undeformed geometry in a new model, to which the pressure and material properties are then applied to obtain a new deformed geometry x_i. The difference between x_i and X_0 is calculated, and subtracted from stress-free form X_i, to create X_{i+1}. This process was repeated for three iterations. This ensured a consistent geometry even with varying IOP.

The air-puff is applied as a quasi-static load, in 6 load steps totaling 20 ms. The air-puff magnitude has been previously characterized and quantified (Bronte-Ciriza et al., 2021) as a spatially and temporally varying pressure load, with a maximum pressure of 15.4 kPa at 20 ms. The unloading region of the deformation event is not considered. The load is applied in the equatorial region of the sclera, centered at the uppermost point (described in Section 2.2.3).

After solving the FE model, the position of each node at every load step is exported into a.txt file and processed in MATLAB (Mathworks, Natick, MA).

2.1.4 Input parameters of finite element model

The input parameters (or variables) for the model were selected on the basis of their potential relevance to the deformation response. The initial values and evaluated ranges were selected from laboratory measurements and literature data.

The input parameters can be divided into "direct" and "indirect" (see Table 1). "Direct" parameters are those acting directly on the air-puff excitation point. These are: the material coefficient, the scleral thickness at the location of air-puff, and the IOP (typically parameters evaluated as well in corneal APDI). "Indirect" model parameters are not directly acting on the air-puff excitation point, and include the axial and equatorial length of the eye, and the posterior material coefficient (see Eq. 1). Indirect parameters are expected to have less influence on the deformation response. The posterior material coefficient μ_{post} is applied as a ratio of the material coefficient ranging from 0.25 to 1, such that $\mu_{post} \leq \mu$.

The initial value of the material coefficient was chosen so that when the model was evaluated with the initial values of the other

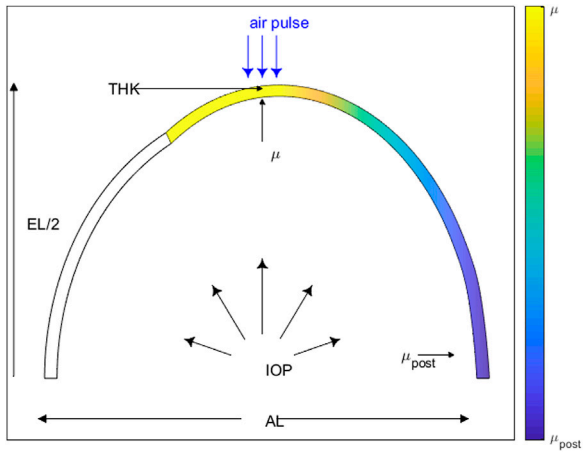

FIGURE 1
Rabbit eye model schematic displaying the FE model input parameters: material coefficient (μ), posterior material coefficient (μ_{post}), intraocular pressure (IOP), thickness (THK), axial length (AL) and equatorial length (EL).

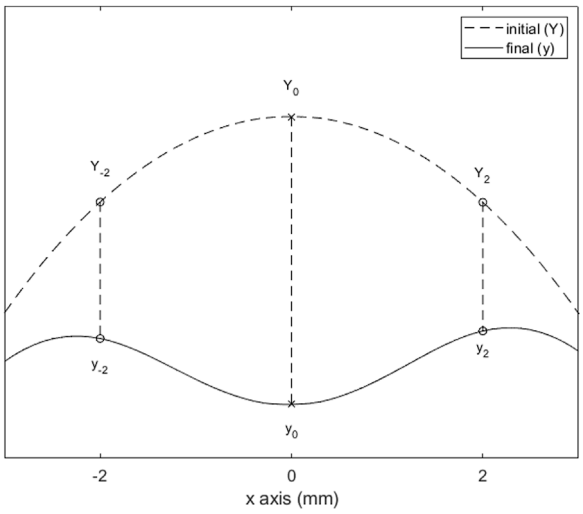

FIGURE 2
Relevant deformation points of the sclera after air-puff loading. The difference between initial (Y) and final (y) heights at x = −2, 0, and 2 mm are used to calculate the output parameters (defined in Table 2).

input parameters, the Apex Displacement (AD) value was 1 mm (see Section 2.1.5 *Output parameters of Finite Element Model*). The range was selected to obtain AD values from 0.5–2.5 mm. The initial value of the posterior material coefficient was set to $\mu_{post} = \mu$. The range was selected so that the ratio of μ_{post}/μ = 0.25–1. The initial thickness was set at 0.35 mm and evaluated in a range of 0.34–0.40 mm, on the basis of laboratory measurements and expected age-related variations (Barathi et al., 2002). Axial and equatorial length were set at 18 and 19 mm and evaluated at ranges of ±0.5 mm from initial value, on the basis of laboratory measurements, estimation from experimental data (Barathi et al., 2002), and standard deviation of measured eyes (Bozkir et al., 1997). Initial IOP was set at 15 mmHg and evaluated at ranges 10–25 mm, on the basis of IOP variation range in rabbits (Vareilles et al., 1977) and on the experimental protocols used for inflation testing. All input parameters are listed in Section 2.2.1. A schematic diagram of the rabbit eye model with the FE model input parameters is displayed in Figure 1.

2.1.5 Output parameters of finite element model

After solving the FE model, the position of each node at every loading step is exported to a.txt file and processed in MATLAB (Mathworks, Natick, MA). The results are used to calculate the output parameters of the FE model.

The parameters are defined in order to assess spatial variation of scleral deformation under air-puff. For the analysis, the sagittal cross-section is used. For convenience, we defined the most anterior point of the location that was to be scanned as the local "scleral apex", and define its x-coordinate as 0. This is also the location where the air-puff is centered. Three displacements were estimated, as the difference between the y-coordinates at initial (Y) and final (y) step of the air-puff at the following x-coordinates: at x = 0 mm, x = −2 mm, and x = +2 mm (as shown in Figure 2). From this data, three output parameters are calculated: 1) the maximum apex displacement (AD), 2) the central peripheral ratio (CPR), and 3) the asymmetry ratio (AR). The parameter definitions are given in Table 2.

TABLE 2 Output parameters evaluated in the parametric study.

Model output parameters	Abbreviation	Definition
Apex displacement (mm)	AD	Y_0-y_0
Central peripheral displacement (mm/mm)	CPR	$(Y_0-y_0)/(Y_2-y_2)$
Asymmetry ratio (mm/mm)	AR	$(Y_2-y_2)/(Y_{-2}-y_{-2})$

CPR and AR are considered relevant because of the non-uniform attributes of the sclera (varying thickness, decreasing material coefficient along the axial length), which will result in asymmetric deformation.

2.2 Parametric studies

The FE model of the rabbit eye was used for three separate analyses: 1) the evaluation of the effect and influence of individual input parameters on the deformation of the sclera, 2) the evaluation of the interplay between input parameters and their effect on the deformation, as well as the strength of the correlations between input and output parameters and 3) a comparison of the results from the FE model with the results from experimental air-puff deformation imaging.

2.2.1 Evaluation of individual input parameters: sensitivity study

The purpose of this study was to assess the type of relationship that exists between the input parameter and the output parameters (proportional, inversely proportional, or no relationship), as well as

the magnitude of the change. The study was conducted according to the following procedure: five input parameters were assigned the initial values from Section 2.2.1. The remaining input parameter was set as a variable and evaluated in the FE model over the range described in Section 2.2.1. The stress-free configuration was used for all evaluations. This procedure was repeated so that each input parameter was evaluated as a variable. Output parameters were calculated for all solutions. The change in the output parameter over the evaluated range of the input parameter was calculated as a percent change.

2.2.2 Simultaneous evaluation of all input parameters: random sampling study

The purpose of this study was to assess which input parameters have a stronger correlation to the output parameters. In this study, and unlike the sensitivity study, all input parameters are evaluated simultaneously. A code was written to 1) generate a random set of input parameters from the ranges presented in Table 1 and 2) evaluate the FE model using this set, and 3) calculate the output parameters from the FE solution. The stress-free configuration was used for all evaluations. A total of 400 random sets were evaluated. From the resulting data, the coefficient of determination (R^2) between each input parameter and each output parameter was calculated.

2.2.3 Comparison of experimental measurements and FE model

The purpose of this study was to compare the FE model to experimental results of scleral APDI. We predicted the corneal response to air puff as a function of IOP in the model, and compared it against experimental measurements of corneal deformation in which the IOP was varied experimentally.

2.2.3.1 Experimental set-up and protocol

All images were acquired using a custom-developed SSOCT system described in previously published work (Curatolo et al., 2020; Bronte-Ciriza et al., 2021). The system uses a Mach-Zender interferometer configuration, a dual balanced photodetector (PDB480C-AC, Thorlabs, United States), and a MEMS-based vertical cavity surface emitting laser swept-source (SL132120, Thorlabs, United States), centered at 1,300 nm. The 3 mm-aperture low coil impedance galvanometric scanning mirrors (Saturn 1B, ScannerMAX, Pangolin, United States) enable ultrafast scanning, which is critical to capture deformation events that last only tens of milliseconds. The system has an axial rate of 200 kHz, an axial resolution of 16 μm, a depth of field of 5.15 mm, a large transverse field of view of 15 mm, and an ultra-fast transverse scanning pattern repetition frequency of 1 kHz. Scleral deformation was induced through a repurposed industry-standard, non-contact tonometer air-puff unit (Nidek Co., Japan) that was placed between the sample and the OCT objective lens so that it was coaxially aligned with the OCT scanning beam.

Three freshly enucleated rabbit eyes (adult New Zealand white rabbits) were obtained from a farm associated with the Veterinary School of the Universidad Complutense de Madrid (Spain), refrigerated at 4°C, and used within 48 h post-mortem. Muscles and conjunctival tissue were removed from the sclera of all eyes. Four different scleral locations were evaluated: superior (S), inferior (I), equatorial nasal (EN), and equatorial temporal (ET). A diagram of the positions can be seen in Figure 3.

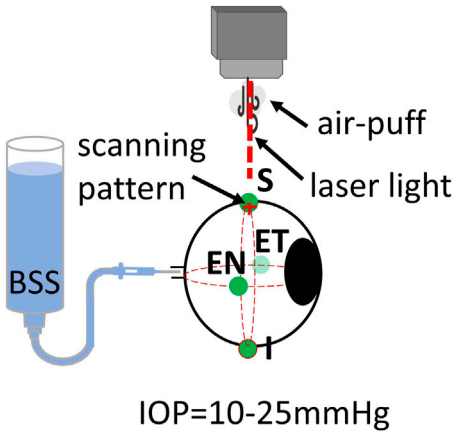

FIGURE 3
Schematic of inflation setup on rabbit eyes. Locations of air-puff excitation are Superior (S), Inferior (I), Equatorial Nasal (EN, and Equatorial Temporal (ET).

All eyes were connected to an automated IOP control system with a needle through the optic nerve. The eye was then placed in a customized holder and aligned with the OCT laser scanning beam. Initially, the IOP was fixed at 10 mmHg. OCT measurements were collected over two orthogonal axes, each of which was 15 mm long. A complete measurement consisted of a total of 100 cross-axes scans, with each axis sampled by 64 A-scans. The total acquisition time of a complete data set was 100 ms (one cross-axes scan per ms). After a set of three measurements for each location, the eye position was carefully changed to the next location. All measurements were repeated for IOP of 15, 20, and 25 mmHg. Temperature and humidity conditions were kept constant throughout the measurements (at 21.0°C ± 2.0°C and 37.2% ± 1.1% respectively). The eye globe was kept moisturized with a balanced salt solution (BSS) with drops applied before and after each measurement.

2.2.3.2 Data analysis

Data analysis included data processing and surface detection of the deforming ocular surfaces. The OCT images were obtained after standard image generation from wavenumber resampled spectra (Gora et al., 2009), using customized MATLAB routines. Air-puff excitation happens through a 2.4-mm-wide hole in a 5-mm-thick methacrylate window, which leads to an optical path difference at the center of the OCT images due to the difference in the refractive index. This difference was corrected using piece-wise registration routines written in ImageJ (National Institutes of Health, Bethesda, Maryland, United States). After obtaining OCT images, the ocular surfaces were segmented using a customized MATLAB routine (Bronte-Ciriza et al., 2021). For the analysis, only images from the sagittal meridian scanned were used.

2.2.3.3 Finite element and inverse model

For the FE model, the apex displacement at an IOP of 10 mmHg was used as the starting point. For each of the

10.3389/fbioe.2024.1426060

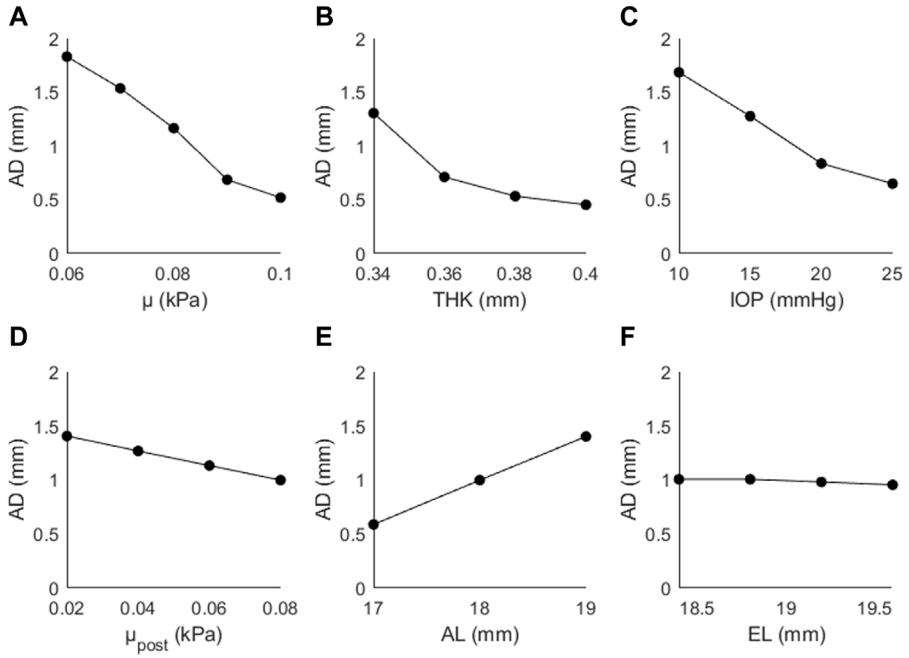

FIGURE 4
Apex displacement (AD) as a function of **(A)** the material coefficient μ, **(B)** thickness (THK), **(C)** intraocular pressure (IOP), **(D)** material coefficient μpost, **(E)** axial length (AL), and **(F)** the equatorial length (EL).

positions in each eye, the material coefficient was estimated using an iterative process, such that the apex displacement at IOP = 10 mmHg in the simulation matches the corresponding experimental displacement. The FE model was then evaluated, for this material coefficient, at IOPs of 15, 20, and 25 mmHg. The simulated apex displacement at IOPs 15–25 mmHg was compared to the experimental values and the RMS error was calculated. The process was done for each position in each eye. In this procedure, the stress-free configuration is used only for IOP = 10 mmHg.

An inverse modelling procedure was programmed in MATLAB to estimate the material coefficient of each eye. First, a function f_{apex} was created. This function takes μ as input, and then calls ANSYS to solve the FE model. The FE model is solved such that the material coefficient is a variable, and the remaining input parameters are those described in Table 1, except for IOP, which is given a value of 10 mmHg.

The function calculates the apex displacement from the FE solver data. Then, the square of the difference between the simulated apex displacement and the experimental apex displacement at IOP = 10 mmHg is calculated. This number is the output of the function.

Then, the *fminbnd* MATLAB function was used to minimize the output of function X. *fminbnd* is a single-variable minimizer, bounded non-linear minimization based on golden-section search and parabolic interpolation. The boundaries were set to $\mu = 0.05–0.15$. This minimization process yields a value of μ that was taken as an estimate of the material coefficient of the evaluated eye.

Using this value of μ, the FE model is evaluated for IOPs of 15, 20, and 25 mmHg, and the resulting apex displacement is calculated. The simulated results at 15–25 mmHg are compared to the experimental results at 15–25 mmHg for each eye.

3 Results

3.1 Sensitivity study

The results of the sensitivity study are presented for each output parameter (AD, CPR, AR). Figure 4 shows the predicted changes in AD as a function of μ, THK, IOP, μ_{post}, AL, and EL. Values in parentheses indicate the percentage increase/decrease from the initial value of the input parameter to the highest investigated value. AD decreased as a function of μ (↓72%), THK (↓65%), IOP (↓61%), μ_{post} (↓29%), and EL (↓5%), and increased as a function of AL (↑138%). The observed changes were greater for the direct parameters (μ, THK, IOP) than for the two indirect parameters (μ_{post}, EL). AL had the greatest effect on AD, and was the only parameter that showed a proportional and not an inversely proportional effect.

Figure 5 shows the changes in CPR as a function of (A) μ, (B) THK, (C) IOP, (D) μ_{post}, (E) AL, and (F) EL. The trends were not as consistent as those seen with AD; CPR increased as a function of μ (↑19%), IOP (↑10%), μ_{post} (↑27%), and EL (↑1%), and decreased as a function of THK (↓9%) and AL (↓14%). The largest changes are seen for the material coefficients, particularly the posterior coefficient.

Figure 6 shows the changes in AR as a function of (A) μ, (B) THK, (C) IOP, (D) μ_{post}, (E) AL, and (F) EL. AR decreased as a function of μ (↓5%), THK (↓2%), μ_{post} (↓20%), and AL (↓1%),

10.3389/fbioe.2024.1426060

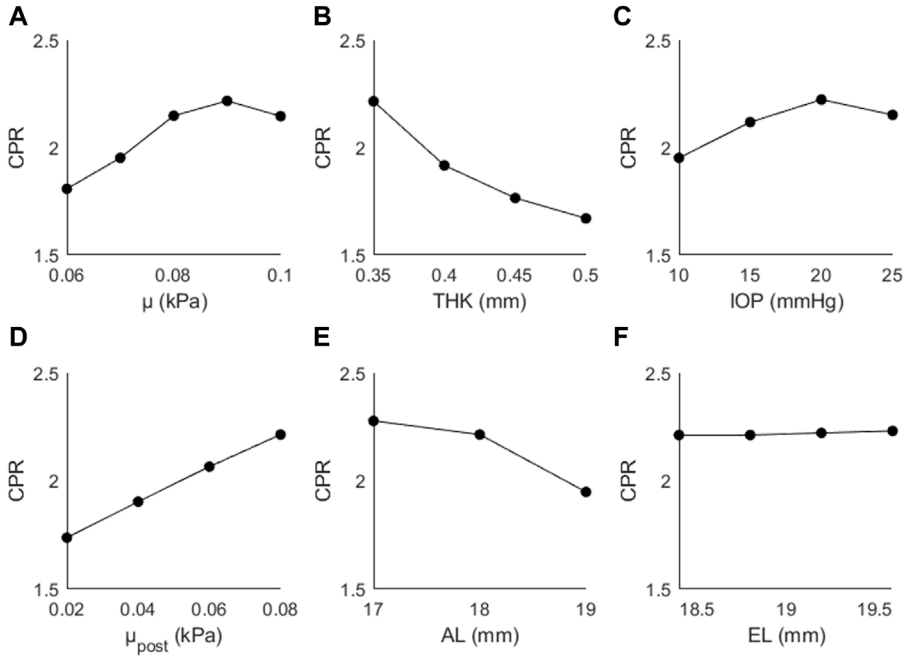

FIGURE 5
CPR as a function of **(A)** the material coefficient μ, **(B)** thickness (THK), **(C)** intraocular pressure (IOP), **(D)** material coefficient μpost, **(E)** axial length (AL), and **(F)** the equatorial length (EL).

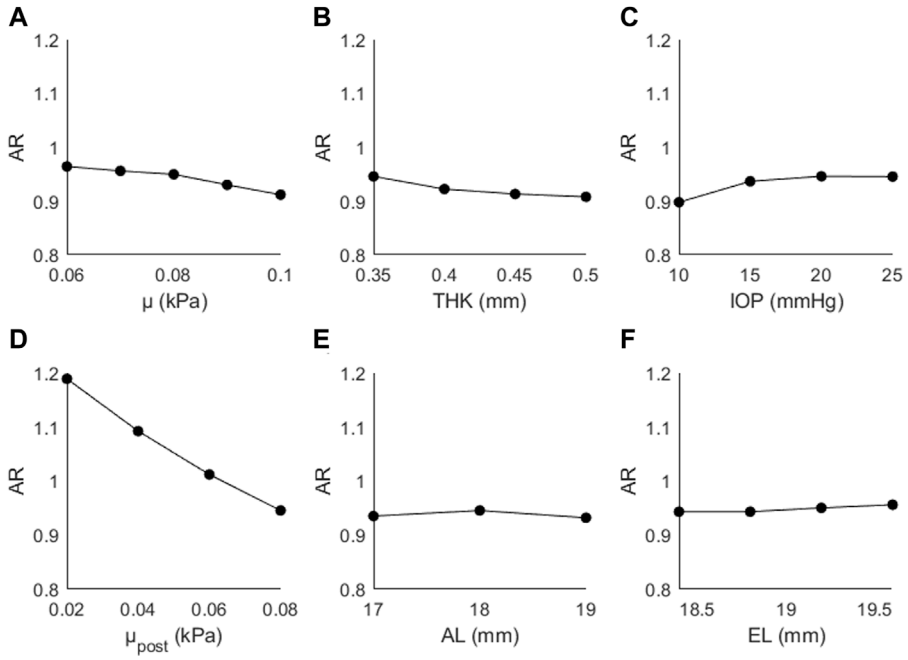

FIGURE 6
Changes in AR as a function of **(A)** the material coefficient μ, **(B)** thickness (THK), **(C)** intraocular pressure (IOP), **(D)** material coefficient μpost, **(E)** axial length (AL), and **(F)** the equatorial length (EL).

and increased as a function of IOP (↑5%) and EL (↑1%). The generally small magnitude of the changes suggests that this parameter is primarily affected by the posterior material coefficient.

3.2 Random sampling study

The results of the random sampling study are presented in Figures 7–9. Figure 7 shows AD as a function of (A) μ, (B)

10.3389/fbioe.2024.1426060

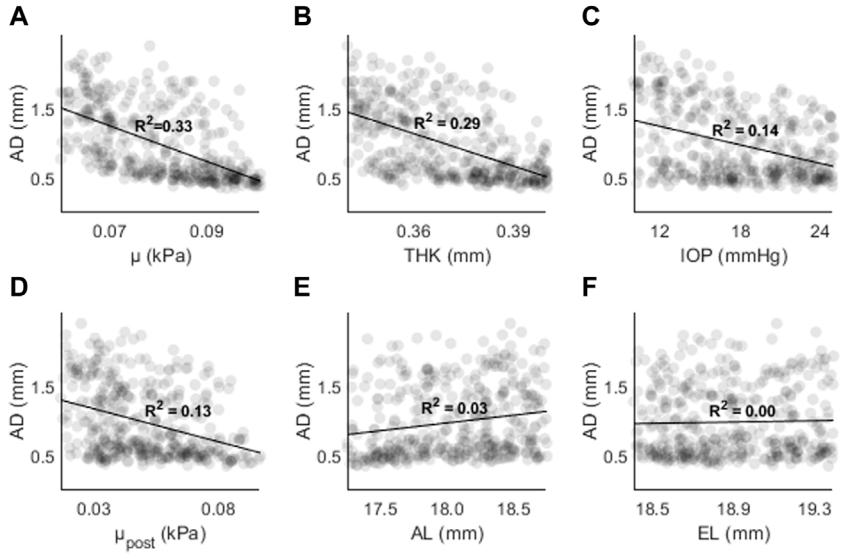

FIGURE 7
AD as a function of **(A)** the material coefficient μ, **(B)** thickness (THK), **(C)** intraocular pressure (IOP), **(D)** material coefficient μpost, **(E)** axial length (AL), and **(F)** the equatorial length (EL).

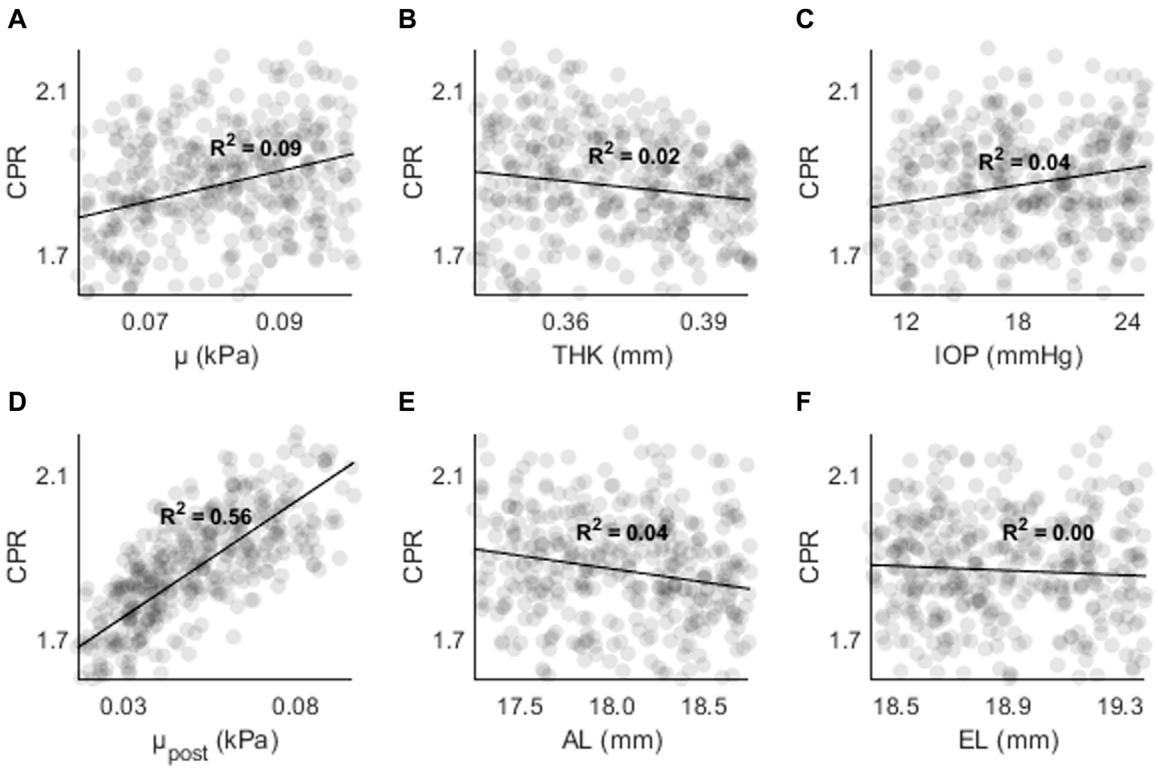

FIGURE 8
CPR as a function of **(A)** the material coefficient μ, **(B)** thickness (THK), **(C)** intraocular pressure (IOP), **(D)** material coefficient μpost, **(E)** axial length (AL), and **(F)** the equatorial length (EL).

THK, (C) IOP, (D) μ_{post}, (E) AL, and (F) EL. The strongest correlations were found for μ (R^2 = 0.33, $p < 0.01$), followed by THK (R^2 = 0.29, $p < 0.01$), IOP (R^2 = 0.14, $p < 0.01$) and μ_{post} (R^2 = 0.13, $p < 0.01$). The correlations for AL and EL were weaker ($R^2 < 0.05$). Compared to the sensitivity study, the effects of IOP and AL were reduced, with the latter showing almost no correlation.

Figures 8, 9 shows CPR as a function of (A) μ, (B) THK, (C) IOP, (D) μ_{post}, (E) AL, and (F) EL. R^2 values are lower overall ($R^2 < 0.05$), except for μ_{post} ($R^2 = 0.56$, $p < 0.01$) and μ ($R^2 = 0.09$, $p < 0.01$). The results are consistent with those found in the sensitivity study, where μ and μ_{post} had the greatest effect on CPR.

Figure 9 shows AR as a function of (A) μ, (B) THK, (C) IOP, (D) μ_{post}, (E) AL, and (F) EL. The highest R^2 values were found for μ_{post} ($R^2 = 0.87$, $p < 0.01$) and μ ($R^2 = 0.11$, $p < 0.01$). For all other input parameters, $R^2 < 0.05$. The results are consistent with those found in the sensitivity study, where μ and μ_{post} resulted in the largest changes to AR.

The highest R^2 values were found between μ_{post} and CPR/AR parameters. For AD the R^2 values were stronger for μ and THK. Overall, the results show that parameters with higher spatial resolution (CPR, AR) are less likely to have dependence on non-material parameters. The results also show that other indirect parameters such as AL and EL are not strongly correlate with AD, CPR, or AR in the presence of other changes. THK and IOP are strongly correlated with AD, but not with CPR and AR.

3.3 Comparison between simulation and experimental data

Figure 10 shows a comparison between experimental (squares) and simulated (lines) apex displacements as a function of IOP at different scleral locations. There was good correspondence between experimental and simulated apex displacements from IOP = 15 mmHg–25 mmHg. The average RMSE was 0.10 mm for Eye 1, 0.08 mm for Eye 2, and 0.20 mm for Eye 3. The RMSE corresponds well with the standard deviation of the experimental displacements at IOPs 15–25 mmHg (0.17 mm for Eye 1, 0.08 mm for Eye 2, 0.18 mm for Eye 3), suggesting that the differences in estimation between eyes are affected by the precision of the experimental measurements. Figure 11 shows the OCT image, segmentation profile, and simulated profile for ET in eye 1 at 20 mmHg.

4 Discussion

In this study, a model of scleral APDI was developed and the deformation was evaluated as a function of different input parameters. Output parameter AD, which was derived from a single point, showed a larger dependence on all input parameters (μ, μ_{post}, THK, IOP, AL, EL), while output parameters CPR and AR, which are derived from multiple points, showed dependence on material parameters (μ, μ_{post}) but were less dependent on THK, IOP, AL, and EL.

The material coefficient μ_{post} was found to greatly affect the values of the parameters CPR and AR. These two parameters are more complex than AD, as they compare the deformation in two regions, one central to the air-puff load and one peripheral. The effect of μ_{post}, and the limited effect of the remaining input parameters, suggests that CPR and AR could be used to estimate material properties away from the region of air-puff application. This is of particular interest for *in vivo* applications, as reaching the posterior sclera with an air-puff is not feasible. Instead, the spatial profile of equatorial scleral deformation could be used to estimate the posterior sclera's stiffness.

The scleral response was most influenced by, in descending order, μ, μ_{post}, THK, and IOP. This was true for both random sampling and sensitivity studies. AL had an influence on the output parameters in the sensitivity study, but the influence was largely absent in the random sampling study, suggesting that the strength of the parameter is largely offset by changes in thickness, IOP, etc. EL on the other hand did not have much influence over the outputs in either study. These results suggest that an estimation of the material properties of the sclera would be aided by approximate knowledge of the thickness of the sclera at the location of air-puff application and the IOP of the eye. The thickness could be estimated from the image obtained in scleral APDI provided that this is a visible region, as is done in corneal APDI. The IOP could be estimated from tonometry measurements of the cornea, where work has been done on estimating IOP without the influence of material and geometric properties (Joda et al., 2016).

The comparison between experimental and simulated AD as a function of IOP showed similar behavior in the FE model and real eyes: a decrease in the apex displacement with increasing IOP, occurring in a non-linear fashion. The estimation varied in each eye, with RMS error of 0.10, 0.08, and 0.20 mm, which likely resulted from the experimental variability. From the FE model, we have also determined that AD as a function of IOP will also be affected by the initial AL, EL, and THK values, as well as by material coefficient α (set as a constant in this model). In this work only the effect of IOP was compared in experimental and simulated results, as this parameter can be controlled *ex vivo*. A full validation would entail a comparison between output parameters and multiple variable inputs (thickness, material properties, globe dimensions, IOP) in order to verify the expected correlations. For full comparison, the material properties would need to be either independently assessed with another method (extensiometry, OCE, etc.) or estimated by association, e.g., to age.

APDI has been primarily used in the cornea, but a comparison can still be made between this study and the literature. In a FE parametric study of corneal APDI, Kling (Kling et al., 2014) found that the material modulus of the cornea, IOP, scleral modulus, and thickness had significant influence over AD, with a decrease of 90% in scleral modulus decreasing AD by 0.20 mm. Nguyen (Nguyen et al., 2019) found the same effect of scleral modulus on corneal AD, with a lower modulus resulting in higher AD. This is consistent with our model, where AD decreased by 0.4 mm after a 90% decrease in μ_{post} in the sensitivity study. Similar effects were seen for other parameters, for instance Kling found a decrease of 0.4 mm in AD with a change in IOP from 15 to 25 mmHg in the porcine cornea; Nguyen found a decrease of 0.142 ± 0.02 mm from 10 to 20 mmHg in an FE model and a decrease of 0.50 ± 0.14 from 10 to 20 mmHg *in vivo* in the human cornea. In our sensitivity study we found a decrease of 0.64 mm in AD from 15 to 25 mmHg.

In any FE parametric study, modeling choices will affect the outcomes. Although we have quantified changes and correlations

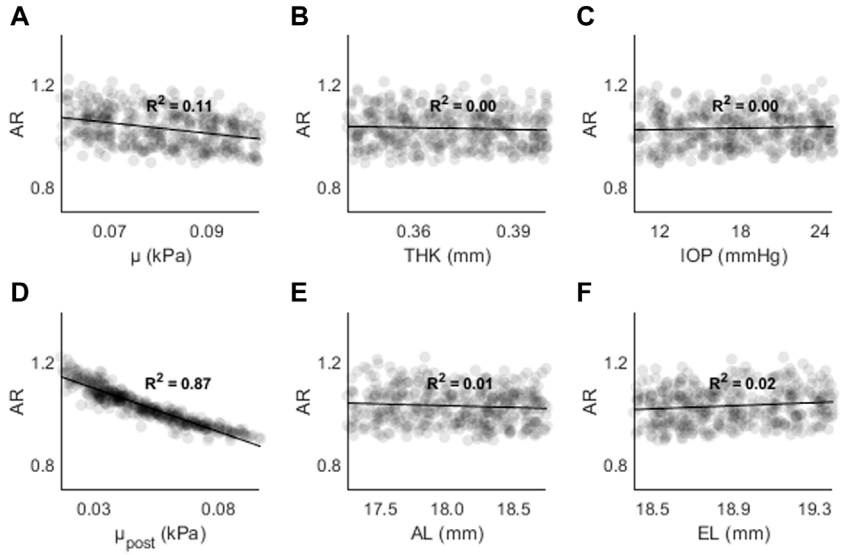

FIGURE 9
AR as a function of **(A)** the material coefficient μ, **(B)** thickness (THK), **(C)** intraocular pressure (IOP), **(D)** material coefficient μpost, **(E)** axial length (AL), and **(F)** the equatorial length (EL).

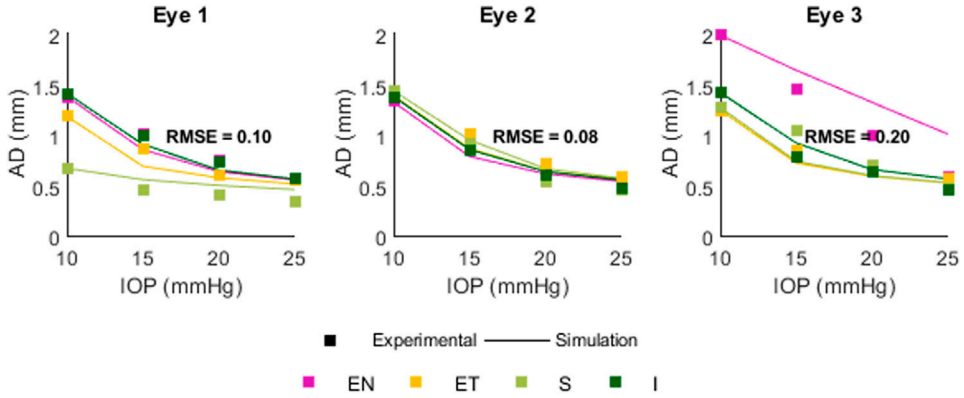

FIGURE 10
Comparison between experimental and simulated AD as a function of IOP. Positions are Superior (S) Inferior (I) Equatorial Nasal (EN) and Equatorial Temporal (ET). The RMSE for each eye was 0.10, 0.08, and 0.20 mm.

between deformation response (AD, CPR, AR) and parameters such as μ and IOP, the strength of the correlations will be dependent on the range of values evaluated for each input parameter.

The random sampling analysis showed a high correlation between $μ_{post}$ and AR, which is worth exploring. First, our model accounts for changes in μ from the equator to the most posterior part of the sclera, but does not account for anterior variation. Changes in material properties in the anterior sclera could affect the peripheral displacement 1, and therefore affect AR. Second, in this model we have used a linear function (Eq. 2) to model the spatial variation of the sclera. Although the sclera's material properties are known to vary along the axial length of the eye, this variation might not follow a linear pattern, i.e., (Elsheikh et al., 2010) find larger changes from anterior to equatorial than equatorial to posterior. In addition, the pattern of variation could be different in subjects with a pathology or a stiffening treatment in the sclera. The choice of a uniform, linear function will affect the deformation profile, output parameters, and strength of the correlations found in this paper. Third, AR is sensitive to the precision of the two displacements. In an FE model the displacement data is highly precise; in an experimental or *in vivo* application, the precision of the displacement will be lower, and the AR estimate noisier and less accurate.

In this work, an isotropic constitutive model was used. This model is not mechanistic, and the material coefficient does not necessarily reflect an intrinsic fiber or extracellular

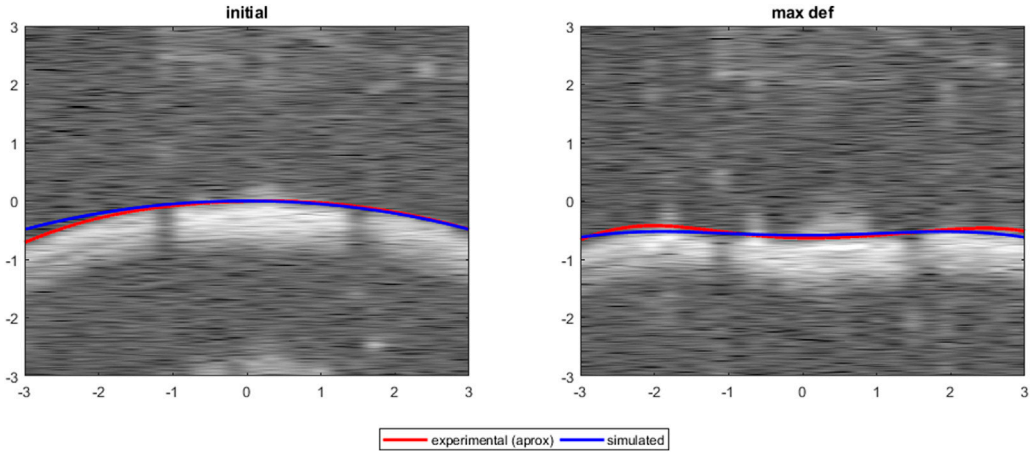

FIGURE 11
Experimental profile from OCT image and simulated profile for Eye 1, ET, IOP = 20 mmHg.

matrix modulus. Corneal APDI has been successful at predicting corneal stiffness through the use of isotropic models, despite the cornea's anisotropy. FE studies of anisotropic scleral models suggest that the extracellular matrix, which is modelled as isotropic, has a larger influence in inflation than the fibers, which are directional (Grytz et al., 2014; Coudrillier et al., 2015). This suggests that the isotropic approach is suitable for scleral APDI. Anisotropic models, while more accurate, still require simplifying assumptions, for example holding material coefficients constant across the studied tissue (Coudrillier et al., 2015; Schwaner et al., 2020). They also typically require complex, multi-step inverse modeling schemes, making their implementation outside the laboratory challenging. Nonetheless, anisotropic considerations in FE modeling of APDI could provide additional information to characterize the sclera from a small number of displacements.

An area where investigating posterior scleral stiffness is relevant is myopia. There are numerous reports in the literature from *ex vivo* eyes (mostly animal myopia models) showing a decrease in posterior scleral stiffness from material (Phillips and McBrien, 1995; Phillips et al., 2000; McBrien et al., 2009) and thickness (Curtin and Teng, 1958). APDI could be a useful tool to further develop computational mechanical models of the sclera to study the effect of the sclera in healthy and myopic eyes. Also relevant to myopia is the ability to assess changes in scleral tissue stiffness after cross-linking treatment (CXL) (Dotan et al., 2014; Liu et al., 2016). CXL has been traditionally used in treating the cornea for conditions such as keratoconus, and the stiffening effects on the corneal tissue have been observed using extensiometry (Cherfan et al., 2003; Kling et al., 2012) and APDI estimations (Kling et al., 2014; Bekesi et al., 2017). Stiffness changes have been measured in extensiometry of cross-linked scleral tissue (Vinas-Pena et al., 2022), suggesting that scleral APDI could be a useful tool to assess scleral CXL.

5 Conclusion

This FE work found that the material properties of the sclera (local and general), thickness of the tissue, and the IOP were the most influential factors for a single-point deformation parameter (apex displacement), with globe dimensions less influential. For multi-point deformation parameters (asymmetry ratio or peripheral ratio), the local and general material properties were most influential, with thickness and IOP less coupled to the response. Scleral APDI could serve as a tool for diagnostics of scleral pathologies that impact its material properties, such as myopia, and treatments that act upon such properties, such as scleral cross-linking.

Data availability statement

The original contributions presented in the study are included in the article/Supplementary Material, further inquiries can be directed to the corresponding author.

Ethics statement

Ethical approval was not required for the study involving animals in accordance with the local legislation and institutional requirements because no animals were euthanized for our study. Eyes were obtained from animals used in veterinary activities (such as birth control, reproductive control, teaching) for which the Faculty of Veterinary of the Complutense University of Madrid ("Universidad Complutense de Madrid" in Spanish) is responsible. These activities have been approved by an animal experimentation committee ("Comité de Experimentación Animal (CEA)" in Spanish) with the number: (CEA) UCM 5414122021 2021.

Author contributions

AD: Conceptualization, Data curation, Formal Analysis, Investigation, Methodology, Software, Validation, Visualization, Writing–original draft, Writing–review and editing. LV: Investigation, Visualization, Writing–review and editing. SM: Conceptualization, Funding acquisition, Methodology, Supervision, Writing–review and editing. JB: Conceptualization, Funding acquisition, Methodology, Supervision, Validation, Writing–review and editing.

Funding

The author(s) declare that financial support was received for the research, authorship, and/or publication of this article. Spanish Government Grant (PRE2018-086169, FIS2017-84753-R, PID2020-115191RB-I00); European Project H2020 IMCUSTOMEYE (779960); European Research Council (2018-ADG-SILKEYE-833106); Ayudas Ramón y Cajal (RYC2022-037910-I); L'Oréal-UNESCO "For Women in Science" Spain; NIH NEI P30EY 001319; Unrestricted Funds Research to Prevent Blindness, NY.

Conflict of interest

The authors declare that the research was conducted in the absence of any commercial or financial relationships that could be construed as a potential conflict of interest.

Publisher's note

Supplementary material

The Supplementary Material for this article can be found online at: https://www.frontiersin.org/articles/10.3389/fbioe.2024.1426060/full#supplementary-material

References

Ariza-Gracia, M. A., Zurita, J. F., Piñero, D. P., Rodriguez-Matas, J. F., and Calvo, B. (2015). Coupled biomechanical response of the cornea assessed by non-contact tonometry. A simulation study. *PLOS ONE* 10 (3), e0121486. doi:10.1371/journal.pone.0121486

Asejczyk-Widlicka, M., Sródka, D. W., Kasprzak, H., and Pierscionek, B. K. (2007). Modelling the elastic properties of the anterior eye and their contribution to maintenance of image quality: the role of the limbus. *Eye* 21 (8), 1087–1094. doi:10.1038/sj.eye.6702464

Barathi, A., Thu, M. K., and Beuerman, R. W. (2002). Dimensional growth of the rabbit eye. *Cells Tissues Organs* 171 (4), 276–285. doi:10.1159/000063123

Bekesi, N., Dorronsoro, C., de la Hoz, A., and Marcos, S. (2016). Material properties from air puff corneal deformation by numerical simulations on model corneas. *PLOS ONE* 11 (10), e0165669. doi:10.1371/journal.pone.0165669

Bekesi, N., Gallego-Muñoz, P., Ibarés-Frías, L., Perez-Merino, P., Martinez-Garcia, M. C., Kochevar, I. E., et al. (2017). Biomechanical changes after *in vivo* collagen cross-linking with rose bengal–green light and riboflavin-UVA. *Invest. Ophthalmol. Vis. Sci.* 58 (3), 1612–1620. doi:10.1167/iovs.17-21475

Birkenfeld, J. S., Germann, J., De Castro, A., de la Hoz, A., Curatolo, A., and Marcos, S. (2019). Assessment of asymmetries in biomechanical properties from corneal deformation imaging. *Invest. Ophthalmol. Vis. Sci.* 60, 6809.

Bozkir, G., Bozkir, M., Dogan, H., Aycan, K., and Güler, B. (1997). Measurements of axial length and radius of corneal curvature in the rabbit eye. *Acta Med. Okayama* 51 (1), 9–11. doi:10.18926/amo/30804

Bronte-Ciriza, D., Birkenfeld, J. S., de la Hoz, A., Curatolo, A., Germann, J. A., Villegas, L., et al. (2021). Estimation of scleral mechanical properties from air-puff optical coherence tomography. *Biomed. Opt. Express* 12 (10), 6341–6359. doi:10.1364/BOE.437981

Chen, K. J., Eliasy, A., Vinciguerra, R., Abass, A., Lopes, B. T., Vinciguerra, P., et al. (2019). Development and validation of a new intraocular pressure estimate for patients with soft corneas. *J. Cataract. Refract Surg.* 45 (9), 1316–1323. doi:10.1016/j.jcrs.2019.04.004

Cherfan, D., Verter, E., Melki, S., Gisel, T. E., Doyle, F. J., Jr, Scarcelli, G., et al. (2003). Collagen cross-linking using rose bengal and green light to increase corneal stiffness. *Invest. Ophthalmol. Vis. Sci.* 54 (5), 3426–3433. doi:10.1167/iovs.12-11509

Coudrillier, B., Boote, C., Quigley, H. A., and Nguyen, T. D. (2013). Scleral anisotropy and its effects on the mechanical response of the optic nerve head. *Biomech. Model Mechanobiol.* 12 (5), 941–963. doi:10.1007/s10237-012-0455-y

Coudrillier, B., Pijanka, J., Jefferys, J., Sorensen, T., Quigley, H. A., Boote, C., et al. (2015). Collagen structure and mechanical properties of the human sclera: analysis for the effects of age. *J. Biomech. Eng.* 137 (4), 041006. doi:10.1115/1.4029430

Coudrillier, B., Tian, J., Alexander, S., Myers, K. M., Quigley, H. A., and Nguyen, T. D. (2012). Biomechanics of the human posterior sclera: age- and glaucoma-related changes measured using inflation testing. *Invest. Ophthalmol. Vis. Sci.* 53 (4), 1714–1728. doi:10.1167/iovs.11-8009

Curatolo, A., Birkenfeld, J. S., Martinez-Enriquez, E., Germann, J. A., Muralidharan, G., Palací, J., et al. (2020). Multi-meridian corneal imaging of air-puff induced deformation for improved detection of biomechanical abnormalities. *Biomed. Opt. Express* 11 (11), 6337–6355. doi:10.1364/boe.402402

Curtin, B. J., and Teng, C. C. (1958). Scleral changes in pathological myopia. *Trans. Acad. Ophthalmol. Otolaryngol. Am. Acad. Ophthalmol. Otolaryngol.* 62, 777–790.

Dorronsoro, C., Daniel, P., Pablo, P.-M., Sabine, K., Susana, M., et al. (2012). Dynamic OCT measurement of corneal deformation by an air puff in normal and cross-linked corneas. *Biomed. Opt. Express* 3 (3), 473–487. doi:10.1364/boe.3.000473

Dotan, A., Kremer, I., Livnat, T., Zigler, A., Weinberger, D., and Bourla, D. (2014). Scleral cross-linking using riboflavin and ultraviolet-a radiation for prevention of progressive myopia in a rabbit model. *Exp. Eye Res.* 127, 190–195. doi:10.1016/j.exer.2014.07.019

Eliasy, A., Chen, K. J., Vinciguerra, R., Lopes, B. T., Abass, A., Vinciguerra, P., et al. (2019). Determination of corneal biomechanical behavior in-vivo for healthy eyes using CorVis ST tonometry: stress-strain index. *Front. Bioeng. Biotechnol.* 7, 105. doi:10.3389/fbioe.2019.00105

Elsheikh, A., Geraghty, B., Alhasso, D., Knappett, J., Campanelli, M., and Rama, P. (2010). Regional variation in the biomechanical properties of the human sclera. *Exp. Eye Res.* 90 (5), 624–633. doi:10.1016/j.exer.2010.02.010

Elsheikh, A., Whitford, C., Hamarashid, R., Kassem, W., Joda, A., and Büchler, P. (2013). Stress free configuration of the human eye. *Med. Eng. Phys.* 35 (2), 211–216. doi:10.1016/j.medengphy.2012.09.006

Geragthy, B., Abass, A., Eliasy, A., Jones, S. W., Rama, P., Kassem, W., et al. (2020). Inflation experiments and inverse finite element modelling of posterior human sclera. *J. Biomech.* 98, 109438. doi:10.1016/j.jbiomech.2019.109438

Gora, M., Karnowski, K., Szkulmowski, M., Kaluzny, B. J., Huber, R., Kowalczyk, A., et al. (2009). Ultra high-speed swept source OCT imaging of the anterior segment of human eye at 200 kHz with adjustable imaging range. *Opt. Express.* 17 (17), 14880–14894. doi:10.1364/OE.17.014880

Grytz, R., Fazio, M. A., Girard, M. J., Libertiaux, V., Bruno, L., Gardiner, S., et al. (2014). Material properties of the posterior human sclera. *J. Mech. Behav. Biomed. Mater* 29, 602–617. doi:10.1016/j.jmbbm.2013.03.027

Jia, X., Liao, S., Duan, X., Zheng, W., and Zou, B. (2017). Anisotropic finite element modeling based on a harmonic field for patient-specific sclera. *Biomed. Res. Int.* 2017, 1–10. doi:10.1155/2017/6073059

Jiménez-Villar, A., Mączyńska, E., Cichański, A., Wojtkowski, M., Kałużny, B. J., and Grulkowski, I. (2019). High-speed OCT-based ocular biometer combined with an air-puff system for determination of induced retraction-free eye dynamics. *Biomed. Opt. Express* 10 (7), 3663–3680. doi:10.1364/boe.10.003663

Joda, A. A., Shervin, M. M., Kook, D., and Elsheikh, A. (2016). Development and validation of a correction equation for Corvis tonometry. *Comput. Methods Biomech. Biomed. Engin* 19 (9), 943–953. doi:10.1080/10255842.2015.1077515

Keeley, F. W., Morin, J. D., and Vesely, S. (1984). Characterization of collagen from normal human sclera. *Exp. Eye Res.* 39 (5), 533–542. doi:10.1016/0014-4835(84)90053-8

Kling, S., Bekesi, N., Dorronsoro, C., Pascual, D., and Marcos, S. (2014). Corneal viscoelastic properties from finite-element analysis of *in vivo* air-puff deformation. *PLOS ONE* 9 (8), e104904. doi:10.1371/journal.pone.0104904

Kling, S., Ginis, H., and Marcos, S. (2012). Corneal biomechanical properties from two-dimensional corneal flap extensiometry: application to UV-riboflavin cross-linking. *Invest. Ophthalmol. Vis. Sci.* 53 (8), 5010–5015. doi:10.1167/iovs.12-9583

Kling, S., and Hafezi, F. (2017). Corneal biomechanics – a review. *Ophthalmic Physiol. Opt.* 37, 240–252. doi:10.1111/opo.12345

Liu, S., Li, S., Wang, B., Lin, X., Wu, Y., Liu, H., et al. (2016). Scleral cross-linking using riboflavin UVA irradiation for the prevention of myopia progression in a Guinea pig model: blocked axial extension and altered scleral microstructure. *PLoS One* 11 (11), e0165792. doi:10.1371/journal.pone.0165792

Markov, P. P., Eliasy, A., Pijanka, J. K., Htoon, H. M., Paterson, N. G., Sorensen, T., et al. (2018). Bulk changes in posterior scleral collagen microstructure in human high myopia. *Mol. Vis.* 24, 818–833.

McBrien, N. A., Cornell, L. M., and Gentle, A. (2001). Structural and ultrastructural changes to the sclera in a mammalian model of high myopia. *Invest. Ophthalmol. Vis. Sci.* 42 (10), 2179–2187.

McBrien, N. A., Jobling, A. I., and Gentle, A. (2009). Biomechanics of the sclera in myopia: extracellular and cellular factors. *Optom. Vis. Sci.* 86, E23–E30. doi:10.1097/opx.0b013e3181940669

McBrien, N. A., Lawlor, P., and Gentle, A. (2000). Scleral remodeling during the development of and recovery from axial myopia in the tree shrew. *Invest. Ophthalmol. Vis. Sci. Nov.* 41 (12), 3713–3719.

Nguyen, B. A., Roberts, C. J., and Reilly, M. A. (2019). Biomechanical impact of the sclera on corneal deformation response to an air-puff: a finite-element study. *Front. Bioeng. Biotechnol.* 6, 210. doi:10.3389/fbioe.2018.00210

Norman, R. E., Flanagan, J. G., Sigal, I. A., Rausch, S. M., Tertinegg, I., and Ethier, C. R. (2011). Finite element modeling of the human sclera: influence on optic nerve head biomechanics and connections with glaucoma. *Exp. Eye Res.* 93 (1), 4–12. doi:10.1016/j.exer.2010.09.014

Pachenari, M., and Hatami-Marbini, H. (2021). Regional differences in the glycosaminoglycan role in porcine scleral hydration and mechanical behavior. *Invest. Ophthalmol. Vis. Sci.* 62 (3), 28. doi:10.1167/iovs.62.3.28

Phillips, J. R., Khalaj, M., and McBrien, N. A. (2000). Induced myopia associated with increased scleral creep in chick and tree shrew eyes. *Invest. Ophthalmol. Vis. Sci.* 41 (8), 2028–2034.

Phillips, J. R., and McBrien, N. A. (1995). Form deprivation myopia: elastic properties of sclera. *Ophthalmic Physiol. Opt.* 15 (5), 357–362. doi:10.1046/j.1475-1313.1995.9500062i.x

Rada, J. A., Nickla, D. L., and Troilo, D. (2000). Decreased proteoglycan synthesis associated with form deprivation myopia in mature primate eyes. *Invest. Ophthalmol. Vis. Sci.* 41 (8), 2050–2058.

Ramier, A., Eltony, A. M., Chen, Y., Clouser, F., Birkenfeld, J. S., Watts, A., et al. (2020). *In vivo* measurement of shear modulus of the human cornea using optical coherence elastography. *Sci. Rep.* 10, 17366. doi:10.1038/s41598-020-74383-4

Schwaner, S. A., Hannon, B. G., Feola, A. J., and Ethier, C. R. (2020). Biomechanical properties of the rat sclera obtained with inverse finite element modeling. *Biomech. Model Mechanobiol.* 19, 2195–2212. doi:10.1007/s10237-020-01333-4

Shao, P., Besner, S., Zhang, J., Scarcelli, G., and Yun, S. H. (2016). Etalon filters for Brillouin microscopy of highly scattering tissues. *Opt. Express* 24 (19), 22232–22238. doi:10.1364/oe.24.022232

Vareilles, P., Conquet, P., and Le Douarec, J. C. (1977). A method for the routine intraocular pressure (IOP) measurement in the rabbit: range of IOP variations in this species. *Exp. Eye Res.* 24 (4), 369–375. doi:10.1016/0014-4835(77)90149-x

Villegas, L., Zvietcovich, F., Marcos, S., and Birkenfeld, J. S. (2024). *Revealing regional variations in scleral shear modulus in a rabbit eye model using multi-directional ultrasound optical coherence elastography*. Available at SSRN 4613761.

Vinas-Pena, M., Feng, X., Li, G. Y., and Yun, S. H. (2022). *In situ* measurement of the stiffness increase in the posterior sclera after UV-riboflavin crosslinking by optical coherence elastography. *Biomed. Opt. Express* 13 (10), 5434–5446. doi:10.1364/boe.463600

Wollensak, G., and Spoerl, E. (2004). Collagen crosslinking of human and porcine sclera. *J. Cataract. Refract. Surg.* 30 (3), 689–695. doi:10.1016/j.jcrs.2003.11.032

Zvietcovich, F., Nair, A., Singh, M., Aglyamov, S. R., Twa, M. D., and Larin, K. V. (2020). Dynamic optical coherence elastography of the anterior eye: understanding the biomechanics of the limbus. *Invest. Ophthalmol. Vis. Sci.* 61 (13), 7. doi:10.1167/iovs.61.13.7

frontiers | Frontiers in Bioengineering and Biotechnology

TYPE Review
PUBLISHED 15 October 2024
DOI 10.3389/fbioe.2024.1455027

OPEN ACCESS

EDITED BY
Jos J. Rozema,
University of Antwerp, Belgium

REVIEWED BY
Kehao Wang,
Beihang University, China
Ying He,
Dalian University of Technology, China

*CORRESPONDENCE
Qiaoyu Meng,
m_qiaoyu@163.com

RECEIVED 26 June 2024
ACCEPTED 03 October 2024
PUBLISHED 15 October 2024

CITATION
Pang G, Wang C, Wang X, Li X and Meng Q (2024) A review of human cornea finite element modeling: geometry modeling, constitutive modeling, and outlooks.
Front. Bioeng. Biotechnol. 12:1455027.
doi: 10.3389/fbioe.2024.1455027

A review of human cornea finite element modeling: geometry modeling, constitutive modeling, and outlooks

Guobao Pang[1], Chenyan Wang[2], Xiaojun Wang[3], Xiaona Li[2] and Qiaoyu Meng[4]*

[1]Shanxi Bethune Hospital, Shanxi Academy of Medical Sciences, Tongji Shanxi Hospital, Third Hospital of Shanxi Medical University, Taiyuan, China, [2]College of Biomedical Engineering, Taiyuan University of Technology, Taiyuan, China, [3]College of Mechanical and Vehicle Engineering, Taiyuan University of Technology, Taiyuan, China, [4]Institute of Advanced Structure Technology, Beijing Institute of Technology, Beijing, China

The cornea is a vital tissue of the human body. The health status of the cornea has a great impact on the quality life of person. There has been a great deal of research on the human cornea biomechancis. However, the difficulty in obtaining the human cornea has greatly limited the research of cornea biomechancis. Using finite element modelling has become a very effective and economical means for studying mechanical properties of human cornea. In this review, the geometrical and constitutive models of the cornea are summarised and analysed, respectively. Some factors affecting of the finite element calculation are discussed. In addition, prospects and challenges for the finite element model of the human cornea are presented. This review will be helpful to researchers performing studies in the relevant fields of human cornea finite element analysis.

KEYWORDS

human cornea, finite element analysis, geometric model, constitutive model, biomechanics property

1 Introduction

The eyes are vital organ of the human. It contains many tissues and delicate structures, such as the cornea, sclera, lens, iris, vitreous, aqueous humor, ciliary muscle, retina, choroid, optic nerve, and aqueous humor (Clevenger et al., 2024; Arestova et al., 2024; Murugan and Cheng, 2022; Neuhuber and Schrödl, 2011; Stefánsson, 2009; Mark, 2010; Fisher, 1977; Jonas et al., 1999). Any slight injury in the eye's tissues can seriously affect eye function. The cornea is located on the outer surface of the eyeball, and the cornea is also one of the most vulnerable parts of the eyeball. Common corneal diseases include refractive errors (myopia, hyperopia, astigmatism), keratoconus, corneal dystrophy, tumors, inflammation, and blindness (Pinazo-Durán et al., 2016; BITAR et al., 2018; Dutta et al., 2021; Rampat et al., 2021). Figure 1 shows some photos of corneal injury: corneal scarring, severe laceration of the cornea, keratoconus, corneal epithelial defect, and corneal foreign body (Barrientez et al., 2019). For refractive errors, refractive surgery, such as laser *in situ* keratomileusis (LASIK), femtosecond laser-assisted *in situ* keratomileusis (Fs-LASIK), and small-incision lenticule extraction (SMILE), is an effective method (Schiefer et al., 2016; Melki and Azar, 2001; Zhang et al., 2016; Sekundo et al., 2011). Ultraviolet light cross-linking therapy surgery is used to treat keratoconus and corneal dystrophy (Santhiago and

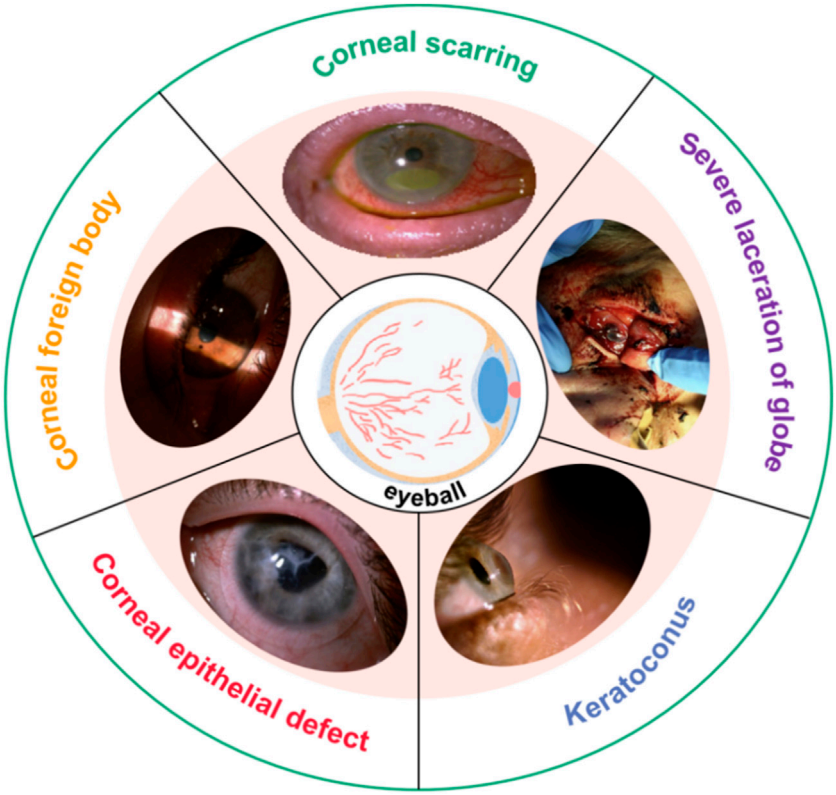

FIGURE 1
Photos of corneal injury (Barrientez et al., 2019).

Randleman, 2021; Wernli et al., 2013; Santodomingo-Rubido et al., 2022). Severe keratoconus, corneal dilation, and corneal tumors can cause corneal perforation or even blindness. Corneal transplantat surgery will become a kind of important means for the repair vision. These surgeries are very complex and require extensive clinical experience. It also presents a significant challenge for surgeons.

The Finite element analysis (FEA) method is widely used in engineering analysis and calculation, and also widely used in biomechanics field (Nikishkov, 2004; Logg, 2007). Common finite element analysis software include Ansys, Abaqus, Comsol, Adina, Dyna, and Marc. In the field of biomechanics, the appearance of finite element soft provides great convenience for the study of the mechanical properties of human tissues *in vivo*. Such as blood vessels, hearts, bone tissue, cells, and eyeballs, finite element analysis software is often applied (Clough, 1990). Compared with laboratory experiments, computer-based simulation has many advantages. Firstly, finite element analysis can effectively simulate, calculate, analyze and predict various mechanical behaviors of human tissues (Tandale et al., 2022). Secondly, it greatly reduces the experiment cost, especially for the study of human tissues that are difficult to obtain. Thirdly, FEA can avoid human ethical problem (Civalek et al., 2020). Finally, finite element analysis can evaluate the experimental results more quickly, efficiently, and accurately. In the past, for many surgeries or corneal studies, researchers often needed to conduct animal experiments to do relevant research. However, animal corneas are quite different from human corneal tissues, and the results are difficult to directly apply to human eyes. Finite element can give full play to its advantages and facilitate researchers to model and analyze human corneas. For the quantitative assessment of corneal refractive surgery or corneal trauma, the finite element methof has played a great role. In addition, for the study of corneal orthokeratology, finite element analysis can also effectively analyze the biomechanical response of the orthokeratology to the cornea. By establishing LASIK and SMILE surgical models, Wang et al. (2022) quantitatively analyzed the stress distribution and displacement distribution of the corneal surface after two kinds of surgery. She believed that SMILE refractive surgery is superior to LASIK surgery in terms of corneal biomechanical stability. Bao et al. (2018) used finite element modeling to simulate LASIK refractive surgery. The effects of LASIK surgery on corneal biomechanical behavior were analyzed and the results were validated using clinical datasets. The results show that the quantitative analysis of the shape and refractive power was reliable and effective.

Finite element analysis also has some disadvantages. The first is that the geometry of the model is often difficult to exactly correspond to the real shape. In finite element modeling, it is often necessary to simplify the geometry of the model. Different degrees of simplification have different effects on the calculation results. Secondly, the constitutive relationship of biological soft tissue materials is very complex, but in order to facilitate the description of material properties, the finite element method often simplifies the description of the constitutive relationship of materials studied. The effect of the simplification of the constitutive

relation on the calculation results can not be ignored. Third, the result of finite element calculation is not a real solution, but a numerical solution. The finite element method divides the computational domain into finite elements by the basic principle of variational and the method of weighted margin (Wang et al., 2021). Select the basis function for each unit, replace the solution of each unit with the linear combination of the basis function. The solution of all the basis function can replace the solution of the whole solution region. As the calculation accuracy becomes higher and higher, the solution will become closer and closer to the real solution. Therefore, for the finite element analysis of human cornea, the accuracy of describing the geometric shape and constitutive relationship of corneal tissue is crucial to the accuracy of the research results.

The finite element technique has greatly promoted the research of cornea-related diseases. Many scholars have proposed that finite element models can accurately predict biomechanical behavior, and it have been proven to have good predictability. Wang et al. (2016) combined FEA and magnetic resonance imaging to estimate the strain on the optic nerve head during horizontal eye movement. Liu et al. (2015) used FEA to study the mechanism of lens capsule rupture. Wu et al. (2021) studied the corneal reshaping mechanism of corneal molding lenses using a numerical model. Bao et al. (2018) analyzed the effects of LASIK on corneal biomechanics using FEA. FEA has been used extensively to study the biomechanical properties of the cornea and related diseases. Generally, the finite element model of the cornea is mainly composed of geometric model and constitutive model. This article summarizes the current research status of the finite element model for the human cornea. The geometric and constitutive model of the human cornea are introduced in Section 2 and Section 3, respectively. Finally, the prospects and outlooks of human cornea finite element model are presented and discussed. The purpose of this article is to provide references and ideas for research on finite element models of the human cornea and provide a framework for future research.

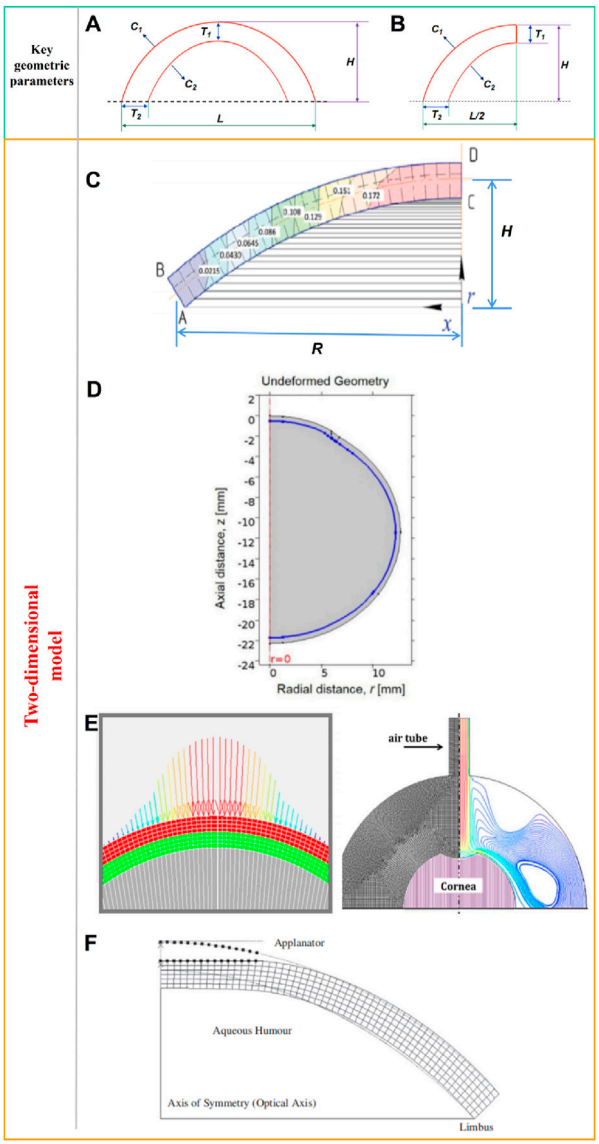

FIGURE 2
(A) Ideal two-dimensional axisymmetric geometric model and key geometric parameters, **(B)** Half of a two-dimensional axisymmetric geometric model, **(C)** two-dimensional corneal model, **(D)** two-dimensional axisymmetric whole-eye geometry model, **(E)** two-dimensional axisymmetric model with limbus, **(F)** two-dimensional axisymmetric model (Spevak and Babailov, 2020; Nguyen et al., 2019; Kling et al., 2014; Kwon et al., 2008).

2 Corneal geometry model

The sense organ of the visual perception system is called the eye, which is composed of the eyeball and the accessory organ of the eye. The eyeball is nearly spherical in shape and is used to receive light stimulation. The accessory organ of the eye is to protect the eyeball from damage. The eyeball structure is the main part of the optometer (Bekerman et al., 2014; Hong et al., 2023). The normal eyeball has a anteroposity-posterior diameter of about 22.0 mm–24.0 mm, a horizontal diameter of about 23.0 mm, a volume of about 6.5 mL, and a weight of about 7.0 g. The walls and contents of the eyeball together make up the eyeball. The role of the ocular wall is to maintain the shape of the eyeball, including the retina, cornea, choroid, sclera, ciliary body and so on (Alcântara et al., 2023). The transparent cornea and sclera form the outer wall of the eyeball. The contents of the eyeball consist of aqueous humor, vitreous body and lens, which are the pathways for light to enter the eye (Zelentsova et al., 2020; Hammer et al., 2024; Toffoletto et al., 2020). These structures together with the cornea constitute the refractive system of the eyeball. When the external light is focused at the center of the retina after the dioptric system, it is called orthotropia. Nearsightedness and farsightedness are due to the focus of the light to the front and back of the retina respectively. When the light focuses on multiple focal points of different planes on the retina, it is called astigmatism (Holladay et al., 2022). Aqueous humor metabolizes waste in the ocular tissues, maintains intraocular pressure and provides nutrients. If the return of aqueous humor is abnormal, it may cause increased intraocular pressure, which is clinically called glaucoma. The intraocular pressure of normal people ranges from 10 mmHg to 21 mmHg (1 mmHg = 0.133 kPa). 98% of vitreous body is water, which mainly plays a role in metabolizing products secreted by tissues and alleviating the influence of vibration on surrounding

tissues. The lens is elastic and transparent, equivalent to a convex lens of 19 D (Da Silva and Lira, 2022). The ciliary muscle regulates the lens so that objects can be clearly imaged in the retina. With the age, the elasticity of the lens, and the adjustment ability of the ciliary muscle gradually weaken, resulting in presbyopia. Cataracts are formed when the lens is damaged and cloudy. There are many contents of the eyeball and its functions are complex, and any abnormality in any part may affect vision and even affect the function of other systems in the body (Stepp and Menko, 2021; Buffault et al., 2020; Sun et al., 2020).

As the outer barrier protects the eyes, the cornea is required to withstand intraocular pressure and the fluid motion from eye movement. The cornea is the first interface that light encounters as it enters the eye, and is transparent with a circular shape (Meek and Knupp, 2015). The center 1/3 of the anterior surface of the cornea is known as the optical zone and has a shape similar to that of a spherical surface (Gardner, 2015). The horizontal and vertical diameter of the human cornea is about 11.00 mm–12.00 mm, and the radius of curvature of the anterior and posterior surfaces is about 7.8 mm and 6.8 mm, respectively (Meek and Knupp, 2015; Gardner, 2015). The width of the human cornea is approximately 1.5 mm–2.0 mm at its edge. Researchers often use the mean value of corneal geometric data to build an ideal corneal model. However, the cornea contributes roughly 70% of the total refractive power of the eye (Meek and Knupp, 2015). Even very small changes in the corneal curvature and thickness can have a significant impact on its refractive power. Therefore, there will be differences between the ideal geometric model and the patient-specific in the simulation and calculation results. In this section, the ideal geometric model and the patient-specific geometric model are summarized. The layered geometric models of the cornea are also reviewed.

2.1 Ideal geometric model

2.1.1 Two-dimensional model

The cornea can be regarded as hemispherical or semi-ellipsoid shape. Many researchers have built models based on the mean curvature and thickness of the cornea to simplify the calculation. As shown in Figure 2A, some key geometric parameters for the cornea model including the corneal center thickness T_1, the corneal margin thickness T_2, the anterior radius of curvature C_1, the posterior radius of curvature C_2, the corneal height H, and the corneal diameter L. Due to the axisymmetric shape of the ideal model, many researchers choose half of the model for calculation to reduce the operation cost, as shown in Figure 2B. There are many ways to obtain these key parameters of cornea model (T_1, T_2, C_1, C_2, H, and L). Experimental measurements, nondestructive detection techniques, and literature reported are effective ways to obtain these key parameters. Each of these methods has its advantages and disadvantages. For experimental measurements, due to the advanced detection technology was not developed in the past, researchers often could only obtain geometric data of the human cornea by measuring the cornea *in vitro*. Many corneas are harvested from cadaver corneas or surgical scraps. Corneal data measured by *in vitro* experiments have some shortcomings. First, a large number of corneal cells die after a short period of time (Wilson, 2020; Méthot et al., 2020; Ruan et al., 2021). The time from corneal acquisition to laboratory measurement often causes corneal cell death and even dramatic changes in corneal geometry. Secondly, corneal transport often needs to be preserved in solution, which will also cause distortion of the true shape of the cornea. Moreover, the number of human corneas available is extremely small, resulting in the scarcity of valid experimental data for reference. Therefore, there are many defects in the method of obtaining the geometric data of human cornea from *in vitro* corneal experiment, and the data accuracy maybe not very accurate. Although *in vitro* measurements of corneal data have a variety of shortcomings. Cornea acquisition is not easy, *in vitro* acquisition data is also an important reference for our research. Hjortdal et al. (Hjortdal and Peter, 1995) studied human eyes taken from *postmortem* bodies. Time of death was less than 96 h. The eyeballs were frozen and stored at −25°C. The central corneal thickness was measured by an optical thickness gauge. The slit light illumines the center of the cornea at an angle of 38.5°, while the viewing angle between the camera and the central surface of the cornea is 0°. The central corneal thickness was 569 μm. A corneal contour image in a meridian was obtained by a computer prism device, and 3 points on the cornea were selected to estimate the central curvature radius of the cornea. Repeated measurements were made and the average corneal curvature was estimated to be 7,998 μm. These *in vitro* measurements are close to those obtained by nondestructive testing. The values of L and H were not measured in this study. For nondestructive detection techniques, at present, the commonly used detection devices are X-ray computed tomography (CT), Magnetic Resonance Imaging (MRI), Corneal visualization Scheimpflug technology (Corvis ST), and three-dimensional anterior segment analyzer (Pentacam and Orbscan II) (Withers et al., 2021; Zwanenburg et al., 2021; Weiskopf et al., 2021; Salouti et al., 2020; Jo et al., 2023; Askarian et al., 2022). CT now enables high-precision three-dimensional inspections of the internal structure. The principle of CT is to reconstruct the image through the X-ray 3D scanning data. Especially for complex objects such as eyeballs, CT technology has a unique advantage, its measurement accuracy and repeatability are high. Similar to CT technology, MRI technology has higher detection accuracy. But MRI technology has the advantage of sparing the body from X-rays. The corneal visualization Scheimpflug technology (Corvis ST) is a common detection device used in the clinic. The detection principle of Corvis ST is to apply a pulse air stream to the cornea *in vivo*. The detection system uses a high-speed imager to dynamically record the deformation and shape reduction of the cornea under the action of the air stream in real time. The system can also measure central corneal thickness (CCT), biomechanical corrected intraocular pressure (IOP), pulse air pressure, corneal vertex displacement change with time, rebound rate, corneal deformation amplitude, first and second flattening time, corneal arc length change crest distance, first and second flattening length, corneal curvature change and other data. Corvis ST plays an important role in the diagnosis of glaucoma, keratoconus and preoperative screening of refractive surgery, and is currently a highly respected biomechanical detection device. Pentacam and Orbscan II are the common three dimensional corneal anterior segment analyzers. Pentacam instrument has high accuracy and repeatability, wide measurement coverage, comprehensive description of corneal morphological characteristics, high

resolution, fast detection process and no damage, and is more sensitive to the diagnosis of eye disease than Orbscan II, which is currently the most commonly used and effective detection instrument for the diagnosis of eye diseaes. The principle is to obtain the image of the front segment through the full Angle rotation Scheimpflug optical principle. The analyzer uses the blue aurora diode to complete the 180° rotation scan within 2 s. Each shooting generates a picture composed of 500 height data, which can automatically generate three-dimensional color stereoscopic images with strong and intuitive image visibility. The system comes with two cameras that can automatically track and correct eye movements, measure the surface shape data, curvature data, thickness, anterior chamber, lens and other anterior segment parameters of the cornea. For the literature, the data in the literature are often obtained through the previous experimental data, empirical data or the average result of some data. These data are often subject to large discrepancies and errors. In conclusion, it is more accurate and easy to obtain these key parameters of cornea model (T_1, T_2, C_1, C_2, H) by means of nondestructive testing techniques. Among them, Corvis ST and Pentacam have unique advantages in the ease of inspection operation, inspection cost, and detection accuracy. Therefore, Corvis ST and Pentacam are also the most popular detection methods in human cornea research at present.

Spevak and Babailov (2020) established a two-dimensional corneal model as shown in Figure 2C, and analyzed the stress-strain state of the cornea. Spevak and Babailov (2020) made 4 simplifications that reduced the dimension of the problem and reduced the amount of finite element calculation. The first one is that the shape is axisymmetric, without eccentricity; The second is that the cornea is simplified to single layer; The third is the cornea material is elastic and isotropic; The last is the model is under isothermal conditions. According to the data reported in the literature, the shape of the model is set to an ideal curve. The geometric parameters were set as the average values reported in the literature. The curvature of the anterior and posterior surfaces is consistent. Corneal thickness was set at 520 μm; the corneal deflection along the symmetry axis (H) was set at 2.5 cm; and the radius along center line (R) was set at 5 cm. Nguyen et al. (2019) established a two-dimensional axisymmetric whole-eye geometry model to simulate the Corvis ST detection process through COMSOL. The geometric data of the model are derived from literature reports. The whole golbe diameter was 24 mm. The axisymmetric geometry of eye include cornea, sclera, and vitreous. The model surrounded by the air region. Central corneal thickness was set to 500 μm, anterior radius of curvature and posterior radius of curvature to 8.00 mm and 6.8 mm, respectively. Corneal diameter was 11 mm, as shown in Figure 2D. For sclera area, the thickness at equator was 400 μm; the thickness at posterior pole was 1,000 μm; the radious of curvature was 12 mm.These parameter values all from revelant literature. Kling et al. (2014) established a two-dimensional axisymmetric model to simulate the effect of air column on corneal deformation, as shown in Figure 2E. The corneal curvature and CCT were form the Scheimpflug cross-sectional images. The central thickness of the cornea was 558 μm, the anterior and posterior surface curvature radii were 8.03 mm and 6.86 mm, respectively, and the corneal diameter was 10 mm. The model also takes into account the sclera and limbus. The scleral diameter was 19.5 mm. Kwon et al. (2008) established a simplified two-dimensional axisymmetric finite element model of the human eye, as shown in Figure 2F. The Figure 2F shows the initial state of the cornea and the shape of the cornea after applanated. A series of Goldmann applanation tonometer simulations were performed on the model to investigate the effects of corneal geometry and material properties on IOP readings. The geometry of the anterior and posterior surfaces of the cornea in the model is represented by the following Formula 1:

$$r^2 + (1 + Q)z^2 - 2zR = 0 \quad (1)$$

where the origin is on the (anterior or posterior) surface of the cornea at the optical axis, the z-axis points inwards along the optical axis, and r is the radial distance from the optical axis. Q is an asphericity parameter and R is the radius of curvature at the apex. These geometry data from literature. The central thickness of the cornea was 550 μm. The R and Q of the anterior surface are 7.77 mm and −0.18, respectively. The R and Q of the posterior surface are 6.40 mm and −0.60, respectively. Here we summarize some values of T_1, T_2, C_1, C_2, H, and L reported in the literature as shown in Table 1. For a fixed value of corneal curvature, only one of the L and H values is needed to determine the two dimensional shape. Therefore, the L is not indicated in Fernandez et al. (2004), and the H is not indicated in Larry et al. (2007), Kling et al. (2014), and Nguyen et al. (2019).

These models have in common that they are two-dimensional symmetric models, and all require the value of C, T, H and L for modeling. The advantage of two-dimensional symmetric model is that it reduces the computational cost to a large extent. First of all, compared with the three-dimensional symmetric model, the number of finite element elements of the two-dimensional symmetric model is significantly reduced, which greatly saves the calculation cost. Secondly, due to the symmetry of the model, the physical response of the cornea is symmetrical when it is stressed or deformed. It is often possible to select half of the computational model to analyze the results.

The accuracy of the calculation is determined by the complexity of the geometric model of cornea. However, there are limbus and other tissues around the cornea, and the biomechanical response of the cornea will be affected by the tissues around the cornea when the cornea is stressed. Both Figures 2D,E took into account the cornea limbus, and the calculation results of the model were more accurate than those of Figure 2C. The disavantage of the two-dimensional symmetric models are not negligible either. When the analysis objective is only to observe the changes of corneal cross-section or corneal contour, it is acceptable to simplify the model using two-dimensional structure. When it is necessary to analyze the stress-strain distribution on the surface or inside of the cornea, the two-dimensional model is not sufficient. For example, when simulating corneal trauma or surgery, the stress state and deformation of the cornea at different locations vary greatly. At this case, the two-dimensional model can not meet the research needs. What's more, the race, the age, the corneal refractive status, and the other multiple factors can lead to the difference of corneal geometric parameters in different people. The average value of the key parameters will cause the error of the model and the error of the calculation result. In addition, the cornea is not completely symmetrical shape, so it is not

TABLE 1 Corneal geometric parameters in the two-dimensional model.

Parameters	Ref.
$C_1 = C_2 = 7.56$ mm, $T_1 = 0.52$ mm, $T_2 = 0.67$ mm, $H = 2.5$ mm	Fernandez et al. (2004)
$T_1 = T_2 = 0.52$ mm, $L = 10$ mm, $H = 2.5$ mm	Spevak and Babailov (2020)
$C_1 = 7.77$ mm, $C_2 = 6.40$ mm, $T_1 = T_2 = 0.55$ mm, L and H are from geometry equation	Kwon et al. (2008)
$C_1 = C_2 = 7.80$ mm, $T_1 = 0.61$ mm, $T_2 = 0.812$ mm, $L = 12.36$ mm	Larry et al. (2007)
$C_1 = 8.03$ mm, $C_2 = 6.86$ mm, $T_1 = T_2 = 0.56$ mm, $L = 10$ mm	Kling et al. (2014)
$C_1 = 8.0$ mm, $C_2 = 6.80$ mm, $T_1 = T_2 = 0.50$ mm, $L = 11$ mm	Nguyen et al. (2019)
$C_1 = 7.96$ mm, $C_2 = 6.20$ mm, $T_1 = 0.549$ mm, $T_2 = 0.75$ mm, $L = 11.76$ mm, $H = 2.4$ mm	Huang et al. (2020)
$C_1 = C_2 = 7.97$ mm, $L = 11.49$ mm, $H = 2.5$ mm, T_1 and T_2 are based on patient thickness	Meng et al. (2020)

very reasonable to idealize the cornea as a symmetrical structure and only calculate half of the model.

2.1.2 Three-dimensional model

For some cases where the surface stress distribution or displacement distribution of the cornea is analyzed, the two-dimensional model cannot meet the requirements. The three-dimensional corneal model can observe the changes of the cornea in the three-dimensional space. Pandolfi and Manganiello (2006) regarded the cornea as a long ellipsoid (Figure 3A), used the ellipsoid to approximate the surface of the myopic cornea and astigmatic cornea in cylindrical coordinate system. The equation of ellipsoid is given by Formula 2.

$$(1-e^2)z^2 + x^2 + y^2 = R^2, e = \sqrt{1-\frac{R^2}{R_Z^2}} \quad (2)$$

Where e is eccentricity, R is the maximum radius in the x and y directions, R_z is the maximum radius in the z direction. The outer in plane diameter of the cornea is 11.46 mm. The maximum elevation at the apex is 2.4 mm. The shell thickness is about 0.53 mm at the center and 0.62 mm at the limbus. The ellipsoid eccentricity e is 0.60 for the internal surface and 0.43 for the external surface. The maximum external and internal curvatures are 7.8 and 6.8 mm, respectively. The slope of the cross section at the limbus is 48°. The model are shown in Figure 3B. Meng et al. (2020) selected 34 myopia patients (total 67 eyes) who underwent LASIK in Shanxi Eye Hospital (China), including 15 males (30 eyes) and 19 females (37 eyes). All patients underwent Corvis ST examination before and after surgery. Biomechanical parameters such as CCT and IOP were obtained before and after surgery. The three-dimensional corneal models of 67 patients before and after surgery were established. The changes of corneal collagen stiffness before and after surgery were analyzed. All preoperative and postoperative corneal models were treated as spherical structures, and unified anterior surface curvature radius R, height H and transverse diameter L were used. As shown in Figure 3C, R was 7.9 mm, H was 2.5 mm, and L was 11.5 mm. These values come from data reported by Pandolfi and Holzapfel (2008). The preoperative corneal model used uniform thickness, that is, the thickness of the cornea was the same at different locations. The corresponding preoperative model was established according to the preoperative CCT value of each patient. The difference between preoperative corneal CCT value and postoperative corneal CCT value is considered as the quantity of surgical cutting. According to the quantity of surgical cutting, the cutting was carried out within the 3.5 mm radius of the apex center of the preoperative model to obtain the postoperative model. Figure 3C also shows a schematic of the post-operative quarter corneal model. The difference in the corneal models of these 67 cases was only reflected in the difference in central corneal thickness, and other geometric parameters were not considered in model. For the more complex keratoconus, some researchers have analyzed the biomechanical properties of keratoconus by idealized models. Gefen et al. (2009) established an idealized keratoconus with one and two thinning regions respectively, and analyzed and predicted the changes of refractive and surface stress in keratoconus under different intraocular pressure. The geometric data is derived from published experimental data. Geometric data of key positions were selected for modeling. The maximum and thinnest thickness of the cornea with one thinning region model was set at 0.6 mm and 0.2 mm, respectively, as shown in Figure 3D. The maximum and minimum thicknesses for two thinning regions model are set to 0.5 mm and 0.35 mm, respectively, as shown in Figure 3E.

2.2 Patient-specific model

The geometry of the cornea varies from person to person. For a certain cornea, the curvature and thickness of each position on the front and back surfaces of the cornea are also different. The difference in surface curvature and thickness between the front and back will directly lead to the difference in the stress state of the cornea at each position. Therefore, surface curvature and thickness are most obviously different parameters for building patient-specific models.

2.2.1 Two-dimensional model

The models of normal, myopic or keratoconus cornea based on the anatomical data have a certain gap with the actual corneal morphology. They cannot accurately restore the irregular surface

10.3389/fbioe.2024.1455027

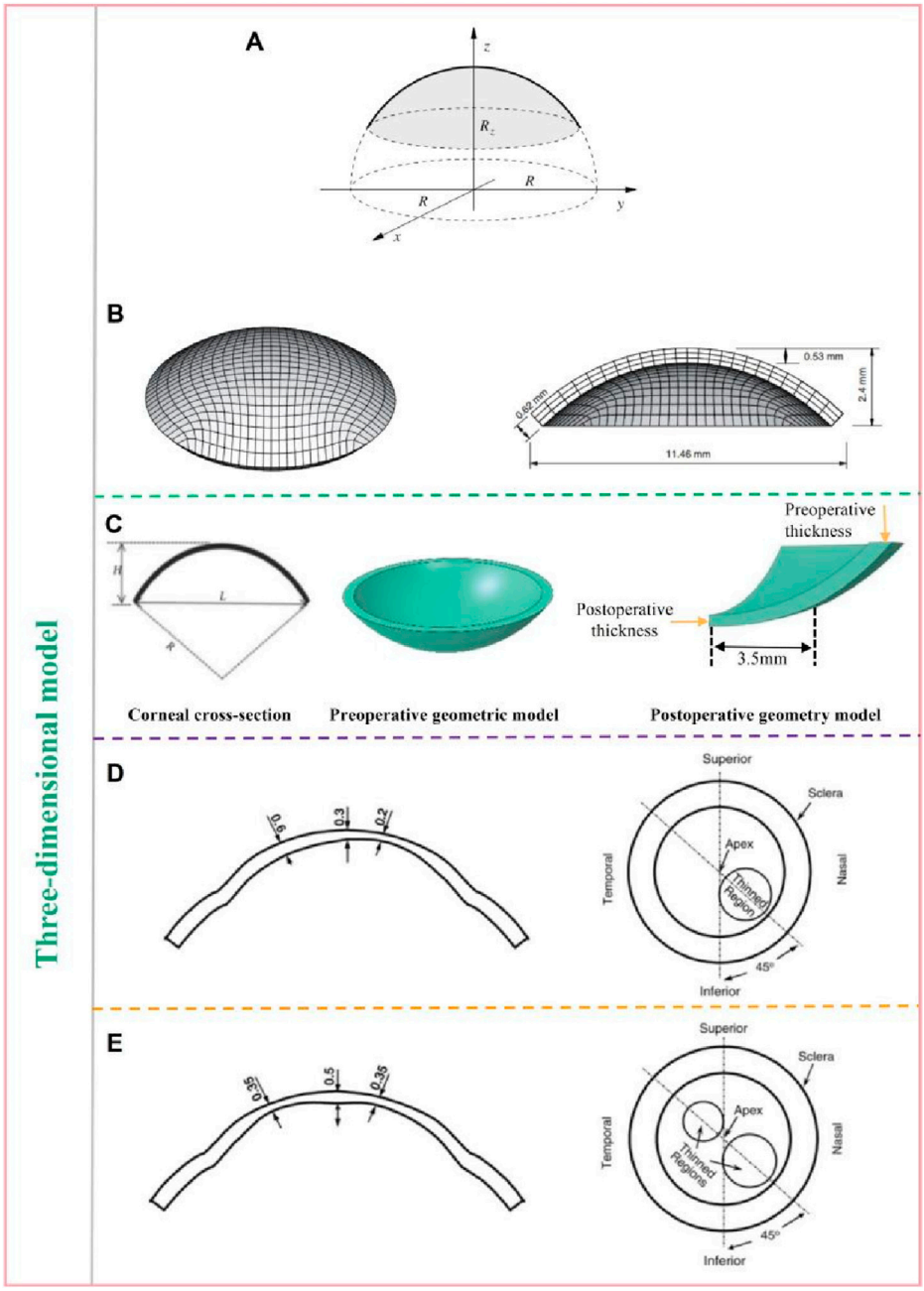

FIGURE 3
Ideal geometric model: three-dimensional model (Meng et al., 2020; Pandolfi and Manganiello, 2006; Gefen et al., 2009). **(A)** the diagram of ellipsoid. **(B)** the model of cornea and the peripheral region. **(C)** the preoperative and preoperativecorneal model. **(D)** the keratoconus model with one thinning region. **(E)** the keratoconus model with two thinning region.

and curvature of the cornea, nor can they accurately predict the changes in the cornea after force. Jannesari et al. (2018) obtained the structure of the cornea without deformation from the images captured by Corvis ST. Using image processing technology, the coordinates of 576 points on the front surface and 576 points on the back surface of the cornea were obtained, and the two-dimensional geometric model of the patient was obtained by interconnecting splines, as shown in Figure 4A. Similarly, Lago et al. (Lago et al., 2015a) used images captured by Corvis ST to build a 2-dimensional corneal model, as shown in Figure 4B. Modeling and simulation were carried out on the images of 12 patients. The corneal thickness distribution in these models ranged from 499 μm to 613 μm, and the intraocular pressure ranged from 8 mmHg to 14.5 mmHg. The deformation of the human cornea during non-contact pressure measurement was simulated, and the properties of corneal materials were calculated by inverse finite element method and genetic algorithm respectively. Stark et al. (Stark et al., 2021) established a two-dimensional model including cornea, sclera, choroid, iris and other tissues, as shown in Figure 4C. The size of the eye was 24.79 mm along anterior-posterior

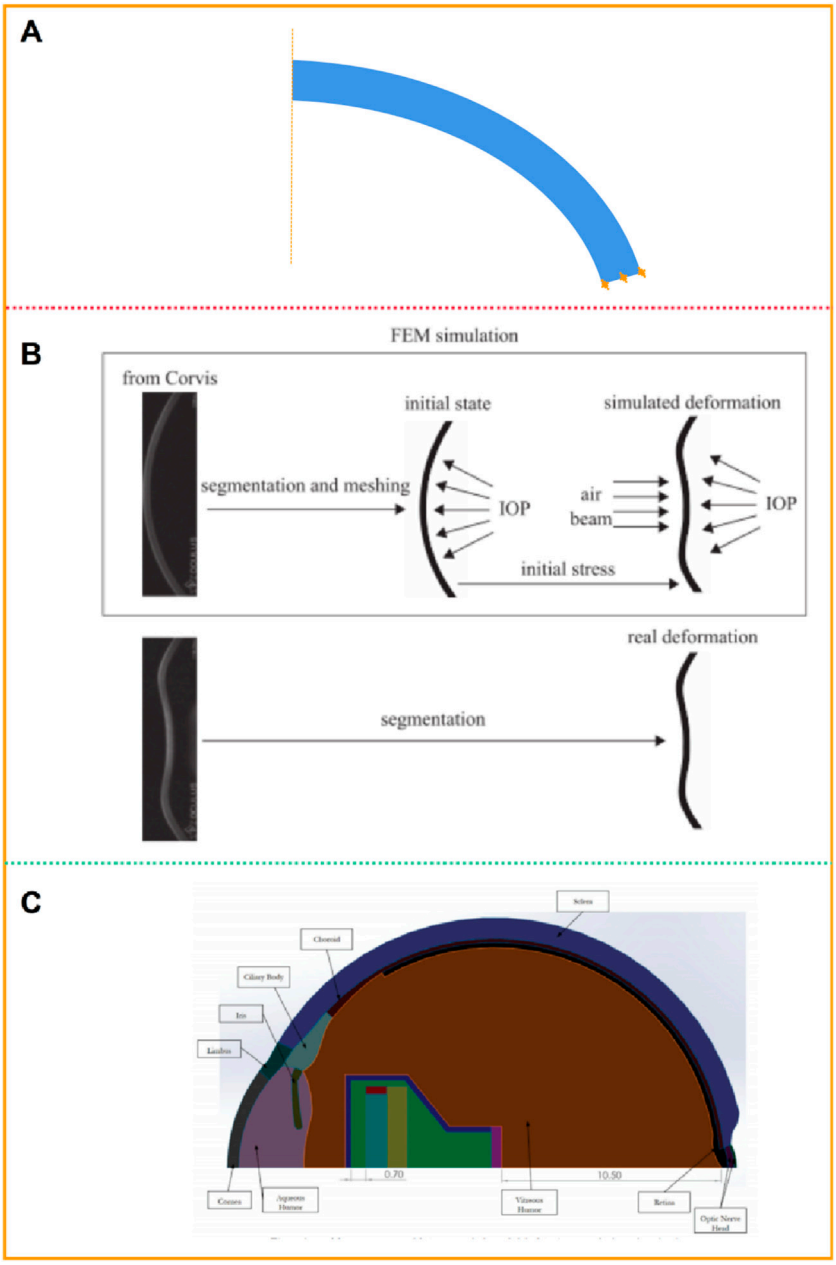

FIGURE 4
Patient-specific geometric model: two-dimensional model (Jannesari et al., 2018; Lago et al., 2015a; Stark et al., 2021). **(A, B)** two-dimensional geometric model. **(C)** two-dimensional model including cornea, sclera, and other tissues.

direction and 24 mm in transverse and vertical directions. The anterior and posterior corneal radius of curvature are 7.76 mm and 6.52 mm, respectively. The central corneal thickness is 0.55 mm. The anterior chamber depth is 3.06 mm. The vitreous chamber depth is 16.6 mm. The lens diameter is about 9.03 mm. The limbal anterior and central thickness are 0.704 mm and 0.767 mm, respectively. The limbal posterior and scleral equatorial thickness are 0.728 mm and 0.556 mm, respectively. The posterior pole thickness is 0.834 mm. Data from the U.S Army and its in-house laboratory simulated the analysis of ocular deformation of the cornea under the action of the intraocular projector.

2.2.2 Three-dimensional model

In order to describe corneal morphology more accurately, many researchers have tried to establish corneal models with the help of detection instruments to study corneal biomechanical properties more accurately. Among them, OCT, CT, MRI, Pentacam and various types of corneal topography instruments are widely used. The basic principles of these instruments are similar, and all of them can accurately describe the morphological characteristics of the cornea and restore the surface morphology of the cornea. Karimi et al. (2018) collected patients' eye data through CT and MRI, and established eye models including cornea, sclera, optic nerve, extraocular muscle and other tissues (Figure 5A). Wang et al.

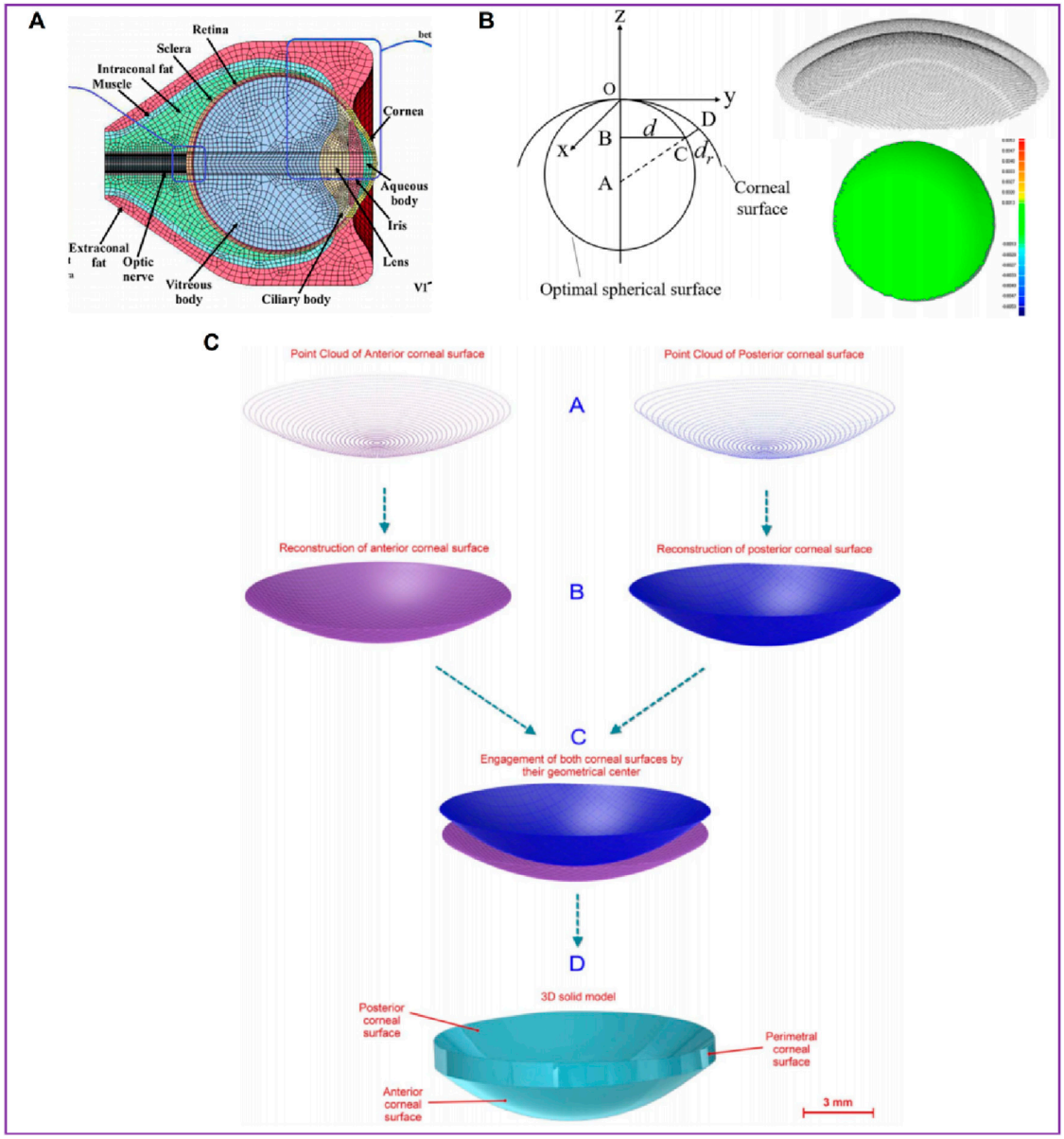

FIGURE 5
Patient-specific geometric model: three-dimensional model (Wang et al., 2022; Karimi et al., 2018; Cavas et al., 2014). **(A)** the cornea data from CT and MRI. **(B)** the cornea data from Pentacam. **(C)** the cornea data from Sirius corneal topographer.

(2022) collected the radial distance between each point on the corneal surface and the optimal spherical surface within the range of 8 mm × 8 mm, the corresponding thickness value of each point on the front surface of the cornea, and the optimal spherical radius value by Pentacam topographic instrument. A three-dimensional space rectangular coordinate system was established, the coordinate values of all points on the cornea in the *z*-axis direction were obtained, and the coordinate point data of the front and back surface of the cornea were imported into the reverse modeling software Geomagic to form the front and back surface profile of the cornea (Figure 5B). The models after LASIK surgery and SMILE surgery were established to accurately analyze the biomechanical changes of the cornea caused by the two kinds of surgery. Roy et al. (Roy and Dupps, 2011) used a three-dimensional anterior segment analyzer combined Zernike polynomial and Gaussian polynomial to fit the geometric expression of cornea. Cavas et al. (2014) used Sirius corneal topographer to obtain point cloud fitting of the geometric shapes of the front and back surfaces of the cornea to produce corneal curves. The modeling process is shown in Figure 5C. Especially for some irregular corneas, such as keratoconus, the thickness is uneven and asymmetrical, the apex position of the cone and the steepening area are not fixed, the surface curvature changes greatly, and the geometric shape is more irregular than that of normal corneas, with great individual differences. It is very effective to obtain corneal geometry by various scanning instruments, and finite element models can be built more accurately. Lago et al. (2015b) reconstructed the patient's keratoconus model. The keratoconus images and topographical data

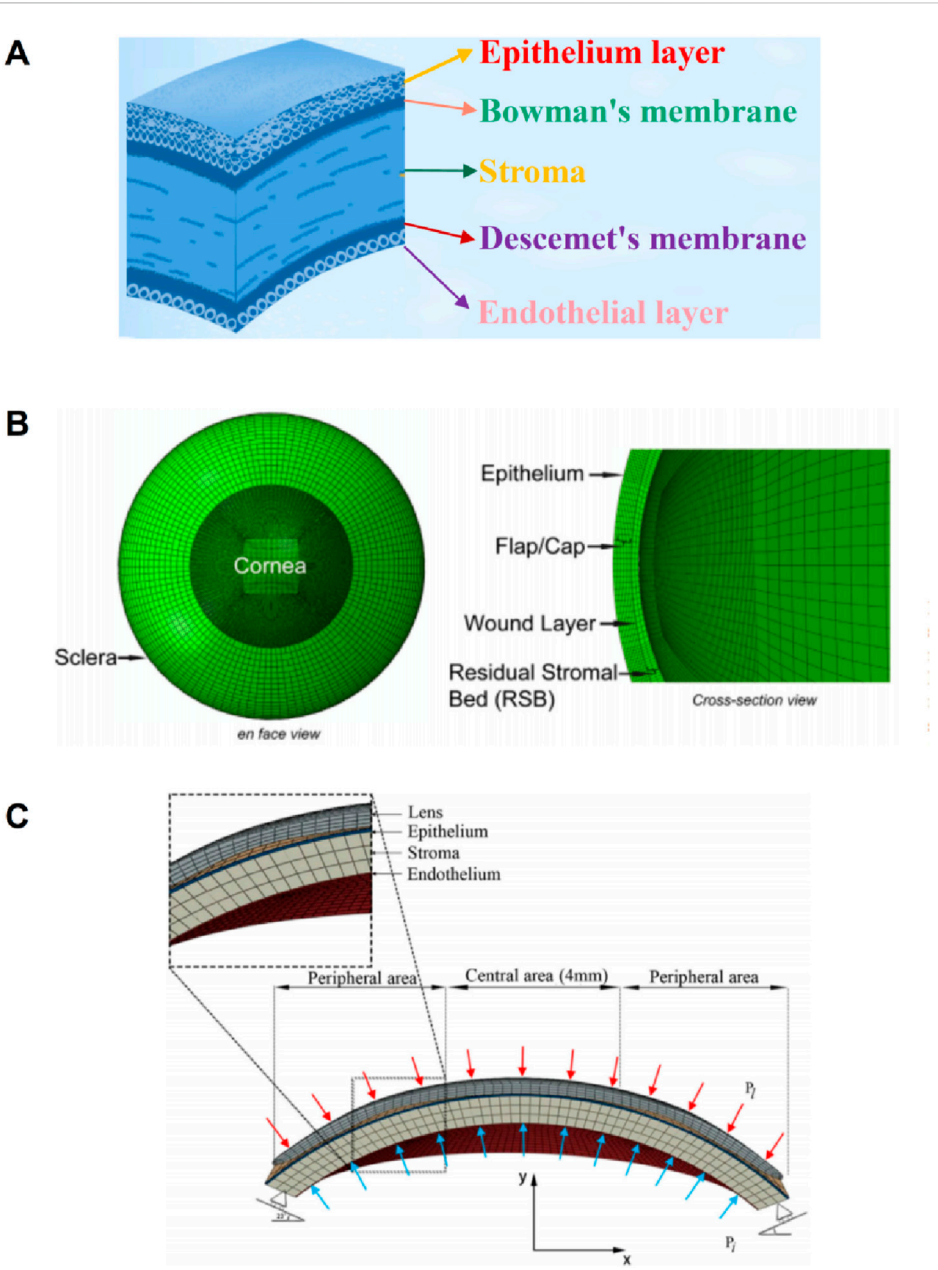

FIGURE 6
The diagram of corneal layering and layering cornea model (Wu et al., 2021; Roy and Dupps, 2011). **(A)** the schematic of corneal layering. **(B, C)** Layered corneal model.

were collected by Pentacam. The restoration of corneal curvature in keratoconus patients after corneal ring segment implantation was simulated.

2.3 Layered geometric models

The cornea's absence of blood vessels, well-organized tissue, and near-dehydrated state all contribute to the cornea's ability to repair itself and its transparency (Tuori et al., 1996). From the front to the back corneal tissue, there are five layers, namely, epithelial layer, bowman's membrane, stromal layer, descemet's membrane, and endothelial layer, as shown in Figure 6A (Parker et al., 2021). The epithelial layer consists of the cell layer and the basement membrane layer. The thickness of the epithelial layer is about 50 μm, the cell life is about 8–10 days, the cell regeneration ability is strong, and the repair after damage is faster. Limbal stem cells are found in the basal cell layer of the limbal, which plays an important role in the repair of the upper cortex. The bowman's membrane has been formed in the embryonic stage, but the boundary between it and the stromal layer is not very clear. The boundary between it and the epithelial layer is obvious, about 10 μm, and it cannot be regenerated after injury. The stromal layer is the core of cornea structure, mechanics, and optics, with a thickness ranging from 400 μm to 550 μm. It is mainly composed of extracellular matrix such as collagen fibers and inorganic salts. There are about 300 stromal layers in the center

of the human cornea and more than 500 layers in the corneal limbal. There are about 2900 endothelial cells per square millimeter in the endothelial layer, a total of more than 1 million endothelial cells, most of the cells are hexagonal, the older the number is less, because it is not mitotic, so it is not renewable. If the endothelial cells are more damaged or the number is reduced to a certain extent, it will cause corneal edema and other keratopathy. However, it is important to note that corneal delamination is technically difficult to achieve, and there is a lack of very accurate experimental data. The contact between layers is not clear, so there are few reports on corneal delamination in previous studies. For corneal refractive surgery, the surgical cutting site spans the epithelial layer, the bowman's membrane, and the stroma layer, and the properties of each layer are often regarded as the same in the finite element simulation, which will also cause some calculation errors.

Larry et al. (2007) simulated corneal oxygen and corneal oxygenation by establishing 2-dimensional axisymmetric cornea and 3D contact lens, and analyzed oxygen distribution in different places of the cornea. The epithelium thickness is 0.050 mm; the stroma thickness is 0.475 mm; the endothelium thickness is 0.005 mm; the stroma perpherial thickness is 0.677 mm. Roy and Dupps (2011) established a 3D whole eyeball model in the normal eye to simulate LASIK. Since the cutting of the cornea in the LASIK surgery reaches the stromal layer, the model considers the epithelium, epithelium, wound layer, and residual stromal bed, as shown in Figure 6B. The effect of flap thickness and residual stroma on corneal surface stress distribution was analyzed with this model. Wu et al. (2021) divided the cornea into three layers: the epithelium, stroma, and endothelium. The layer thickness of the epithelial and Bowman's membrane was presumed to be 50–57.5 μm, as was the Descemet's membrane and endothelium thickness. An orthokeratology lens was applied to the epithelial layer to study the biomechanical response of the orthokeratology lens to the cornea, as shown in Figure 6C. Li et al. (2021) established a corneal model considering 5 layer structure and analyzed the effects of deep anterior lamellar keratoplasty and penetrating keratoplasty surgery on corneal biomechanical properties. The thickness of Descemet's membrane and endothelium is 15 μm; the thickness of epithelial and Bowman's membrane is 45 μm; the stroma thickness is 500 μm.

2.4 Boundary condition

In finite element calculation, the setting of boundary conditions also has a significant influence on the calculation results. For finite element models with only corneal tissue, the fixation of the boundary is usually at the corneal edge. On the one hand, the Angle setting of the corneal edge to the horizontal direction is an influencing factor. For example, in the model shown in Figure 2C, the corneal edges are parallel to the horizontal direction. In the model shown in Figure 4A, the corneal edge is parallel to the corneal cross-section at an Angle to the horizontal plane. In Figure 6C, the corneal margin is at an acute Angle to the horizontal surface. The shape of the corneal edge and the Angle from the horizontal plane are set differently by different researchers. However, the influence of corneal edge and horizontal Angle on simulation results has been rarely evaluated. On the other hand, the way the corneal edge is fixed also affects the calculation results. At present, the methods of fixing edge are also different in the literature reports. For example, Wang et al. (2022) and Wu et al. (2021) fixed the corneal edge by limiting the degree of freedom of angle at the corneal edge. Alastrue fixed the position of the corneal edge by limiting the degree of freedom of displacement. Qin et al. (2019) set the boundary conditions to limit all the degrees of displacement and rotation of the corneal edge. In short, the corneal edge shape and boundary conditions should be determined according to the calculation method and the actual research situation. For whole-eye models or models with more tissue components (such as Figure 5A), the setting of boundary conditions is more complicated, and the boundary conditions have a greater impact on the results. At this time, the boundary fixation method should be chosen carefully.

2.5 Analysis and discussion of geometric models

Very small changes in corneal shape can cause large changes in corneal refraction or performance. In the past, due to the limited technical level, researchers had a limited cognition level of cornea shape, and often simplified the cornea into a spherical or ellipsoid shape. After the model is simplified, the geometric model can be established directly by anatomic parameters without testing instruments. On the other hand, because the simplified models are more regular, it is easier to divide the grid in the finite element software, and the calculation is easier to converge, reducing the calculation cost. Corneal morphology varies greatly from patient to patient, for example, the difference in corneal thickness in the population can reach up to 300 μm. Conclusions calculated with a simplified model cannot be applied to everyone. Therefore, the idealized model can be regarded as a semi-quantitative or qualitative model to some extent. The advent of more and more sophisticated instruments has made it easy to accurately describe the geometry of the cornea. At present, a growing trend of clinical research is precision and individuation. Accurately describing the corneal morphology of specific patients greatly improves the accuracy of corneal research and simulation prediction results. In general, the accuracy of the 3D model is higher than that of the 2D model. Patient-specific models are more accurate than idealized models. It should be pointed out that, however, not all studies require patient-specific 3D models. This needs to be determined in conjunction with the needs and objectives of the research. In addition, the edge shape of the corneal model are also important factors affecting the calculation results. In the human eye, the corneal margin is connected to the sclera. The junction is often called the limbus, which interweaves corneal and scleral components. The thickness of the limbus is greater than that of the cornea. Moreover, the size, content, and interweaving direction of collagen fibers in the sclera are different from the distribution of the cornea collagen fibers. Therefore, the biomechanical properties and structural stiffness of the sclera are different from those of the cornea, and even differ greatly. Therefore, whether the shape of corneal limbus and material properties are considered in the model will affect the accuracy of the calculation results. However, there are few reports considering limbal geometry and material properties in current simulations.

There are few reports on the layered finite element model of cornea. There are two main reasons. One is the difficulty in calibrating the geometric parameters of each layer of the cornea. The difficulty of acquiring human cornea greatly limits the calibration of corneal parameters. Human corneas are often harvested from cadavers and stored in a solution. But inevitably, the cornea in the solution will absorb the solution leading to corneal swelling and distortion of corneal geometry. The thickness of each layer of the cornea is at the micron level, and the observation through the equipment may also cause large errors. Another reason is that the properties of corneal layers and the contact relationship between layers are difficult to describe accurately. The material properties and the number of cells in each layer of the cornea are different. It is technically difficult to separate the layers of the cornea, and there are currently no very effective means to fully peel the layers and to accurately determine the mechanical properties of the layers. Therefore, when the layered model is established, the material properties of each layer are set without an accurate basis. Theoretically, the contact relationship between the 5 layers is not the same. Whether there is a slip or friction relationship between the 5 layers remains to be studied. In brief, more accurate corneal stratification data needs further experiments and studies.

In finite element calculation, the geometry needs to be discrete into small elements. Usually, element is just an approximate representation of the actual structure geometry. Element type, shape and total number all affect the simulation results. In general, the more quantity of element, the more accurate the simulation results will be. But the problem is that the cost of computing increases. Therefore, it is necessary to analyze the convergence of the number of element in order to obtain more accurate results at the lowest computational cost. For the interest areas, the element should be partially encrypted for more accurate results. When meshing, hexahedral elements tend to give the best results at the lowest cost. In the field of computational mechanics, there is a lot of discussion and research on meshing. Hexahedral elements have a high degree of reliability and accuracy in the simulation of many incompressible biological materials (Karimi et al., 2021). In medical applications, Ramos and Simões (2006) reported that hexahedral mesh is more stable than tetrahedral mesh in femur model, and the result is less affected by mesh refinement. In the simulation of cardiac biomechanics, Oliveira and Sundnes (Lino De Oliveira and Sundnes, 2016) show that the secondary hexahedron is slightly superior to the secondary tetrahedron in mechanics. Benzley et al. (1995) reported that the computational stability and accuracy of linear hexahedral mesh are better than that of linear tetrahedral mesh. In the nonlinear elastic-plastic analysis experiment, the linear hexahedral mesh is slightly better than the quadratic tetrahedral mesh. Biswas and Strawn (1998) showed that for the same number of edges, a hexahedral mesh will produce a more accurate solution than a tetrahedral mesh. However, the most of patient-specific corneal and keratoconus shape is often irregular. It is difficult to fully divide into hexahedral element. It is also necessary to divide into tetrahedral element or wedge element. In some calculations these two elements are prone to "hourglassing phenomenon." Therefore, these two types of elements should be used with caution and validity verification. In addition to the method of automatically generating mesh in finite element software, the hypermesh software is also an effective means of mesh division and processing. In some irregular models, hypermesh can effectively handle irregular regions and partition hexahedral meshes (Wang et al., 2017).

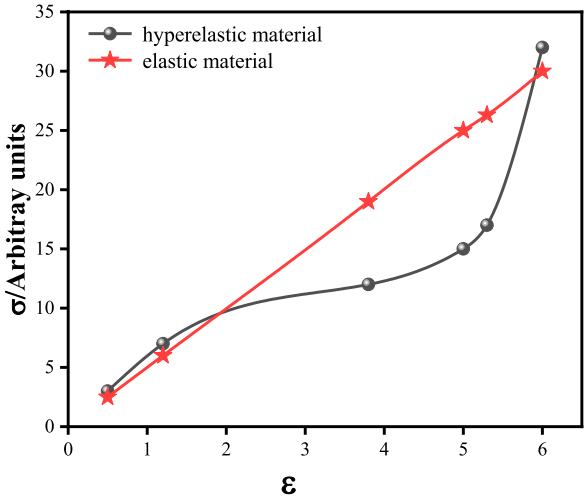

FIGURE 7
The stress-strain relationship diagram of hyperelastic and linear elastic materials.

3 Corneal constitutive model

Fung (Fung, 1972) first pointed out that most biological soft tissues are viscoelastic materials, and so is corneal tissue. Corneal mechanical properties are more complex. The cornea contains both solid and liquid components. It is an anisotropic, viscoelastic, and incompressible material. Viscoelastic materials have both elastic and viscous deformation properties under the external forces (Williams, 1964; Sladek et al., 2022). The mechanical properties of viscoelastic materials are related to time, strain rate and other factors. The stress-strain relationship of corneal materials does not satisfy the linear elastic constitutive relationship. The elastic modulus of corneal materials is significantly different in the direction of longitude and latitude. In the finite element calculation, there are four common types of the corneal constitutive relations: linear elastic relation, exponential function relation, hyperelastic relation, and viscoelastic relation.

3.1 Linear elastic constitutive model

The stress-strain relationship of the cornea is not linear. The observation of cornea *in vitro* showed that corneal fiber bundles had obvious directions. In the central cornea, the distribution of corneal collagen fibrolamella was generally cross-arranged. In the corneosclera margin, the distribution of collagen fibrolamella was circumferential. This distribution direction results in anisotropic mechanical properties of the cornea. Due to the difference in experimental conditions, experimental methods and materials, the measurement results of human corneal elastic modulus are

TABLE 2 Elastic modulus and Poisson ratio parameters.

Elastic modulus	Poisson ratio	Ref.
0.363 MPa	0.49	Cavas et al. (2014)
14.3 MPa	0.45	Spevak and Babailov (2020)
1.5 MPa	0.49	Nguyen et al. (2019)
0.16–0.8 MPa	0.49	Fung (1972)
0.14–0.30 MPa	0.49	Qin et al. (2019)
0.40 MPa	0.42	Ramasubramanian et al. (2022)
20.33 MPa	0.49	Baek and Park (2019)
0.20 MPa	0.43	Bharathi et al. (2022)
0.05–19 MPa	0.49	Rossi et al. (2011)

wide. In order to simplify the calculation, many researchers treat the cornea as a linear elastic and isotropic material. The properties of corneal linear elastic materials can be determined by stretching experiments, and there are few undetermined parameters in the simulation. The only undetermined parameters are elastic modulus and Poisson's ratio. Therefore, linear elastic properties are the most widely used in corneal simulation. The stress-strain relationship of linearly elastic materials is linear, as shown in Figure 7. The curve in Figure 7 is drawn from random data, not from some experiment or literature report. In this figure, the ordinate is stress in any unit, and the abscissa is strain. The red line describes the stress and strain relationship of the linearly elastic material, which is linear. The black lines describe the stress-strain relationship of the hyperelastic material, which is non-linear. Nguyen et al. (2019) simulated Corvis ST detection process by setting the cornea as linear elastic material. Bao et al. (2018) established a linear elastic three-dimensional corneal model, and simulated LASIK surgery to study the relationship between postoperative corneal eminence and various parameters. The cornea is regarded as a linear elastic material, which is easy to test in experiment and calculate in simulation. We summarized the values of elastic modulus reported in some literatures, as shown in Table 2. As can be seen from the table, the value of human eye elastic modulus reported in literature ranges from 0.05 MPa to 20.33 MPa. The values of corneal elastic modulus measured by different experimental methods are very different, and the range distribution of elastic modulus is relatively discrete. When different reference modulus values are set in finite element calculation, there will be large errors. Secondly, for the linear elastic model, the relationship between stress and strain changes linearly. The deformation and mechanical response of cornea are not linear. Especially when analyzing the surface or internal stress distribution of the cornea, the error caused by the linear elastic model may be more obvious.

3.2 Exponential function constitutive model

In order to avoid the error caused by linear elastic model describing corneal constitutive relation, the authors adopted the constitutive relation of exponential function to describe the nonlinear stress-strain relation of cornea. The function expression is shown in Formula 3:

TABLE 3 Exponential function parameters.

α	β	Ref.
0.2 kPa	62	Asejczyk-Widlicka and Srodka (2020)
1.75 kPa	48.3	Fernandez et al. (2004) Xie et al. (2008)

$$\sigma = \alpha\left(e^{\beta\varepsilon} - 1\right) \tag{3}$$

Where, α and β are material constants, σ and ε are stress and strain, respectively. The values of α and β in literature reports are shown in Table 3. For Poisson's ratio, the cornea is generally considered to be almost incompressible row material. Therefore, 0.49 is set in both online elastic and exponential functions. But the flaws of the exponential model are also obvious. When the strain is small, the stress change is moderate. When the strain is a little greater, the stress will rise sharply. As reported by Asejczyk-Widlicka and Srodka (2020), when the stress variable is greater than 0.05, the stress value will increase sharply.

3.3 Hyperelastic constitutive model

The stress-strain relationship of hyperelastic materials has several characteristics: hysteresis, stress relaxation, creep, Mullins effect or Pyane effect. The linear elastic constitutive method of human corneal material is not accurate enough to describe corneal hyperelastic properties. Fang et al. (2020a) established a post-LASIK corneal model containing a flap using a hyperelastic constitution. The biomechanical changes induced by the flap were evaluated and the displacement, stress and strain of the corneal surface were analyzed. Zhou et al. (2017) established a finite element model of the eyeball. The cornea and sclera were described by a self-defined nonlinear, incompressible, and anisotropic hyperelastic constitutive equation, and the particle swarm optimization algorithm was used to invert the constitutive parameters of the corneal material. Simonini et al. (2016) established a corneal model of patients after PRK, regarded cornea as anisotropic hyperelastic material. The influence of corneal cutting on corneal stress distribution and intraocular pressure fluctuation on refraction were analyzed. Fang Lihua et al. (2020) regarded cornea as heterogeneous, hyperelastic and isotropic material, and used Neo-Hookan constitutive model to study the mechanical parameters of acupuncture into the cornea. Elsheikh and Wang (2007) used the third-order Ogden hyperelastic model to describe the corneal constitutive, and used the iterative method to restore the state of the eye without intraocular pressure. Karimi et al. (2018) applied the Mooney-Rivlin constitutive to the conus and normal corneal models, studied the stress distribution of the two corneas. An artificial neural network algorithm for the diagnosis of keratoconus was proposed. Pandolfi et al. (Pandolfi and Manganiello, 2006; Pandolfi et al., 2009) established a hyperelastic three-dimensional finite element corneal model considering the distribution of collagen fibers. He believed that the distribution of stress and refractive power on the corneal surface

TABLE 4 Strain energy function of hyperelastic model.

Model	Strain energy function
Mooney-Rivlin	$U = C_{10}(\bar{I}_1 - 3) + C_{01}(\bar{I}_2 - 3) + \frac{1}{D_1}(J-1)^2$
Neo-Hookean	$U = C_{10}(\bar{I}_1 - 3) + \frac{1}{D_1}(J-1)^2$
Ogden	$U = \sum_{i=1}^{N} \frac{2\mu_i}{\alpha_i^2}(\bar{\lambda}_1^{\alpha_i} + \bar{\lambda}_2^{\alpha_i} + \bar{\lambda}_3^{\alpha_i} - 3) + \sum_{i=1}^{N} \frac{1}{D_i}(J-1)^{2i}$
Yeoh	$U = \sum_{i=1}^{N} C_{i0}(\bar{I}_1 - 3)^i + \sum_{i=1}^{N} \frac{1}{D_i}(J-1)^{2i}$
HGO	$U = C_{10}(\bar{I}_1 - 3) + \frac{1}{D}(\frac{I^2-1}{2} - \ln J) + \frac{k_1}{k_2}\sum_{\alpha=1}^{N}\left(e^{k_2\overline{E_\alpha}^2} - 1\right)$

and in the direction of corneal thickness were related to material properties and fiber distribution. This study did not consider the differences in the distribution of collagen fibers in different corneas and the differences in mechanical parameters.

In the present study of corneal finite element simulation, the cornea as a hyperelastic material is closer to the real cornea properties. Common hyperelastic models include Mooney-Rivlin model, Neo-Hookean model, Yeoh model, Ogden model, and Holzapfel-Gasser-Ogden (HGO) models (Peng et al., 2021; Horgan, 2021; Melly et al., 2022; Lohr et al., 2022; Anssari-Benam et al., 2022; Karlsson et al., 2023; Gruber et al., 2024). The correspondence between the stress tensor and strain tensor of hyperelastic materials is not linear and does not satisfy Hooke's law, but corresponds to in elastic potential energy function, as shown in Figure 7. The constitutive relation can be given by strain energy function. The characteristics of hyperelastic materials are that the stress is only related to the strain, and has nothing to do with the path, rate, and history of the load applied. The deformation of the material can be restored after the load is released. The expression of strain energy function is shown in Table 4. These hyperelastic constitutive models are widely used in cornea research. The Mooney-Rivlin form is seen as an extension of the Neo-Hookean form, where one term is determined by the second invariant of the isotonic Cauchy-Green tensor. In many cases, the Neo-Hookean form is closer to the experimental data than the Mooney-Rivlin form. The accuracy of the two models is similar. Their strain energy is a linear function of invariants, and they cannot reflect the 'steep rise' behavior of the stress-strain curve in the large strain part, but they can well simulate the characteristics of materials under small and medium strains. For Ogden model, the strain energy is variable by three principal elongation ratios: λ_1, λ_2, λ_3. If N = 1, $\alpha_1 = 2$, $\alpha_2 = -2$, then get the Mooney-Rivlin model. If N = 1, $\alpha_1 = 2$, then get the Neo-Hookean model. In the Ogden model, μ_0 is all determined by coefficient: $\mu_0 = \sum_{i=1}^{N}\mu_i$. Arruda-Boyce model and Van-der-Waals model are also common hyperelastic models, but these two constitutive relations are obtained based on thermodynamic statistical methods (Kumar et al., 2022; Castellanos-Gomez et al., 2022). Thermodynamic coupling is rarely involved in corneal simulation, so these two models are not described and discussed in this review. Where, $\bar{I}_1 = \sum_{i=1}^{3}\bar{\lambda}_i^2$, $\bar{I}_2 = \sum_{i=1}^{3}\bar{\lambda}_i^{(-2)}$; $\overline{E_\alpha} = \kappa(\bar{I}_1 - 3) + (1-3\kappa)(\bar{I}_{4(\alpha)} - 1)$; $\bar{I}_{4(\alpha)} = A_\alpha \bar{C} A_\alpha$; $\bar{C} = J^{-2/3}C$; $J = (\det C)^{1/2}$; $C = F^T F$; C_{ij}, D_i, α, and μ are material constants; $\bar{I}_1$ is the first invariant of the modified right Cauchy-Green tensor; $\bar{\lambda}_i$ is deviatoric principal stretches; J is the elastic volume ratio; C_{10} is matrix stiffness; $\frac{1}{D}(\frac{J-1}{2} - \ln J)$ is corneal volume strain energy; D represents the inverse of the volumetric modulus. Considering that the cornea is almost incompressible material, it is set to a very small value in the setting. k_1 represents fiber stiffness; n is the number of families of fibers; k_2 is a dimensionless parameter referring to fiber nonlinearity; $\bar{E}_\alpha$ characterizes the deformation of the family of fibers with mean direction; κ describes the level of dispersion in the fiber, $0 \le \kappa \le 1/3$; $\kappa = 0$ indicates that collagen fibers are strictly distributed in the main direction of collagen fibers; $\kappa = 1/3$ indicates that collagen fibers are randomly distributed. A_α is the direction vector of the fiber bundle; $\bar{I}_{4(\alpha)}$ represents the square of the stretch along the direction of the α-th family of fibers; F is the deformation gradient; C is right Cauchy-Green strain tensor. The parameter settings of these models from literature reports are shown in Table 5.

The determination of material parameters is the result of experimental fitting by researchers. However, it can be seen from the literature that the parameters used by different researchers for the same constitutive model are not the same, or even quite different. This is because there are many factors that affect the results of corneal hyperelastic parameters, such as the difference of materials, the difference of mechanical testing methods, and different fitting algorithms. As for the sampling factors, the common corneal sources are cadavers and corneal surgical scraps. First of all, corneal cells and collagen fibers of different ages have great differences, and their macroscopic mechanical properties are also different. The method of corneal preservation and the time after cornea isolation also have a great influence. Next is the area where the cornea is surgically obtained. The remaining corneal tissue after corneal transplantation is often the corneosclera region, which is thicker than the central cornea. The corneas obtained from SMILE surgery tend to be the central cornea. The anisotropy difference of cornea also directly leads to the different mechanical properties of different regions. For the mechanical testing methods, the common methods include axial tensile test and expansion test. The stretching test is to cut the cornea into strips for stretching test, while the swelling test is generally to test the cornea as a whole. Two different test methods are the cause of the difference in parameters. Since the hyperelastic constitutive model needs many undetermined parameters in the calculation software, it is necessary to use the calculation software to fit the measured stress-strain curve. For a certain test result, different fitting algorithms may fit many kinds of parameter combination results that are consistent with the experimental curve. Xiang et al. (2018) conducted a uniaxial stretching experiment with the corneal lens removed by SMILE surgery. Parameters of HGO model were fitted by least square method to 34 experimental results. The average values of C_{10}, k_1 and k_2 were 0.220, 0.615 and 121.633. These values are significantly different from the results of Ariza-Gracia et al. (2016) fitting (C_{10} = 0.05, k_1 = 130.9, k_2 = 2490). Xiang et al. (2018) also suggested that the change of κ value has a very large effect on corneal stress-strain, and also affects the values of k_1 and k_2. The κ value of each cornea is different, which means the results of other parameters fitting may not be accurate.

TABLE 5 Hyperelastic model parameters.

Model	Values		Ref.
Mooney-Rivlin	Material-1	C_{10} = 0.3MPa, C_{01} = 0.12 MPa	Bekesi et al. (2016)
	Material-2	C_{10} = 0.55MPa, C_{01} = 0.17 MPa	
	Material-3	C_{10} = 0.62MPa, C_{01} = 0.41 MPa	
Neo-Hookean	D = 0, C_{10} = 0.15–1.00 MPa		Han and Yang (2019)
Ogden	First-order	μ_1 = 0.0541 MPa α_1 = 110.4	Bao et al. (2018)
	First-order	μ_1 = 0.6042 MPa α_1 = 16.45	Fang et al. (2020b)
	Second-order	μ_1 = 0.0260 MPa α_1 = 75.11 μ_2 = 0.0229 MPa α_2 = 63.70	Lago et al. (2015a)
	Second-order	μ_1 = 0.0035 MPa α_1 = 104.06 μ_2 = 0.0035 MPa α_2 = 103.94	Song et al. (2021)
Yeoh	Third-order	D = 0, C_{10} = 0.81 MPa,C_{20} = 56.05 MPa,C_{30} = 2332.26 MPa	Ariza-Gracia et al. (2016)
HGO	C_{10} = 0.050MPa, D = 0, k_1 = 25–130.9MPa, k_2 = 2490, κ = 0.33329		Ariza-Gracia et al. (2016)
	C_{10} = 0.025MPa, D = 0, k_1 = 0.092MPa, k_2 = 785.68, κ = 0.3		Xu et al. (2018)
	C_{10} = 0.220MPa, D = 0, k_1 = 0.615MPa, k_2 = 121.633, κ = 0.3		Xiang et al. (2018)

3.4 Viscoelastic constitutive model

Compared with linear elastic materials and hyperelastic materials, viscoelastic materials are more accurate in describing the constitutive relationship of the cornea. However, viscoelastic constitutive complexity is higher than linear elastic and hyperelastic constitutive complexity. Therefore, there are few corneal viscoelastic constitutive models reported in the literature. Kling et al. (2014) developed a viscoelastic finite element model to predict the experimental deformation response of the cornea to inflation under different conditions. Corneal tissue was studied by linear viscoelastic constitutive method. Therefore, only the shear response is considered, as it usually dominates the volume response. The viscoelastic constitutive is shown in Formula 4:

$$\sigma = \int_0^t 2G(t-\tau)\frac{de}{d\tau}dt, G(t) = G_0 \cdot \left[\alpha_1^G \cdot \exp\left(-\frac{t}{\tau_1^G}\right)\right], G_0 = G_\infty + G_1, \alpha_1^G = \frac{G_i}{G_0} \quad (4)$$

where σ is the Cauchy stress, e the deviatoric strain and τ past time. G(t) is the Prony shear modulus; α_1^G is the relative modulus; G_0 is instantaneous elastic moduli; G_∞ is infinite elastic moduli; G_1 is the current shear elastic moduli. τ_1^G is the relaxation times for the Prony component. Many viscoelastic models are composed of elastic and viscous elements (Banks et al., 2011; Bonet, 2001). MaxwelL model and Kelvin model are the basic models of viscoelasticity. Maxwell model is a series connection between spring and shock absorber (Renaud et al., 2011). The Kelvin model is a parallel connection between the spring and the shock absorber (Xu et al., 2015). The relationship of stress-strain is shown in Formula 5:

$$\sigma(t) = E_{equ} \cdot \varepsilon(t) + \sum_{i=1}^{m} E_i \cdot \dot{\varepsilon} \cdot \tau_i \cdot \left(1 - e^{-\frac{t}{\tau_i}}\right) \quad (5)$$

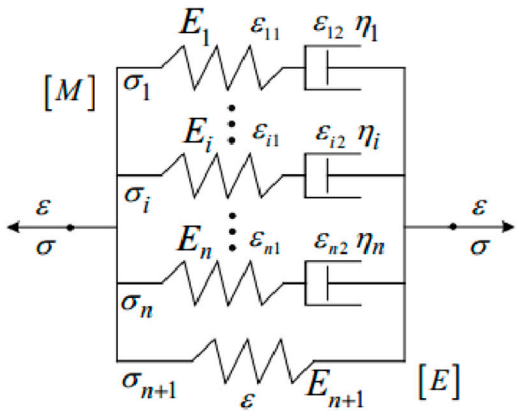

FIGURE 8
Modified Maxwell viscoelastic model of cornea (Melly et al., 2022).

where Eequ is the equilibrium modulus, Ei is the relaxation modulus of the ith branch, τ_i is the time constant of the ith branch, ε is the strain, and $\dot{\varepsilon}$ is the strain rate. Su et al. (2015) proposed a modified Maxwell viscoelastic model of the cornea from the perspective of material mechanics, as shown in Figure 8. The viscoelastic parameters were determined by the uniaxial tensile test and stress relaxation test. Through the simulation of corneal material properties, the validity of the superviscoelastic model is verified. The model is composed of Maxwell model [M] in parallel. Each Maxwell model [M] has a series damper. If the external load is applied long enough, the internal stress of the material will be close to zero. In Figure 8, the elastic element is connected in parallel with the generalized Maxwell model. This model is also called the modified Maxwell viscoelastic model of the cornea. The solid properties shown by the parallel elastic element [E] reflect the

residual stress of the cornea in the relaxation curve. The stress and strain in the model are described by the Formula 6:

$$\sigma = \sum_{i=1}^{n+1} \sigma_i \; \varepsilon = \varepsilon_{i1} + \varepsilon_{i2} \; (i = 1, 2, \ldots i, \ldots, n) \tag{6}$$

where σ_i is the stress in the ith sub-model; ε_{i1} is the strain of the ith elastic element; ε_{i2} is the strain of the ith viscous element.The constitutive equation of [M] model can be expressed as Formula 7:

$$\sum_{i=1}^{n} \sigma_i + \sum_{i=1}^{n} \frac{\eta_i}{E_i} \sigma_i = \sum_{i-1}^{n} \eta_i \varepsilon_i \tag{7}$$

E_i and η_i are the elastic modulus and viscosity coefficient of the ith Maxwell model element.

3.5 Comparison and analysis of different constitutive models

An ideal constitutive model should have the following requirements: contain as few parameters as possible; it can correctly predict the arbitrary complex deformation behavior of materials. But there seems to be some contradiction between these two points. In general, the higher the order of a constitutive equation, or the more undetermined parameters, the higher the accuracy of the constitutive equation. However, the more parameters to be determined, the more difficult the calculation is. The appropriate constitutive relation should be selected according to the different simulation and experiment requirements. The models in Table 5 have different characteristics. Yeoh model and Neo-Hookean model are the simplest in terms of form. Yeoh model requires few undetermined parameters, which can be obtained only from uniaxial tensile data. The model has a wide range to describe the superelastic behavior and deformation of materials. It is also most commonly used by researchers in corneal simulations. However, when the stress-strain curve of equiaxial tensile is predicted, the error is large and it is easy to show the phenomenon of "soft phenomenon." Therefore, when the corneal experiment is through uniaxial stretching experiment, it is more suitable to use this model to fit the parameters. When dealing with complex strain states with large deformation, such as corneal biaxial tensile tests, large deviations can occur. In this case, the model should be used with caution. The Neo-Hookean model is derived based on classical statistical thermodynamics. The model is simple in form, requires only two parameters, and has strong universality. It is generally suitable for small deformation uniaxial drawing with strain rate of 30%–40%. Since corneal are generally considered incompressible material, the number of undetermined parameters in the model is reduced to one. Only one parameter, the initial shear modulus, needs to be fitted from the experimental data, and the amount of testing is small. The polynomial model proposed by Mooney-Rivlin can accurately simulate the stress-strain relationship under various deformation modes. However, the model is complex and requires several experiments to obtain individual parameters. The model has 3 orders, 5 orders, and 9 orders. The higher the order, the higher the accuracy of calculation. With the increase of the order, it becomes more difficult to determine the material parameters. Ogden model can also accurately simulate stress-strain relationship under various deformation modes, but it also needs to obtain parameters through multiple experiments. The HGO hyperelastic model takes into account the distribution direction of stromal collagen fiber clusters in human cornea, which can more accurately describe the biomechanical properties of cornea *in vitro* and *in vivo*. Moreover, there are also fewer undetermined parameters. In the simulation of human cornea, it is the most popular and widely used constitutive model.

Theoretically, the accuracy of viscoelastic model is higher than that of hyperelastic model. However, it can also be seen from the form that there are three mathematical variables of stress-strain-time in the viscoelastic model, which is more complicated than the hyperelastic model. The viscoelastic model is mainly composed of elastic elements and viscous elements in parallel or in series. The model can be composed of two or more components. The more the number of components, the more complex the connection mode, the more difficult the parameters to be determined. But each model has some drawbacks. For example, the Maxwell model consisting of an elastic element and a viscous element in series cannot describe the phenomenon of stress relaxation. The Kelvin model, which consists of an elastic element and a viscous element in parallel, cannot describe the instantaneous elastic phenomenon or the plastic deformation. Other viscoelastic models (Ering, Burgers, Bingham, Nishihara) also have mechanical states that cannot be described exactly. Although the more complex the model, the higher the accuracy of the description. In selecting the surface model, we should choose the appropriate viscoelastic model to calculate according to different research problems.

For different simulation case, the appropriate constitutive model should be selected for simulation. The choice of constitutive model should not blindly pursue complexity. For example, Wu et al. (2021) studied the corneal biomechanical response of orthokeratology. The stress changes of corneal center and peripheral region were analyzed for models with different corneal curvature and corneal thickness under the action of orthokeratology. This kind of model focuses more on qualitative analysis than on the absolute value of stress or strain at a certain location. In this case, we can appropriately choose a simpler model, such as the first or second-order Ogden model. However, for the simulation analysis of myopia surgery with corneal flap or cap, we often pay more attention to the numerical value of the local area. For example, the amount of displacement and stress in the corneal cap or flap area. In this case, we choose as complex constitutive models as possible for simulation, such as HGO model or viscoelastic model.

The human corneathe environment is usually room temperature or constant temperature. Therefore, no matter what kind of model, the influence of temperature on constitutive relationship is often ignored. If the simulated case is not constant temperature, the effect of temperature on the material properties should be considered in the constitutive relationship.

4 Prospect and outlook

The development of finite element software has played an important role in promoting the study of cornea. The finite element model is often used in the study of eye diseases such as prediction of corneal refractive surgery, early prediction and

diagnosis of keratoconus, diagnosis and treatment of eye trauma and glaucoma. Over the past few decades, researchers have established finite element models for different purposes and methods to study the human cornea, which has greatly promoted research in cornea-related fields. It plays an important role in our further understanding of corneal material properties and biomechanical response, and helps us in-depth analysis of postoperative corneal and keratopathy research. Moreover, virtual surgical simulation system using computer simulation is a new development direction in the future. Compared with traditional surgery, virtual surgery has the advantages of non-injury, repeatability and referencability. It saves the cost and time of training medical personnel and greatly reduces the risk of operation by unskilled personnel, which has special significance for improving the efficiency and quality of medical education and training and improving the unbalanced development of medical operation level. Finite element model is the most important part of virtual surgical system. Therefore, the accurate establishment of the corneal finite element model lays an important foundation for exploring the research of cornea-related surgical digital system.

The accuracy of geometric description of cornea plays an important role in visual simulation results. The tissue around the cornea and its morphology also affect the corneal simulation results. Like the effects of aqueous humor, the effects of the pericorneal sclera. Aqueous humor occupies a small volume, it is believed that the influence on the cornea is small. However, the sclera plays the role of boundary conditions in simulation, and the influence of boundary conditions on simulation results cannot be ignored. It is difficult to accurately describe the geometry of cornea and surrounding tissues with a single instrument. We can combine multiple devices, using the advantages of each device to try to achieve an accurate description of the cornea and surrounding tissues. For the surface of the cornea, the Pentacam can be used to obtain accurate information about the front and back surfaces of the cornea. For peripheral tissue, CT and MRI techniques can effectively obtain geometric information. The combined application of multiple devices may lead to a more comprehensive and accurate description of the geometry of the cornea and surrounding tissues. In addition, we obtain the cornea *in vivo* as a state of intraocular pressure. This state is not the same as the state before applying intraocular pressure in the simulation. Therefore, before the calculation, it is necessary to find the shape of the cornea in the absence of intraocular pressure. Ariza-Gracia et al. (2016) quantitatively analyzed the calculation results of zero-pressure model and image-based model. It is proved that the calculation results of the two models are significantly different. Therefore, zero-pressure state is also an important factor to be considered in geometric models.

Characterization of corneal material properties is also an important challenge. Because of individual differences, corneal biomechanical properties are different in different populations, different ages, and after corneal injury. However, at present, there are few relevant studies, which also leads to the error of corneal parameter setting during simulation. Therefore, the constitutive relationship of cornea in different populations remains to be studied. It is still an important way to obtain corneal constitutive relationship through corneal experiment. The stress-strain relationship of cornea can obtain by corneal swelling test, creep test, stress relaxation test and other mechanical properties tests. It may be more accurate to deduce the parameters of the constitutive relation from the stress-strain relation. It is difficult for some stress-strain data to fit well into the existing models in finite element software. We can add subroutines to the constitutive model so that the experimental data can be better fitted to the constitutive model.

Ultimately, this review aims to provide some thoughts of human cornea finite element model of geometry model and constitutive model for related researchers, and we hope will promote their future research.

Author contributions

GP: Writing–original draft, Validation, Methodology, Investigation, Formal Analysis, Data curation, Conceptualization. CW: Writing–original draft, Methodology, Investigation. XW: Writing–original draft, Visualization, Investigation, Formal Analysis. XL: Writing–original draft, Visualization, Investigation, Formal Analysis. QM: Writing–review and editing, Supervision, Methodology, Conceptualization.

Funding

The author(s) declare that no financial support was received for the research, authorship, and/or publication of this article.

Conflict of interest

The authors declare that the research was conducted in the absence of any commercial or financial relationships that could be construed as a potential conflict of interest.

Publisher's note

References

Alcântara, L. O., de Sousa, J. R., Andrade, F. K., Teixeira, E. H., Cerqueira, M. Â., da Silva, A. L. C., et al. (2023). Extraction and characterization of hyaluronic acid from the eyeball of Nile Tilapia (Oreochromis niloticus). *Int. J. Biol. Macromol.* 226, 172–183. doi:10.1016/j.ijbiomac.2022.12.016

Anssari-Benam, A., Destrade, M., and Saccomandi, G. (2022). Modelling brain tissue elasticity with the Ogden model and an alternative family of constitutive models. *Philosophical Trans. R. Soc. A* 380 (2234), 20210325. doi:10.1098/rsta.2021.0325

Arestova, N. N., Arestov, D. O., and Panova, A. Y. (2024). Influence of various factors on the efficiency of trabeculectomy in pediatric patients with congenital glaucoma. *Russ. Pediatr. Ophthalmol.* 19 (2), 59–72. doi:10.17816/rpoj629264

Ariza-Gracia, M. Á., Zurita, J., Piñero, D. P., Calvo, B., and Rodríguez-Matas, J. F. (2016). Automatized patient-specific methodology for numerical determination of biomechanical corneal response. *Ann. Biomed. Eng.* 44, 1753–1772. doi:10.1007/s10439-015-1426-0

Asejczyk-Widlicka, M., and Srodka, W. (2020). Finite element simulation of Goldmann tonometry after refractive surgery. *Clin. Biomech.* 71, 24–28. doi:10.1016/j.clinbiomech.2019.09.007

Askarian, B., Ankur, T., Ho, P., and Chong, J. W. (2022). A Novel method for detecting keratoconus using smartphones.

Baek, J. W., and Park, S. J. (2019). Finite element analysis of cornea deformation and curvature change during the keratoplasty suturing process. *Biomed. Eng. Lett.* 9, 203–209. doi:10.1007/s13534-019-00100-4

Banks, H. T., Hu, S., and Kenz, Z. R. (2011). A brief review of elasticity and viscoelasticity for solids. *Adv. Appl. Math. Mech.* 3 (1), 1–51. doi:10.4208/aamm.10-m1030

Bao, F., Wang, J., Cao, S., Liao, N., Shu, B., Zhao, Y., et al. (2018). Development and clinical verification of numerical simulation for laser *in situ* keratomileusis. *J. Mech. Behav. Biomed. Mater.* 83, 126–134. doi:10.1016/j.jmbbm.2018.04.016

Barrientez, B., Nicholas, S. E., Whelchel, A., Sharif, R., Hjortdal, J., and Karamichos, D. (2019). Corneal injury: clinical and molecular aspects. *Exp. eye Res.* 186, 107709. doi:10.1016/j.exer.2019.107709

Bekerman, I., Gottlieb, P., and Vaiman, M. (2014). Variations in eyeball diameters of the healthy adults. *J. Ophthalmol.* 2014 (1), 1–5. doi:10.1155/2014/503645

Bekesi, N., Dorronsoro, C., de la Hoz, A., and Marcos, S. (2016). Material properties from air puff corneal deformation by numerical simulations on model corneas. *PLoS One* 11 (10), e0165669. doi:10.1371/journal.pone.0165669

Benzley, S. E., Perry, E., Merkley, K., Clark, B., and Sjaardama, G. (1995). A comparison of all hexagonal and all tetrahedral finite element meshes for elastic and elasto-plastic analysis. *Proc. 4th Int. Meshing Roundtable* 17, 179–191.

Bharathi, R. B., Poojary, R. G., Prabhu, G. K., and Ve, R. S. (2022). Finite element method for estimation of applanation force and to study the influence of intraocular pressure of eye on tonometry. *Int. Ophthalmol.* 42 (7), 1997–2005. doi:10.1007/s10792-021-02157-6

Biswas, R., and Strawn, R. C. (1998). Tetrahedral and hexahedral mesh adaptation for CFD problems. *Appl. Numer. Math.* 26 (1), 135–151. doi:10.1016/s0168-9274(97)00092-5

Bitar, M., Hara, Y., Sethi, D., and Couser, N. L. (2018). Genetic abnormalities of the cornea. *Ophthalmic Genet. Dis. A Quick Reference Guide Eye Extern. Ocular Adnexa Abnorm.*, 61–80. doi:10.1016/b978-0-323-65414-2.00005-2

Bonet, J. (2001). Large strain viscoelastic constitutive models. *Int. J. Solids Struct.* 38 (17), 2953–2968. doi:10.1016/s0020-7683(00)00215-8

Buffault, J., Labbé, A., Hamard, P., Brignole-Baudouin, F., and Baudouin, C. (2020). The trabecular meshwork: structure, function and clinical implications. A review of the literature. *J. francais d'ophtalmologie* 43 (7), e217–e230. doi:10.1016/j.jfo.2020.05.002

Castellanos-Gomez, A., Duan, X., Fei, Z., Gutierrez, H. R., Huang, Y., Huang, X., et al. (2022). Van der Waals heterostructures. *Nat. Rev. Methods Prim.* 2 (1), 58. doi:10.1038/s43586-022-00139-1

Cavas, M. F., Fernández, P. D. G., De, C. S., Nieto Martínez, J., Fernández Cañavate, F. J., Vega-Estrada, A., et al. (2014). Geometrical custom modeling of human cornea *in vivo* and its use for the diagnosis of corneal ectasia. *PLoS ONE* 9 (10), e110249. doi:10.1371/journal.pone.0110249

Civalek, Ö., Uzun, B., Yaylı, M. Ö., and Akgöz, B. (2020). Size-dependent transverse and longitudinal vibrations of embedded carbon and silica carbide nanotubes by nonlocal finite element method. *Eur. Phys. J. Plus* 135 (4), 381. doi:10.1140/epjp/s13360-020-00385-w

Clevenger, L. M., Cao, J. L., Steinkerchner, M. S., Nowacki, A. S., and Yuan, A. (2024). Demographics, presenting features, and outcomes of adult patients with ocular trauma. *J. Ophthalmol.* 2024 (1), 8871776. doi:10.1155/2024/8871776

Clough, R. W. (1990). Original formulation of the finite element method. *Finite Elem. analysis Des.* 7 (2), 89–101. doi:10.1016/0168-874x(90)90001-u

Da Silva, F., and Lira, M. (2022). Intraocular pressure measurement: a review. *Surv. Ophthalmol.* 67 (5), 1319–1331. doi:10.1016/j.survophthal.2022.03.001

Dutta, P., Gogoi, M., and Bordoloi, N. (2021). Prevalence of pediatric eye diseases in Assam, India-a hospital-based retrospective data. *Ophthalmol. J.* 6, 215–222. doi:10.5603/oj.2021.0035

Elsheikh, A., and Wang, D. (2007). Numerical modelling of corneal biomechanical behaviour. *Comput. methods biomechanics Biomed. Eng.* 10 (2), 85–95. doi:10.1080/10255840600976013

Fang, L., Wang, Y., Yang, R., Deng, S., and Deng, J. (2020a). Effects of the LASIK flap thickness on corneal biomechanical behavior: a finite element analysis. *BMC Ophthalmol.* 20, 67–69. doi:10.1186/s12886-020-01338-8

Fang, L., Wang, Y., Yang, R., Deng, S., Deng, J., and Wan, L. (2020b). Effects of the LASIK flap thickness on corneal biomechanical behavior: a finite element analysis. *BMC Ophthalmol.* 20, 67–69. doi:10.1186/s12886-020-01338-8

Fernandez, D. C., Niazy, A. M., Kurtz, R. M., Djotyan, G. P., and Juhasz, T. (2004). "Computational modeling of corneal refractive surgery," in *Ophthalmic technologies XIV* (SPIE), 59–70.

Fisher, R. F. (1977). The force of contraction of the human ciliary muscle during accommodation. *J. physiology* 270 (1), 51–74. doi:10.1113/jphysiol.1977.sp011938

Fung, Y. C. B. (1972). Stress-strain-history relations of soft tissues in simple elongation. *Biomechanics its Found. objectives*, 181–208.

Gardner, S. (2015). Studies of corneal structure and transparency. *Cardiff Univ.*

Gefen, A., Shalom, R., Elad, D., and Mandel, Y. (2009). Biomechanical analysis of the keratoconic cornea. *J. Mech. Behav. Biomed. Mater.* 2 (3), 224–236. doi:10.1016/j.jmbbm.2008.07.002

Gruber, G., Nicolini, L. F., Ribeiro, M., Lerchl, T., Wilke, H. J., Jaramillo, H. E., et al. (2024). Comparative FEM study on intervertebral disc modeling: holzapfel-Gasser-Ogden vs. structural rebars. *Front. Bioeng. Biotechnol.* 12, 1391957. doi:10.3389/fbioe.2024.1391957

Hammer, M., Muuss, M., Herbster, L., Herth, J., Scheuerle, A., Khoramnia, R., et al. (2024). Viscoelastic, optical, and surgical properties of vitreous body replacement hydrogels after aging compared to porcine vitreous bodies and silicone oils. *Transl. Vis. Sci. and Technol.* 13 (7), 5. doi:10.1167/tvst.13.7.5

Han, S. F., and Yang, Y. (2019). Influence of needling conditions on the corneal insertion force. *Comput. Methods Biomechanics Biomed. Eng.* 22, 1239–1246. doi:10.1080/10255842.2019.1655002

Hjortdal, J. Ø., and Peter, K. J. (1995). *In vitro* measurement of corneal strain, thickness, and curvature using digital image processing. *Acta Ophthalmol. Scand.* 73 (1), 5–11. doi:10.1111/j.1600-0420.1995.tb00004.x

Holladay, J. T., Wilcox, R. R., Koch, D. D., and Wang, L. (2022). Astigmatism analysis and reporting of surgically induced astigmatism and prediction error. *J. Cataract and Refract. Surg.* 48 (7), 799–812. doi:10.1097/j.jcrs.0000000000000871

Hong, Y., Ning, L., Sun, Y., Qian, H., and Ji, Y. (2023). The growth and shape of the eyeball and crystalline lens *in utero* documented by fetal MR imaging. *Heliyon* 9 (1), e12885. doi:10.1016/j.heliyon.2023.e12885

Horgan, C. O. (2021). A note on a class of generalized neo-Hookean models for isotropic incompressible hyperelastic materials. *Int. J. Non-Linear Mech.* 129, 103665. doi:10.1016/j.ijnonlinmec.2020.103665

Huang, L., Shen, M., Liu, T., Zhang, Y., and Wang, Y. (2020). Inverse solution of corneal material parameters based on non-contact tonometry: a comparative study of different constitutive models. *J. biomechanics* 112, 110055. doi:10.1016/j.jbiomech.2020.110055

Jannesari, M., Kadkhodaei, M., Mosaddegh, P., Kasprzak, H., and Behrouz, M. J. (2018). Assessment of corneal and fatty tissues biomechanical response in dynamic tonometry tests by using inverse models. *Acta Bioeng. biomechanics* 20 (1), 39–48. doi:10.5277/ABB-00969-2017-02

Jo, M. S., Moon, J. Y., Chung, S. K., Kim, E. K., Park, K. H., and Choi, J. S. (2023). Efficacy of biometry using swept-source optical coherence tomography for posterior chamber phakic intraocular lens implantation. *J. Korean Ophthalmol. Soc.* 64 (5), 374–381. doi:10.3341/jkos.2023.64.5.374

Jonas, J. B., Budde, W. M., and Panda-Jonas, S. (1999). Ophthalmoscopic evaluation of the optic nerve head. *Surv. Ophthalmol.* 43 (4), 293–320. doi:10.1016/s0039-6257(98)00049-6

Karimi, A., Grytz, R., Rahmati, S. M., Girkin, C. A., and Downs, J. C. (2021). Analysis of the effects of finite element type within a 3D biomechanical model of a human optic nerve head and posterior pole. *Comput. methods programs Biomed.* 198, 105794. doi:10.1016/j.cmpb.2020.105794

Karimi, A., Razaghi, R., Biglari, H., Sera, T., and Kudo, S. (2018). Collision of the glass shards with the eye: a computational fluid-structure interaction model. *J. Chem. Neuroanat.* 90, 80–86. doi:10.1016/j.jchemneu.2017.12.008

Karlsson, J., Stålhand, J., Carlhäll, C. J., Länne, T., and Engvall, J. (2023). An *in vivo* study of isotropic and anisotropic wall stress in a hyperelastic holzapfel-gasser-ogden model in the human abdominal aorta: effects of age and sex. *Front. Physiology* 14, 1128131. doi:10.3389/fphys.2023.1128131

Kling, S., Bekesi, N., Dorronsoro, C., Pascual, D., and Marcos, S. (2014). Corneal viscoelastic properties from finite-element analysis of *in vivo* air-puff deformation. *PloS one* 9 (8), e104904. doi:10.1371/journal.pone.0104904

Kumar, S., Singh, S. S., and Rozycki, P. (2022). Numerical simulation of strain-softening behavior of glass-filled polymer composites: comparison of two-dimensional and three-dimensional analyses using Arruda-Boyce and Three-Network viscoplastic models. *Mech. Mater.* 175, 104481. doi:10.1016/j.mechmat.2022.104481

Kwon, T. H., Ghaboussi, J., Pecknold, D. A., and Hashash, Y. (2008). Effect of cornea material stiffness on measured intraocular pressure. *J. biomechanics* 41 (8), 1707–1713. doi:10.1016/j.jbiomech.2008.03.004

Lago, M. A., Rupérez, M. J., Martínez-Martínez, F., Monserrat, C., Larra, E., Güell, J., et al. (2015a). A new methodology for the *in vivo* estimation of the elastic constants that

characterize the patient-specific biomechanical behavior of the human cornea. *J. biomechanics* 48 (1), 38–43. doi:10.1016/j.jbiomech.2014.11.009

Lago, M. A., Rupérez, M. J., Monserrat, C., Martínez-Martínez, F., Martínez-Sanchis, S., Larra, E., et al. (2015b). Patient-specific simulation of the intrastromal ring segment implantation in corneas with keratoconus. *J. Mech. Behav. Biomed. Mater.* 51, 260–268. doi:10.1016/j.jmbbm.2015.07.023

Larry, A., Hall, W. J., Keyes, L. D., Morgan, C. F., and Winterton, L. C. (2007). Corneal oxygen distribution with contact lens wear. *Cornea* 26 (6), 654–664. doi:10.1097/ico.0b013e31804f5a22

Li, H., Chen, M., Zhou, Q., Pan, X., Cheng, J., Cong, L., et al. (2021). Biomechanical effects of deep anterior lamellar keratoplasty and penetrating keratoplasty for keratoconus: a finite element analysis. *Transl. Vis. Sci. and Technol.* 10 (9), 15. doi:10.1167/tvst.10.9.15

Lino De Oliveira, B., and Sundnes, J. (2016). "Comparison of tetrahedral and hexahedral meshes for finite element simulation of cardiac electro-mechanics," in *Proceedings of the VII European congress on computational methods in applied sciences and engineering (ECCOMAS Congress'16)* (Institute of Structural Analysis and Antiseismic Research School of Civil Engineering National Technical University of Athens (NTUA) Greece).

Liu, X., Wang, L., Du, C., and Fan, Y. (2015). Mechanism of lens capsular rupture following blunt trauma: a finite element study. *Comput. methods biomechanics Biomed. Eng.* 18 (8), 914–921. doi:10.1080/10255842.2014.975798

Logg, A. (2007). Automating the finite element method. *Archives Comput. Methods Eng.* 14, 93–138. doi:10.1007/s11831-007-9003-9

Lohr, M. J., Sugerman, G. P., Kakaletsis, S., Lejeune, E., and Rausch, M. K. (2022). An introduction to the Ogden model in biomechanics: benefits, implementation tools and limitations. *Philosophical Trans. R. Soc. A* 380 (2234), 20210365. doi:10.1098/rsta.2021.0365

Mark, H. H. (2010). Aqueous humor dynamics in historical perspective. *Surv. Ophthalmol.* 55 (1), 89–100. doi:10.1016/j.survophthal.2009.06.005

Meek, K. M., and Knupp, C. (2015). Corneal structure and transparency. *Prog. Retin. eye Res.* 49, 1–16. doi:10.1016/j.preteyeres.2015.07.001

Melki, S. A., and Azar, D. T. (2001). LASIK complications: etiology, management, and prevention. *Surv. Ophthalmol.* 46 (2), 95–116. doi:10.1016/s0039-6257(01)00254-5

Melly, S. K., Liu, L., Liu, Y., and Leng, J. (2022). Modified Yeoh model with improved equibiaxial loading predictions. *Acta Mech.* 233 (2), 437–453. doi:10.1007/s00707-021-03105-2

Meng, Q., Wang, X., Chen, W., Li, X., and He, R. (2020). Finite element analysis of determining corneal biomechanical properties *in vivo* based on Corvis ST. *Sheng wu yi xue Gong Cheng xue za zhi=Journal Biomed. Engineering=Shengwu Yixue Gongchengxue Zazhi* 37 (4), 608–613. doi:10.7507/1001-5515.201911081

Méthot, S. J., Proulx, S., Brunette, I., and Rochette, P. J. (2020). Chronology of cellular events related to mitochondrial burnout leading to cell death in Fuchs endothelial corneal dystrophy. *Sci. Rep.* 10 (1), 5811. doi:10.1038/s41598-020-62602-x

Murugan, S., and Cheng, C. (2022). Roles of eph-ephrin signaling in the eye lens cataractogenesis, biomechanics, and homeostasis. *Front. Cell. Dev. Biol.* 10, 852236. doi:10.3389/fcell.2022.852236

Neuhuber, W., and Schrödl, F. (2011). Autonomic control of the eye and the iris. *Aut. Neurosci.* 165 (1), 67–79. doi:10.1016/j.autneu.2010.10.004

Nguyen, B. A., Roberts, C. J., and Reilly, M. A. (2019). Biomechanical impact of the sclera on corneal deformation response to an air-puff: a finite-element study. *Front. Bioeng. Biotechnol.* 6, 210. doi:10.3389/fbioe.2018.00210

Nikishkov, G. P. (2004). Introduction to the finite element method. *Univ. Aizu*, 1–70.

Pandolfi, A., Fotia, G., and Manganiello, F. (2009). Finite element simulations of laser refractive corneal surgery. *Eng. Comput.* 25, 15–24. doi:10.1007/s00366-008-0102-5

Pandolfi, A., and Holzapfel, G. A. (2008). Three-dimensional modeling and computational analysis of the human cornea considering distributed collagen fibril orientations. *J. Biomechanical Eng.* 130 (6), 061006. doi:10.1115/1.2982251

Pandolfi, A., and Manganiello, F. (2006). A model for the human cornea: constitutive formulation and numerical analysis. *Biomechanics Model. Mechanobiol.* 5 (4), 237–246. doi:10.1007/s10237-005-0014-x

Parker, J., Dockery, P., Preda-Naumescu, A., Jager, M., van Dijk, K., Dapena, I., et al. (2021). Descemet membrane endothelial keratoplasty and bowman layer transplantation: an anatomic review and historical survey. *Ophthalmic Res.* 64 (4), 532–553. doi:10.1159/000516093

Peng, X., Han, L., and Li, L. (2021). A consistently compressible Mooney-Rivlin model for the vulcanized rubber based on the Penn's experimental data. *Polym. Eng. and Sci.* 61 (9), 2287–2294. doi:10.1002/pen.25757

Pinazo-Durán, M. D., Zanón-Moreno, V., García-Medina, J. J., Arévalo, J. F., Gallego-Pinazo, R., and Nucci, C. (2016). Eclectic ocular comorbidities and systemic diseases with eye involvement: a review. *BioMed Res. Int.* 2016 (1), 1–10. doi:10.1155/2016/6215745

Qin, X., Tian, L., Zhang, H., Chen, X., and Li, L. (2019). Evaluation of corneal elastic modulus based on corneal visualization Scheimpflug technology. *Biomed. Eng. OnLine* 18, 42–16. doi:10.1186/s12938-019-0662-1

Ramasubramanian, V. S., Meenatchi Sundaram, S., Thomas, R., Ramesh, S. V., Raghuvir Pai, B., Hazarika, M., et al. (2022). Finite element analysis of cornea and lid wiper during blink, with and without contact lens. *J. Ophthalmol.* 2022 (1), 1–13. doi:10.1155/2022/7930334

Ramos, A., and Simões, J. A. (2006). Tetrahedral versus hexahedral finite elements in numerical modelling of the proximal femur. *Med. Eng. and Phys.* 28 (9), 916–924. doi:10.1016/j.medengphy.2005.12.006

Rampat, R., Deshmukh, R., Chen, X., Ting, D. S., Said, D. G., Dua, H. S., et al. (2021). Artificial intelligence in cornea, refractive surgery, and cataract: basic principles, clinical applications, and future directions. *Asia-Pacific J. Ophthalmol.* 10 (3), 268–281. doi:10.1097/apo.0000000000000394

Renaud, F., Dion, J. L., Chevallier, G., Tawfiq, I., and Lemaire, R. (2011). A new identification method of viscoelastic behavior: application to the generalized Maxwell model. *Mech. Syst. Signal Process.* 25 (3), 991–1010. doi:10.1016/j.ymssp.2010.09.002

Rossi, T., Boccassini, B., Esposito, L., Iossa, M., Ruggiero, A., Tamburrelli, C., et al. (2011). The pathogenesis of retinal damage in blunt eye trauma: finite element modeling. *Investigative Ophthalmol. and Vis. Sci.* 52 (7), 3994–4002. doi:10.1167/iovs.10-6477

Roy, A. S., and Dupps, W. J. (2011). Patient-specific modeling of corneal refractive surgery outcomes and inverse estimation of elastic property changes. *J. Biomechanical Eng.* 133 (1), 011002. doi:10.1115/1.4002934

Ruan, Y., Jiang, S., Musayeva, A., Pfeiffer, N., and Gericke, A. (2021). Corneal epithelial stem cells–physiology, pathophysiology and therapeutic options. *Cells* 10 (09), 2302. doi:10.3390/cells10092302

Salouti, R., Bagheri, M., Shamsi, A., Zamani, M., Ghoreyshi, M., and Nowroozzadeh, M. H. (2020). Corneal parameters in healthy subjects assessed by Corvis ST. *J. Ophthalmic and Vis. Res.* 15 (1), 24–31. doi:10.18502/jovr.v15i1.5936

Santhiago, M. R., and Randleman, J. B. (2021). The biology of corneal cross-linking derived from ultraviolet light and riboflavin. *Exp. Eye Res.* 202, 108355. doi:10.1016/j.exer.2020.108355

Santodomingo-Rubido, J., Carracedo, G., Suzaki, A., Villa-Collar, C., Vincent, S. J., and Wolffsohn, J. S. (2022). Keratoconus: an updated review. *Contact Lens Anterior Eye* 45 (3), 101559. doi:10.1016/j.clae.2021.101559

Schiefer, U., Kraus, C., Baumbach, P., Ungewiß, J., and Michels, R. (2016). Refractive errors: epidemiology, effects and treatment options. *Dtsch. Ärzteblatt Int.* 113 (41), 693–702. doi:10.3238/arztebl.2016.0693

Sekundo, W., Kunert, K. S., and Blum, M. (2011). Small incision corneal refractive surgery using the small incision lenticule extraction (SMILE) procedure for the correction of myopia and myopic astigmatism: results of a 6 month prospective study. *Br. J. Ophthalmol.* 95 (3), 335–339. doi:10.1136/bjo.2009.174284

Simonini, I., Angelillo, M., and Pandolfi, A. (2016). Theoretical and numerical analysis of the corneal air puff test. *J. Mech. Phys. Solids* 93, 118–134. doi:10.1016/j.jmps.2016.04.012

Sladek, J., Sladek, V., Tian, X., and Deng, Q. (2022). Mixed FEM for flexoelectric effect analyses in a viscoelastic material. *Int. J. Solids Struct.* 234, 111269. doi:10.1016/j.ijsolstr.2021.111269

Song, Y., Fang, L., Du, R., Lin, L., and Tao, X. (2021). The corneal biomechanical changes after SMILE and LASIK refractive surgery were compared based on finite element analysis. *E3S web of conferences*. Vol. 271. 03045. doi:10.1051/e3sconf/202127103045

Spevak, L. F., and Babailov, N. A. (2020). A finite element model of the stress-strain state of the human cornea. *AIP Conf. Proc.* 2315 (1), 040038. doi:10.1063/5.0036717

Stark, J. A., Foster, C. D., and Yu, C. (2021). Axisymmetric thermal finite element analysis of effects of intraocular projector in the human eye. *Am. J. Undergrad. Res.* 17 (4), 49–57. doi:10.33697/ajur.2020.035

Stefánsson, E. (2009). Physiology of vitreous surgery. *Graefe's archive Clin. Exp. Ophthalmol.* 247, 147–163. doi:10.1007/s00417-008-0980-7

Stepp, M. A. N. N., and Menko, A. S. U. E. (2021). Immune responses to injury and their links to eye disease. *Transl. Res.* 236, 52–71. doi:10.1016/j.trsl.2021.05.005

Su, P., Yang, Y., and Song, Y. (2015). Corneal hyper-viscoelastic model: derivations, experiments, and simulations. *Acta Bioeng. Biomechanics* 17 (2), 73–84. doi:10.5277/ABB-00142-2014-03

Sun, C., Wang, Y., Liu, G., and Liu, Z. (2020). Role of the eye in transmitting human coronavirus: what we know and what we do not know. *Front. public health* 8, 155. doi:10.3389/fpubh.2020.00155

Tandale, S. B., Markert, B., and Stoffel, M. (2022). Smart stiffness computation of one-dimensional finite elements. *Mech. Res. Commun.* 119, 103817. doi:10.1016/j.mechrescom.2021.103817

Toffoletto, N., Saramago, B., and Serro, A. P. (2020). Therapeutic ophthalmic lenses: a review. *Pharmaceutics* 13 (1), 36. doi:10.3390/pharmaceutics13010036

Tuori, A., Uusitalo, H., Burgeson, R. E., Terttunen, J., and Virtanen, I. (1996). The immunohistochemical composition of the human corneal basement membrane. *Cornea* 15 (3), 286–294. doi:10.1097/00003226-199605000-00010

Wang, C., Li, X., Guo, Y., He, R., Guo, H., and Chen, W. (2022). Effects of laser *in situ* keratomileusis and small-incision lenticule extraction on corneal biomechanical behavior: a finite element analysis. *Front. Bioeng. Biotechnol.* 10, 855367. doi:10.3389/fbioe.2022.855367

Wang, M., Gao, J., and Wang, X. (2017). High-quality mesh generation for human hip based on ideal element size: methods and evaluation. *Comput. Assist. Surg.* 22 (Suppl. 1), 212–220. doi:10.1080/24699322.2017.1389399

Wang, X., Rumpel, H., Lim, W. E. H., Baskaran, M., Perera, S. A., Nongpiur, M. E., et al. (2016). Finite element analysis predicts large optic nerve head strains during horizontal eye movements. *Investigative Ophthalmol. and Vis. Sci.* 57 (6), 2452–2462. doi:10.1167/iovs.15-18986

Wang, Z., Wang, H., Wang, J., and Tian, N. (2021). Finite element analyses of constitutive models performance in the simulation of blast-induced rock cracks. *Comput. Geotechnics* 135, 104172. doi:10.1016/j.compgeo.2021.104172

Weiskopf, N., Edwards, L. J., Helms, G., Mohammadi, S., and Kirilina, E. (2021). Quantitative magnetic resonance imaging of brain anatomy and *in vivo* histology. *Nat. Rev. Phys.* 3 (8), 570–588. doi:10.1038/s42254-021-00326-1

Wernli, J., Schumacher, S., Spoerl, E., and Mrochen, M. (2013). The efficacy of corneal cross-linking shows a sudden decrease with very high intensity UV light and short treatment time. *Investigative Ophthalmol. and Vis. Sci.* 54 (2), 1176–1180. doi:10.1167/iovs.12-11409

Williams, M. L. (1964). Structural analysis of viscoelastic materials. *AIAA J.* 2 (5), 785–808. doi:10.2514/3.2447

Wilson, S. E. (2020). Corneal wound healing. *Exp. eye Res.* 197, 108089. doi:10.1016/j.exer.2020.108089

Withers, P. J., Bouman, C., Carmignato, S., Cnudde, V., Grimaldi, D., Hagen, C. K., et al. (2021). X-ray computed tomography. *Nat. Rev. Methods Prim.* 1 (1), 18. doi:10.1038/s43586-021-00015-4

Wu, J., Fang, W., Xu, H., Liu, X., Zhao, D., and Rong, Q. (2021). The biomechanical response of the cornea in orthokeratology. *Front. Bioeng. Biotechnol.* 9, 743745. doi:10.3389/fbioe.2021.743745

Xiang, Y., Shen, M., Xue, C., Wu, D., and Wang, Y. (2018). Tensile biomechanical properties and constitutive parameters of human corneal stroma extracted by SMILE procedure. *Journal Mech. Behav. Biomed. Mater.* 85, 102–108. doi:10.1016/j.jmbbm.2018.05.042

Xie, J., Wang, B., Ju, Y., and Wu, S. (2008). "Analytic modeling and simulating of the cornea with finite element method," in *Medical imaging and informatics: 2nd international conference, MIMI 2007, Beijing, China, august 14-16, 2007 revised selected papers* (Springer Berlin Heidelberg).

Xu, M., Lerner, A. L., Funkenbusch, P. D., Richhariya, A., and Yoon, G. (2018). Sensitivity of corneal biomechanical and optical behavior to material parameters using design of experiments method. *Comput. methods biomechanics Biomed. Eng.* 21, 287–296. doi:10.1080/10255842.2018.1447104

Xu, Z. D., Xu, C., and Hu, J. (2015). Equivalent fractional Kelvin model and experimental study on viscoelastic damper. *J. Vib. Control* 21 (13), 2536–2552. doi:10.1177/1077546313513604

Zelentsova, E. A., Yanshole, L. V., Melnikov, A. D., Kudryavtsev, I. S., Novoselov, V. P., and Tsentalovich, Y. P. (2020). Post-mortem changes in metabolomic profiles of human serum, aqueous humor and vitreous humor. *Metabolomics* 16, 80–10. doi:10.1007/s11306-020-01700-3

Zhang, Y., Shen, Q., Jia, Y., Zhou, D., and Zhou, J. (2016). Clinical outcomes of SMILE and FS-LASIK used to treat myopia: a meta-analysis. *J. Refract. Surg.* 32 (4), 256–265. doi:10.3928/1081597x-20151111-06

Zhou, B., Sit, A. J., and Zhang, X. (2017). Noninvasive measurement of wave speed of porcine cornea in *ex vivo* porcine eyes for various intraocular pressures. *Ultrasonics* 81, 86–92. doi:10.1016/j.ultras.2017.06.008

Zwanenburg, E. A., Williams, M. A., and Warnett, J. M. (2021). Review of high-speed imaging with lab-based x-ray computed tomography. *Meas. Sci. Technol.* 33 (1), 012003. doi:10.1088/1361-6501/ac354a

frontiers | Frontiers in Medicine

TYPE Original Research
PUBLISHED 10 December 2024
DOI 10.3389/fmed.2024.1484449

OPEN ACCESS

EDITED BY
Norberto López Gil,
University of Murcia, Spain

REVIEWED BY
Kehao Wang,
Beihang University, China
Bernardo Yanez-Soto,
Universidad Autónoma de San Luis Potosí, Mexico

*CORRESPONDENCE
Mohammadali Shahiri
✉ Shahiri.mohammad22@gmail.com

RECEIVED 21 August 2024
ACCEPTED 22 November 2024
PUBLISHED 10 December 2024

CITATION
Shahiri M, Kasprzak H and Asejczyk M (2024) Pilot study on the dynamic interactions between cardiac activity and corneal biomechanics during eye movements. *Front. Med.* 11:1484449. doi: 10.3389/fmed.2024.1484449

Pilot study on the dynamic interactions between cardiac activity and corneal biomechanics during eye movements

Mohammadali Shahiri*, Henryk Kasprzak and Magdalena Asejczyk

Department of Optics and Photonics, Wrocław University of Science and Technology, Wrocław, Poland

Background and objective: The study examines the relationship between ocular rotations and cardiovascular functions through detailed biomechanical analysis. The study documents specific patterns of ocular movements and their synchronization with cardiovascular activity, highlighting significant correlations. These findings provide a basis for understanding the opto-biomechanical interplay between ocular and cardiovascular dynamics.

Methods: Authors employed a custom-designed prototype, integrating a camera and numerical pulse oximeter, to analyze the right eyeballs of participants. The corneal surface reflections were recorded, along with concurrent blood pulsation (BP) signal acquisition. Numerical analysis helped determine the reflection positions and orientations to study eye movements and corneal deformations. Time and frequency domain analyses, including coherence functions, were utilized.

Results: Significant correlations were found between variations in corneal curvature, selected fixational eye movements (FEM) parameters, and Pulsatile ocular blood flow (POBF), revealing synchronized expansions of the corneal surfaces with cardiovascular activity. Furthermore, FEM displayed spectral correlations with BP, indicating an interrelation between ocular rotations and cardiovascular functions.

Conclusion: These findings reveal the complex interactions between the cornea and Pulsatile Ocular Blood Flow (POBF), as well as between Fixational Eye Movements (FEM) and POBF. While the influence of POBF on both corneal dynamics and FEM is clear, further research is necessary to directly link corneal dynamics and FEM. These insights hold potential for non-invasive diagnostic applications and provide a deeper understanding of ocular biomechanics.

KEYWORDS

corneal deformations, corneal dynamics, fixational eye movements, blood pulsation, eye biomechanics

1 Introduction

The cornea, a critical component in the ocular system, is known for its significant optical power and accessibility (1, 2). It displays a range of complex biomechanical and optical properties that are essential for vision. Consequently, there has been a substantial amount of research focused on decoding the biomechanical and optical aspects of the cornea. Despite

this, most studies have examined its properties in isolation, overlooking the inherent interconnections. It's important to recognize that the corneal optical parameters are linked to its geometrical and biomechanical characteristics (3). These characteristics are further influenced by the cornea's heterogeneous and anisotropic nature, shaped by physiological factors (4). This complexity implies that the mechanical properties of the cornea are distributed in a three-dimensional pattern, akin to what is observed in conditions such as keratoconus (5). Adding to this complexity is the observation that the corneal elastic modulus and other mechanical properties vary along different radial meridians (6, 7). When assessing the cornea, it's crucial to consider the influence of various external structures and media, particularly intraocular pressure (IOP). For example, an elevation in IOP leads to anterior displacement of the cornea, which in turn alters the axial length of the eye (8). Such changes create a combination of compressive and tensile forces within the cornea, complicating the measurement of its elastic properties (3). Traditionally, the cornea has been viewed as a relatively static element in tonometric examinations. However, it is vital to acknowledge that the cornea is subject to continuous and rapid movements (9). These movements are influenced by deformations stemming from pulsatile fluctuations in IOP, driven by variations in blood pressure (BP) (10–12). These BP changes are characterized by both slow diurnal shifts and rapid, heartbeat-induced fluctuations (10). In light of these complexities, recent research has pivoted toward exploring corneal dynamics *in vivo*. This shift addresses the limitations of both *ex vivo* and *in vivo* studies, including challenges in translating observed tissue behavior to living conditions, potential tissue degradation in *ex vivo* studies, and notable variations between individual eyes in both study types (13–20). These individual differences, such as variations in biomechanical properties and intraocular pressure responses, complicate the generalization of findings across studies.

An area of particular interest is the quasi-periodic nature of eye expansion and its relation to BP. Research in corneal dynamics has highlighted how alterations in IOP and ocular pulse blood flow (POBF) can induce changes in eye shape, such as corneal surface expansion and modifications in eye length (21–24). A key study linked longitudinal corneal apex displacement (LCAD) with pulsatile blood flow (21). This study used a non-invasive approach involving ultrasonic distance sensors to track LCAD and head movements, revealing a correlation between these movements and cardiovascular activity. However, the complex relationship between BP and ocular pulse remains partially understood. Further investigations using high-speed videokeratoscopy have examined how longitudinal eye movements influence corneal shape (25). While these studies identified signals in the movement data related to the pulse, respiration, and blinking, a direct link between longitudinal apex movements and corneal curvature changes is yet to be firmly established.

Additionally, the study of oculomotor movements, predominantly considered as rotational movements of the eye, presents another layer of complexity. While these movements are extensively studied due to their direct impact on visual processes and perception, particularly in relation to saccades and movements over 1 degree, their effect on corneal expansion is less understood. Our research, which involved the use of a standard ophthalmic headrest to stabilize the head during measurements, considered these oculomotor movements. Unexpectedly, detailed analysis of the data obtained revealed spectral correlations with heart activity and BP. Prior studies (26, 27) have observed the influence of such movements on anterior eye measurements, but the spectral correlations of these effects remain under-explored. Our approach, which includes spectral coherence analysis between FEM data and BP, provides new insights into these complex interactions (28, 29). Time-domain analysis alone may overlook underlying periodic patterns and frequency-specific influences, whereas spectral analysis provides insights into the frequency components and dynamic relationships between these physiological signals and eye measurements. It's crucial to note that even minor head movements can significantly affect ophthalmological measurements (30–32). While often regarded as random, research has shown that these movements exhibit clear spectral correlations with the cardiopulmonary system (33).

In conclusion, understanding the multifaceted nature of the cornea and its interaction with various external factors is vital. In-depth research into *in vivo* corneal dynamics can offer invaluable insights into the cornea's behavior and its relationship with elements like IOP, POBF, and head movements. This knowledge is crucial for the development of non-invasive diagnostic techniques and enhancing our grasp of the complex mechanisms underlying vision. The present work contributes to this area, specifically focusing on the Finite Element (FE) modeling of the optomechanical self-adjustment mechanism (8), which is a crucial step toward integrating this model with finite element analysis.

2 Materials and methods

2.1 Participants

This study involved eight healthy volunteers, comprising three females and five males. None of the participants were contact lens users and had no history of dry eye symptoms or any known corneal and heart conditions. Participants were fully informed about the study's rationale and procedures' risks. The project was affirmed by the Ethics Committee of the Wroclaw University of Science and Technology (O-22-30) and adhered to the tenets of the Declaration of Helsinki. In this study, the right eyes of the subjects were exclusively examined. Participants were instructed to refrain from blinking for approximately 10 s during each testing session to ensure measurement accuracy. Prior to each session, the instrument was meticulously calibrated to maintain consistent measurement standards. All measurements were conducted by the same experienced investigator, ensuring uniformity in the testing procedure. The experiment was repeated four times for each subject to confirm the reliability and reproducibility of the data. The repetition rate is adopted from best practices observed in existing studies (34–36). This consistency not only supports the robustness of our dataset but also enables comprehensive statistical analysis, ensuring that our findings are reliable and can be generalized to a broader population.

2.2 Measurement protocol

A custom-designed prototype (Figure 1) with the Canon camera was used for the non-invasive recording of the reflecting

Abbreviations: POBF, Pulsatile ocular blood flow; FEM, Fixational eye movements; IOP, Intraocular pressure; LCAD, longitudinal corneal apex displacement; BP, Blood pulsations.

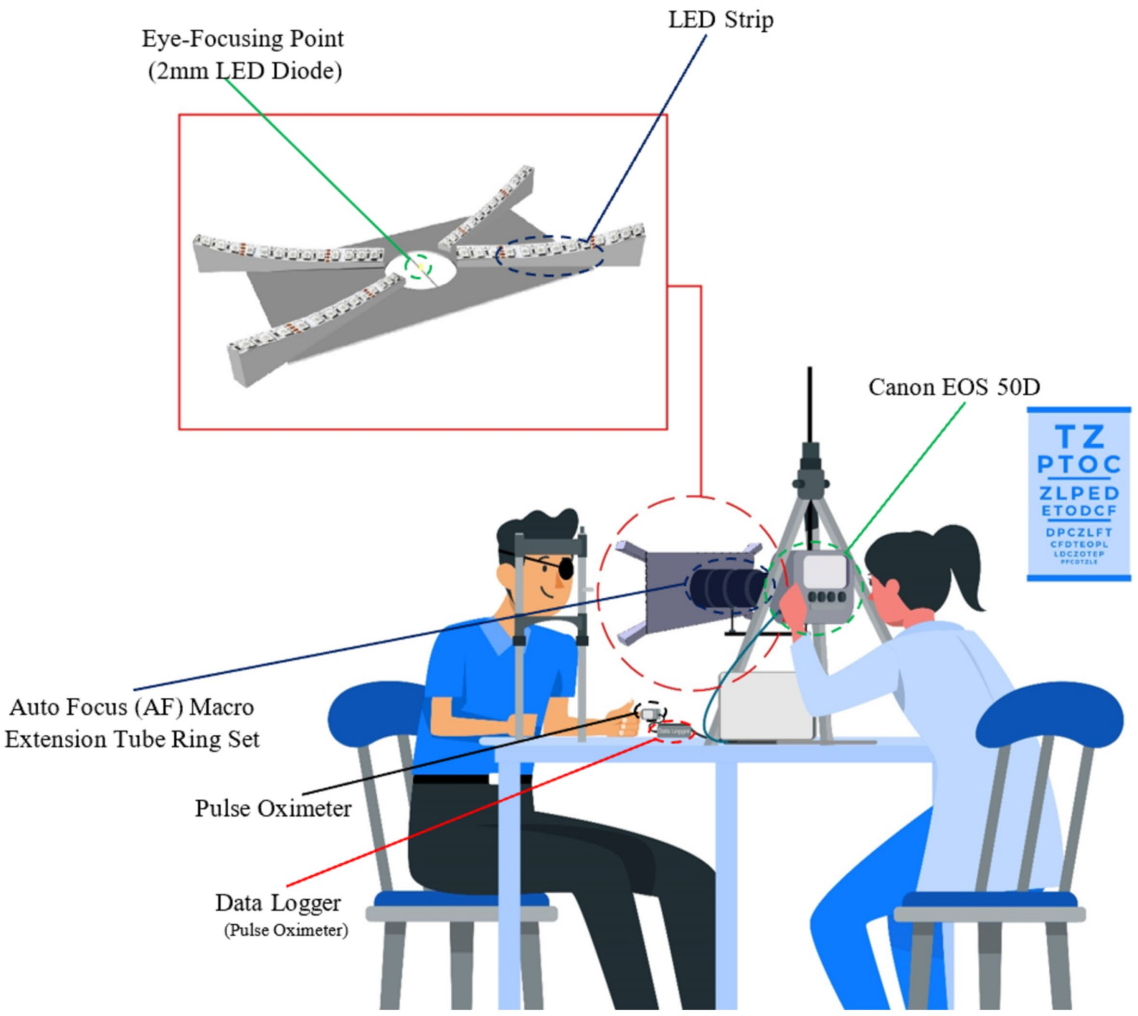

FIGURE 1
Measurement protocol overview.

LEDs illuminating the corneal surface, as shown in Figure 1 scheme. This custom-designed prototype offers enhanced resolution and accuracy over traditional videokeratometers, paving the way for more detailed insights into corneal deformations. To facilitate the data analysis process, 4 LEDs (1 LED in each fork, as shown in Figure 1) were considered, and the rest were covered. The primary diode, positioned near the pupil's center, served as a focal point for eye fixation during measurements. The other four diodes, located at the corneal periphery, facilitated additional data capture. Video sequences were recorded from the right eyes of the subjects at the frequency of 25 fps. Synchronously, a numerical pulse oximeter acquired the blood pulsation signal with a frequency of 100 Hz. As head movements affect the measurement accuracy of the corneal deformations and light spot displacements, an ophthalmic headrest was applied to stabilize the head position. As was shown in the paper (33), the ophthalmic headrest stabilizes the head movements only partially, and quasi-periodical head movements due to blood pulsation transfer to some degree from the head based on the headrest. However, such quasi-fixation of the head significantly facilitates experiments and image analysis.

2.3 Data analysis

In order to synchronize recorded images of points reflected from the cornea and pulse oximeter signal, the start time of the video sequences coincided with the appropriate time of the blood pulsation signal. To make the spectral and coherence analysis for the same frequency, only every fourth sample of this blood pulsation signal was taken into account to get the same frequency 25 Hz as the frequency of recorded images. The video sequences were divided into frames in MATLAB software, and then the specific rectangular area corresponding to each test was considered, including the LED reflections. Each bright reflection spot from the cornea contained a dozen or several dozens of pixels. The center of mass of each bright spot was calculated to increase the accuracy of calculations of the corneal deformations and to get subpixel accuracy. Due to mass center calculations of each reflection from the cornea, the accuracy of measurements was significantly smaller than one pixel.

The coordinates of these mass centers in each picture were next analyzed numerically to find variability of their positions and orientations of their movements. These data describe eye movements during measurements. Analysis of distances between appropriate spot

mass centers shows deformations of the corneal surface. Figure 2 shows a simple schematic of the pre-calculation flow.

Figure 3 presents five analyzed reflection points on the cornea located in the coordinate system and their numbers. To simplify the calculation process, the bright reflection spot will be identified with subscripts ranging from 1 to 5, as shown in Figure 3.

To precisely assess changes in corneal curvature, we focused on measuring the distance between specific reflective points on the corneal surface, with primary attention given to d24, the diagonal spanning from point 2 (temporal side) to point 4 (nasal side) on the cornea. This oblique distance, as illustrated in Figure 3, is the diagonal of the rectangular configuration formed by the reflective points. By positioning d24 along this diagonal, we capture the combined effects of horizontal (nasal-temporal) and vertical (superior–inferior) deformations, offering a more holistic measure of corneal curvature variations.

The rationale behind selecting d24 as a curvature indicator lies in its sensitivity to changes across multiple axes, which is particularly valuable when assessing corneal deformations. Corneal curvature directly influences the spatial relationships between fixed surface points: when the curvature steepens, the radius of curvature decreases, leading to a contraction along the diagonal, thereby reducing d24. Conversely, as the cornea flattens, the radius of curvature increases, and d24 expands. This geometric relationship allows d24 to reflect subtle adjustments in the corneal surface shape. The orientation of d24 as a diagonal distance makes it particularly responsive to variations that occur along both the horizontal and vertical planes, effectively capturing overall curvature changes rather than limiting the analysis to a single direction.

Additionally, this approach is consistent with established reflection-based measurement techniques in corneal topography and keratometry, where inter-point distances are commonly used to infer surface curvature. By tracking the shifts in d24, which represents the corneal surface's response to internal and external forces, we gain insights into the biomechanical dynamics at play. The reliability of this measure is further enhanced by our use of high-resolution imaging and subpixel tracking, which ensure the precision and accuracy needed for such detailed curvature assessment.

Figure 4 provides a schematic representation of the orientation angle α of the analyzed reflection across three consecutive frames. The orientation angle α is utilized to examine directional variations in corneal curvature. Defined as the angle between the line connecting reflective points and the horizontal (nasal-temporal) axis, α allows us to assess how curvature changes differ across orientations. This parameter is essential for evaluating the anisotropic nature of corneal deformations and determining whether systemic influences, such as intraocular pressure and pulsatile ocular blood flow, affect corneal dynamics differently along specific axes. By exploring α, we aim to identify any directional dependencies in the cornea's biomechanical response (37, 38).

Time and frequency domain analyses were conducted on the signals and their derivatives using MATLAB and MATHCAD software. Derivative-based analysis is crucial for capturing the rate of change in the signals, providing insights into the dynamics and rapid fluctuations that might not be apparent from the raw data alone.

Frequency domain analysis, though informative, often falls short in fully describing non-stationary signals whose characteristics change over time. To address this limitation, we utilized Short-Time Fourier Transform (STFT) with Hamming Windows. The STFT allows for a time-localized frequency analysis by segmenting the signal into overlapping windows, thereby enabling the observation of how spectral characteristics vary temporally. The application of the Hamming Window enhances the accuracy of the frequency domain representation by reducing spectral leakage and improving the clarity of the results. Additionally, the coherence function was employed to elucidate the spectral correlation between two signals within the frequency domain. Coherence measures the degree of correlation between the frequency components of the signals, providing valuable insights into the interrelationship between corneal deformations and ocular pulsations.

2.4 Validation of measurement method

To ensure the reliability and accuracy of our measurement method and to minimize the impact of potential confounding factors such as corneal surface roughness and tear film evaporation, we implemented specific participant selection criteria and standardized measurement protocols. Young healthy participants were carefully screened to exclude individuals with known ocular surface abnormalities, dry eye symptoms, or corneal conditions that could affect the quality of corneal reflections. Prior to each measurement session, participants were instructed to blink naturally to refresh the tear film, ensuring a smooth and uniform corneal surface. The measurement protocol required participants to refrain from blinking for approximately 10 s during data acquisition; however, if a participant blinked during this period, the measurement was paused and restarted to maintain data integrity. Repeated measurements were conducted for each participant to assess the consistency and repeatability of the data. The standard deviation of these repeated measurements was calculated to evaluate equipment variability, confirming that the fluctuations observed in the live data were significantly greater than the inherent variability of the measurement system. This approach ensured that our measurements reliably captured physiological changes in the cornea rather than artifacts arising from equipment limitations or external factors.

Moreover, in this study, all displacement and distance measurements of the corneal reflection points were recorded in pixel units. Due to the consistent experimental setup, camera settings, and equipment configuration across all measurements, we were able to compare relative changes in pixel units between participants and across different time points. This approach allowed us to analyze patterns and correlations within the data effectively.

3 Results

Exemplary results for one measurement of a young subject, AD, are provided in this chapter on behalf of the entire recorded data. The captured video series consists of $N = 325$ frames, and this sequence took 13 s to complete. The presented results display specific parameters that were primarily obtained for two selected images on the cornea, specifically point No. 2 and 4, in each measurement. Nonetheless, numerical analysis was performed for all five marked points. The achieved subpixel accuracy in determining the position of these points enabled a precise, comprehensive examination of both corneal deformations and eye movements. To evaluate the consistency of our

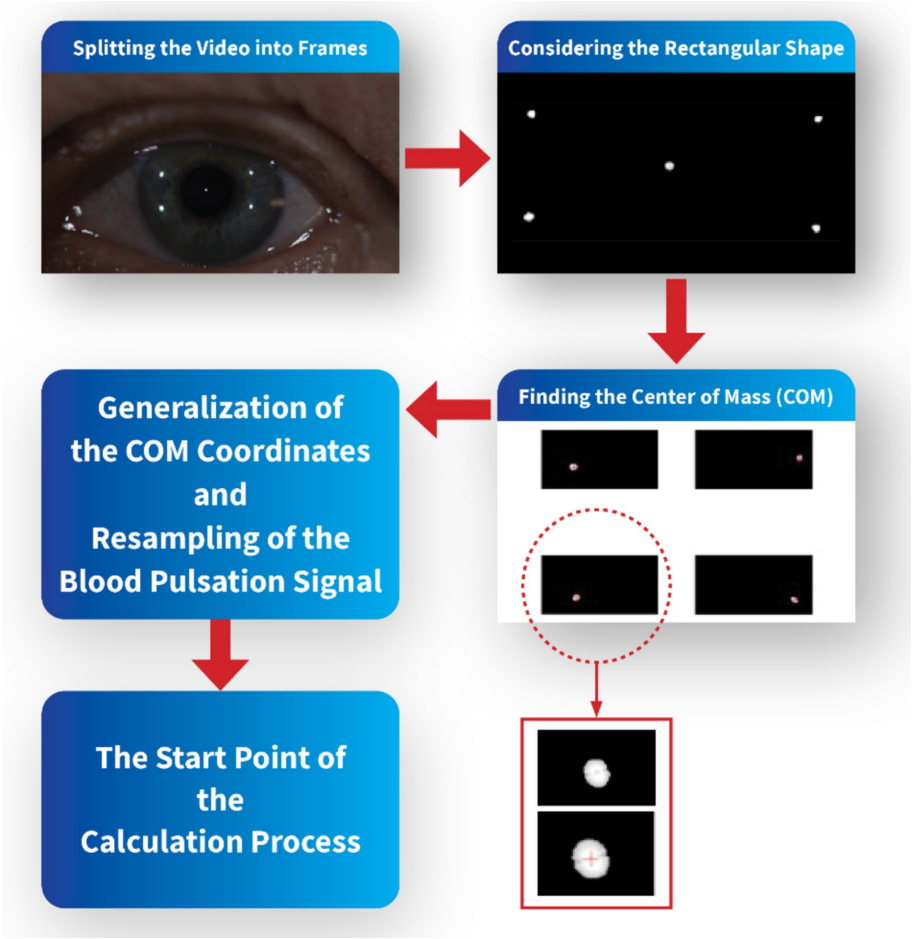

FIGURE 2
Schematic of the pre-calculation/processing flow.

findings across all subjects, we conducted a group-level statistical analysis. Correlation coefficients were calculated for each parameter pair: d24 (distance variability between points 2 and 4 on the corneal surface), dSC (variability in the quadrangle area formed by points 1, 2, 4, and 5), and dPu (derivative of the blood pulsation signal). The mean correlation coefficients were 0.66 (d24 vs. dPu), 0.59 (dSC vs. dPu), and 0.71 (d24 vs. dSC), with corresponding standard deviations of 0.05, 0.06, and 0.04, respectively. Each parameter pair showed statistical significance ($p < 0.01$), suggesting a reliable association across the cohort. These results indicate consistent relationships between corneal dynamics and cardiovascular activity among all eight subjects, supporting the generalizability of our observations within the context of this pilot study.

Figure 5A illustrates the *X*-coordinates for point 2 (X2, adjusted by adding 400 pixels for clearer comparison, shown as the black line) and point 4 (X4, shown as the blue line). The red line (DX24d) represents the linearly detrended difference between these two points, highlighting the dynamic distance changes over time. Figure 5B displays the *Y*-coordinates for point 2 (Y2, blue line) and point 4 (Y4, adjusted by adding 150 pixels, shown as the black line). Similarly, the red line (DY24d) shows the detrended difference between the Y-coordinates of these points, providing insights into the vertical relative movement dynamics. Detrending is applied to the position data to remove any overarching linear trends, allowing for a clearer observation of the subtle, short-term variations in corneal dynamics. By isolating these fluctuations, we can better capture and analyze the directional deformations of the corneal surface. This process enhances the focus on biomechanical responses that may be related to influences, such as pulsatile ocular blood flow or fixational eye movements. This detailed tracking of corneal positions and their relative changes is crucial for understanding the biomechanics of eye movements in relation to the corneal structure.

In the exploration of corneal and cardiovascular interactions, Figure 6 provides a dual perspective on both temporal and spectral dynamics. Figure 6A captures the time-domain fluctuations of the linearly detrended distance between corneal points 2 and 4 (d24), place side by side with the derivative of the blood pulsation signal (dPu). The graphical representation highlights not only the magnitude of changes but also the temporal synchronicity between corneal motion and blood flow dynamics. Figure 6B extends the analysis into the frequency domain, where the Fourier spectra of d24 and dPu are plotted. The spectra elucidate the prevalent frequency components within each signal, with marked peaks indicating areas of significant physiological interaction. The correspondence of peaks across the two spectra suggests a strong harmonic relationship, potentially indicative of the biomechanical coupling between the cornea's structural

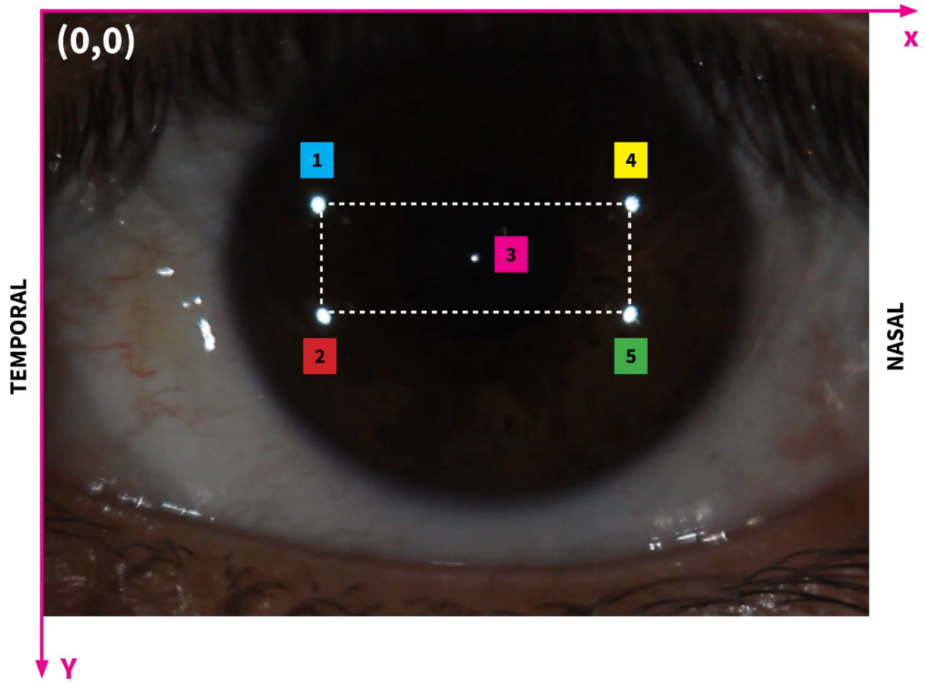

FIGURE 3
Image showing the region of interest on the corneal surface with the highlighted rectangular area. The rectangle encompasses the primary area of bright reflection spots that are critical for our analysis. This specific range facilitates a focused examination of the interactions between these spots and the corneal deformations. Subscripts 1 to 5 illustrate different bright reflection spots, their positions and distances.

responses and blood pulsations. This comprehensive portrayal, through both temporal and frequency analyses, underscores the complex interdependencies characterizing corneal and cardiovascular behaviors. The observed spectral similarities affirm the hypothesis that corneal dynamics are closely linked with cardiovascular activities. The observed spectral similarities affirm the hypothesis that corneal dynamics are closely linked with cardiovascular activities, suggesting potential for non-invasive diagnostics that monitor these biomechanical interactions. To quantitatively assess the synchronization between the two signals, we applied cross-correlation analysis. This method calculates the similarity between the signals across time-lags, enabling us to identify the peak correlation coefficient and the time-lag at which synchronization is strongest. By demonstrating a high cross-correlation value near zero lag, we can quantitatively confirm the temporal alignment of the signals (39).

In our findings, significant correlations were observed between the variations in distances (d24) among corneal reflection points and the pulsatile ocular blood flow (POBF), suggesting synchronized corneal expansions with cardiovascular activity. The correlation between variations in d24 and POBF was primarily observed within the 1–8 Hz frequency range, a band associated with cardiovascular influences on ocular biomechanics. We applied coherence analysis to evaluate this relationship, focusing on this specific range. The high coherence values within this band indicate a significant correlation, capturing the dynamic interactions most relevant to POBF without suggesting a uniform correlation across the entire frequency spectrum.

In examining the mechanical responsiveness of the corneal structure to cardiovascular dynamics, we specifically analyzed the variability of the area formed by points 1, 2, 5, and 4, designated as dSC. This area's analysis, as shown in Figure 7A, was conducted to assess the homogeneous or heterogeneous nature of corneal expansion and contraction in relation to blood pulsation. The linear detrending applied to the area measurements highlights the cornea's dynamic response to the rhythmic blood flow, as evidenced by the temporal correlation with the derivative of the blood pulsation signal (dPu). Further extending our analysis to the frequency domain, Figure 7B elucidates the spectral characteristics of both dSC and dPu. By examining the Fourier spectra, we observe significant peaks at specific frequencies, indicating potential frequencies where corneal deformation patterns align closely with cardiovascular signals. This spectral analysis not only confirms the temporal observations from the top panel but also enhances our understanding of the underlying physiological interactions, suggesting that certain frequencies of blood flow have a more marked impact on corneal dynamics. These findings contribute to a deeper understanding of the biomechanical properties of the cornea, particularly how it behaves in response to internal physiological changes. Such insights are crucial for developing predictive models of corneal behavior in clinical settings, potentially aiding in the non-invasive assessment of cardiovascular health based on ocular biometrics.

Figure 8 focuses on the coherence analysis between pairs of signals derived from our measurements of corneal dynamics and cardiovascular activity. The coherence function, a statistical measure of the degree to which two signals are linearly related at each frequency, was utilized to assess the phase relationships between d24 (distance variability between points 2 and 4), dSC (variability in the quadrangle area), and dPu (derivative of the blood pulsation signal). The analysis revealed significant coherence at several key frequencies, particularly within the 5–8 Hz range. For example, the coherence between d24 and dSC, represented by the black line, shows notable

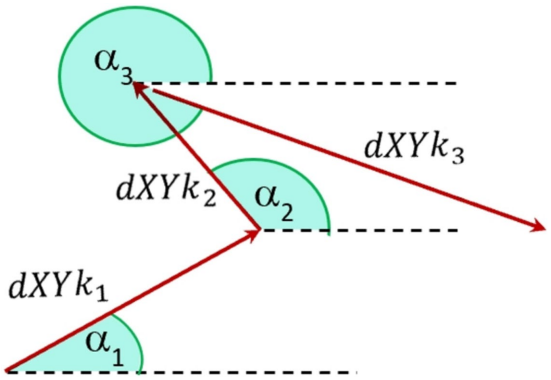

FIGURE 4
Schematic notation of orientation angles a [0–360 deg] of fast eye movements of the diode reflection on the cornea between three separate frames, where *k* represents the number of analyzed points.

peaks around 5 and 8 Hz, suggesting synchronized physiological responses between these two measures of corneal dynamics. Similarly, the coherence between d24 and dPu (red line) and between dSC and dPu (blue line) exhibits strong correlations at similar frequencies within the 5–8 Hz band. Although the cardiac pulse rate and its harmonics (e.g., 1.2, 2.4, and 3.6 Hz) are relevant, the significant coherence peaks occur at higher frequencies (5–8 Hz). This suggests that higher-order harmonics or other physiological factors may contribute to the observed synchronization. The high coherence values in this frequency range imply that the movements of the corneal surface and the variations in blood pulsation are not random but are indeed synchronized. The coherence at these specific frequencies suggests that corneal deformation and the cardiovascular system respond to the same physiological stimuli or share common regulatory mechanisms. Such findings underscore the complex interplay between ocular biomechanics and cardiovascular dynamics. These findings underscore the complex interplay between ocular biomechanics and cardiovascular dynamics, revealing phase relationships that could be critical for the development of non-invasive diagnostic and monitoring tools based on synchronized ocular signals.

In our analysis of fixational eye movements, detailed tracking of corneal points 2 and 4 provided insights into the dynamic behavior of these specific regions on the cornea. Figure 9 visually represents the trajectories of these points during the video sequence, captured as part of our comprehensive study on eye movement dynamics. Figure 9A depicts the trajectories at point 2, where complex patterns of movement are observable. Each line represents a separate trajectory over time, showing the variability and the extent of fixational movements within the observational window. Similarly, Figure 9B shows the movement patterns at point 4, which, while analogous to those at point 2, exhibit their unique characteristics and minor deviations in movement paths. The similarity in the patterns between these two points underscores the synchronized nature of fixational eye movements across different corneal regions. However, the subtle differences highlighted upon closer examination of the trajectories reveal the nuanced behaviors of each point, likely influenced by localized corneal biomechanics and broader ocular dynamics. These observations are pivotal in understanding the complexity of ocular fixational movements, which, despite their subtlety, play significant roles in visual stabilization and image processing. This analysis not only confirms the presence of these movements but also enhances our understanding of their behavioral patterns across the corneal surface.

In order to quantify the dynamic characteristics of fixational eye movements at point 4 on the cornea, we analyzed the distances traveled by this point from one video frame to the next over the entire sequence. Given a consistent frame interval of 40 milliseconds, these distances effectively represent the instantaneous speeds of the point's movement. Figure 10 presents a histogram of these speeds, illustrating the distribution of movement lengths across 324 instances within the 325-frame sequence. The analysis revealed that the majority of these movements are relatively subtle, with the most common speeds being approximately 1 pixel per frame. However, the histogram also captures instances where speeds reach up to 4 pixels per frame, indicating occasional faster movements. This distribution provides insights into the nature of fixational eye movements, which are predominantly minor but can occasionally include more rapid shifts. Understanding these patterns is crucial for interpreting the stability and micro-movements of the eye, which have implications for both physiological studies and applications in visual tracking technologies.

In our detailed examination of fixational eye movements, particularly focusing on the speeds of these movements as captured by the length of movement per frame (dXY4) at point 4, we observed notable temporal correlations with physiological signals. Figure 11 presents these findings, showing the variability in movement lengths alongside the derivative of the blood pulsation signal (dPu) over approximately half of the recorded sequence to ensure clearer visualization. The black line (dXY4) in the figure tracks the micro-movements, which are predominantly fixational eye movements such as microsaccades and drifts. These movements, while subtle, show a pattern of periodicity that interestingly aligns with the fluctuations observed in the red line representing the blood pulsation signal (dPu). This alignment may indicate that systemic physiological processes like blood flow could influence or synchronize with the subtle dynamics of ocular movements. While our analysis did not specifically differentiate between types of fixational movements, such as microsaccades or drifts, because the data was not detailed enough, the histogram of movement speeds suggests a relatively consistent distribution across the different types of movements. This pattern reinforces the understanding that fixational eye movements, even those of minimal amplitude, contribute significantly to overall ocular stability and may reflect underlying physiological rhythms. The correlation observed between these two measurements underscores potential areas for further research, particularly in the exploration of how health conditions might impact or be inferred from ocular movement patterns. The correlation between these two measurements opens up avenues for further research into how health conditions might influence or be inferred from ocular movement patterns, emphasizing the diagnostic potential of tools that integrate both ocular and cardiovascular dynamics.

To further understand the dynamics of fixational eye movements, we analyzed the orientation angles of these movements at point 4 relative to the horizontal axis. Figure 12 captures the distribution of these orientation angles, which range from 0 to 360 degrees, representing the complete possible spectrum of movement directions. Figure 12A displays a histogram on a rectangular plot, categorizing the frequency of each orientation angle. This analysis shows a relatively uniform distribution across all angles, suggesting that there is no clear

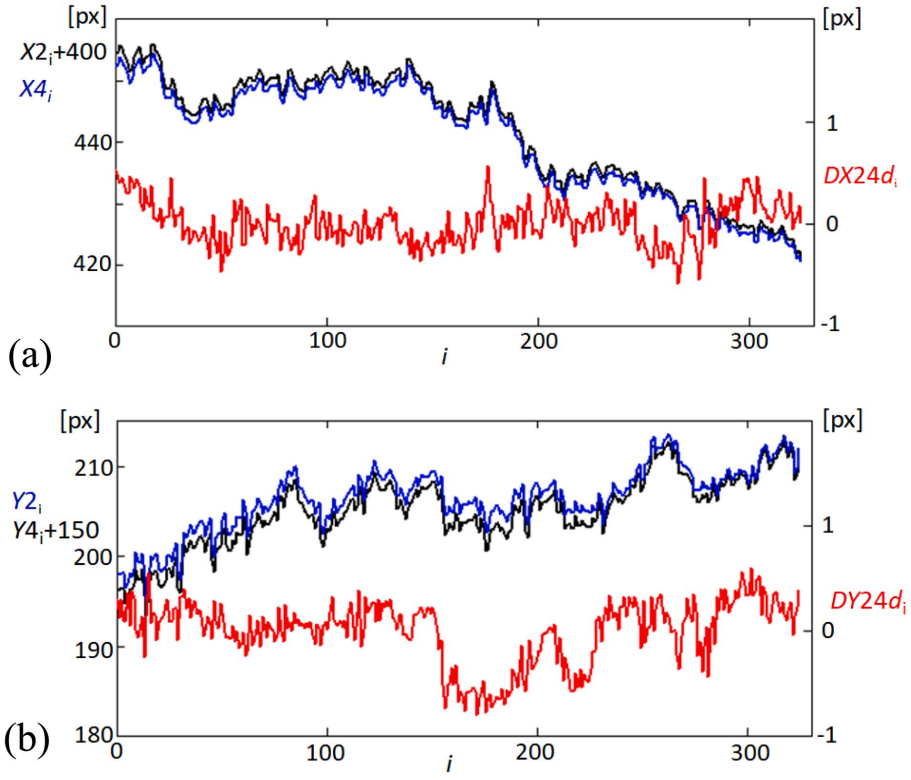

FIGURE 5
Temporal variability in corneal coordinates and their differences. **(A)** Graph showing the variability in the *X*-coordinates of points 2 (X2, black line) and 4 (X4, blue line) on the cornea, offset by adding 400 pixels to X2 for visualization clarity. The red line (DX24d) illustrates the difference between these coordinates, linearly detrended to highlight relative movements. **(B)** Corresponding graph for *Y*-coordinates, showing Y2 (blue line) and Y4 (black line), offset by adding 150 pixels to Y4. The red line (DY24d) depicts the detrended difference between these coordinates, emphasizing the variability over time.

predominant direction in the fixational movements recorded. The movements appear isotropic, indicating that the eye may drift or make microsaccades in virtually any direction with similar likelihood. Figure 12B presents these data in a polar plot, which visually emphasizes the lack of a clear directional bias in these movements. The radial dispersion of points shows that while certain angles may have slightly higher occurrences, there is no significant concentration in any particular direction. This isotropic distribution is critical as it suggests that fixational eye movements, while seemingly random, provide the necessary minute adjustments for continuous visual perception and stabilization of the visual field. Understanding these patterns is essential for interpreting how the visual system maintains image stability despite constant small-scale movements. The lack of a predominant orientation further supports theories that fixational eye movements are adaptive responses to maintain retinal image variability, which is crucial for preventing sensory adaptation and enhancing perceptual sensitivity.

Figure 13 offers a detailed view of the temporal dynamics between ocular orientation and cardiovascular activity, specifically through the analysis of the orientation angle α at point 4 (α4) and its relationship with the blood pulsation signal (dPu). The angle α4 was processed through linear detrending to normalize its range between −180 and 180 degrees, facilitating a direct comparison with the rhythmic blood pulsation signals. The black line representing α4 in the figure illustrates the angle's fluctuation over time, while the red line (dPu) indicates the derivative of the blood pulsation, capturing the instantaneous rate of change in blood flow. Observing these two signals together, the graph reveals periods where the variability in the angle and the pulsation signal appears synchronized, suggesting a potential interaction between ocular orientation dynamics and systemic blood flow. This synchronous behavior highlighted in the graph could reflect physiological interactions where vascular activities might influence or be reflected in the orientation dynamics of the eye.

Figure 14 provides a spectral analysis of the coherence between different ocular and physiological parameters, revealing surprising correlations that underscore the complex interplay within the visual system. The coherence functions measure the degree of linear correlation between two signals at each frequency, and significant coherence suggests a possible physiological linkage or synchronized behavior between the variables being analyzed. The black line in the graph represents the coherence between the orientation angle α4 and the blood pulsation signal dPu, indicating periods of high correlation that could reflect the influence of cardiovascular dynamics on ocular orientation. Similarly, the red line illustrates the coherence between the lengths of movements dXY4 and the blood pulsation dPu, showing how the dynamics of eye movements are potentially synchronized with pulsatile blood flow changes. Most intriguingly, the blue line depicts the coherence between the orientation angle α4 and the variability of the quadrangle area dSC, suggesting that the orientation of eye movements may be related to broader changes in the corneal

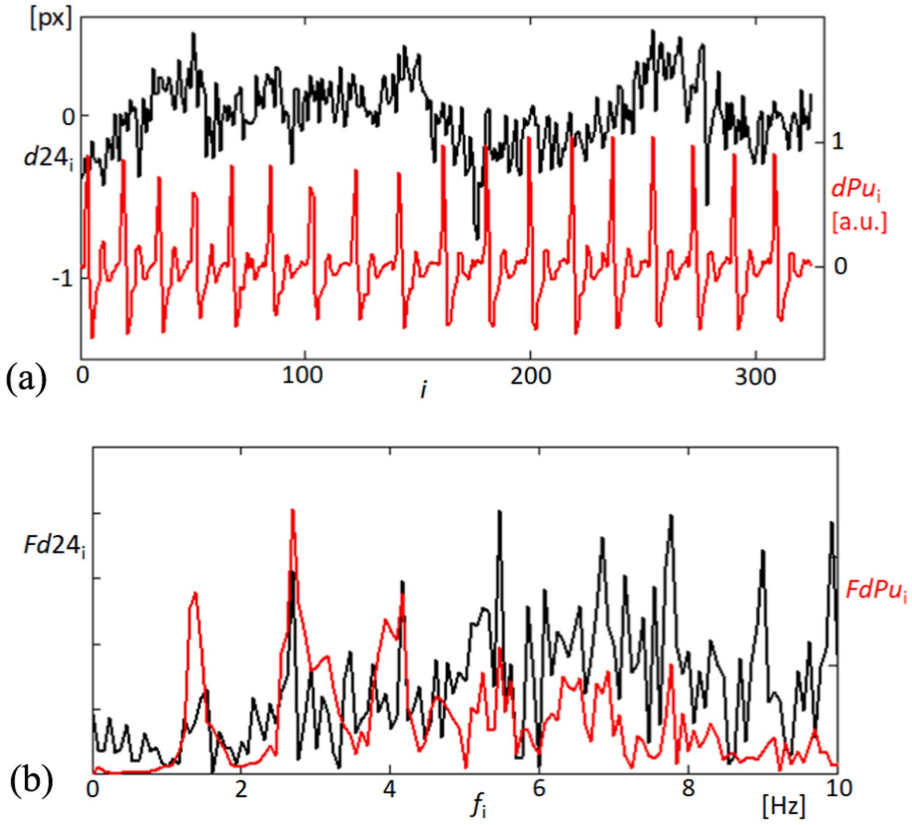

FIGURE 6
Temporal and frequency analysis of corneal displacement and blood pulsation signals. **(A)** The top panel illustrates the variability in the linearly detrended distance between points 2 and 4 on the cornea (d24, black line), alongside the derivative of the blood pulsation signal (dPu, red line), showcasing dynamic physiological interactions. **(B)** The bottom panel displays the Fourier spectra of both d24 (black line) and dPu (red line), revealing the frequency components up to 10 Hz.

surface shape or tension, possibly driven by underlying physiological processes. These coherence results are significant as they provide a window into the multifaceted relationships that govern eye movements and their synchronization with physiological responses. Such findings could have implications for understanding how various factors, from blood flow to corneal biomechanics, interact to influence ocular stability and visual processing.

Figure 15 offers a detailed exploration of the dynamic interactions between physiological signals and corneal surface behavior through time-frequency analysis. This approach enables us to observe fluctuations over time and how these variations are distributed across different frequency ranges. In Figure 15A, we focus on the derivative of the blood pulsation signal (dPu), illustrating how its intensity and frequency vary throughout the recorded sequence. The color gradients reflect consistent rhythmic components, which are particularly prominent in the lower frequency ranges. Figure 15B presents the variability of the quadrangle area (dSC), representing changes in the corneal surface. Both signals exhibit rhythmic components within the 2–6 Hz range, suggesting the presence of periodic behavior. While there is not a precise alignment in waveform patterns, the shared frequency range highlights similar rhythmic elements, contributing to our analysis of temporal patterns.

The similarity in these temporal frequency patterns between dPu and dSC aligns with the findings from our coherence analysis shown in Figure 8, which indicates consistent rhythmic elements within the 2–6 Hz range. This supports the hypothesis that cardiovascular dynamics may influence, or be reflected in, the biomechanical properties of the cornea.

Due to the constraints on the length of the article, the pertinent results regarding one measurement of the second subject, MI, have been included in Appendix 1 for detailed review. These results have been presented in a manner consistent with the format adopted in Figures 5–15, thereby maintaining continuity and ease of understanding. The recorded video sequence comprised 336 frames and spanned 13.44 s. Nearly all figures exhibit similar dependencies and correlations. However, the final two graphs in Supplementary Figures S10, S11 present some distinct dependencies. In place of a single coherence function between dXY4 – dPu, as shown in Figure 14, there is one coherence function between α4 – dXY4 in Supplementary Figure S10. Supplementary Figure S11B presents the time-frequency analysis of the orientation angle α, whereas Figure 15B displays the variability of the quadrangle area dSC.

4 Discussion

Our research aimed to investigate the corneal shape deformations that are correlated with quasi-periodic expansions of the ocular surface and displacements of the corneal apex, which are linked to heart activity. Previous studies (27, 40) have successfully observed and

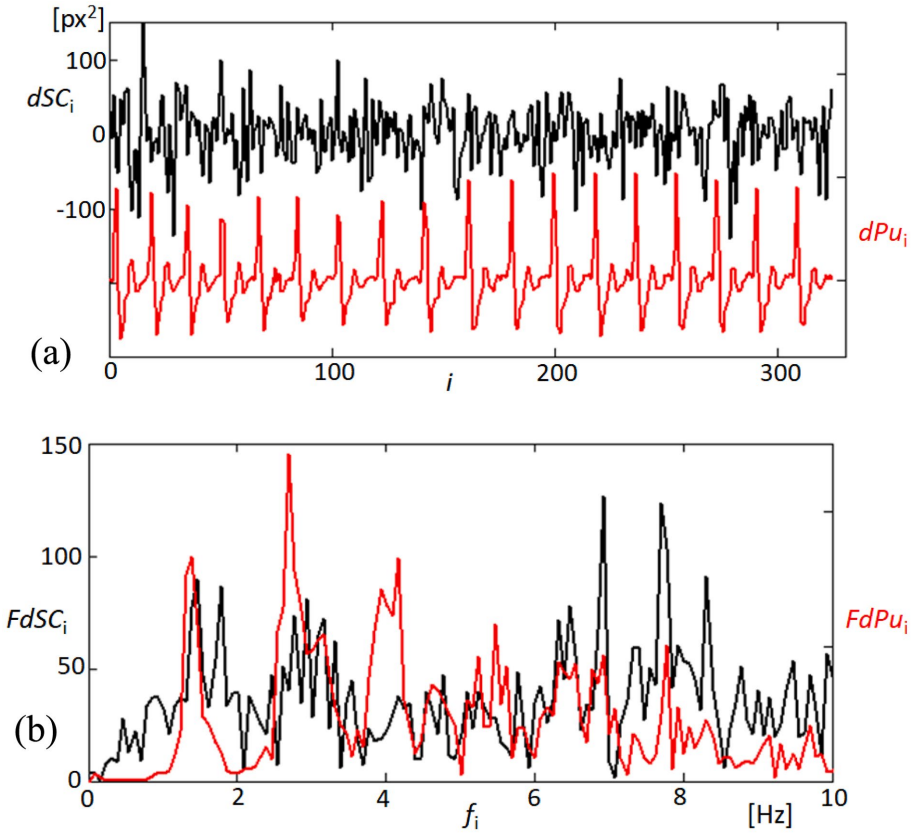

FIGURE 7
Analysis of quadrangle area dynamics and corresponding blood pulsation. **(A)** The top panel depicts changes in the quadrangle area (dSC, black line) formed by points 1, 2, 5, and 4 on the cornea, showing the linearly detrended variability in response to blood pulsation (dPu, red line). This graph reflects the corneal surface's responsiveness to fluctuations in blood flow. **(B)** The bottom panel presents the Fourier spectra of both dSC (black line) and dPu (red line), illustrating the frequency components up to 10 Hz.

examined the axial displacements of the corneal apex and corneal surface deformations. However, these measurements primarily focused on linear displacements of different points on the cornea or sclera, typically measured in micrometers. It is important to note that corneal deformations should also manifest as changes in the distribution of corneal curvature. Therefore, it would be expected to observe these effects in a fine variation of size in videokeratoscopic images obtained from video sequences. However, previous examinations and analyses of such video sequences using videokeratometers did not yield clear results. One of the limitations was the small aperture of the camera lenses used in videokeratometers, which restricted the resolution and accuracy of the captured images. To overcome this limitation, the authors made the decision to employ a camera with a significantly higher aperture and perform a numerical analysis of the reflected corneal images with subpixel accuracy.

The analysis of the obtained results reveals specific variations in lengths such as d24 (distance between points 2 and 4) and d15 (distance between points 1 and 5, not included in the results section) and the area of quadrangle SC. These variations exhibit spectral correlations with the blood pulsation, as demonstrated by the coherence functions presented in Figure 8 and Supplementary Figure S4. The observed correlations suggest corresponding variations in corneal curvature, which also display a correlation with blood pulsation. The coherence analysis highlights strong correlations between specific frequency bands and physiological signals, particularly in the 1–3 Hz and 3–6 Hz ranges. The lower band (1–3 Hz) aligns with heart rate frequencies, reflecting the influence of pulsatile ocular blood flow (POBF) on corneal deformation. POBF, driven by the cardiac cycle, induces rhythmic intraocular pressure fluctuations, subtly impacting corneal shape. Meanwhile, the 3–6 Hz band likely reflects both cardiovascular-related microfluctuations and minor fixational eye movements, such as microsaccades, which influence corneal surface dynamics. This alignment supports the notion that cardiovascular rhythms and eye movement dynamics contribute meaningfully to corneal deformations within these frequency ranges, reinforcing our findings on the spectral coupling between the cornea and blood pulsation (27, 41, 42). Figure 15 illustrates that the time-frequency spectrum of dSC (variation in the distance of quadrangle SC) and the blood pulsation variations dPu exhibit similarities at frequencies around 5–8 Hz. Additionally, for other measurements, these similarities are observed at higher frequencies ranging from approximately 4–9 Hz, with varying magnitudes. This indicates that the variations in corneal curvature are spectrally correlated with blood pulsation. However, it is important to note that the accuracy of these measurements is lower than the accuracies achieved in papers (16, 43) where ultrasound heads measured displacements of the cornea and sclera. Variations in individual points' *X* and *Y* positions, specifically points 2 and 4, are

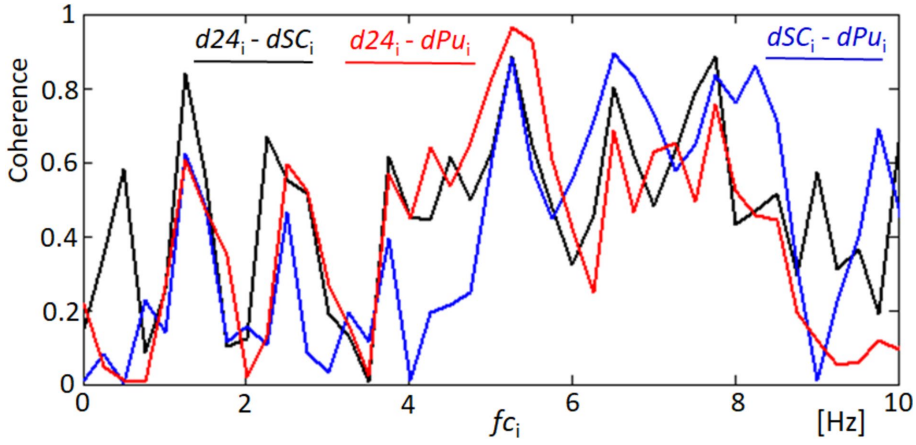

FIGURE 8
Coherence analysis between corneal and cardiovascular dynamics. This figure shows the coherence functions for three pairs of signals: d24 and dSC (black line), d24 and dPu (red line), and dSC and dPu (blue line). Significant coherence peaks are observed at key frequencies indicating synchronized responses that may correspond to blood harmonics.

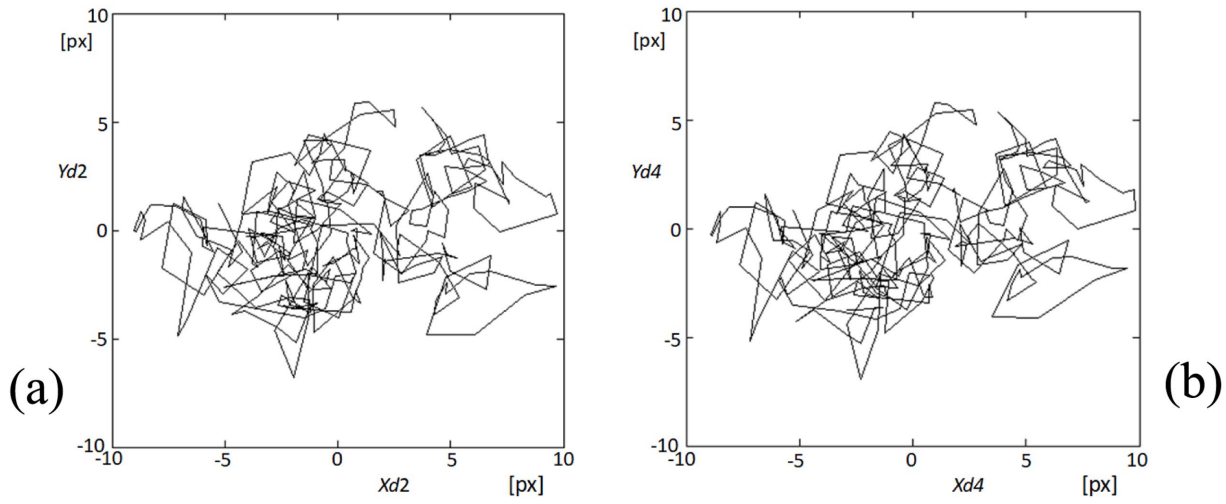

FIGURE 9
Visualization of fixational eye movements at points 2 and 4. **(A)** The plot shows the trajectories of fixational eye movements at point 2 (Xd2, Yd2) on the cornea, depicting complex movement patterns within the recorded video sequence. **(B)** Similarly, this plot displays the movement trajectories at point 4 (Xd4, Yd4), illustrating similar complex patterns to those observed at point 2, but with distinct, slight variations in trajectory dynamics.

several times larger than in their mutual distance variations, d24. These relatively great variations of all five points' *X*- and *Y*-coordinates represent FEM. The measurements of the five reflection points consistently exhibit very similar variations, as depicted in Figure 9 and Supplementary Figure S5. The presence of such similarities motivated us to conduct a thorough analysis of the selected properties of these variations and their potential correlations with blood pulsation, which is a reflection of heart activity. However, while these findings are crucial, it's essential to consider other factors that might influence them. While our study provides novel insights into the relationship between FEM, corneal deformations, and heart activity, it's worth noting the potential influence of head movements on FEM measurements. Although head movements were not independently measured in our study, their potential interference, especially during rapid movements, cannot be ignored. Future studies aiming for a more comprehensive understanding might benefit from integrated measurements that account for both FEM and fine head movements.

The interesting findings of our study include the quasiperiodic characteristics of the FEM speeds, representing the displacements of analyzed points between separate frames (within 40 ms), as demonstrated in Figure 11 and Supplementary Figure S7. Moreover, a notable high spectral correlation was observed between these FEM speeds and the blood pulsation, illustrated by the coherence function between dXY4 and dPu in Figure 14. In Figure 14, the coherence analysis reveals that the highest coherence values occur at approximately 1.3 Hz and 2.6 Hz (blue graph). These frequencies correspond to the blood pulsation's first and second harmonics. Similarly, for the second subject (Appendix 1), the highest coherence values between the same signals appear at approximately 2 and 4 Hz, which are also the first and the second harmonics of the blood pulsation, as evident in Supplementary Figure S2.

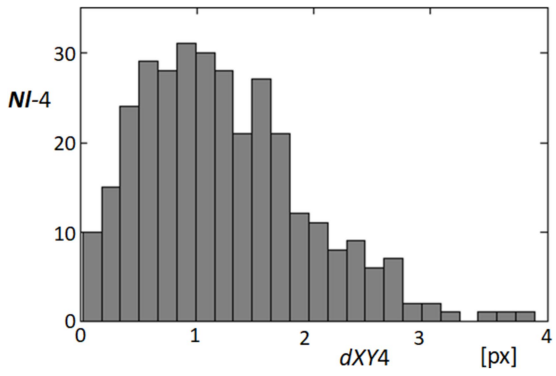

FIGURE 10
Histogram of fixational movement speeds at point 4. This histogram represents the distribution of speeds (measured in pixels per frame) for fixational movements at point 4, calculated from the distances moved from one frame to the next across the video sequence. The *x*-axis represents the speed in pixels per frame (dXY4), and the *y*-axis shows the frequency of these speeds occurring within the dataset.

The results obtained in our study can be treated as an extension or generalization of the findings presented by Peng et al. (29). Specifically, our results demonstrate the spectral coupling between the FEM and the blood pulsation (heartbeat). Notably, this coupling takes into account Heart Rate Variability (HRV), as indicated by the high coherence values observed between dXY4 and Pu (blood pulsation) across a relatively wide range of frequencies, as depicted in Figure 14.

Figure 12 indicates that the orientations of the FEM (regardless of their speeds) are relatively independent of specific directions. In contrast, in Supplementary Figure S8, the orientations are clearly defined, with approximately 60- and 220-degree angles. However, experimental observations have shown that such distinct orientations of FEM movements can vary for the same subject. In cases where a measured subject exhibits a consistent orientation across multiple measurements, the specific directions tend to be relatively similar. The most unexpected results pertained to the temporal variations of movement orientations, specifically the angle αk, where k represents the image point number. The variations in α4 orientations, as illustrated in Figure 13 and Supplementary Figure S9, exhibit a distinct quasi-periodic character. Further analysis revealed their relatively strong spectral correlations, including the Fourier spectrum (not shown in the paper) and coherence functions with the blood pulsation and movement speeds (Figure 14 and Supplementary Figure S10). Notably, most investigations regarding FEM properties have focused on their relationships with visual processes and their role in foveal perception (32, 44, 45). However, our research brings novel insights by highlighting the intriguing temporal variations and spectral correlations associated with movement orientations, expanding the understanding of FEM dynamics beyond their visual implications. The remarkable resemblance observed between the values and variations of the second, third, and partially fourth harmonics of the blood pulsation (heart activity) and the α4 angles, as illustrated in Supplementary Figure S11, indicates a strong spectral correlation between these variables. Notably, the distinct waving effect of these three harmonics, with a period of approximately 3.5 s (i @ 90 frames), is likely associated with the subject's breathing pattern.

One limitation of this study is the relatively small sample size of eight subjects. To ensure statistical robustness, we conducted a preliminary power analysis using G*Power software. This analysis, based on an anticipated effect size of $d = 0.5$, an alpha level of 0.05, and a power of 0.80, confirmed that eight subjects would provide a statistical power of 82% to detect significant effects, particularly in identifying changes in corneal deformations linked to cardiovascular dynamics. This approach aligns with similar exploratory studies (21, 38), which have also utilized small cohorts to investigate complex physiological interactions. While the high-resolution data collected enabled detailed analyses, larger studies are necessary to enhance the generalizability and validation of our findings. Another potential limitation of our study is the influence of confounding factors such as corneal surface roughness and tear film dynamics on the measurement of corneal deformations. Variations in the corneal surface or instability of the tear film could potentially affect the reflections of the LEDs and, consequently, the accuracy of our measurements. We mitigated these factors by implementing stringent participant selection criteria to exclude individuals with known corneal abnormalities or dry eye symptoms. Additionally, we standardized the measurement protocol by instructing participants to blink immediately before data acquisition and limiting measurement durations to approximately 10 s to minimize tear film evaporation. Measurements affected by blinking were repeated to ensure consistency and data integrity. We assessed equipment variability through repeated measurements under identical conditions, demonstrating that the observed fluctuations in corneal reflections were significantly greater than the system's inherent variability. Moreover, the study lacks a calibration procedure to convert pixel measurements into physical distances. While the consistent experimental conditions and equipment settings allowed us to compare relative changes across participants effectively, we recognize that quantifying these changes in physical units would enhance the scientific significance of the results. Without calibration, it's difficult to determine the exact magnitude of corneal deformations and assess their clinical relevance. In future studies, we plan to incorporate a detailed calibration process using a micrometric calibration grid or a model eye. This will allow us to establish the precise conversion factor between pixels and micrometers, enabling a more accurate interpretation of the corneal deformations and their physiological implications. By converting the measurements into physical units, we will be able to compare our findings with established biomechanical properties of the cornea and better understand the potential impact of these deformations on ocular health and function. This enhancement will also facilitate the comparison of our results with other studies and contribute to the advancement of knowledge in the field of corneal biomechanics.

Future advancements in imaging technology could allow for more precise three-dimensional assessments of the cornea. Techniques such as advanced corneal topography and three-dimensional biomechanical modeling could revolutionize our understanding of the corneal response to physiological stimuli, providing a more detailed exploration of its biomechanical properties.

The use of a standardized headrest significantly reduced the impact of head movements on our measurements, but achieving perfect immobilization remains challenging. Future research could focus on integrating real-time motion correction technologies or more sophisticated head stabilization systems that adapt to and compensate for subtle movements. Employing advanced data analysis techniques to account for movement artifacts could further enhance the accuracy and reliability of corneal movement measurements.

The temporal orientations of head movements and fixational eye movements (FEM) differ significantly due to the substantial

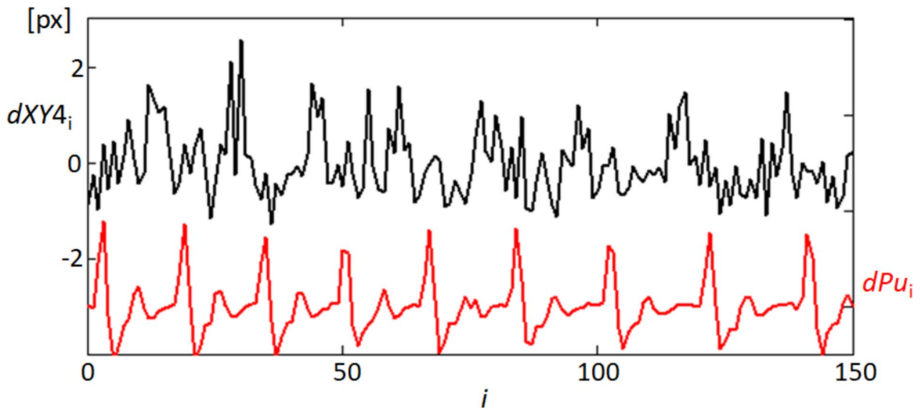

FIGURE 11
Temporal correlation of fixational eye movements and blood pulsation. This graph shows the temporal variability of movement lengths dXY4 (black line), representing the speeds of fixational eye movements at point 4, and the blood pulsation signal dPu (red line). Only the first half of the recording sequence is displayed to enhance clarity.

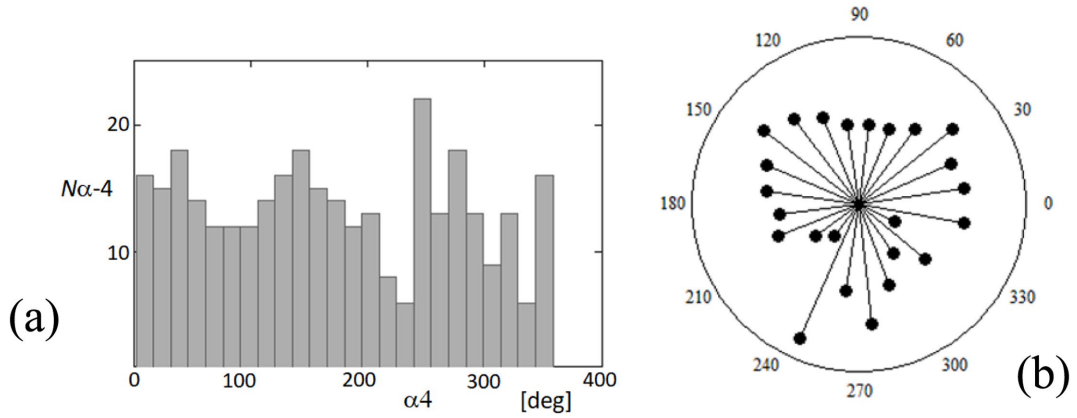

FIGURE 12
Distribution of orientation angles for fixational eye movements at point 4. **(A)** The histogram on the rectangular plot shows the distribution of orientation angles (α4) of fixational eye movements at point 4 over a complete 360-degree cycle. **(B)** The polar plot illustrates the same data, providing a visual representation of the directionality of these movements. Each point represents the frequency of movements at specific angles.

difference in mass between the head and the eye, with FEM being faster and more complex. The influence of fast head movements on FEM remains an open question, as the effect of head movements is often overlooked and not measured in many FEM experiments. However, it is essential to recognize that head movements can significantly impact results and their interpretation. Fine measurements of head movements, including rotations and displacements, pose significant challenges. Achieving the desired accuracy in capturing head movements is crucial for high precision in FEM analysis. One approach is to mount a device on the head to record FEM and minimize head movements. However, this method has limitations, as contact with the head skin introduces potential confounding factors like blood pulsation, which can cause deviations from actual head movements. Developing techniques that accurately measure fine head movements without interference from external factors, such as blood pulsation, is crucial for ensuring the integrity and validity of FEM studies, ultimately enhancing our understanding of the relationship between head movements and FEM dynamics.

To our knowledge, the literature lacks previous presentations of similar findings. While Ohl et al.'s study demonstrates intriguing results primarily focused on microsaccades, it does not consider the influence of heart rate variability (HRV). This raises compelling questions about the potential impact or interdependence of the examined effects and observed correlations on visual processes. These influences could be associated with factors such as visibility during fixation or dynamic image quality, specifically on the fovea. Further research into adaptive optics effects, known to enhance image quality, and their relationship with fine and fast eye and head movements would be extremely interesting.

While our current study is observational and demonstrates significant correlations between cardiovascular activity and corneal biomechanics, we recognize the importance of establishing causality to fully understand the underlying mechanisms. Future research will focus on experimental designs that allow for controlled manipulation of cardiovascular parameters and the use of sophisticated analytical methods to analyze the resulting data. Moreover, we acknowledge that respiratory patterns could influence corneal dynamics and that simultaneous recording of breathing could provide valuable insights

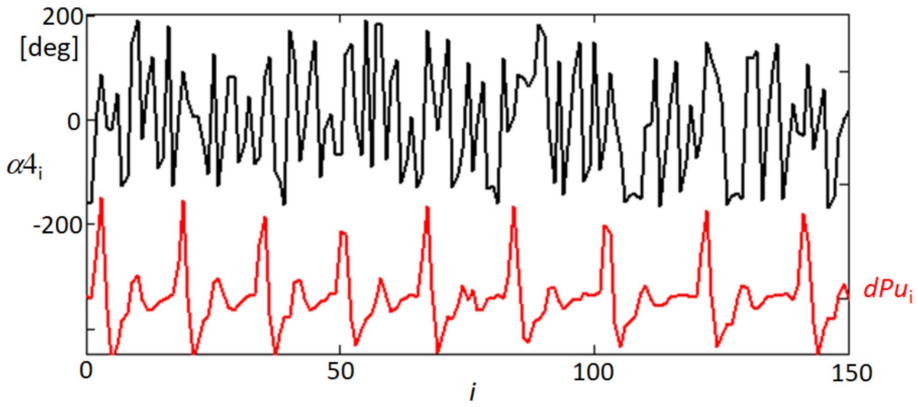

FIGURE 13
Temporal variability of orientation angle α4 and blood pulsation signal dPu. This graph displays the linearly detrended time variability of the orientation angle α of point 4 (α4, black line) alongside the derivative of the blood pulsation signal (dPu, red line) for approximately half of the recorded sequence. The detrending process adjusts α4 within a range of −180 to 180 degrees.

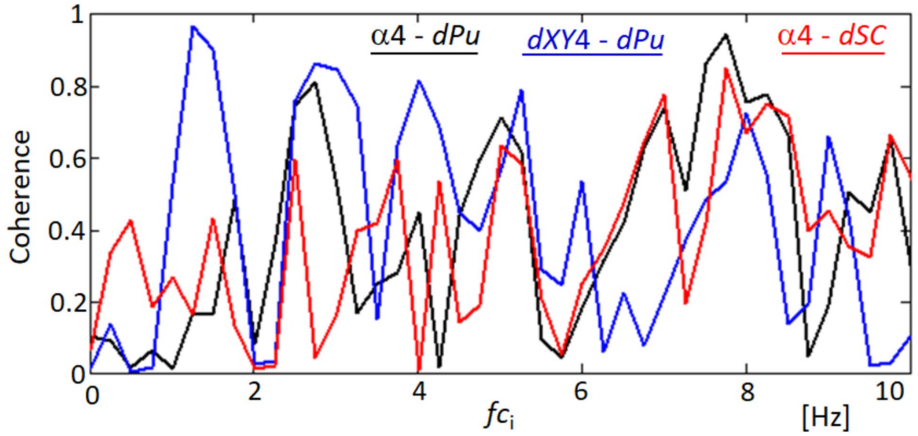

FIGURE 14
Coherence functions demonstrating correlations among ocular movement parameters. This figure shows the coherence functions between various parameters: orientation angle α4 and blood pulsation signal dPu (black line), lengths of movements dXY4 and blood pulsation dPu (blue line), and orientation angle α4 and the variability of the quadrangle area dSC (red line).

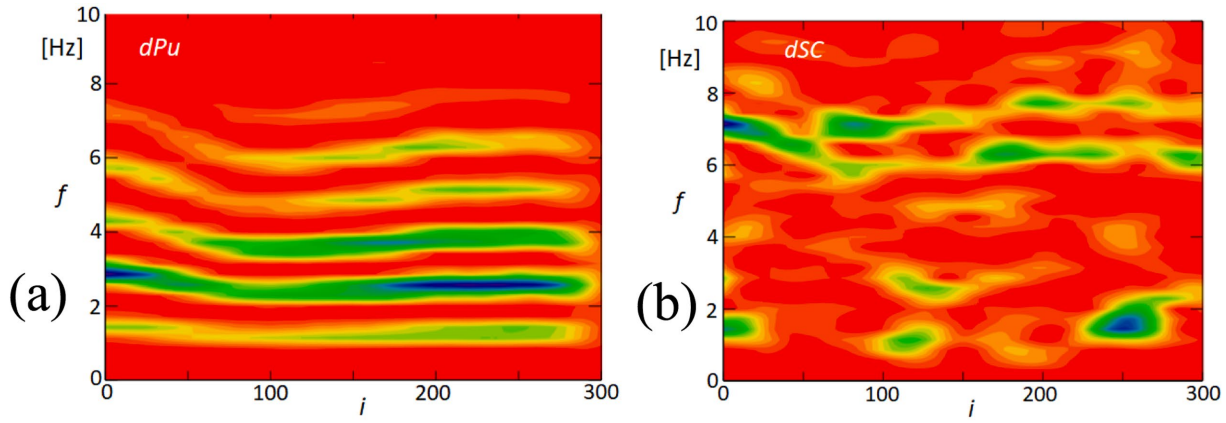

FIGURE 15
Time-frequency analysis of blood pulsation and quadrangle area variability. **(A)** This panel displays the time-frequency analysis of the blood pulsation derivative (dPu), highlighting the spectral components over time. **(B)** This panel shows the time-frequency analysis of the variability of the quadrangle area (dSC), illustrating how this parameter fluctuates across different frequencies. The color scale represents the amplitude of the signal, with red indicating high amplitude and blue indicating low amplitude.

into this relationship. While our primary focus in this study was on cardiovascular-induced corneal deformations, future research will incorporate respiratory monitoring to explore its potential impact on the corneal surface. In addition to our core findings, it is essential to consider the broader physiological interactions that may influence our results. Specifically, fluctuations in cardiac activity are known to impact intraocular pressure (IOP), which can subsequently alter corneal deformation. Variations in blood flow and heart rate have been hypothesized to lead to corresponding changes in IOP, potentially affecting the biomechanical behavior of the cornea (34). These dynamics are crucial for understanding ocular biomechanics, particularly how health impacts eye function. Future studies should aim to integrate more comprehensive physiological monitoring to quantify these interactions more effectively, employing technologies that can simultaneously track cardiovascular dynamics and ocular biomechanical responses.

5 Conclusion

Our study provides compelling evidence of the complex interplay between corneal deformations, fixational eye movements, and cardiovascular activity. Through detailed biomechanical analyses, we demonstrated that variations in corneal curvature, particularly observed through distances such as d24 and d15, are significantly correlated with pulsatile ocular blood flow. These findings not only enhance our understanding of ocular biomechanics under cardiovascular influences but also offer potential avenues for developing non-invasive diagnostic methods that could leverage these dynamics.

Moreover, our research has opened pathways for exploring how these biomechanical insights could be applied in clinical settings, particularly in diagnosing and monitoring conditions that affect both ocular and cardiovascular systems. However, while promising, our conclusions are tempered by the recognition that our study's limited sample size may constrain the generalizability of these findings. Therefore, future research with larger cohorts is crucial to validate and potentially expand upon our conclusions.

Finally, the potential influence of head movements on FEM measurements, while not directly measured in this study, highlights an area for further research. Addressing this challenge is essential for refining the accuracy of our biomechanical models and enhancing the applicability of our findings in real-world clinical and diagnostic settings.

Data availability statement

The original contributions presented in the study are included in the article/Supplementary material, further inquiries can be directed to the corresponding author.

Ethics statement

The studies involving humans were approved by the Ethics Committee of the Wroclaw University of Science and Technology (O-22-30). The studies were conducted in accordance with the local legislation and institutional requirements. The participants provided their written informed consent to participate in this study.

Author contributions

MS: Writing – review & editing, Writing – original draft, Visualization, Validation, Software, Resources, Methodology, Investigation, Formal analysis. HK: Writing – review & editing, Supervision, Software, Resources, Methodology, Investigation, Formal analysis, Conceptualization. MA: Writing – review & editing, Validation, Supervision, Methodology, Funding acquisition, Formal analysis, Data curation.

Funding

The author(s) declare that financial support was received for the research, authorship, and/or publication of this article. This work was supported by the Horizon Europe Marie Sklodowska-Curie ITN-ETN Action, under the OBERON project (grant number 956720).

Acknowledgments

The authors acknowledge the use of ChatGPT-4, a generative AI tool developed by OpenAI, for paraphrasing and grammar checking during the preparation of this manuscript. All final edits and approvals were made by the authors to ensure the accuracy and integrity of the content.

Conflict of interest

The authors declare that the research was conducted in the absence of any commercial or financial relationships that could be construed as a potential conflict of interest.

Publisher's note

Supplementary material

The Supplementary material for this article can be found online at: https://www.frontiersin.org/articles/10.3389/fmed.2024.1484449/full#supplementary-material

References

1. Sridhar MS. Anatomy of cornea and ocular surface. *Indian J Ophthalmol*. (2018) 66:190–4. doi: 10.4103/ijo.IJO_646_17

2. Esporcatte LP, Salomão MQ, Lopes BT, Vinciguerra P, Vinciguerra R, Roberts C, et al. Biomechanical diagnostics of the cornea. *Eye Vision*. (2020) 7:9–2. doi: 10.1186/s40662-020-0174-x

3. Blackburn BJ, Jenkins MW, Rollins AM, Dupps WJ. A review of structural and biomechanical changes in the cornea in aging, disease, and photochemical crosslinking. *Front Bioeng Biotechnol*. (2019) 7:66. doi: 10.3389/fbioe.2019.00066

4. Luce DA. Determining in vivo biomechanical properties of the cornea with an ocular response analyzer. *J Cataract Refract Surg*. (2005) 31:156–62. doi: 10.1016/j.jcrs.2004.10.044

5. Izquierdo L, Henriquez M, Mannis MJ. Keratoconus Diagnosis and Management. Elsevier - Health Sciences Division. (2022). 51–63.

6. Nambiar MH, Liechti L, Müller F, Bernau W, Studer H, Roy AS, et al. Orientation and depth-dependent mechanical properties of the porcine cornea: experiments and parameter identification. *Exp Eye Res*. (2022) 224:1092. doi: 10.1016/j.exer.2022.109266

7. Wang B, Yang L, Cheng J, Wang J, Mei Y. In-vivo high-speed biomechanical imaging of the cornea using Corvis ST and digital image correlation. *Comput Biol Med*. (2023) 153:106540. doi: 10.1016/j.compbiomed.2023.106540

8. Shahiri M, Jóźwik A, Asejczyk M. Opto-mechanical self-adjustment model of the human eye. *Biomed Opt Express*. (2023) 14:1923–44. doi: 10.1364/BOE.484824

9. Mahanama B, Jayawardana Y, Rengarajan S, Jayawardena G, Chukoskie L, Snider J, et al. Eye movement and pupil measures: a review. *Front Comput Sci*. (2022) 3:733531. doi: 10.3389/fcomp.2021.733531

10. Kiely PM, Carney LG, Smith G. Diurnal variations of corneal topography and thickness. *Am J Optom Physiol Optic*. (1982) 59:976–82. doi: 10.1097/00006324-198212000-00007

11. Kiel JW. The Ocular Circulation. San Rafael (CA): Morgan & Claypool Life Sciences. Integrated Systems Physiology: From Molecule to Function to Disease. (2010) doi: 10.4199/C00024ED1V01Y201012ISP012,

12. Mansouri K, Shaarawy T. Continuous intraocular pressure monitoring with a wireless ocular telemetry sensor: initial clinical experience in patients with open angle glaucoma. *Br J Ophthalmol*. (2011) 95:627–9. doi: 10.1136/bjo.2010.192922

13. Vellara HR, Patel DV. Biomechanical properties of the keratoconic cornea: a review. *Clin Exp Optom*. (2015) 98:31–8. doi: 10.1111/cxo.12211

14. Bao F, Chen W, Wang Y, Elsheikh A. How can corneal biomechanics help with clinical applications? *Front Bioeng Biotechnol*. (2023) 11:1184840. doi: 10.3389/fbioe.2023.1184840

15. Wang J, Liu X, Bao F, Lopes BT, Wang L, Eliasy A, et al. Review of ex-vivo characterisation of corneal biomechanics. *Med Novel Technol Dev*. (2021) 11:100074. doi: 10.1016/j.medntd.2021.100074

16. Kwon TH, Ghaboussi J, Pecknold DA, Hashash YMA. Effect of cornea material stiffness on measured intraocular pressure. *J Biomech*. (2008) 41:1707–13. doi: 10.1016/j.jbiomech.2008.03.004

17. Piñero DP, Alcón N. In vivo characterization of corneal biomechanics. *J Cataract Refract Surg*. (2014) 40:870–87. doi: 10.1016/j.jcrs.2014.03.021

18. Danielewska ME, Iskander DR, Kowalska M, Kasprzak HT. Phase dependencies between longitudinal corneal apex displacement and cardiovascular signals: is the ocular pulse influenced by the electrical activity of the heart? *Clin Exp Optom*. (2012) 95:631–7. doi: 10.1111/j.1444-0938.2012.00775.x

19. Gatzioufas Z, Seitz B. Determination of corneal biomechanical propertiesin vivo: a review. *Mater Sci Technol*. (2015) 31:188–96. doi: 10.1179/1743284714Y.0000000612

20. Hamilton KE, Pye DC. Young's modulus in normal corneas and the effect on applanation tonometry. *Optom Vis Sci*. (2008) 85:445–50. doi: 10.1097/OPX.0b013e3181783a70

21. Liu J, Roberts C. J. Influence of corneal biomechanical properties on intraocular pressure measurement: Quantitative analysis. *J Catar Refrac Surgery*. (2005) 31:146–155. doi: 10.1016/j.jcrs.2004.09.031

22. Roberts C. The cornea is not a piece of plastic. *J Refract Surg*. (2000) 16:407–13. doi: 10.3928/1081-597X-20000701-03

23. Iskander RD, Kasprzak HT. Dynamics in longitudinal eye movements and corneal shape. *Ophthalmic Physiol Opt*. (2006) 26:572–9. doi: 10.1111/j.1475-1313.2006.00415.x

24. Szmigiel MA, Kasprzak H, Klysik A. Dependences between kinetics of the human eye pupil and blood pulsation In: Applications of digital image processing XXXIX, SPIE Proceedings Series, International Society for Optics and Photonics, San Diego, USA. (2016). 9971, 1–9.

25. Kowalska M, Mas D, Kasprzak H. Analysis of keratoscopic images for detecting fixational eye movements and ocular surface deformation. In: Videometrics, Range Imaging, and Applications X, SPIE Proceedings, art. 74470N. SPIE - The International Society for Optics and Photonics, Bellingham, WA, USA. 7447.

26. Ohl S, Wohltat C, Kliegl R, Pollatos O, Engbert R. Microsaccades are coupled to heartbeat. *J Neurosci*. (2016) 36:1237–41. doi: 10.1523/JNEUROSCI.2211-15.2016

27. Hoogerbrugge AJ, Strauch C, Oláh ZA, Dalmaijer ES, Nijboer TC, Van der Stigchel S. Seeing the Forrest through the trees: oculomotor metrics are linked to heart rate. *PLoS One*. (2022) 17:e0272349. doi: 10.1371/journal.pone.0272349

28. Iskander DR, Collins MJ. Applications of high-speed videokeratoscopy. *Clin Exp Optom*. (2005) 88:223–31. doi: 10.1111/j.1444-0938.2005.tb06700.x

29. Peng GC, Hain TC, Peterson BW. Predicting vestibular, proprioceptive, and biomechanical control strategies in normal and pathological head movements. *IEEE Trans Biomed Eng*. (1999) 46:1269–80. doi: 10.1109/10.797986

30. Holmqvist K, Örbom SL, Zemblys R. Small head movements increase and colour noise in data from five video-based P–CR eye trackers. *Behav Res Methods*. (2022) 54:845–63. doi: 10.3758/s13428-021-01648-9

31. Kasprzak HT, Iskander DR. Ultrasonic measurement of fine head movements in a standard ophthalmic headrest. *IEEE Trans Instrum Meas*. (2010) 59:164–70. doi: 10.1109/TIM.2009.2022431

32. Antończyk A, Kubiak Nowak D, Borawski W, Kiełbowicz Z, Danielewska ME. The effect of changes in cardiovascular activity on corneal biomechanics and pulsation in rabbits. *Sci Rep*. (2020) 10:22249. doi: 10.1038/s41598-020-79219-9

33. Kasprzak HT, Jaronski JW. Measurement of fine dynamic changes of corneal topography by use of interferometry. In Interferometry XI: Applications, SPIE. (2010). 4778, 169–176.

34. Kwok S, Clayson K, Hazen N, Pan X, Ma Y, Hendershot AJ, et al. Heartbeat-induced corneal axial displacement and strain measured by high-frequency ultrasound elastography in human volunteers. *Transl Vis Sci Technol*. (2020) 9:33. doi: 10.1167/tvst.9.13.33

35. Dupps WJ, Wilson SE. Biomechanics and wound healing in the cornea. *Exp Eye Res*. (2006) 83:709–20. doi: 10.1016/j.exer.2006.03.015

36. Kotecha A. What biomechanical properties of the cornea are relevant for the clinician? *Surv Ophthalmol*. (2007) 52:S109–14. doi: 10.1016/j.survophthal.2007.08.004

37. Bendat JS, Piersol AG. Random Data: Analysis and Measurement Procedures (4th ed.). Hoboken, New Jersey, USA: Wiley. (2010).

38. Martinez-Conde S, Macknik SL, Hubel DH. The role of fixational eye movements in visual perception. *Nat Rev Neurosci*. (2004) 5:229–40. doi: 10.1038/nrn1348

39. Rolfs M. Microsaccades: small steps on a long way. *Vis Res*. (2009) 49:2415–41. doi: 10.1016/j.visres.2009.08.010

40. Yang S, Zhang J, Tan Y, Wang Y. Unraveling the mechanobiology of cornea: from bench side to the clinic. *Front Bioeng Biotechnol*. (2022) 10:953590. doi: 10.3389/fbioe.2022.953590

41. Lopes BT, Bao F, Wang J, Liu X, Wang L, Abass A, et al. Review of in-vivo characterisation of corneal biomechanics. *Med Novel Technol Dev*. (2021) 11:100073. doi: 10.1016/j.medntd.2021.100073

42. Engbert R, Kliegl R. Microsaccades uncover the orientation of covert attention. *Vis Res*. (2003) 43:1035–45. doi: 10.1016/S0042-6989(03)00084-1

43. Sun C, Ding N, Zhuang D, Liu X. Eye movement evidence in investigative identification based on experiments. *J Saf Sci Resil*. (2023) 4:316–28. doi: 10.1016/j.jnlssr.2023.07.003

44. Danielewska M, Kasprzak H, Kowalska M. Correlations between longitudinal corneal apex displacement, head movements, and pulsatile blood flow In: XII Mediterranean Conference on Medical and Biological Engineering and Computing 2010. Berlin, Heidelberg: Springer (2010). 128–31.

45. Van Rijn LJ, Van der Steen J, Collewijn H. Instability of ocular torsion during fixation: cyclovergence is more stable than cycloversion. *Vis Res*. (1994) 34:1077–87. doi: 10.1016/0042-6989(94)90011-6

frontiers | Frontiers in Bioengineering and Biotechnology

TYPE Original Research
PUBLISHED 26 February 2025
DOI 10.3389/fbioe.2025.1548539

OPEN ACCESS

EDITED BY
Jos J. Rozema,
University of Antwerp, Belgium

REVIEWED BY
Andrea Montanino,
International Center for Numerical Methods in Engineering, Spain
Ibrahim Seven,
Teclens, United States

*CORRESPONDENCE
Benedetta Fantaci,
bfantaci@unizar.es

RECEIVED 19 December 2024
ACCEPTED 04 February 2025
PUBLISHED 26 February 2025

CITATION
Fantaci B, Rodriguez Matas JF, Squartecchia V, Vavassori L and Calvo B (2025) Unraveling the impact of laser refractive surgery on corneal ectasia: an *in silico* study.
Front. Bioeng. Biotechnol. 13:1548539.
doi: 10.3389/fbioe.2025.1548539

Unraveling the impact of laser refractive surgery on corneal ectasia: an *in silico* study

Benedetta Fantaci[1]*, José Félix Rodriguez Matas[2], Vittoria Squartecchia[2], Lucia Vavassori[2] and Begoña Calvo[1,3]

[1]Aragon Institute of Research Engineering (I3A), Universidad de Zaragoza, Zaragoza, Spain, [2]LaBS, Department of Chemistry, Materials and Chemical Engineering "Giulio Natta", Politecnico di Milano, Milan, Italy, [3]Bioengineering, Biomaterials and Nanomedicine Networking Biomedical Research Centre (CIBER-BBN), Universidad de Zaragoza, Zaragoza, Spain

Introduction: Laser refractive surgeries are a safe option for low-to-moderate refractive corrections, providing excellent visual outcomes. Over the years, various procedures have been introduced into clinical practice, but the most performed today remain Photorefractive Keratectomy (PRK), Laser *In-Situ* Keratomileusis (LASIK), and Small Incision Lenticule Extraction (SMILE). Although laser refractive treatments are considered safe, clinicians have focused on the risk of post-surgical ectasia, a rare but serious complication. Ectasia is characterized by progressive corneal thinning and steepening, leading to vision distortion, irregular astigmatism, and in some cases, a reduction of visual acuity. It is still debated whether laser refractive surgeries can cause ectasia as an iatrogenic condition or merely accelerate the progression of an underlying corneal pathology, not detected during pre-surgical screening. The proposed work investigates the relationship among three laser refractive surgeries (PRK, LASIK and SMILE), currently performed in clinical practice, and ectasia onset and progression by means of an *in silico* analysis.

Methods: An average 3D finite-element corneal model is developed and a pathological area, characterized by reduced stiffness of varying severity grades, is defined to analyze its influence on ectasia development and progression in the pre-surgical state. Three laser treatments (PRK, LASIK and SMILE) are simulated on healthy and pathological models. Pre- and post-surgical conditions are compared to check whether any procedure worsens the pre-surgical pathological state. The optomechanical effect of each procedure on the cornea is analyzed at both healthy and pathological conditions and compared to establish which refractive procedure mostly affects corneal structure.

Results and discussion: While the three refractive procedures showed different behaviors in terms of mechanical changes affecting the cornea, from an optical perspective, as the pathology severity worsened, none of the surgeries caused a worsening in the cone's severity with respect to pre-surgical pathological conditions. This result suggests that surgeries may have a limited role in causing post-surgical ectasia, as it seems more plausible that they accelerate the progression of an underlying pathological condition. Among the three

procedures, PRK was found to be the least invasive treatment from a mechanical perspective, while SMILE showed the greatest impact on the posterior surface, suggesting a potential long-term risk for ectasia progression.

KEYWORDS

corneal biomechanics, laser refractive surgery, PRK, LASIK, SMILE, ectasia, finite element model, *in silico* analysis

1 Introduction

Laser refractive surgeries are a safe and effective option for low-to-moderate refractive corrections, providing excellent visual outcomes and allowing to achieve spectacle independence (Kim et al., 2019). As the outermost layer of the eye, the cornea is responsible for two-thirds of its refractive power and is easily accessible for receiving such treatments. Over the past 40 years, various procedures have been introduced into clinical practice, all based on the same principle: reshaping the anterior surface of the cornea with a laser to correct refractive defects (myopia, astigmatism, or hyperopia) by shifting the focal point onto the retina.

Photorefractive Keratectomy (PRK) was the first procedure to be invented in the 1980s, involving surface ablation of the stroma with an excimer laser after removing the epithelium. After the treatment, the epithelium regenerates over the ablated stroma. PRK is known to preserve corneal biomechanics better than other procedures, as it leaves a higher percentage of residual stromal bed (RSB), which helps support the cornea under the remaining post-surgical loads. However, in this procedure, the Bowman's layer–a thin, non-regenerating layer between the epithelium and stroma that helps maintain corneal shape–is removed during laser ablation. Consequently, the removal of both the epithelium and Bowman's layer triggers a wound healing process that can impact refractive correction and lead to scarring, causing post-surgical discomfort for the patient (Fogla et al., 2020).

Later, in the 1990s Laser *In Situ* Keratomileusis (LASIK) surpassed PRK, establishing itself as the preferred procedure by the surgeons. In LASIK a hinged flap is created with a femto-second laser and lifted, the tissue below is ablated with an excimer laser and the flap is put back in place after the ablation, with no sutures needed. The creation of a flap promotes faster recovery and less discomfort by preserving the epithelium, but results in a lower percentage of RSB, thereby reducing corneal biomechanical strength (Sutton et al., 2014; Kim et al., 2019).

Finally, the most recent procedure to enter the market in the 2000s was Small Incision Lenticule Extraction (SMILE), where a lenticule, tailored for the desired refractive target, is created with the femto-second laser in the corneal stroma and extracted through a small incision. SMILE is a flapless procedure, believed to better preserve corneal structural integrity (Reinstein et al., 2014).

Although laser refractive treatments are generally considered safe with few adverse effects, clinicians and scientists have focused on the risk of post-surgical ectasia, a rare but serious complication (Wolle et al., 2016). The incidence variability of ectasia after LASIK reported in the literature ranges from 0.013% (13 eyes per 100,000) to 0.935% (935 eyes per 100,000), while its occurrence after PRK and SMILE remains poorly understood (Moshirfar et al., 2021). Ectasia is characterized by progressive corneal thinning and steepening, leading to vision distortion, irregular astigmatism, and in some cases, a significant loss of visual acuity. While it can develop within months after surgery, it may also appear years later (Wolle et al., 2016). It usually first manifests in one eye as a bulge in the infero-temporal region of the cornea and later in time in the fellow eye (Santodomingo-Rubido et al., 2022).

The development and progression of ectasia are believed to be closely related to the health of the corneal tissue (Santhiago et al., 2014), particularly the stroma. The stroma is primarily responsible for the cornea's biomechanical response, accounting for 90% of its total thickness. It features a highly organized structure of collagen fibers arranged into fibrils, which are grouped into lamellae and embedded within the extracellular matrix (ECM). The ECM plays an adhesive role, maintaining the lamellae's arrangement. In ectasia, this organization is disrupted due to ECM alterations that reduce matrix stiffness and impair its embedding function, allowing the fibers to move freely and eventually break (Santodomingo-Rubido et al., 2022). As the tissue degrades, the cornea thins and bulges outward under the influence of intraocular pressure (IOP).

Ectasia histopathology has been extensively described in the literature, but its etiology remains a topic of debate, as the exact triggering cause is still unclear. Environmental factors, such as chronic eye rubbing and contact lens wear Ferrari and Rama (2020), may contribute to its progression, although genetic predisposition is considered the primary factor in the disease's genesis Santodomingo-Rubido et al. (2022).

The role of refractive surgeries in triggering ectasia remains unclear. It is still debated whether these procedures cause ectasia as an iatrogenic condition or merely accelerate the progression of an underlying corneal pathology (Moshirfar et al., 2021), not detected during pre-surgical screening. Several risk factors have been identified as potential contributors to the disease and are assessed during pre-surgical evaluation to determine patient eligibility for laser refractive treatment. Pre-existing corneal abnormalities significantly increase the risk of post-surgical ectasia (Martínez-Abad and Piñero, 2017; Santhiago et al., 2016). Even minor geometric irregularities may indicate the presence of an underlying condition. For example, high myopia or astigmatism require more invasive refractive corrections, which can lead to structural instability due to the ablation of a thicker portion of the corneal tissue. Each surgical procedure inevitably weakens corneal biomechanical strength to varying degrees, primarily due to the reduction in corneal thickness. Thin corneas are more prone to post-surgical complications (Santhiago et al., 2014; Wolle et al., 2016). Moreover, depending on the chosen procedure, the reduction in thickness may be greater, as the flap or cap thickness also contributes to a lower percentage of RSB. As a result, surgeons typically avoid performing surgery when the RSB is less than 250 μm (Randleman et al., 2003). In general, preserving the RSB is crucial for maintaining corneal biomechanical strength.

Given the lack of a clear understanding of ectasia development and behavior, various authors have attempted to gain a deeper understanding of the disease using finite element (FE) models. These models are versatile tools that enable the investigation of multiple aspects of the disease, from structural to optomechanical changes, and allow to analyze the influence of different corneal tissue components.

Many studies focused on reproducing the progression of the disease in terms of corneal bulging and thinning, with the aim to better understand the underlying processes that may trigger the development of the pathology (Pandolfi and Manganiello, 2006; Gefen et al., 2009; Falgayrettes et al., 2023). Other authors exploited FE models of ectatic corneas to investigate the optomechanical effect of treatments currently applied in clinics to stop the progression, such as cross-linking (Roy and Dupps, 2011; Roy et al., 2013) or intracorneal segment ring implantation (Flecha-Lescún et al., 2018; Ariza-Gracia et al., 2020). The work by Dupps et al. (Dupps and Seven, 2016) investigated the risk of developing ectasia after LASIK, by proposing strain as a metric for the expression of structural risks in laser refractive surgeries. The same research group highlighted the advantages of employing patient-specific computational analyses in the mechanical evaluation of corneal structure after laser refractive surgery (Vahdati et al., 2016). Recently, FE models have been employed to predict post-surgical ectasia in patients who underwent refractive treatments and developed the condition (Francis et al., 2023).

The proposed work fits within the finite element modeling framework and primarily investigates the role of laser refractive surgeries in contributing to post-surgical ectasia through FE analysis, aiming to determine which refractive treatment is the most invasive from a biomechanical perspective, if any. Corneal FE models, characterized by a weak area of increasing severity, will be analyzed at pre- and post-surgical conditions. Simulations of the three refractive procedures (PRK, LASIK, and SMILE) will be conducted on pathological corneas to analyze their optomechanical impact on ectasia and assess whether any procedure exacerbates the pre-existing pathological condition, highlighting its potential role in ectasia progression. Both the optical and mechanical effects of each procedure on the cornea will be examined under healthy and pathological conditions. The results will then be compared to determine which procedure has the greatest impact on corneal biomechanics, which is the least mechanically invasive, or whether their optomechanical effects are comparable.

2 Materials and methods

In the following section, we will describe the model's characteristics and the set-up of the laser refractive surgeries simulations for both healthy and pathological corneas, characterized by an area of reduced stiffness.

2.1 Material model

Corneal tissue is made of five layers (epithelium, Bowman's layer, stroma, Descemet's membrane and endothelium), among which the stroma is responsible for the biomechanical response, since it constitutes 90% of the corneal thickness. The stroma is arranged in a highly organized structure, contributing to the transparency that characterizes the cornea as a lens (Sridhar, 2018). In the posterior third of the stroma, the lamellae are orthogonally oriented along the nasal-temporal and inferior-superior directions, while in the anterior two-thirds, they progressively adopt an isotropic distribution. Toward the limbus, the lamellae assume a circumferential orientation (Winkler et al., 2011) (Figure 1A).

In this work, the cornea was modeled as a monolayer stromal tissue, following the assumption made in our previous study (Fantaci et al., 2024a). This approach is widely adopted in literature (Pandolfi et al., 2009; Sánchez et al., 2014; Simonini and Pandolfi, 2015; Simonini et al., 2022), given the stroma's primary role in determining the corneal mechanical response and the current lack of mechanical characterization for the other corneal layers.

Figure 1A illustrates a theoretical scheme of fibers orientation; however, collagen fibers exhibit varying degrees of dispersion depending on their location within the cornea and are not perfectly aligned. As a consequence, in-plane and out-of-plane dispersion (Figures 1C, D), as derived by (Pandolfi and Holzapfel, 2008; Wang and Hatami-Marbini, 2021), must be considered to account for point-wise fibers distribution.

The following strain energy density function (SEDF) for a nearly-incompressible material was used to model corneal tissue behavior (Equation 1, Wang and Hatami-Marbini, 2021):

$$\psi(\bar{\mathbf{C}}, J) = \psi^{matrix}(\bar{I}_1, \bar{I}_2) + \sum_{i=4,6} \psi^{fibers}(\bar{\mathbf{C}}, \mathbf{H}_i) + \psi(J), \tag{1}$$

where $\psi^{matrix}(\bar{I}_1, \bar{I}_2)$ represents the isotropic contribution of the ECM, $\psi^{fibers}(\bar{\mathbf{C}}, \mathbf{H}_i)$ accounts for the anisotropic contribution given by the fibers of the model, and $\psi(J)$ is the volumetric term.

$\bar{\mathbf{C}}$ is the deviatoric right Cauchy-Green tensor (Equation 2):

$$\bar{\mathbf{C}} = J^{-2/3}\mathbf{C}, \tag{2}$$

where $\mathbf{C} = \mathbf{F}^T\mathbf{F}$ is the right Cauchy-Green tensor. The invariants of $\bar{\mathbf{C}}$ are (Equations 3–5):

$$\bar{I}_1 = \mathrm{tr}\bar{\mathbf{C}}, \tag{3}$$

$$\bar{I}_2 = \frac{1}{2}\left(\bar{I}_1^2 - \bar{\mathbf{C}} : \bar{\mathbf{C}}\right), \tag{4}$$

$$\bar{I}_3 = \det(\bar{\mathbf{C}}) = 1. \tag{5}$$

The anisotropy of the cornea is characterized by the fabric tensor $\mathbf{H}_i$, $i = \{4, 6\}$, that accounts for fibers dispersion and is defined as (Equation 6):

$$\mathbf{H}_i = A\mathbf{1} + B\mathbf{a}_0^i \otimes \mathbf{a}_0^i + (1 - 3A - B)\mathbf{a}_n \otimes \mathbf{a}_n, \tag{6}$$

with constants $A = 2k_{ip}k_{op}$ and $B = 2k_{op}(1 - 2k_{ip})$. The unit vectors $\mathbf{a}_0^4$ and $\mathbf{a}_0^6$ are associated with the mean preferential directions of the two families of fibers that characterize the corneal stroma (see Figure 1A), whereas $\mathbf{a}_n$ is the unit vector normal to the cornea, that identifies the out-of-plane direction.

The following equations for in-plane dispersion k_{ip} were used (Equations 7, 8, Figure 1C):

$$k_{ip}(\theta) = \left(\frac{k_{ip}^{min} + k_{ip}^{max}}{2}\right) - \left(\frac{k_{ip}^{max} - k_{ip}^{min}}{2}\right)\cos 4\,\theta \tag{7}$$

$$k_{ip}(\theta, r) = k_{ip}^{min} + \frac{1}{2}\left(k_{ip}(\theta) - k_{ip}^{min}\right)\left(1 - \cos\frac{2\pi r}{R_{TZ}}\right), \tag{8}$$

where $k_{ip}^{min} = 0.1$ is the minimum value (completely anisotropic distribution), $k_{ip}^{max} = 0.5$ is the maximum (completely isotropic distribution) and $R_{TZ} = 5.5$ mm is the radius of the transition zone from the cornea to the limbus.

Out-of-plane dispersion varies in depth, being the fibers more orthogonally distributed within the posterior two-thirds and more isotropically oriented within the anterior third. To define k_{op}, a local coordinate $s \in [0, 1]$ must be used, parallel to the normal unit vector. This local coordinate is 0 at the anterior surface and one at the posterior surface (Figure 1D). The following equation for the out-of-plane dispersion was used (Equation 9):

$$k_{op}(s) = k_{op}^{min} + \left(k_{op}^{max} - k_{op}^{min}\right)\left(1 - e^{-\gamma_d s}\right), \tag{9}$$

where $k_{op}^{min} = 1/3$ (completely isotropic distribution) and $k_{op}^{max} = 1/2$ (completely anisotropic distribution) and the constant γ_d controls the non linearity of Equation 9 (Figure 1D). A value of $\gamma_d = 1$ was assigned to the model.

To describe the behavior of the ECM, the Neo-Hookean model was used (Equation 10):

$$\psi^{matrix}(\bar{I}_1) = C_{10}(\bar{I}_1 - 3), \tag{10}$$

where C_{10} regulates matrix's stiffness.

The hyperelastic Holzapfel-Gasser-Odgen model with dispersion parameters was used (Pandolfi and Holzapfel, 2008; Wang and Hatami-Marbini, 2021) to model the anisotropic contribution of the collagen fibers (Equation 11):

$$\psi^{fibers}(\bar{\mathbf{C}}, \mathbf{H}_i) = \sum_{i=4,6} \frac{k_1}{2k_2}\left(e^{k_2(\bar{I}_i^{\star}-1)^2} - 1\right), \tag{11}$$

where k_1 and k_2 are constants that control the fibers stiffness and fibers non-linearity, respectively. The distorsional generalized invariant $\bar{I}_i^{\star}$ has the following form (Equations 12–14):

$$\begin{aligned}\bar{I}_i^{\star} = \mathbf{H}_i : \bar{\mathbf{C}} = 2k_{ip}k_{op}\bar{I}_1 + 2k_{op}\left(1 - 2k_{ip}\right)\bar{I}_i \\ + \left(1 - 6k_{ip}k_{op} - 2k_{op}\left(1 - 2k_{ip}\right)\right)\bar{I}_n,\end{aligned} \tag{12}$$

with

$$\bar{I}_i = \bar{\mathbf{C}} : \mathbf{a}_0^i \otimes \mathbf{a}_0^i, \tag{13}$$

$$\bar{I}_n = \bar{\mathbf{C}} : \mathbf{a}_n \otimes \mathbf{a}_n. \tag{14}$$

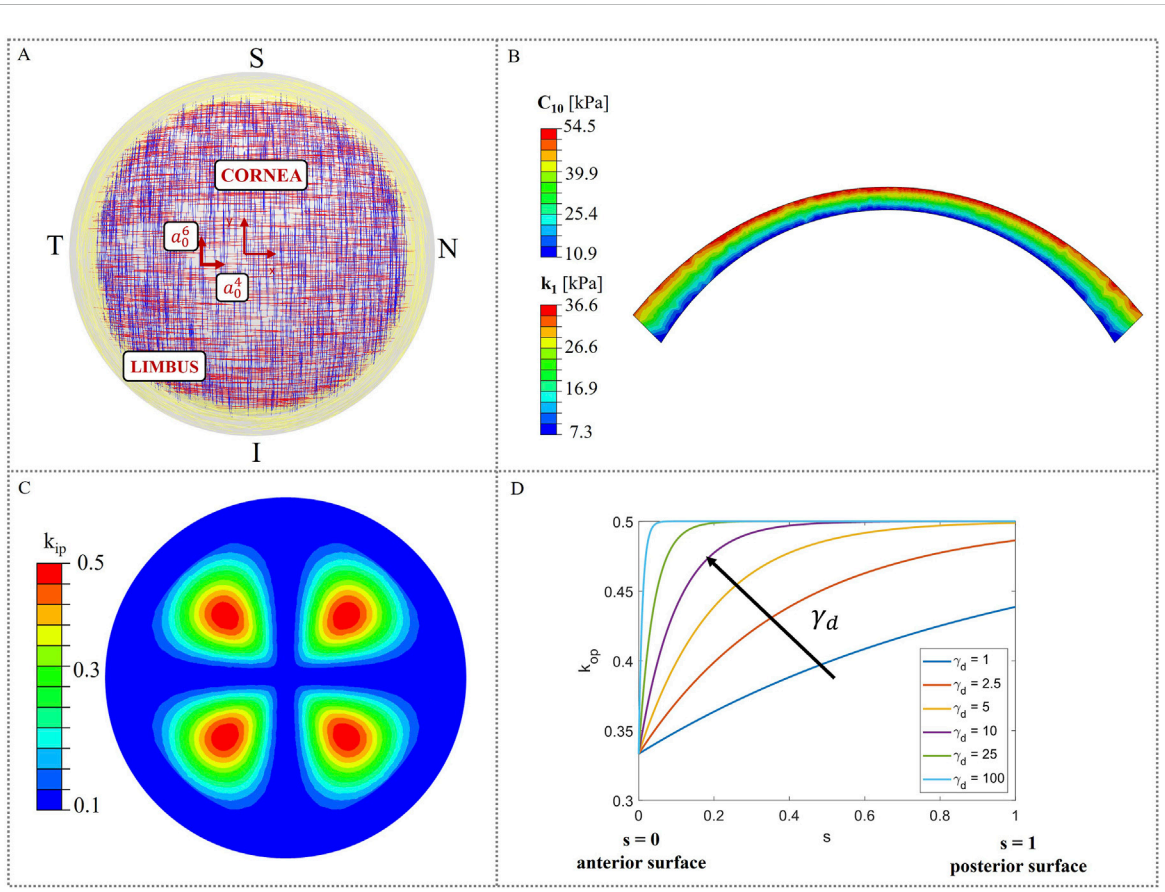

FIGURE 1
Material model characteristics. **(A)** Theoretical distribution of collagen fibers (Meek and Boote, 2009); **(B)** Heterogeneous distribution of material properties (C_{10} and k_1) in corneal thickness; **(C)** In-plane dispersion k_{ip} distribution in the corneal model; **(D)** Variation of the out-of-plane dispersion k_{op} as a function of the local coordinate s.

TABLE 1 Corneal material parameters along the thickness.

	C_{10} [kPa]	k_1 [kPa]	k_2 [-]	k_{ip}-k_{op} [-]
First layer (anterior surface)	54.5	36.3	400	Equations 8, 9
Second layer	39.9	26.6	400	Equations 8, 9
Third layer	25.4	16.9	400	Equations 8, 9
Fourth layer (posterior surface)	10.9	7.3	400	Equations 8, 9

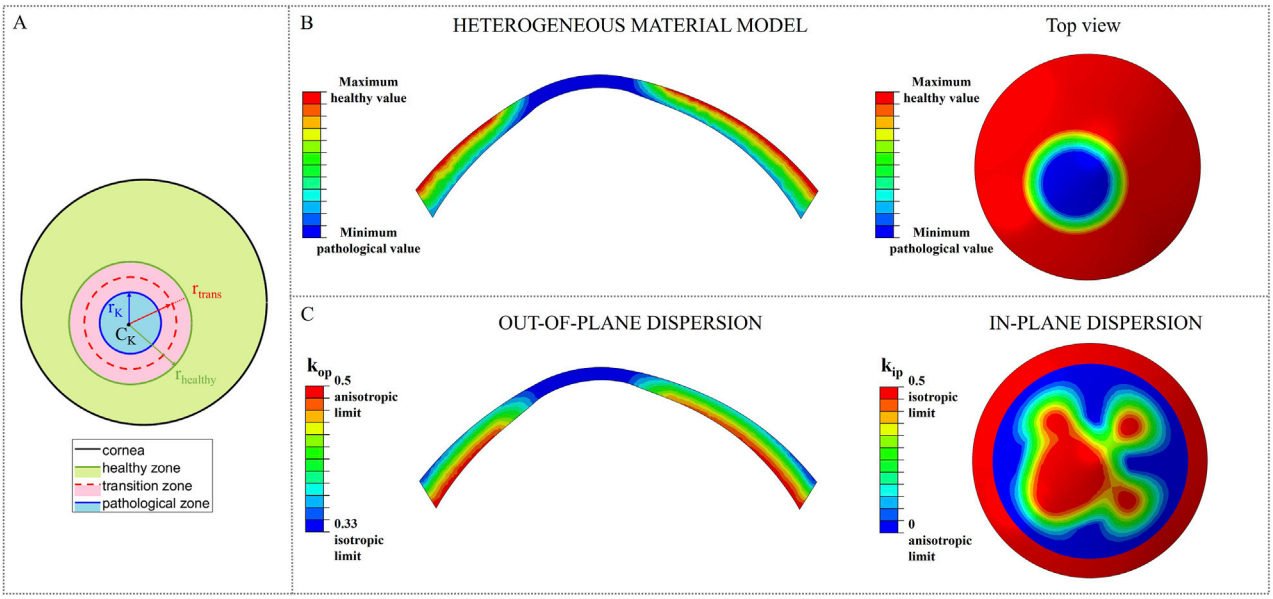

FIGURE 2
Stiffness reduction of the material properties of the model. **(A)** Location and dimension of the pathological area; **(B)** Pathological material properties distribution in the heterogeneous material models for constants C_{10} and k_1; **(C)** Change of k_{ip} and k_{op} towards their isotropic limit due to the loss of fibers orientation in the pathological area.

Finally, the volumetric term is (Equation 15):

$$\psi(J) = \frac{1}{D}(\log J)^2, \tag{15}$$

where $D = 3.6 \cdot 10^{-4}$ is the volumetric constant.

Stromal tissue is characterized by a stiffness gradient from the posterior to the anterior surface, throughout its thickness, as demonstrated by (Randleman et al., 2008). In this work, depth-dependent stiffness was introduced in the model, by assigning heterogeneous material properties to the model. To reproduce the stiffness gradient characteristic of human corneas, the corneal model was divided into four different layers (Figure 1B) and material properties with a linear variation from the posterior surface to the anterior were assigned (Randleman et al., 2008; Reinstein et al., 2013; Dias and Ziebarth, 2013; Dupps and Seven, 2016). More specifically, the maximum values of the material properties were assigned at the anterior surface and gradually decrease until they reach a 20% of the initial value at the posterior surface (Falgayrettes et al., 2023). We assumed a linear variation for the matrix stiffness constant C_{10} and for the fibers stiffness constant k_1, while the constant that controls fibers non-linearity k_2 was kept constant throughout the entire thickness (Pandolfi and Holzapfel, 2008). The constant values assigned to each layer were determined through an optimization process aimed at matching the apical displacement of a homogeneous monolayer corneal model reported in the literature (Wang and Hatami-Marbini, 2021). The material parameters assigned to each layer of our model are shown in Table 1.

2.2 Likelihood of ectasia onset: local stiffness reduction

To analyze the likelihood of ectasia onset and progression in pre- and post-surgical conditions, a circular weakened area of radius r_K = 1.5 mm and center C_K = [-0.663, −1.019] [mm] (Eliasy et al., 2020), characterized by reduced stiffness, was introduced in the nasal inferior position, where ectasia usually develops (Figure 2A). Around the central pathological area of radius r_K, a transition zone of radius r_{trans} was defined to avoid any abrupt change of properties from the pathological to the healthy tissue. Ten different cases with increasing pathology severity were considered (Table 2); each case represents a different degree of severity correlated to a specific stiffness reduction γ in the pathological area. Starting from healthy corneal tissue properties (labeled as γ = 1), a 10% reduction

TABLE 2 Material properties in the pathological area for the ten selected cases with increasing severity corresponding to a stiffness reduction γ.

Layer	γ	1	0.9	0.8	0.7	0.6	0.5	0.4	0.3	0.2	0.1
1	C_{10} [kPa]	54.5	49.1	43.6	38.2	32.7	27.3	21.8	16.4	10.9	5.5
	k_1 [kPa]	36.3	32.7	29	25.4	21.8	18.2	14.5	10.9	7.3	3.6
2	C_{10} [kPa]	39.9	35.9	31.9	27.9	23.9	20	16	12	8	4
	k_1 [kPa]	26.6	23.9	21.3	18.6	16	13.3	10.6	8	5.3	2.7
3	C_{10} [kPa]	25.5	23	20.4	17.9	15.3	12.8	10.2	7.7	5.1	2.6
	k_1 [kPa]	16.9	15.2	13.5	11.8	10.1	8.5	6.8	5.1	3.4	1.7
4	C_{10} [kPa]	10.9	9.8	8.7	7.6	6.5	5.5	4.4	3.3	2.2	1.1
	k_1 [kPa]	7.3	6.6	5.8	5.1	4.4	3.7	2.9	2.2	1.5	0.7
Transition zone Width	[mm]	0	0.167	0.33	0.5	0.67	0.83	1	1.167	1.33	1.5

of the material properties stiffness is progressively applied to the pathological area until reaching a maximum stiffness reduction of 90% with respect to the initial healthy properties (labeled as γ = 0.1) (i.e., γ decreases from 1 to 0.1 with step 0.1). These stiffness reductions were applied to the ECM stiffness constant C_{10} and to the fibers stiffness constant k_1, while the fibers non-linearity constant k_2 was left unvaried (Figure 2B). The dispersion parameters k_{ip} and k_{op} were linearly changed until reaching their isotropic limits, 0.5 and 0.33, respectively, given the disorganization of collagen fibers, typically observed in keratoconic corneas (Alkanaan et al., 2017) (Figure 2C). The stiffness reduction was applied to each layer of the model for all the cases considered (Figure 2B; Table 2).

As the degree of pathology severity increases, the transition zone expands: starting from the less severe case (γ = 0.9), a transition zone of 0.1667 mm was defined and gradually expands throughout the pathological cases, until reaching a final width of 1.5 mm (r_{trans} = $r_{healthy}$ = 3 mm) for the most severe case (γ = 0.1) (Table 2). A linear variation of the material properties from the pathological to the healthy value was assigned to the transition zone of the model, to smooth the stiffness change between the two areas of the cornea.

2.3 Laser refractive surgeries simulations

A 3D FE conic model (Fantaci et al., 2024a) with average dimensions (anterior surface: apical radius R_{AS} = 8.18 mm and asphericity Q_{AS} = −0.25; posterior surface: apical radius R_{PS} = 6.63 mm and asphericity Q_{PS} = −0.26; central corneal thickness: CCT = 579 μm; corneal diameter \diameter = 12 mm) was built to simulate the laser refractive surgeries. The FE model was meshed with quadratic tetrahedrons of 0.1 mm dimension with the software ANSA version 22.0.1 by BETA CAE Systems. Mesh sensitivity analysis was conducted in a previous study (Fantaci et al., 2024a). The limbus was fixed to ensure model's stability and an average physiological IOP of 15 mmHg was applied to the posterior surface of the cornea to mimic the pressure acting inside the eye cavity. The zero-pressure algorithm from (Ariza-Gracia et al., 2016) was used to recover the unpressurized geometry, that became the initial geometry for the surgeries simulation. The stress-free configuration was recovered only in the healthy case, and then the pathological area was incorporated. All the simulations were run with the proprietary software ABAQUS 2022.

For each surgery simulation (shown in Figure 3), the ablation profile for −4 D myopic correction was defined by following Equations 1, 5, 6 from our previous work (Fantaci et al., 2024a) and the ablation depth was established by following Table 2 of the same work. In all the surgical simulations, an optical zone of \diameter = 6.5 mm was defined, that represents the diameter of the ablation tissue that will be removed. This value is the most used in clinical practice for the three procedures and rarely varies.

When constructing the finite element model, specific adjustments must be made depending on the selected surgery procedure.

2.3.1 PRK

PRK model is built so that two different element sets are created to separate the ablation volume from the rest of the cornea (i.e., the post-surgical corneal volume). The ablation depth was 60 μm for simulating a myopic correction of −4 D in PRK, leaving a RSB of 519 μm.

PRK surgery consisted of two steps (Figure 3):

- first step - Pressurization: the model is pressurized with an IOP applied to the posterior surface of the cornea.
- second step - Ablation: the ablation volume is removed.

2.3.2 LASIK

In LASIK treatment, a hinged corneal flap is created with a femtosecond laser and lifted to allow direct ablation of the stroma using an excimer laser. The characteristic dimension of the flap selected to simulate the surgery were the following (Moshirfar et al., 2019): flap \diameter = 9 mm, flap thickness = 100 μm, hinge length = 4 mm. The hinge of the flap is always placed in the superior central region of the cornea, to reduce the probability of post-surgical flap dislocation. As for PRK, LASIK surgery required an ablation depth of 60 μm. The RSB, considering flap and lenticule thickness, was of 419 μm.

Before running the simulation, contacts between the parts of the corneal geometry must be defined and adjusted during the simulation. Specifically, a hard contact with infinite friction is established between the bottom surface of the flap and the

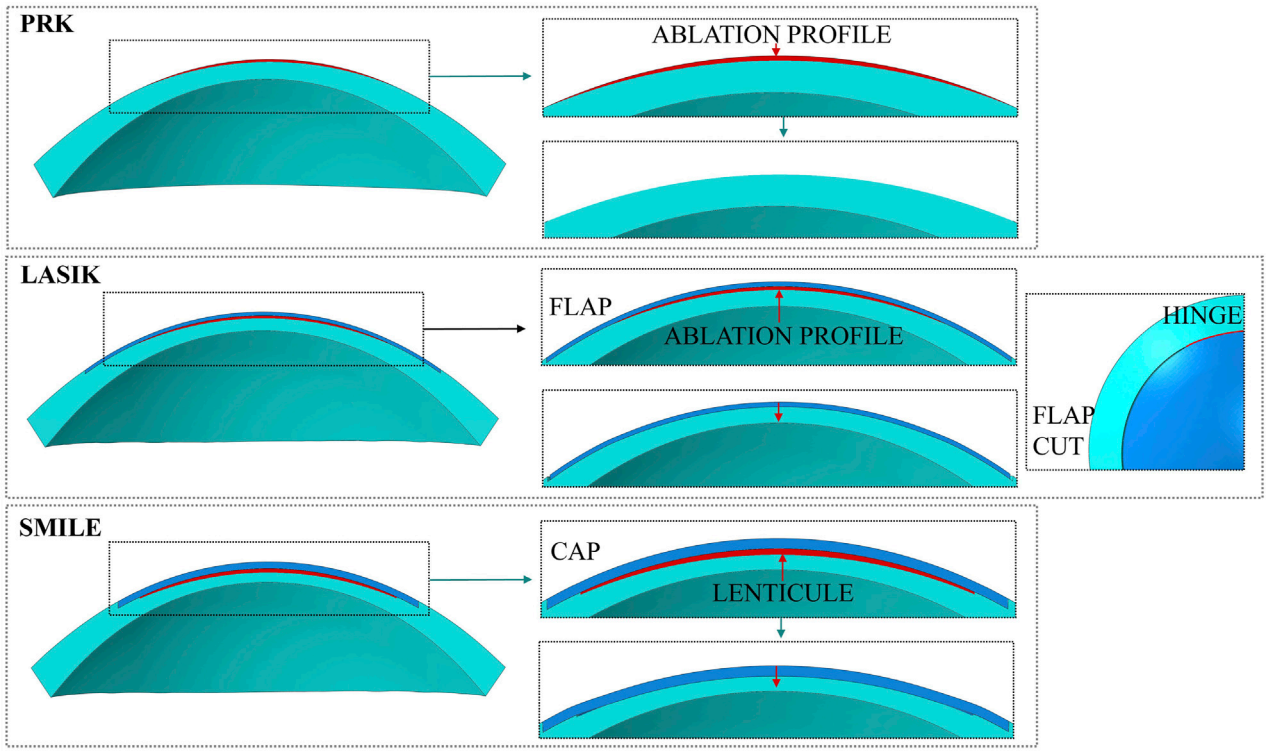

FIGURE 3
FE models of the laser refractive surgeries.

underlying corneal surface to prevent penetration and sliding. This contact ensures model continuity as an initial condition when the model is pressurized. A hard contact with friction coefficient of 0.5 is then defined between the flap and the post-surgical cornea, activated in the second step when the surgery is simulated. The decision to restrict the flap from freely sliding on the underlying cornea–despite this being its typical behavior during surgery–was made because the focus of this study is on analyzing the effects of laser surgery on ectasia onset after the corneal geometry has stabilized (Katzengold et al., 2021; Wang et al., 2022), rather than in the immediate post-surgical phase.

LASIK surgery consisted of three steps (Figure 3):

- First step - Pressurization: the model is pressurized with an IOP applied to the posterior surface of the cornea.
- Second step - Flap cut and ablation: the flap is cut by deactivating the previously defined contact between the flap and the rest of the cornea; afterward, the ablation volume is removed, and a superficial pressure of P = 0.01 mmHg is applied on the flap to push it down and activate the contact between its bottom surface and the post-surgical cornea.
- Third step - Equilibrium step: in this last step, the previously applied pressure P is removed in order to allow the model to reach its equilibrium state.

After the flap was cut, no changes to its material properties (e.g., transitioning from an anisotropic to an isotropic material model (Dupps and Seven, 2016)) were applied. Only the contact at the new interface created during the surgery was defined. For further details on the mechanical influence of the material model on flap behavior, refer to Supplementary Figure S1 in the Supplementary Material.

2.3.3 SMILE

In the SMILE model, a 6.5 mm lenticule was created and placed at a 120 μm of depth with respect to the anterior surface, constituting the cap thickness, as it is done in clinical practice (Lv et al., 2023). The cap diameter is usually set as 7.6 mm and determines the dimension of the pocket that is created to extract the lenticule. When performing SMILE in daily clinical practice, a 10% is added to the target correction to ensure optical accuracy and an additional 15 μm thickness is added to the lenticule to avoid rupture during its surgical extraction (Wang et al., 2022). Therefore, a correction of −4.4 D was set in order to correct −4 D with a total lenticule thickness of 85 μm, to replicate surgical conditions. The RSB, considering cap and lenticule thickness, was of 374 μm.

SMILE surgery consisted of two steps (Figure 3):

- First step - Pressurization: the model is pressurized with an IOP applied to the posterior surface of the cornea.
- Second step - Lenticule extraction: the lenticule is removed and a hard self-contact with friction coefficient of 0.5 is defined to avoid penetration of the two internal corneal surfaces, that come into contact due to the action of the IOP.

As in the LASIK model, no changes to the cap material properties were applied in the SMILE model (see Supplementary Material for further details).

TABLE 3 Belin classification for the heterogeneous model at increasing pathology severity.

γ	$K_{m\ AS}$ [D]	$K_{m\ PS}$ [D]	Thinnest pachymetry [μm]	Belin ABCD
1	40.90	−5.95	578.84	A0, B0, C0
0.9	41.61	−6.05	574.94	A0, B0, C0
0.8	42.61	−6.18	570.18	A0, B0, C0
0.7	43.91	−6.36	564.35	A0, B0, C0
0.6	45.63	−6.59	556.98	A0, B0, C0
0.5	47.94	−6.89	547.22	A1, B1, C0
0.4	51.66	−7.39	531.83	A2, B2, C0
0.3	56.03	−7.96	514.31	A4, B3, C0
0.2	62.64	−8.77	488.82	A4, B4, C1
0.1	68.18	−9.38	463.47	A4, B4, C1

2.4 Pre- and post-surgical optomechanical analyses

In the following section, the analyses conducted to investigate the onset and progression of ectasia in both pre- and post-surgical conditions will be presented.

In the first analysis, the optomechanical response of the constitutive model to a localized circular area of corneal tissue undergoing degradation was investigated, to assess its ability to reproduce ectasia progression, characterized by corneal bulging and thinning. For this analysis, the material properties of the model (C_{10}, k_1, k_{ip} and k_{op}) were degraded at once, as it is likely that more processes coexist during the development of the disease.

In the second analysis, the effect of three laser surgeries on the post-surgical corneal model was examined in both healthy and pathological scenarios, aiming to identify which procedure induces the greatest optomechanical changes in the presence of a softened area. As for the previous analysis, the material properties (C_{10}, k_1, k_{ip} and k_{op}) were degraded at once.

In all simulations performed in this study, the zero-pressure algorithm was first applied to the healthy cornea, after which the pathological tissue was introduced.

To evaluate ectasia progression across increasing severity stages, both mechanical and optical analyses were conducted in pre- and post-surgical configurations. From a mechanical perspective, the stress and strain distributions within the model were examined. On the optical side, the Belin ABCD staging system (Belin et al., 2020) was used, as it is the classification currently employed in clinical practice and integrated into the Pentacam topographer by Oculus Optikgeräte GmbH (Wetzlar, Germany).

This staging system assigns a severity grade to corneas that developed ectasia, based on four parameters (ABCD): A is the anterior surface curvature in a 3 mm zone centered on the thinnest pachymetry ($K_{m\ AS}$ in Table 3); B is the posterior surface curvature in a 3 mm zone centered on the thinnest pachymetry ($K_{m\ PS}$); C is the thinnest pachymetry point in μm and D is distance best corrected visual acuity. Depending on the computed values, five different stages for classifying keratoconus can be assigned (see (Belin et al., 2020) for more details). In this work, an algorithm that computed the parameters (ABC) was developed. Parameters A and B were computed as the tangential curvature of the center of the cone at the anterior and posterior surfaces respectively (the center of the cone is known, since it is the center of the degraded zone), by performing a sphere fitting at each point of the anterior surface (Doll et al., 2020). Tangential curvature is measured in diopters (D), derived by multiplying its value with the difference in refractive indices between two media of interest (Klein and Mandell, 1995) (Equation 16):

$$K_m = \frac{n_2 - n_1}{R} \tag{16}$$

For the anterior surface, $n_2 = 1.3375$ represents the keratometric index 1.3375 and $n_1 = 1$ corresponds to the refractive index of the air. For the posterior surface $n_2 = 1.336$ represents the refractive index of the aqueous humor and $n_1 = 1.376$ corresponds to the refractive index of the cornea. These values align with the refractive indices used by the Pentacam topographer to compute standard keratometric values. Parameter C was calculated as the minimum normal distance between the anterior and posterior surface nodes. Parameter D could not be included in the study as it is not machine generated and depends on the patient's subjective visual acuity.

3 Results

In the following sections, the main results of the conducted analysis are presented. First, the impact of the degradation of the tissue components on the model is analyzed in a pre-surgical scenario. Then, the effect of the different refractive procedures on the final optomechanical outcome at both healthy and pathological conditions is investigated.

3.1 Pre-surgical evaluation of corneal tissue degradation

In this first analysis, ectasia progression in the model was evaluated relative to healthy homeostatic conditions (i.e., before performing the surgery, when the model is pressurized only), by introducing a weakened area with progressively reduced stiffness.

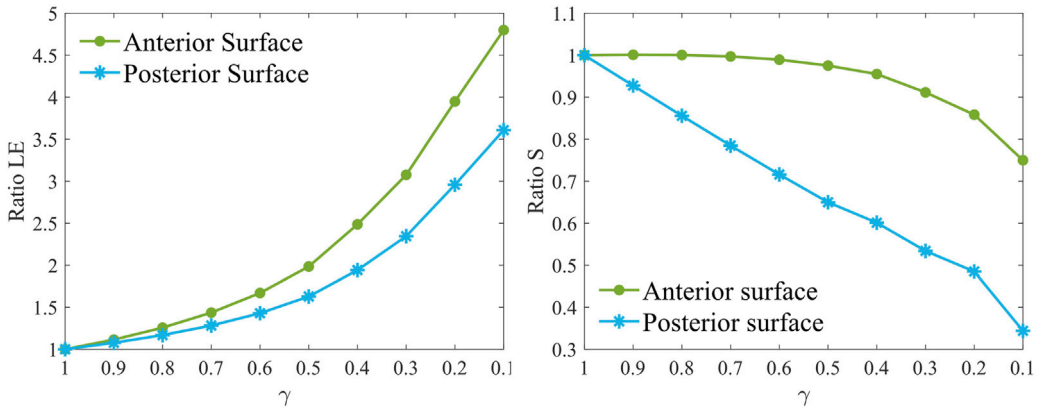

FIGURE 4
Maximum principal strain ratio (left) and maximum principal stress ratio (right) for increasing pathology severity (γ = 1.0–0.1) in the degraded area at the anterior (AS) and posterior (PS) surfaces at pre-surgical homeostatic conditions. The ratio is computed with respect to pre-surgical healthy conditions (γ = 1).

From a mechanical perspective, the evolution of the principal maximum strain and stress was evaluated by computing their ratio relative to the healthy case (γ = 1). The ratio for each stiffness reduction was computed relative to pre-surgical healthy conditions (γ = 1) by averaging the stress and strain values of five elements selected from the pathological area at both the anterior and posterior surfaces, respectively. As the pathology worsens, the strains on the anterior and posterior surfaces of the weakened area increase non-linearly (Figure 4), increasing up to 5 times the healthy value on the anterior surface and up to 3.5 times on the posterior surface in the most severe case. In contrast, stresses at the anterior surface remain almost constant until a 60% loss of material properties has occurred (γ = 0.4), after which they decrease rapidly to 80% relative to healthy conditions. On the posterior surface, the maximum principal stress ratio follows a linear downward trend, ultimately decreasing by 70%.

From an optical perspective, the Belin ABCD staging system was used to assess ectasia progression and evaluate the model's ability to replicate varying degrees of disease severity (Table 3; Figure 5).

Table 3 shows that the anterior and posterior curvatures ($K_{m\ AS}$ and $K_{m\ PS}$) gradually increase starting from the less severe cases, while pachymetry decreases. The anterior curvature increases slowly in the degraded area, until a 50% loss of mechanical properties is reached. Beyond this point, the progression of the cone accelerates, resulting in a final curvature increase of approximately 28 D with respect to healthy conditions (γ = 1). A similar behavior is observed on the posterior surface, although the increase in curvature is smaller compared to the anterior surface (approximately −3 D). When the material properties are reduced by 50% (γ = 0.5), the cone reaches stage 1 severity based on the anterior and posterior surface curvatures (A1 and B1, Table 3). Beyond this point, ectasia progresses rapidly, until reaching stage 4, the most severe classification according to the Belin classification system in terms of curvature values (A4 and B4). Both the anterior and posterior surfaces presented similar percentage changes in dioptric changes from the healthy state to the most severe condition.

Figure 5 presents a qualitative representation of the information reported in Table 3, showing the tangential curvature maps of the anterior surface and the pachymetry for each reduction in stiffness γ considered. The tangential curvature maps of the posterior surface are omitted to avoid redundancy. An asymmetry in the curvature map is already visible when a 30% loss of mechanical properties has occurred (γ = 0.7), where the location of the pathological zone becomes noticeable.

The pachymetry map is less sensitive to micrometric node displacements compared to the tangential curvature. Therefore, thinning in the model becomes more noticeable from cases with γ = 0.6–0.5. As the pathology progresses, both the points of highest curvature and thinnest pachymetry shift toward the center of the degraded area, which also expands in size. Similar to the evolution of anterior and posterior tangential curvature, pachymetry decreases more gradually in cases of less severe stiffness loss (approximately 30 microns for γ = 0.9–0.5). As the pathology worsens, the thinning progresses more rapidly. The model exhibits a final pachymetry decrease of 115.4 microns relative to the initial central corneal thickness (CCT), classified as a stage 1 cone (C1).

3.2 Analysis of the post-surgical impact of laser treatments on the pathological cornea

In this second analysis, the optomechanical impact of three refractive procedures (PRK, LASIK and SMILE) on the pathological cornea was investigated. Figure 6 shows the ratios of the maximum principal stress and the maximum principal logarithmic strain in the degraded area on the anterior and posterior surfaces, for increasing pathology severity (γ = 1.0–0.1). Stress and strain values of the 10 elements previously selected in the pathological area (five elements at the anterior surface and five at the posterior) were averaged. The ratios were calculated relative to the pre-surgical condition of each specific pathological case to isolate changes caused solely by the refractive procedures (e.g., $Ratio\ S = S_{Post\text{-}surgical\ (\gamma=0.1)} / S_{Pre\text{-}surgical\ (\gamma=0.1)}$).

Analyzing Figure 6 in detail, differences among the three procedures are evident even in the healthy case (γ = 1.0). PRK surgery caused an approximate 25% increase in both strains and stresses on the anterior surface, whereas its effect on the posterior

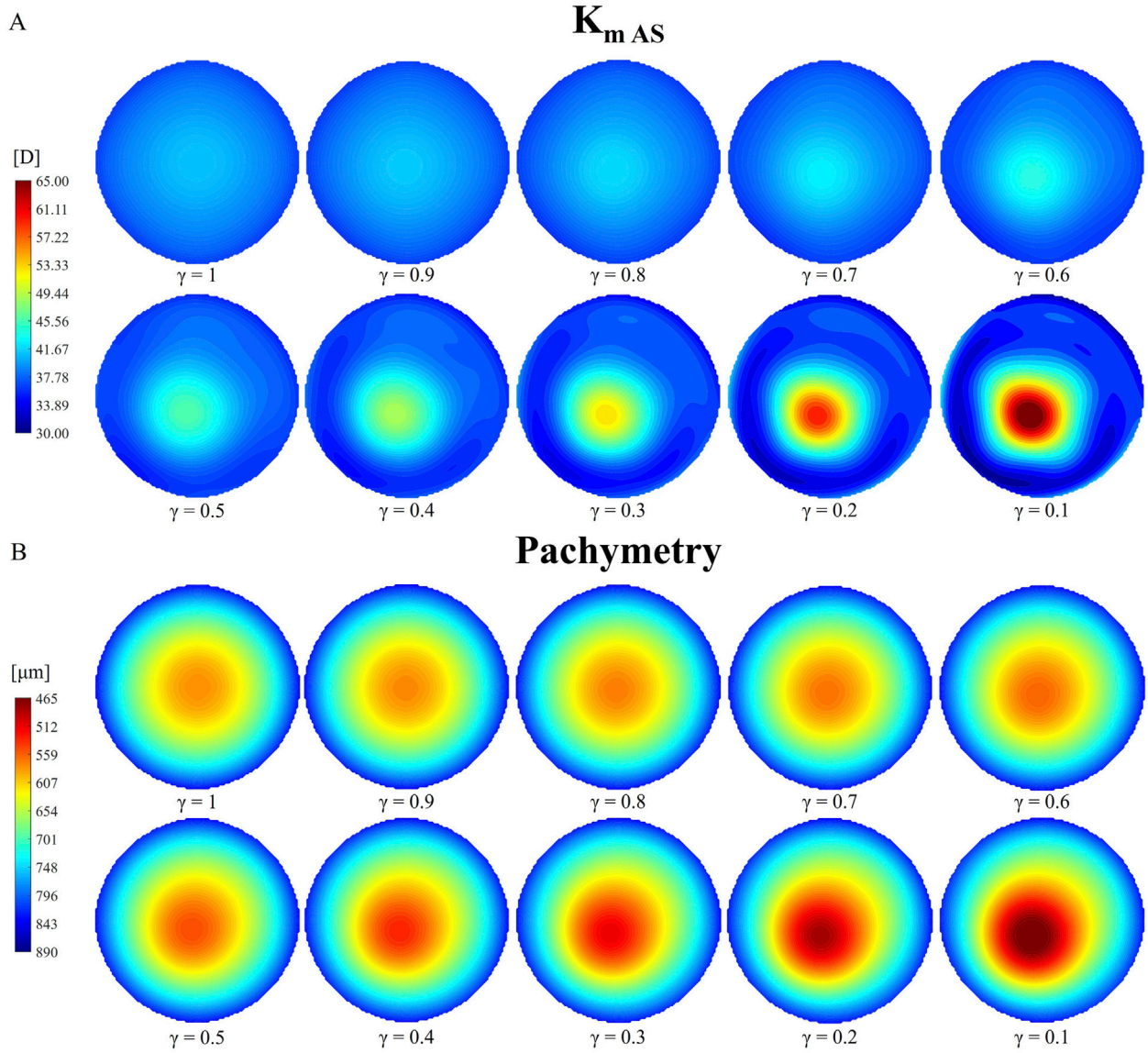

FIGURE 5
Evolution of tangential curvature of the anterior surface [$K_{m\ AS}$, **(A)**] and pachymetry thinning (B) with increasing pathology severity (γ = 1.0–0.1) under pre-surgical homeostatic conditions.

surface was less pronounced, resulting in a 7% increase in strain and a 13% increase in stress. These increments remained constant on the anterior surface until a 60% loss of material properties (γ = 0.4) occurred, suggesting that the surgery did not exacerbate the pre-existing pathological condition of the cornea. Beyond this point, strains decrease toward a ratio of one due to the fact that the model is already highly deformed in pre-surgical conditions, and the surgery no longer induces additional deformation. In contrast, stresses increase by 10% compared to less severe cases. At the posterior surface, strains increase linearly until γ = 0.4, after which the ratio decreases toward 1, similar to the behavior observed on the anterior surface. Stresses increase by up to 10% compared to healthy conditions (γ = 1.0), as observed on the anterior surface.

LASIK resulted in a decrease in both strains and stresses on the anterior surface (22% and 30%, respectively) in the healthy case (γ = 1.0), while causing a greater increase in both strains and stresses on the posterior surface (18% and 35%, respectively) compared to PRK. When the degraded area is introduced and the pathology progresses (γ = 0.9–0.1), the stress and strain ratios on the anterior surface increase non-linearly towards 1, indicating that surgery does not worsen the severity of the disease, similar to what was observed for PRK. On the posterior surface, a similar evolution to PRK is observed for both strain and stress ratios, but shifted by 10% and 22%, respectively, due to the higher mechanical impact of LASIK on the posterior cornea. Compared to γ = 1, stresses increased by 25% on the posterior surface in the most severe case (γ = 0.1).

Regarding the SMILE procedure, the strain ratio on the anterior surface remains consistently close to one across all stiffness reduction levels γ considered. The stress ratio, on the other hand, remains constant up to γ = 0.4, after which it decreases to a value close to 9%. For the posterior surface, SMILE exhibits a similar trend in strain ratio to that observed in PRK and LASIK, with an initial

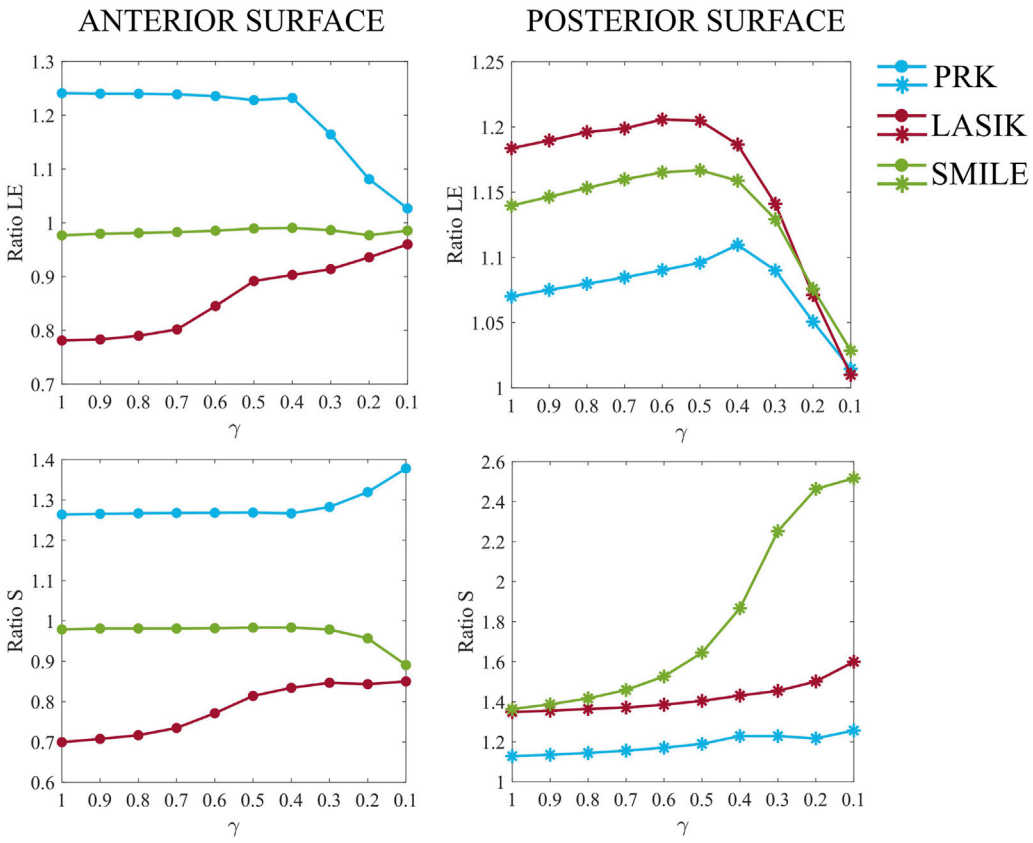

FIGURE 6
Maximum principal logarithmic strain and maximum principal stress ratios relative to pre-surgical conditions in the degraded area at the anterior (left) and posterior (right) surfaces, for increasing pathology severity (γ = 1.0–0.1).

increase of 14% compared to pre-surgical healthy conditions. This positions SMILE at an intermediate value among the three procedures. The strain ratio increases gradually until γ = 0.4, after which it decreases toward a ratio of 1. In terms of stress, SMILE causes a 36% increase in post-surgical stresses on the posterior surface under healthy conditions, similar to what is observed with LASIK. However, as the pathology progresses, SMILE displays a distinct behavior compared to the other procedures. The stress ratio follows a sigmoid trend, ultimately reaching a final value 2.5 times higher than its corresponding pre-surgical pathological configuration.

More generally, LASIK caused a decrease in both stresses and strains on the anterior surface, whereas PRK led to an increase. On the contrary, SMILE had little to no effect on stresses and strains on the anterior surface. On the posterior surface, all three procedures caused an initial increase in both stress and strain values. The greatest deformation on the anterior surface was observed for the PRK procedure, whereas the posterior surface was most deformed by LASIK. In terms of the stresses, PRK caused the highest increase on the anterior surface, whereas LASIK and SMILE similarly affected the stresses on the posterior surface, resulting in an approximate 35% increase under healthy conditions (γ = 1.0).

Moving to the optical analysis, we compared anterior and posterior post-surgical curvatures in the pathological area with respect to the pre-surgical condition (Figure 7). In a healthy cornea, when laser refractive surgery is performed, the post-surgical curvature of the anterior surface decreases, whereas the curvature of the posterior surface increases due to the removal of ablation tissue (see Figure 7, γ = 1). This effect is more pronounced on the posterior surface due to the direct action of intraocular pressure (IOP).

As the material degrades, the curvature of both the anterior and posterior surfaces increases, with the difference in curvature between pre-surgical and post-surgical conditions decreasing as degradation progresses. On the anterior surface, this difference becomes almost negligible for γ < 0.5 in all cases. By contrast, on the posterior surface, the post-surgical curvature is always greater than the pre-surgical curvature, becoming equal only when γ close to 0.1.

4 Discussion

Despite the widespread use of laser refractive surgeries in clinical practice, their potential role in keratoconus development remains highly debated (Moshirfar et al., 2021). This study aimed to analyze the optomechanical impact of three laser refractive procedures (PRK, LASIK, and SMILE) on both healthy and pathological corneas at varying stages of disease severity. A finite element analysis was conducted to determine whether any procedure could significantly exacerbate the pathology, highlighting its potential role in ectasia progression. Through FE models, we were able to investigate the

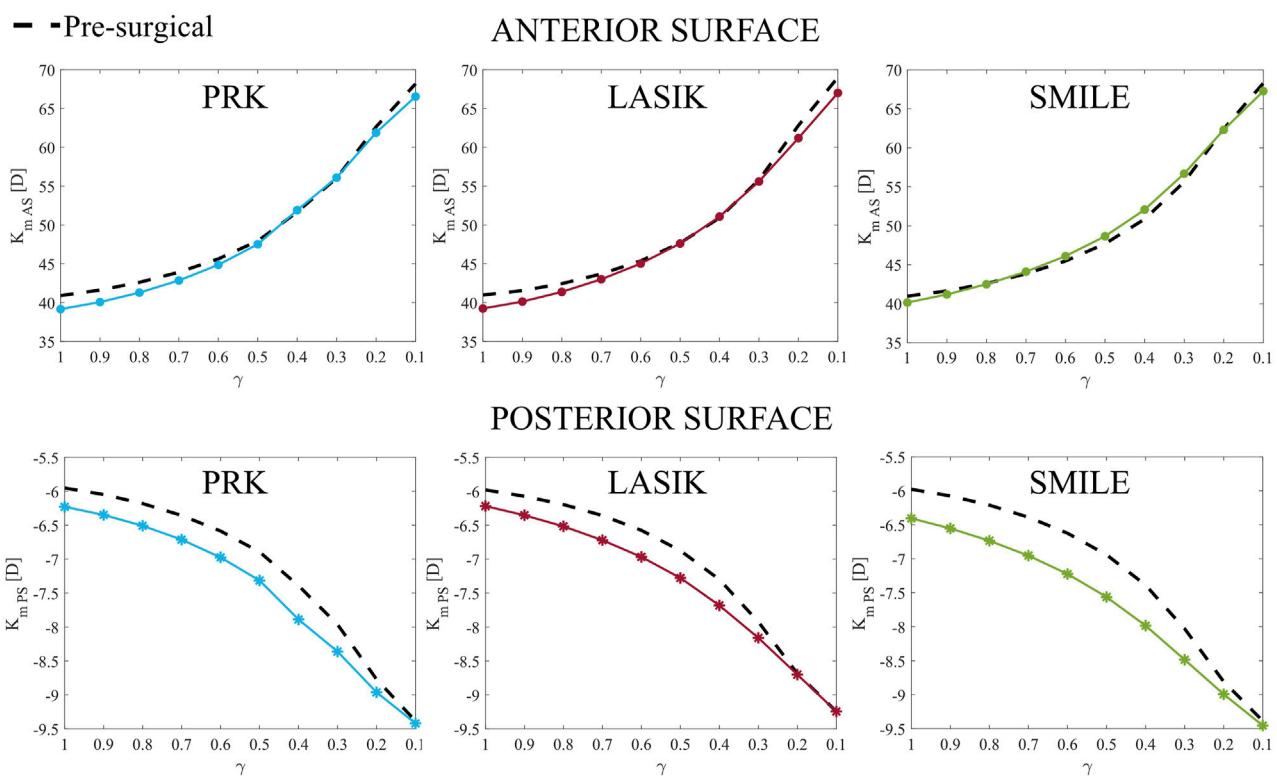

FIGURE 7
Anterior ($K_{m\,AS}$, top) and posterior ($K_{m\,PS}$, bottom) post-surgical curvature evolution at increasing disease severity (γ = 1.0–0.1) in the pathological area. They represent parameters A and B of Belin grading system.

effects of refractive procedures in pathological cases that would not typically be treated in clinical practice. In fact, when a patient is suspected to be at risk of post-surgical ectasia during pre-surgical screening, surgeons opt not to proceed with the surgery. Since it remains unclear whether keratoconus primarily develops as a post-surgical complication, i.e., as an iatrogenic disease, or if surgery exacerbates a pre-existing condition, as discussed by (Moshirfar et al., 2021), the relationship between refractive procedures and keratoconus progression was investigated.

In the first analysis of this work (Section 3.1), ectasia progression was evaluated at homeostatic conditions, by introducing a weakened area with progressively reduced stiffness. Most changes occur when the model is pressurized, as the stress-free configuration was computed only for the healthy case (γ = 1), and the pathological area was introduced afterward. The unpressurized geometry was computed only for the healthy case to analyze when the cone might develop following the onset of a weakened area. Introducing the pathological area before computing the zero-pressure configuration would prevent the cone from forming when the model is returned to its homeostatic condition, even in the presence of a softer pathological area, which would lack physical relevance.

As the pathology progresses, strains increase non-linearly, while stresses decrease following a more linear trend (Figure 4). Strain plays a key role in regulating cell activation to maintain and remodel the ECM under healthy homeostatic conditions. The pivotal role of strain as a driving force for ectasia progression was also discussed in a previous study by our group (Fantaci et al., 2024b). It has been hypothesized that alterations in protein expression observed in keratoconic corneas may cause oxidative damage, leading to ECM degradation (Santodomingo-Rubido et al., 2022; Kenney and Brown, 2003) and changes in the strain distribution within corneal tissue. As a result of ECM degradation, it loses its adhesive function, causing collagen fibers to shift, eventually break, and lose their specific orientation. The major mechanical changes occurring on the posterior surface may indicate that the structural changes due to tissue degradation observed in pathological corneas could initiate from the posterior surface and propagate towards the anterior, as previously hypothesized by various authors (Akhtar et al., 2008; Alkanaan et al., 2017; Falgayrettes et al., 2023).

To evaluate the progression of the disease from an optical perspective, the Belin ABCD staging system was used. As shown in Table 3, the disease begins to progress already from the less severe cases. Once a 50% loss of tissue stiffness is reached, the pathology worsens more rapidly, reaching stage 4 in the most severe cases (γ = 0.2–0.1) for both anterior and posterior curvatures (A4 and B4) in the area where the cone has developed. Tangential curvature is more sensitive to micrometric node displacements and better highlights geometric changes in the model compared to pachymetry maps (Figure 5). In fact, curvature maps allowed us to identify cone development from the earliest stages of the disease.

Pachymetry thinning, along with localized curvature steepening, is a characteristic sign of ectasia development. Our model showed a final pachymetric thinning of 115 microns compared to the initial healthy CCT (578.84 microns) and was classified as stage 1 (C1, Table 3) according to the Belin classification. This result highlights a limitation of Belin ABCD staging system. Despite the model

showing a significant reduction in pachymetry (115.4 microns), the initial CCT in the model was higher than the average (usually around 550 microns), leading to the most severe case being classified as only grade 1. This is because Belin system does not account for the relative change in pachymetry from its initial value. Moreover, tracking disease progression is challenging, as patients need to undergo check-ups before the disease develops and be monitored annually. This is likely why the Belin staging system does not consider parameter evolution over time.

When the initial pachymetry is higher than average (as in this case), it becomes more challenging for the model to reach lower pachymetric values as the mechanical properties deteriorate. If the model's initial CCT had been lower (490–550 microns), as is common in many patients, a final pachymetric thinning of 115.4 microns would have corresponded to stage 2 or three according to the Belin classification. However, the constitutive model used in this study (Equation (1)) captures the thinning behavior only up to a certain extent. A maximum thinning of 115.4 microns (Table 3) is achieved for the highest stiffness loss ($\gamma = 0.1$). Beyond this point, the model cannot reproduce further cone progression, as numerical issues would arise when tissue stiffness is further reduced. This result may suggest that a purely elastic continuum-based formulation may not be appropriate to mimic advanced stages of the disease (stage 4) in terms of pachymetry thinning, as it is not able to capture the complex processes of structural disorganization occurring in the stroma during disease's progression, as highlighted in our previous work (Fantaci et al., 2024b).

In the second analysis of this work, the optomechanical impact of three refractive procedures on healthy and pathological corneas was investigated. PRK surgery had the highest mechanical impact on the anterior surface and the lowest on the posterior. LASIK showed an opposite behavior with respect to PRK, as it lowered both stresses and strains on the anterior surface, while it had a higher impact on the same variables on the posterior surface. LASIK significantly affects the posterior surface because the creation of the flap (or the cap in SMILE) during the procedure introduces a geometrical discontinuity in the corneal thickness, leaving the anterior surface nearly unloaded. As pointed out in (Montanino et al., 2023), while cap in SMILE partially collaborates in sustaining the IOP, flap contribution in LASIK to the IOP is almost null. Consequently, stresses and strains concentrate on the posterior cornea, which is further exacerbated by a thinner RSB in LASIK (419 microns) compared to PRK (519 microns). This may be attributed to the limited healing capacity of corneal tissue after being cut, with only 2.4% of its original strength being recovered (Schmack et al., 2005).

For the healthy case ($\gamma = 1$), SMILE showed an intermediate mechanical impact, falling between PRK and LASIK, as also observed in (Montanino et al., 2023). As the disease progresses to more severe stages, SMILE was found to be the treatment that caused the highest increase in stresses on the posterior surface (Figure 6). This consistent increase in the stresses is probably due to the fact that a thicker lenticule is removed in this surgical procedure to avoid its rupture during the extraction, leaving a lower percentage of RSB (374 microns). In the model, the posterior portion of the cornea is around a 50% softer (Randleman et al., 2008; Reinstein et al., 2013) with respect to the anterior part. Having a lower percentage of RSB at the softer posterior cornea lead to higher stresses that may promote the progression of the pathology. This would also explain why the risk of post-surgical ectasia is higher when the RSB is lower than 250 microns and the surgeons prefer not to operate (Kim et al., 2007). In general, it is recommended to preserve the RSB as much as possible to minimize the risk of post-surgical complications. In this study, the RSB remained above the threshold in all three simulated surgical procedures.

Moreover, careful consideration should be given when selecting the appropriate treatment for each patient, taking into account which procedure induces the highest deformations, particularly on the posterior surface, where ectasia is believed to originate (Falgayrettes et al., 2023; Fantaci et al., 2024b). Currently, the mechanical impact of different laser refractive surgeries is often overlooked in clinical practice, and FE models could help bridge this gap.

In this work, the introduction of pathological tissue into the model did not amplify the mechanical impact of the refractive treatments: stresses and strains remained constant in the majority of the cases until a 60%–70% loss of mechanical properties occurred, suggesting that the refractive procedures were not worsening the pre-existing pathological condition, except for SMILE, that caused larger stresses on the posterior surface for more severe pathological cases. As the pathology progressed ($\gamma = 0.4$–0.1), the changes in the strain field with respect to the pre-surgical situation are very small, since the cornea was already highly deformed at pre-surgical conditions due to tissue degradation and the procedures were not causing any further deformation.

From an optical perspective, as the severity of the pathology worsened, none of the three procedures appeared to exacerbate the cone's development in terms of anterior and posterior curvature (Figure 7) compared to pre-surgical conditions (dashed line), as they demonstrated similar behavior. This observation suggests that surgeries may play a limited role in directly causing post-surgical ectasia. Instead, it seems more plausible that the mechanical changes induced by refractive procedures may accelerate the progression of an underlying pathological condition rather than being the primary cause of an iatrogenic disease. However, long-term observation was not included in this study to analyze the progression of ectasia. As it will be discussed in the study's limitations, only snapshots of the pathology at progressive severity were analyzed. Our hypothesis for the long-term evolution of the disease is that refractive treatments causing significant mechanical changes in the corneal structure (particularly in the posterior region) carry a higher risk of causing further worsening of the pathology.

In the review by Moshirfar et al. (Moshirfar et al., 2021), LASIK was identified as the surgery with the highest rate of post-surgical ectasia compared to PRK and SMILE. However, this result is influenced by the fact that LASIK is the most commonly performed procedure, inherently increasing the likelihood of encountering post-surgical complications. Although SMILE was developed to be less invasive and more preserving of stromal tissue, it remains relatively new, making it challenging to determine definitively whether it is safer than LASIK. While SMILE avoids the creation of a flap, the removal of a lenticule from the corneal thickness introduces a geometric discontinuity, likely resulting in the residual load being entirely borne by the RSB rather than the cap above the lenticule removal site. In our study, SMILE was found to exert the greatest mechanical impact on the posterior region of pathological corneas in the immediate post-surgical scenario. This finding suggests that SMILE could potentially increase the risk of ectasia progression in a pathological cornea over the long-term. PRK, on the other hand,

shows a lower rate of post-surgical ectasia compared to LASIK (Moshirfar et al., 2021), likely because it involves only surface ablation, thereby preserving a larger percentage of the RSB. In this study, we observed that the posterior cornea was minimally affected by PRK, even in the most severe cases, making it less likely to promote the progression of ectasia, when present.

In summary, the three refractive procedures exhibited distinct mechanical behaviors in both healthy and pathological corneal models. However, their impact on the final cone severity, as classified by the Belin system, was equivalent in the immediate post-surgical scenario. To ensure safety, the refractive treatment with the lowest mechanical impact should be selected, as it may reduce the long-term risk of ectasia progression.

Finally, this work is not exempt from limitations that may restrict the observations drawn from this study. First, time has not been considered as variable to evaluate the progression of the disease; specific moments of the disease were analyzed, but the disease progression over time could not be evaluated: in this way, the effect of the surgeries on the pathological cornea is evaluated in the immediate post-surgical condition and not after some time (months or years), which can be relevant in ectatic diseases. In the future, time should be included in the simulations to analyze the post-surgical impact of the refractive procedure in the long-term.

As already discussed above, the choice of a continuum-based purely elastic formulation may not be the most appropriate for mimicking advanced stages of ectasia disease, as it appears to be incapable of capturing the complex processes undergoing at the microscopic level in corneal tissue, that cause a significant reduction of the thickness. A growth model better replicates advanced stages of ectasia, as it is able to capture the structural changes associated with the disease (Fantaci et al., 2024b).

Patient-specific data were not included in this study, as the aim was to eliminate inter-patient variability due to the specific geometrical characteristics of individual corneas. In future work, it would be valuable to investigate the impact of refractive procedures on patients who developed post-surgical ectasia, acknowledging the challenges in acquiring such data. With the versatility of FE models, it may be possible to assess whether a specific surgical procedure would have a greater or lesser impact on patient's corneas. This approach could also serve as a decision-making tool for surgeons, aiding in the selection of the most appropriate procedure for individual patients.

5 Conclusion

This study presented an optomechanical analysis of healthy and pathological corneas before and after laser refractive surgery. The analysis focused on the immediate post-surgical response of corneal tissue to different refractive procedures and demonstrated that, even in the most severe cases, the surgeries did not exacerbate the pre-existing pathological condition. These findings suggest that laser refractive surgeries might act as a catalyst for the progression of a sub-clinical pathological state of the corneal tissue rather than being the primary cause of post-surgical ectasia in entirely healthy corneas. Among the three procedures, PRK was found to be the least invasive treatment from a mechanical perspective, making it less likely to promote the progression of ectasia, when present. In contrast, SMILE showed the greatest impact on the posterior surface in more advanced stages of the disease, suggesting a potential long-term risk for ectasia progression.

Data availability statement

The original contributions presented in the study are included in the article/Supplementary Material. Further inquiries can be directed to the corresponding author.

Author contributions

BF: Conceptualization, Investigation, Methodology, Writing–original draft, Writing–review and editing. JR: Methodology, Supervision, Writing–review and editing. VS: Investigation, Writing–review and editing. LV: Investigation, Writing–review and editing. BC: Methodology, Supervision, Writing–review and editing.

Funding

The author(s) declare that financial support was received for the research, authorship, and/or publication of this article. This project has received funding from the European Union's Horizon 2020 research and innovation program under the Marie Skłodowska-Curie grant agreement No 956720 and the Department of Industry and Innovation (Government of Aragon) through the research group Grant T24–23R (cofinanced with Feder 2014-2020: Construyendo Europa desde Aragon). Part of the work was performed by the ICTS "NANBIOSIS" specifically by the High Performance Computing Unit (U27), of the CIBER in Bioengineering, Biomaterials and Biomedicine (CIBER-BBN at the University of Zaragoza-Spain).

Conflict of interest

The authors declare that the research was conducted in the absence of any commercial or financial relationships that could be construed as a potential conflict of interest.

Generative AI statement

The author(s) declare that no Generative AI was used in the creation of this manuscript.

Publisher's note

Supplementary material

The Supplementary Material for this article can be found online at: https://www.frontiersin.org/articles/10.3389/fbioe.2025.1548539/full#supplementary-material

SUPPLEMENTARY FIGURE S1

Distribution of maximum principal stress and maximum principal logarithmic strain in the LASIK model, with anisotropic (left) and isotropic (right) material models assigned to the post-surgical flap. Very small differences in stress and strain distribution are observed when varying the flap material properties in the LASIK model, suggesting they can be neglected.

References

Akhtar, S., Bron, A. J., Salvi, S. M., Hawksworth, N. R., Tuft, S. J., and Meek, K. M. (2008). Ultrastructural analysis of collagen fibrils and proteoglycans in keratoconus. *Acta Ophthalmol.* 86, 764–772. doi:10.1111/j.1755-3768.2007.01142.x

Alkanaan, A., Barsotti, R., Kirat, O., Almubrad, T., Khan, A., and Akhtar, S. (2017). Ultrastructural study of peripheral and central stroma of keratoconus cornea. *Br. J. Ophthalmol.* 101, 845–850. doi:10.1136/bjophthalmol-2016-309834

Ariza-Gracia, M., Zurita, J., Piñero, D. P., Calvo, B., and Rodríguez-Matas, J. F. (2016). Automatized patient-specific methodology for numerical determination of biomechanical corneal response. *Ann. Biomed. Eng.* 44, 1753–1772. doi:10.1007/s10439-015-1426-0

Ariza-Gracia, M. A., Flecha-Lescún, J., Büchler, P., and Calvo, B. (2020). Corneal biomechanics after intrastromal ring surgery: optomechanical *in silico* assessment. *Transl. Vis. Sci. Technol.* 9, 26. doi:10.1167/tvst.9.11.26

Belin, M. W., Kundu, G., Shetty, N., Gupta, K., Mullick, R., and Thakur, P. (2020). Abcd: a new classification for keratoconus. *Indian J. Ophthalmol.* 68, 2831–2834. doi:10.4103/ijo.IJO_2078_20

Dias, J. M., and Ziebarth, N. M. (2013). Anterior and posterior corneal stroma elasticity assessed using nanoindentation. *Exp. Eye Res.* 115, 41–46. doi:10.1016/j.exer.2013.06.004

Doll, T., Moore, J., Shihab, A. H., Lopes, B. T., Eliasy, A., Maklad, O., et al. (2020). Which feature influences on-eye power change of soft toric contact lenses: design or corneal shape? *PLoS ONE* 15, e0242243. doi:10.1371/journal.pone.0242243

Dupps, B. W. J., and Seven, I. (2016). A large-scale computational analysis of corneal structural response and ectasia risk in myopic laser refractive surgery (an american ophthalmological society thesis). *Trans. Am. Ophthalmol. Soc.* 114, 1.

Eliasy, A., Abass, A., Lopes, B. T., Vinciguerra, R., Zhang, H., Vinciguerra, P., et al. (2020). Characterization of cone size and centre in keratoconic corneas. *J. R. Soc. Interface* 17, 20200271. doi:10.1098/rsif.2020.0271

Falgayrettes, N., Patoor, E., Cleymand, F., Zevering, Y., and Perone, J. M. (2023). Biomechanics of keratoconus: two numerical studies. *PLoS ONE* 18, e0278455. doi:10.1371/journal.pone.0278455

Fantaci, B., Calvo, B., Barraquer, R., Picó, A., and Ariza-Gracia, M. A. (2024a). Establishing standardization guidelines for finite-element optomechanical simulations of refractive laser surgeries: an application to photorefractive keratectomy. *Transl. Vis. Sci. and Technol.* 13, 11. doi:10.1167/tvst.13.5.11

Fantaci, B., Calvo, B., and Rodríguez, J. F. (2024b). Modeling biological growth of human keratoconus: on the effect of tissue degradation, location and size. *Comput. Biol. Med.* 180, 108976. doi:10.1016/j.compbiomed.2024.108976

Ferrari, G., and Rama, P. (2020). The keratoconus enigma: a review with emphasis on pathogenesis. *Ocul. Surf.* 18, 363–373. doi:10.1016/j.jtos.2020.03.006

Flecha-Lescún, J., Calvo, B., Zurita, J., and Ángel Ariza-Gracia, M. (2018). Template-based methodology for the simulation of intracorneal segment ring implantation in human corneas. *Biomechanics Model. Mechanobiol.* 17, 923–938. doi:10.1007/s10237-018-1013-z

Fogla, R., Luthra, G., Chhabra, A., Gupta, K., Dalal, R., and Khamar, P. (2020). Preferred practice patterns for photorefractive keratectomy surgery. *Indian J. Ophthalmol.* 68, 2847–2855. doi:10.4103/ijo.IJO_2178_20

Francis, M., Shetty, R., Padmanabhan, P., Vinciguerra, R., Vinciguerra, P., Lippera, M., et al. (2023). New simulation software to predict postoperative corneal stiffness before laser vision correction. *J. Cataract Refract. Surg.* 49, 620–627. doi:10.1097/j.jcrs.0000000000001169

Gefen, A., Shalom, R., Elad, D., and Mandel, Y. (2009). Biomechanical analysis of the keratoconic cornea. *J. Mech. Behav. Biomed. Mater.* 2, 224–236. doi:10.1016/j.jmbbm.2008.07.002

Katzengold, R., Gefen, A., Sorkin, N., Smadja, D., and Varssano, D. (2021). Simulation of the biomechanical effects induced by laser *in situ* keratomileusis (LASIK) for different levels of ablation in normal corneas. *Eye Lond.* 35, 996–1001. Epub 2020 Jun 16. doi:10.1038/s41433-020-1017-7

Kenney, M. C., and Brown, D. J. (2003). The cascade hypothesis of keratoconus. *Contact Lens Anterior Eye* 26, 139–146. doi:10.1016/S1367-0484(03)00022-5

Kim, T. H., Lee, D., and Lee, H. I. (2007). The safety of 250 μm residual stromal bed in preventing keratectasia after laser *in situ* keratomileusis (LASIK). *J. Korean Med. Sci.* 22, 142–145. doi:10.3346/jkms.2007.22.1.142

Kim, T. I., Alió del Barrio, J. L., Wilkins, M., Cochener, B., and Ang, M. (2019). Refractive surgery. *Lancet* 393, 2085–2098. doi:10.1016/S0140-6736(18)33209-4

Klein, S. A., and Mandell, R. B. (1995). Axial and instantaneous power conversion in corneal topography. *Investigative Ophthalmol. and Vis. Sci.* 36, 2155–2159.

Lv, X., Zhang, F., Song, Y., Zhai, C., Guo, N., Lai, L., et al. (2023). Corneal biomechanical characteristics following small incision lenticule extraction for myopia and astigmatism with 3 different cap thicknesses. *BMC Ophthalmol.* 23, 42. doi:10.1186/s12886-023-02786-8

Martínez-Abad, A., and Piñero, D. P. (2017). New perspectives on the detection and progression of keratoconus. *J. Cataract Refract. Surg.* 43, 1213–1227. doi:10.1016/j.jcrs.2017.07.021

Meek, K. M., and Boote, C. (2009). The use of x-ray scattering techniques to quantify the orientation and distribution of collagen in the corneal stroma. *Prog. Retin. Eye Res.* 28, 369–392. doi:10.1016/j.preteyeres.2009.06.005

Montanino, A., van Overbeeke, S., and Pandolfi, A. (2023). Modeling the biomechanics of laser corneal refractive surgery. *J. Mech. Behav. Biomed. Mater.* 145, 105998. doi:10.1016/j.jmbbm.2023.105998

Moshirfar, M., Brown, M. W., Heiland, T. W., Rosen, M. B., Ronquillo, D. B., and Hoopes, Y. C. (2019). Comparative analysis of lasik flap diameter and its centration using two different femtosecond lasers. *Med. Hypothesis, Discov. and Innovation Ophthalmol. J.* 8, 241–249.

Moshirfar, M., Tukan, A. N., Bundogji, N., Liu, H. Y., McCabe, S. E., Ronquillo, Y. C., et al. (2021). Ectasia after corneal refractive surgery: a systematic review. *Ophthalmol. Ther.* 10, 753–776. doi:10.1007/s40123-021-00383-w

Pandolfi, A., Fotia, G., and Manganiello, F. (2009). Finite element simulations of laser refractive corneal surgery. *Eng. Comput.* 25, 15–24. doi:10.1007/s00366-008-0102-5

Pandolfi, A., and Holzapfel, G. A. (2008). Three-dimensional modeling and computational analysis of the human cornea considering distributed collagen fibril orientations. *J. Biomechanical Eng.* 130, 061006. doi:10.1115/1.2982251

Pandolfi, A., and Manganiello, F. (2006). A model for the human cornea: constitutive formulation and numerical analysis. *Biomechanics Model. Mechanobiol.* 5, 237–246. doi:10.1007/s10237-005-0014-x

Randleman, J. B., Dawson, D. G., Grossniklaus, H. E., McCarey, B. E., and Edelhauser, H. F. (2008). Depth-dependent cohesive tensile strength in human donor corneas: implications for refractive surgery. *J. Refract. Surg.* 24, S85–S89. doi:10.3928/1081597x-20080101-15

Randleman, J. B., Russell, B., Ward, M. A., Thompson, K. P., and Stulting, R. D. (2003). Risk factors and prognosis for corneal ectasia after lasik. *Ophthalmology* 110, 267–275. doi:10.1016/S0161-6420(02)01727-X

Reinstein, D. Z., Archer, T. J., and Gobbe, M. (2014). Small incision lenticule extraction (SMILE): history, fundamentals of a new refractive surgery technique and clinical outcomes. *Eye Vis. Lond.* 1, 3. doi:10.1186/s40662-014-0003-1

Reinstein, D. Z., Archer, T. J., and Randleman, J. B. (2013). Mathematical model to compare the relative tensile strength of the cornea after prk, lasik, and small incision lenticule extraction. *J. Refract. Surg.* 29, 454–460. doi:10.3928/1081597X-20130617-03

Roy, A. S., and Dupps, W. J. (2011). Patient-specific computational modeling of keratoconus progression and differential responses to collagen cross-linking. *Investigative Ophthalmol. Vis. Sci.* 52, 9174–9187. doi:10.1167/iovs.11-7395

Roy, A. S., Rocha, K. M., Randleman, J. B., Stulting, R. D., and Dupps, W. J. (2013). Inverse computational analysis of invivo corneal elastic modulus change after collagen crosslinking for keratoconus. *Exp. Eye Res.* 113, 92–104. doi:10.1016/j.exer.2013.04.010

Sánchez, P., Moutsouris, K., and Pandolfi, A. (2014). Biomechanical and optical behavior of human corneas before and after photorefractive keratectomy. *J. Cataract Refract. Surg.* 40, 905–917. doi:10.1016/j.jcrs.2014.03.020

Santhiago, M. R., Giacomin, N. T., Smadja, D., and Bechara, S. J. (2016). Ectasia risk factors in refractive surgery. *Clin. Ophthalmol.* 10, 713–720. doi:10.2147/OPTH.S51313

Santhiago, M. R., Smadja, D., Gomes, B. F., Mello, G. R., Monteiro, M. L., Wilson, S. E., et al. (2014). Association between the percent tissue altered and post-laser *in situ* keratomileusis ectasia in eyes with normal preoperative topography. *Am. J. Ophthalmol.* 158, 87–95.e1. Epub 2014 Apr 13. doi:10.1016/j.ajo.2014.04.002

Santodomingo-Rubido, J., Carracedo, G., Suzaki, A., Villa-Collar, C., Vincent, S. J., and Wolffsohn, J. S. (2022). Keratoconus: an updated review. *Contact Lens Anterior Eye* 45, 101559. doi:10.1016/j.clae.2021.101559

Schmack, I., Dawson, D. G., McCarey, B. E., Waring, G. O. I., Grossniklaus, H. E., and Edelhauser, H. F. (2005). Cohesive tensile strength of human lasik wounds with histologic, ultrastructural, and clinical correlations. *J. Refract. Surg.* 21, 433–445. doi:10.3928/1081-597X-20050901-04

Simonini, I., Annaidh, A. N., and Pandolfi, A. (2022). Numerical estimation of stress and refractive power maps in healthy and keratoconus eyes. *J. Mech. Behav. Biomed. Mater.* 131, 105252. doi:10.1016/j.jmbbm.2022.105252

Simonini, I., and Pandolfi, A. (2015). Customized finite element modelling of the human cornea. *PLoS ONE* 10, 01304266–e130523. doi:10.1371/journal.pone.0130426

Sridhar, M. S. (2018). Anatomy of cornea and ocular surface. *Indian J. Ophthalmol.* 66, 190–194. doi:10.4103/ijo.IJO_646_17

Sutton, G., Lawless, M., and Hodge, C. (2014). Laser *in situ* keratomileusis in 2012: a review. *Clin. Exp. Optometry* 97, 18–29. doi:10.1111/cxo.12075

Vahdati, A., Seven, I., Mysore, N., Randleman, J. B., and Dupps, W. J. (2016). Computational biomechanical analysis of asymmetric ectasia risk in unilateral post-lasik ectasia. *J. Refract. Surg.* 32, 811–820. doi:10.3928/1081597X-20160929-01

Wang, C., Li, X., Guo, Y., He, R., Guo, H., and Chen, W. (2022). Effects of laser *in situ* keratomileusis and small-incision lenticule extraction on corneal biomechanical behavior: a finite element analysis. *Front. Bioeng. Biotechnol.* 10, 855367. doi:10.3389/fbioe.2022.855367

Wang, S., and Hatami-Marbini, H. (2021). Constitutive modeling of corneal tissue: influence of three-dimensional collagen fiber microstructure. *J. Biomechanical Eng.* 143, 031002. doi:10.1115/1.4048401

Winkler, M., Chai, D., Kriling, S., Nien, C. J., Brown, D. J., Jester, B., et al. (2011). Nonlinear optical macroscopic assessment of 3-d corneal collagen organization and axial biomechanics. *Investigative Ophthalmol. Vis. Sci.* 52, 8818–8827. doi:10.1167/iovs.11-8070

Wolle, M. A., Randleman, J. B., and Woodward, M. A. (2016). Complications of refractive surgery: ectasia after refractive surgery. *Int. Ophthalmol. Clin.* 56, 127–139. doi:10.1097/IIO.0000000000000102

frontiers | Frontiers in Bioengineering and Biotechnology

TYPE Original Research
PUBLISHED 05 March 2025
DOI 10.3389/fbioe.2025.1504769

OPEN ACCESS

EDITED BY
Norberto López Gil,
University of Murcia, Spain

REVIEWED BY
Brian Vohnsen,
University College Dublin, Ireland
Maciej Bartuzel,
Nicolaus Copernicus University in Toruń, Poland

*CORRESPONDENCE
Milad Salimibani,
milad.salimibani@pwr.edu.pl

RECEIVED 01 October 2024
ACCEPTED 11 February 2025
PUBLISHED 05 March 2025

CITATION
Dahaghin A, Salimibani M, Boszczyk A, Jóźwik A, Grasa J, Przeździecka-Dołyk J and Siedlecki D (2025) Biomechanical simulations of crystalline lens oscillations resulting from the changes in the gaze in an accommodated eye. *Front. Bioeng. Biotechnol.* 13:1504769. doi: 10.3389/fbioe.2025.1504769

Biomechanical simulations of crystalline lens oscillations resulting from the changes in the gaze in an accommodated eye

Ali Dahaghin[1], Milad Salimibani[1]*, Agnieszka Boszczyk[1], Agnieszka Jóźwik[1], Jorge Grasa[2,3], Joanna Przeździecka-Dołyk[4,5,6] and Damian Siedlecki[1]

[1]Department of Optics and Photonics, Wroclaw University of Science and Technology, Wrocław, Poland, [2]Aragón Institute of Engineering Research (I3A), University of Zaragoza, Zaragoza, Spain, [3]Centro de Investigación Biomédica en Red en Bioingeniería, Biomateriales y Nanomedicina (CIBER-BBN), Zaragoza, Spain, [4]Deanery of Clinical Sciences, University of Edinburgh, Edinburgh, United Kingdom, [5]Department and Clinic of Ophthalmology, Wroclaw Medical University, Wroclaw, Poland, [6]CREO Research and Development Centre SPEKTRUM Clinical Ophthalmic Center, Wroclaw, Poland

Purpose: The goal of the study is to introduce a generic, versatile biomechanical model that aims to reproduce the dynamic wobbling phenomenon.

Methods: A systematic strategy is used, which includes a) capturing the *in vivo* data on a group of healthy volunteers, b) analyzing the changes in Purkinje images over time, and c) performing the combined biomechanical and optical simulations to develop the model that might be useful for understanding the mechanical behavior of the lens during wobbling and its influence on ocular dynamics.

Results: Examples of lens wobbling patterns for six measured eyes were presented, and parameters characterizing the oscillatory motion were determined, including frequency of oscillations, Q-factor, damping factor and time constant. The average values of these parameters are the following: frequency: 20.0 $\pm$ 2.4 Hz; Q-factor: 1.86 $\pm$ 0.44; damping factor: 0.27 $\pm$ 0.06; time constant: 0.11 $\pm$ 0.06 s. The data reproduced by means of simulations: frequency: 19.3 Hz; Q-factor: 2.17; damping factor: 0.23; time constant: 0.15 s. This comparison reveals a good agreement between the measured and reconstructed data with the values being within the standard deviation limits.

Conclusion: The developed generic model together with the presented methodology is able to reconstruct the typical crystalline lens wobbling dynamics with a satisfying accuracy. However, the observed intersubject variability highlights the need for personalized biomechanical models. The introduced model may constitute the basis for future individualization of the data, bringing broad perspectives for prospective investigations aimed to explain the biomechanical mechanisms within the eye.

KEYWORDS

***in vivo* crystalline lens oscillations, lens inertial motion, lens wobbling, finite element method, Purkinje imaging, ocular biomechanics**

1 Introduction

The human eye possesses one of the fastest muscles in the human body, capable of generating 40° rotations in roughly 100 ms (Silva et al., 2020). This rapid movement allows us to quickly shift our gaze towards objects or points of interest in our field of vision. Focusing on objects involves adjusting the focal length of our eyes to make the selected object appear sharp and clear (Wang and Pierscionek, 2019; Cabeza-Gil et al., 2021), a process that becomes less effective with age. This process, called accommodation, is controlled by the contraction and relaxation of the ciliary muscles. When we look at distant object, our lens becomes thinner, the curvatures of its surfaces become smaller; whereas when we look at something near, the lens becomes thicker, and its curvatures increase. These changes in the shape of the lens are accompanied by a change in the tension of the zonular fibers that suspend the lens in place.

The crystalline lens, as a vital component of the eye's optical system, is also known to display intriguing wobbling movements within the eye. The impact of changing the direction of gaze on the dynamic movement of the crystalline lens is not yet completely understood. This movement is attributed to the lens being suspended by a network of delicate fibers known as zonular fibers. It is described as "inertial oscillatory", which means that it occurs due to the lens's inertia, or resistance to changes in motion, and it follows a back-and-forth or oscillatory pattern (Tabernero and Artal, 2014; Pan et al., 2023). These movements may become smaller, and the oscillations may be less apparent in older individuals due to increased tissue stiffness. They also tend to be larger when the eye accommodates (Deubel and Bridgeman, 1995; Nyström et al., 2015). Studies indicate that an optical setup can indirectly measure and study lens wobbling (Tabernero et al., 2016), by utilizing the variations in the locations of the 1st and the 4th Purkinje images, which are reflections of light from the first surface of the cornea (*PI*) and the second surface of the lens (*PIV*). This approach uses Purkinje image eye-tracking techniques to analyze lens wobbling effects indirectly.

Exploring the complexities of crystalline lens wobbling has become a rapidly growing and challenging area of study (Tabernero et al., 2016; Yamagishi et al., 2020; Mardanbegi et al., 2020; Llapashtica et al., 2024). In addition, in modelling research, it is known that the lens wobbling phenomenon can be reproduced either for natural crystalline lens or for artificial implant (Martin et al., 2009; Boszczyk et al., 2023). However, to date, there has not been a sufficient number of research papers that focus on providing an accurate representation of biomechanical simulations based on finite elements (Dahaghin et al., 2024). This gap in the literature can be overcome with the studies presenting a thorough investigation into this critical aspect of eye biomechanics. In this paper, we focus on capturing and analysing Purkinje image trajectories, followed by simulating the mechanical behavior of the lens during wobbling. Subsequently, these findings are used to conduct optical simulations, which aim to simulate a wobbling pattern of the Purkinje images trajectories, caused by the mechanically simulated lens movement. This research provides valuable insights into how the gaze changes affect the dynamic arrangement of the lens, which is manifested as a temporal separation of Purkinje images *PIV* and *PI*.

2 Materials and methods

The research study followed a structured approach, as depicted in Figure 1. The first step involved capturing the movement of the 4th and the 1st Purkinje images in response to eye rotation, as well as determining the spatial separation of these images due to lens wobbling.

At this point it is important to note that what one can observe through Purkinje imaging is not the direct motion of the lens itself, but rather the optical effect of this motion—the relative motion of *PIV* and *PI*, which are specular reflections from the posterior surface of the lens and the anterior surface of the cornea, respectively. The information retrieved from Purkinje images reflects only the *PIV-PI* separation, not the exact arrangement of the lens within the eye. Therefore, to derive the physical arrangement of the lens from Purkinje image data, a workflow combining both mechanical and optical simulations need to be applied. This integrated approach allows us to model the lens dynamic behavior and its corresponding optical effects, enabling the extraction of lens arrangement data from the observed Purkinje performance. This methodology, described in detail in our previous work (Boszczyk et al., 2023), bridges the gap between optical observations and mechanical lens dynamics.

Therefore, the next stage of our investigation, we implemented this data workflow, aiming to determine the lens wobbling pattern and its parameters, using finite element simulations under the same conditions as the *in vivo* experimental setup, i.e.,: rotation amplitude, average dimensions, IOP, etc. The output of these mechanical simulations was subsequently utilized as an input for optical simulations in the third stage. The objective of these optical simulations was to illustrate the paths of Purkinje images and to assess the temporal spatial distance between them. Finally, the image separations obtained from the combined mechanical and optical simulations were compared to the *in vivo* data for further analysis and validation.

2.1 *In vivo* experiment

2.1.1 Optical setup

The *in vivo* data were captured with use of the optical setup (see Figure 2) based on the architecture of a Dynamic Purkinje-meter introduced by Tabernero and Artal (2014). In order to increase both the sampling frequency and the spatial resolution a 1.3-megapixel CMOS image sensor (resolution: 1,280 × 1,024 pixels; pixel size: 10 μm × 10 μm) was incorporated in the compact high-speed camera system (FASTCAM Mini UX50, Photron Limited, Tokyo, Japan). Such a modification enabled us to capture sequences of Purkinje images at the speed of 640 frames per second. The camera was equipped with 0.5× telecentric lens (GoldTL™ line, Edmund Optics), ensuring the constant magnification across the image. The effective size of the pixel on the recorded image was estimated to be 19.5 μm. A semicircular illuminator (SI), consisting of 7 infrared diodes (dominant wavelength of 850 nm), was placed approximately 12 cm in front of the eye. The peripheral fixational yellow diodes were mounted on a plastic plate at an angular distance of 10° from the central diode in order to stimulate the subject to change the gaze (Figure 2B). The fixation target (F) was operated by the software in order to adjust both its brightness and flickering frequency. The flickering frequency

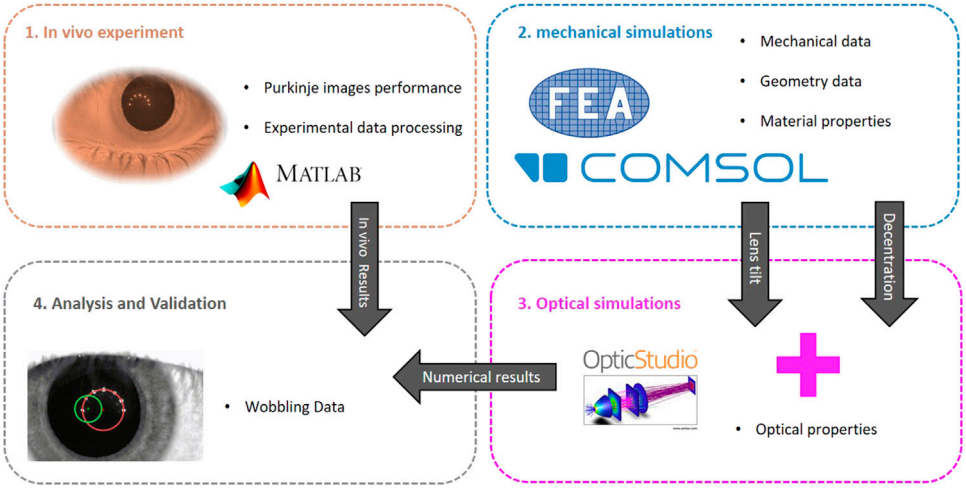

FIGURE 1
Steps involved in the study and simulation process. The diagram outlines the key stages and their interconnections, providing a visual guide to the overall workflow.

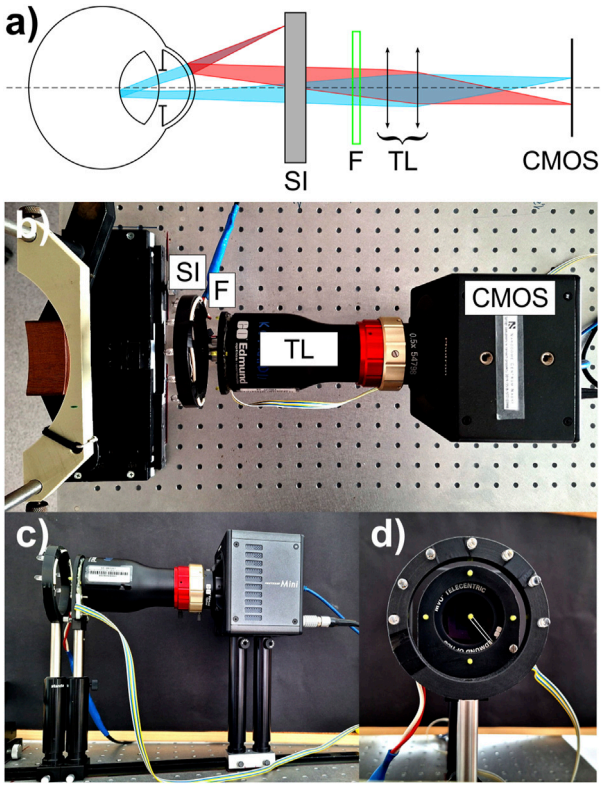

FIGURE 2
Experimental setup: **(A)** schematic presentation, **(B)** top view, **(C)** side view, **(D)** front view. Explanation of abbreviations: SI, semicircular illuminator; F, fixation target; TL, telecentric lens; CMOS, image sensor (camera).

between the central and the peripheral diodes was set to 1.25 Hz. This value facilitated multiple saccades between blinks, while also enabling the positions of the Purkinje images to stabilize prior to the subsequent eye movement. The measurements were conducted under conditions of low brightness of fixation target, chosen to ensure that the tracking of the diodes was comfortable for the subject while minimizing the visibility of reflections from the corneal surface. This approach allowed the fixation diode images to remain unobtrusive, thereby not interfering with the readings of the positions of the Purkinje images generated by the infrared diodes.

2.1.2 Human subjects and protocol

In order to obtain the original *in vivo* data for further processing and validation with optical/mechanical simulations outcomes, five subjects (3 males and 2 females), aged 21, 45, 23, 23 and 25 y.o., respectively, took part in the experimental part. Informed consent was obtained from them and the study protocol was in accordance with the guidelines of the Declaration of Helsinki. It was approved by Bioethics Committee of Wrocław Medical University (application No: 2021/0131). The subjects' eyes were randomly chosen for examination. All the subjects–apart from Subject #5 – were either emmetropic or slightly myopic up to −1.0 D in spherical equivalent. Spherical equivalent of Subject #5 left was equal to −2.5 D. None of the subjects has ever experienced any ocular intervention or treatment. The effective amplitude of accommodation was estimated to be about 8–9 D (5 D for the eldest Subject #3). The location of the near point of accommodation was previously verified to determine whether the person was able to see the target clearly at a distance of 12 cm. Examination was monocular. The subjects were asked to attentively follow the fixation target with the measured eye. The captured video contained a set of up to 4 both temporal-central-nasal and nasal-central-temporal saccades. In order to unify the processing methodology, it was assumed that only the saccades that finished in central position will be selected for further consideration and quantitative analysis.

2.2 Simulations

Optomechanical simulation of the crystalline lens refers to a computational modelling approach that combines mechanics

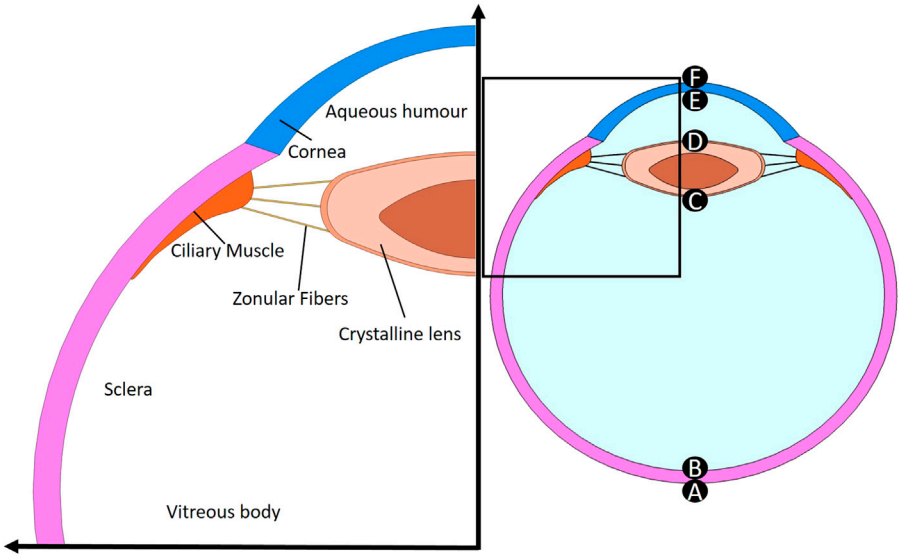

FIGURE 3
Geometry of the model containing the main and the most influential elements in eye biomechanics: lens, vitreous body, zonular fibers, cornea, sclera, aqueous humour and ciliary muscle. Letters from A to F represent the apical points of the interfaces of the eye.

TABLE 1 Summary of geometrical parameters extracted from Zapata-Díaz et al. (2019) studies for 20 years old eye with an accommodation state of 2.5 dioptries.

Modelled structure	Radius [mm]	Thickness[a][mm]	Refractive index	Conic constant
Anterior corneal surface	7.87	0.574	1.376	−0.18
Posterior corneal surface	6.40	2.996	1.336	−0.12
Anterior lens surface	9.825	3.522	1.4332	−7.05
Posterior lens surface	−5.649	16.908	1.336	−4.6
Retina	−12.9	n.a.	n.a.	0.193

[a]Central thickness to the next surface.
The values marked with blue colour were subject to change with accommodation.

(structural properties) and optics (optical propagation and construction of Purkinje images) to simulate the oscillatory dynamics of the lens in response to saccadic eye motion. These simulations refer to computational modelling and analysis of the mechanical movement or vibrations of the crystalline lens in the human eye, taking into account its optical properties.

2.2.1 Mechanical simulations

The mechanical simulation of lens wobbling analyses the intricate dynamics of the lens' oscillatory motion. Its effective pattern is a complex outcome of the mechanical parameters of the neighbouring ocular structures and their interaction within the eye globe. This simulation aims to accurately replicate the physical behavior of the lens as it wobbles. To conduct these analyses, a 2D numerical model was developed in COMSOL Multiphysics v5.6, using a mechanical design of the eye globe. A 2D model was considered sufficiently precise for this analysis because the Purkinje images generated by lens rotation occur within the same plane, allowing the out-of-plane dimension to be neglected. This model contains the main and most influential elements in eye biomechanics: lens, vitreous body, zonular fibers, cornea, sclera, aqueous humour and ciliary muscle (see Figure 3).

2.2.1.1 Geometry

Accurate representation of the eye's geometry is a crucial consideration for realistic and reliable Finite Element simulations. In this study, all the geometry data was adopted from an accommodated and age-dependent optical eye model based on *in vivo* measurements presented by Zapata-Díaz et al. (2019).

The most commonly used optical surface in the eye is a conic surface. For surfaces, such as those found in lens and cornea and when working with a cylindrical coordinate system, the z-coordinate is given by an equation that depends on the specific conic shape. The z-coordinate of the standard surface depends on the type of surface is used and is determined by Equation (1):

$$z = \frac{cr^2}{1 + \sqrt{1 - (1 + k)c^2r^2}} \tag{1}$$

where c represents the curvature, r stands for the radial coordinate, and k is the conic constant.

TABLE 2 Zonular fibers arrangement data. Connection points and thickness of the band.

Zonular fibers	X [mm]	Y [mm]	Thickness [mm]
Anterior	0.34	0.67	0.40
Equatorial	0.00	0.00	0.50
Posterior	0.26	0.74	0.50

Table 1 shows the calculated model parameters for 20 years old eye, with an accommodation state of 2.5 diopters. The total distance between the posterior surface of the eyeball and the anterior cornea is typically referred to as the axial length of the eye, which here is 24 mm.

The lens is suspended in place by thin zonular fibers that attach to the lens capsule and extend to the ciliary body. Due to their different locations three zones are distinguished: anterior, equatorial, and posterior (Table 2). Together, these fibers create a support system that keeps the lens in place while allowing it to change shape as needed for clear vision at different distances. This strategy follows the approach of Lanchares et al. (2012), using the three connection points to attach the idealized zonular fibers and replicating their methodology for modeling fiber attachment to the lens and ciliary body, although Lanchares do not explicitly represent the fibers themselves but rather the direction of the forces they exert. Figure 4 presents the arrangement of the fibres on the lens capsule, with the dimensions shown in Table 2 used to position them according to the reference system located at the lens equator.

The minimal thickness of the capsule is 0.1 mm (Dai et al., 2017); other dimensions from the literature was employed for forming the lens' nucleus (Cabeza-Gil et al., 2021).

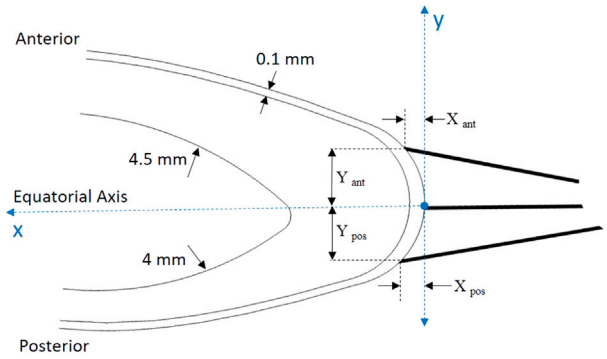

FIGURE 4
Position of the connection points where zonular fibers are attached in the capsule.

2.2.1.2 Material properties

The choice of material properties depends on the type of analysis being conducted, which varies based on the specific focus of the research, such as the deformation of particular tissues or, in our case, the dynamic response of the lens to the rotational motion of the eye.

To replicate the physiological conditions, vitreous body and aqueous humour are both modeled as viscous Newtonian incompressible fluids with constant pressure.This means that their behavior follows Newton's law of viscosity, where the shear stress is directly proportional to the rate of deformation (velocity gradient). Dynamic viscosity, which represents the resistance of fluids to flow under an applied shear stress, and density are, respectively, 0.00074 Pa·s and 1,000 kg/m^3 (Singh et al., 2017), which are assumed to be constant throughout the simulation.

In this study, other tissues are treated as linear elastic, isotropic, and homogeneous. This means that the materials were assumed to respond to mechanical stress linearly and have the same mechanical properties in all directions. Although their true behavior deviates from this idealization, this assumption remains valid for this first approach, as the focus of the study is on the lens movement, and the tissues will not experience large deformations. This approach allows us to simplify the model and focus on specific mechanical aspects relevant to the study. Different material properties for a normal eye are considered, to provide a comprehensive understanding of the mechanical properties. Table 3 presents the values of Young's modulus, Poisson's ratio, and density for the different eye components used in FE simulations.

2.2.1.3 Boundary conditions

The sclera is the white outer layer of the eyeball. It is a tough and fibrous tissue that provides the eyeball with structural support. During eye movement, it was assumed that the shape and size of the sclera remained constant and did not undergo any deformation; additionally, its center, acting as the pivot point for the rotation of the eyeball, remains fixed and does not undergo any linear movement. It underwent a 10 deg rotation (angular movement), and the angular velocity was assumed to follow the 10 deg range gaze profile reported by Collewijn et al. (1988) with the peak velocity of 300 deg/s (c.a. 5.67 rad/s). Throughout this movement, mechanical displacement data were recorded for the apical points noted as A to F in Figure 3. Under the assumption of negligible deformation of the cornea and lens due to rotation, the apical points A-F provide sufficient information regarding the arrangement (tilt and decentration) of the lens within the eye globe. This allows for the optical simulation of the location of Purkinje images in accordance with Equation 2.

The eye contains a clear fluid that helps to maintain the eye globe shape by intraocular pressure (IOP). IOP plays a crucial role, therefore any changes in it can have an impact on the ocular structure and may be associated with certain diseases. To simulate the normal conditions in the described model, an initial pressure of 15 mmHg was set for the fluid part (Sarmiento et al., 2023). This value is within the typical range in a healthy eye. This pressure was applied to the inner surface of the sclera, lens, and ciliary body.

2.2.1.4 Mesh

Triangular elements are particularly useful for analyzing irregular or complex geometries, so to discretize both the solid and fluid domains, those elements were employed. A built-in quality assessment was used to evaluate the element quality, which is based on the equiangular skew. This assessment assigns a rating between 0 and 1, where a quality above 0.5 is considered acceptable (Etminan et al., 2023). This model contains a total of 44,522 elements and has an average element quality of 0.82. This optimal mesh size was selected after performing a sensitivity analysis of the model. It was

TABLE 3 Mechanical properties assigned to ocular tissues (Cabeza-Gil et al., 2021; Bocskai and Bojtár, 2013; Issarti et al., 2021; Osmers et al., 2021).

Modelled tissue		Young's modulus [kPa]	Poisson's ratio [-]	Density [kg/m^3]
Ciliary Muscle		350	0.47	1,225
Crystalline lens	Capsule	1,000	0.49	1,078
	Cortex	3	0.49	1,078
	Nucleus	0.3	0.49	1,078
Sclera		3,000	0.47	1,400
Cornea		400	0.42	1,400
Zonular Fibers		1,500	0.49	1,000

found that reducing the global mesh size parameter in the program did not significantly affect the outcome.

2.2.2 Optical simulations

To verify the experiment with the mechanical simulation results, an optical model of the eye including an illumination and a Purkinje reflection imaging system was created using Zemax OpticStudio (Zemax, 2024) software. The non-sequential software mode was used for this purpose. Detailed information about the designed system can be found in our previous paper (Boszczyk et al., 2023), with the modification that the parameters of the accommodated eye (Table 1) were used for the model, not the relaxed one. The output of the mechanical simulations (changes of x and y coordinates of each eye surface during the time) was used as an input data for optical simulations. The result of optical simulations are images showing the first and fourth Purkinje reflections (*PI* and *PIV*), corresponding to individual configurations of the eye surface positions obtained in mechanical simulations.The created optical model allows for determining a simple linear relationship between different alignments of the crystalline lens and the difference in the positions of *PIV-PI* images, when the eye (cornea) is positioned in front of the imaging system. For this purpose, images showing the corresponding Purkinje reflections were simulated for various lens locations and orientations. Then, the positions of these images were established through a systematic process. Initially, the centroids of the *PI* and *PIV* images corresponding to each diode were identified. Subsequently, two circles were fitted to these centroids—one for the *PI* reflections and another for the *PIV* reflections. The position of each Purkinje image was then defined as the center of the fitted circle.

3 Results

The relationship between the distance of Purkinje images (*PIV-PI*) and the position of the lens (derived through a linear fit of data estimated by means of optical simulations with $R^2 = 0.999$), took a form:

$$PIV - PI = 0.04147\,tilt - 1.059\,dec - 0.003 \quad (2)$$

where *PIV-PI* is expressed in mm, *dec*–a decentration of the anterior surface of the lens from corneal optical axis is expressed in mm, and lens *tilt* relative to an axis perpendicular to the corneal axis is expressed in degrees. The standard deviations for the determined coefficients were 0.00029 for *tilt*, 0.003 for *dec*, and 0.002 for the intercept, respectively. The above equation allowed for simplification and acceleration of the comparative analysis for various mechanical simulations with the experiment, without the need to perform optical simulations and detect the positions of Purkinje reflections for each mechanically simulated lens wobbling patterns.

For the *in vivo* experiment, the whole video recording captured for each of the subject was divided into two sets of sequences: one manifesting the rotation of the eye from the nose to the center and one presenting the motion from the temple to the center. Each set contained up to four sequences. Then, each sequence was then processed in order to retrieve the relative displacement of *PIV-PI* position that is associated with the arrangement of the crystalline lens within the eye globe. As it can be seen on an exemplary sequence video (Supplementary Material S1) the relative distance between *PIV* and *PI* Purkinje images varies with time (Figures 5, 6) so as the crystalline lens undergoes some fine, evanescent motion due to ocular inertia. It should be noted that on each of these plots the time = 0 s was set to the moment, when the maximum distance (maximum wobbling) between *PIV* and *PI* appeared. It can be seen that over time, the wobbling in these graphs is settling down. The outcomes imply that the eye rotations, both from the nose to the center and from the temple to the center, manifest consistent and stable behavior across the tested sequences.

As Tabernero and Artal (2014) pertinently noted, the crystalline lens wobbling motion can be successfully described by a harmonic oscillator characteristics, therefore we decided to use this description in analysis of the results (see the text boxes in Figures 5, 6). The focus of the analysis was on comprehensively examining key parameters including frequency, Q-factor, damping factor, and time constant. The variability of the parameters revealed distinct features for each individual subject and gaze direction, highlighting the importance of further investigation of the factors that influence energy dissipation (Behling et al., 2021) and temporal characteristics during these rotational movements.

As for frequency stability, rotations in both directions displayed roughly stable average frequencies, suggesting consistent oscillatory behavior. Q-factor variations highlight differences in energy

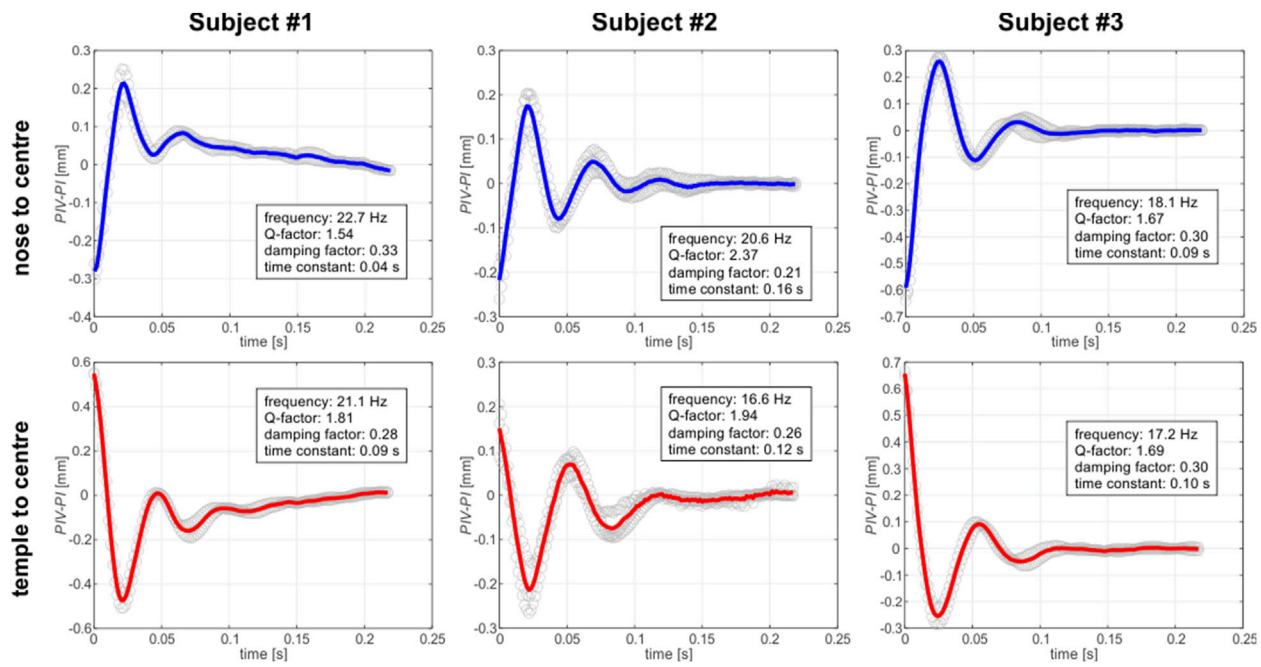

FIGURE 5
Wobbling patterns for captured for right eye (ER) of three different subjects, depending on the saccade direction. Each plot displays the *PIV-PI* separation as a function of time. Gray open circles correspond to the experimental data. Each single experimental dataset was shifted up or down so that the average level of the last 30 datapoints was equal to zero. Solid lines correspond to mean pattern of the experimental data: blue one for the nose-to-center direction of the gaze and the red one for the temple-to-center direction.

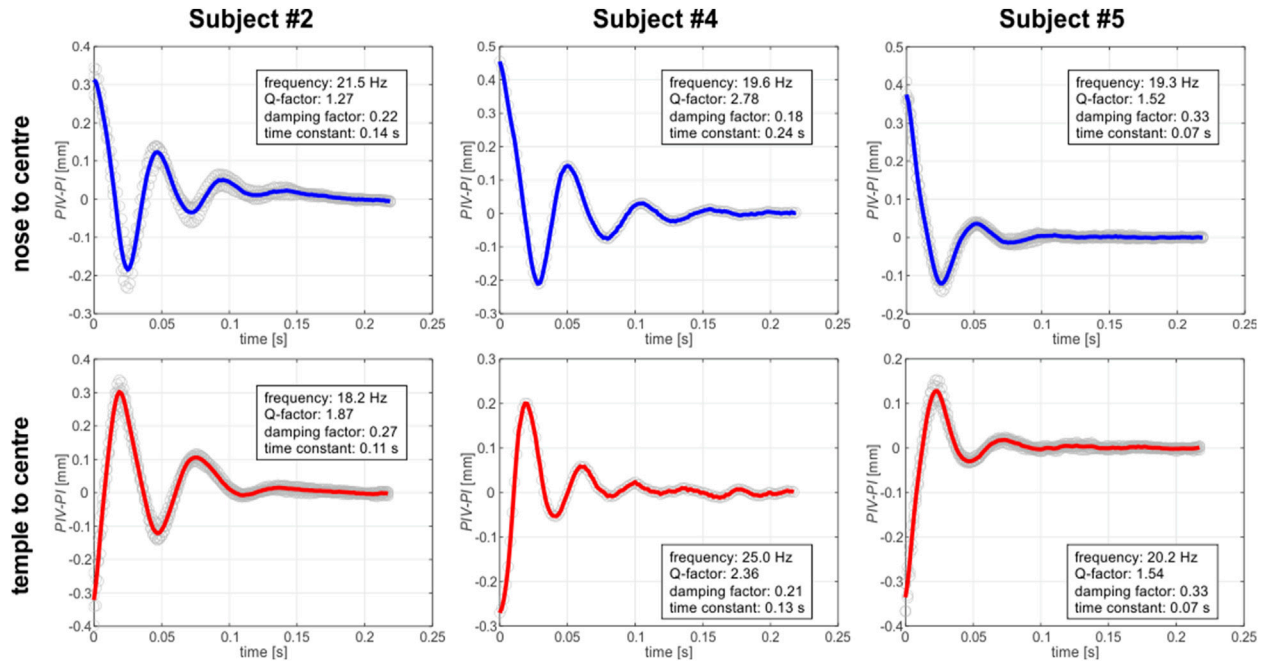

FIGURE 6
Wobbling patterns for captured for left eye (EL) of three different subjects, depending on the saccade direction. Each plot displays the *PIV-PI* separation as a function of time. Gray open circles correspond to the experimental data. Each single experimental dataset was shifted up or down so that the average level of the last 30 datapoints was equal to zero. Solid lines correspond to mean pattern of the experimental data: blue one for the nose-to-center direction of the gaze and the red one for the temple-to-center-direction.

TABLE 4 Averaged parameters of the wobbling trajectories for the whole group of subjects.

	Mean	Std dev	Range (min÷max)
Frequency [Hz]	20.0	2.4	(16.6÷25.0)
Q-factor	1.86	0.44	(1.27÷2.78)
Damping factor	0.27	0.06	(0.18÷0.33)
Time constant [s]	0.11	0.06	(0.04÷0.24)

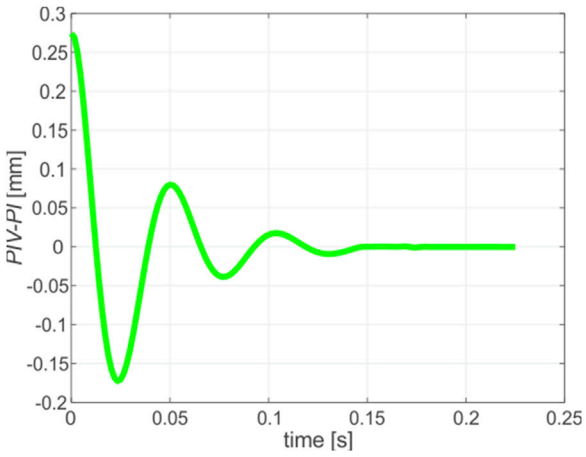

FIGURE 7
Wobbling trajectory obtained by means of combined FEM and opticals simulations.

dissipation during rotations, emphasizing the intricate nature of the eye's biomechanics. Intersubject variations of damping factors showed ability of the individual's eye to dampen oscillations, contributing to overall stability.

The averaged frequencies estimated for the examined group of subjects have comparatively small standard deviations (equal to 12%), suggesting relative stability in the lens oscillatory behavior across examined individuals (Table 4). The mean Q-factors show a moderate level of variability, suggesting differences in energy dissipation between the subjects. Damping factors exhibit the relative standard deviation of about 20%, implying intersubject variations in ability to dampen lens oscillations. However, when one takes into account the damping factors estimated in both directions for each individual, a relative consistency can be observed. Also, a similar observation can be conducted in case of time constants, which manifest rather large standard deviations for the group as a whole, but for each particular subject its values remain relatively constant for both gaze directions. This may suggest a consistent temporal response in the eye dynamics for each individual during rotations.

The previous sections presented a structured summary of the major results from the experimental analysis of lens displacement data over a specific time period, suggesting potential avenues for further discussion. The combined opto-mechanical simulations that utilize the biomechanical model, display a notable resemblance to the experimental data, as illustrated in Figure 7. The simulated data was processed similarily to the graphs presented in Figures 5, 6: the time stamp equal to zero was set to the moment, when the maximum separation between *PIV* and *PI*, associated with the maximum wobbling amplitude, appeared. By analyzing the temporal evolution of ocular dynamics through lens displacement, a comprehensive understanding is achieved. At the time = 0, a significant positive displacement is observed, which indicates transient relocation of the lens with respect to the cornea regardless of immediate biomechanical interactions within the eye. In particular, periodic variations in lens displacement indicate continuous diminishing motion of the lens.

To assess the effectivity of simulation, a comparison of the wobbling parameters calculated from simulation to the average ones estimated from experiment was performed. Furthermore, to provide clarity, the relative discrepancies were calculated. All these data are presented in Table 5.

4 Discussion

The exploration of ocular dynamics during horizontal eye rotations has revealed intriguing insights into the biomechanics of the human eye. The discussion encompasses the observed patterns in key parameters, their implications, and avenues for future research. Additionally, the documented changes in lens displacement are likely to have a pivotal function in visual accommodation and the eye's aptitude to concentrate on objects positioned at different distances (Seely and Macklem, 2004). When the simulation data are examined along with experimental observations, valuable insights can be obtained regarding the precision of the ocular rotation model. Acknowledging the use of homogeneous, linear elastic constitutive laws in modeling solid ocular tissues is crucial, as this represents a conscious simplification intended to balance computational efficiency with the essential biomechanical behavior of the eye under the study's specific conditions. While this methodology simplifies the model and aligns with the study's aims, it does not adequately address the anisotropic or viscoelastic properties of certain tissues, including the cornea and sclera. Moreover, the sensitivity analysis (Salimibani et al., 2024) emphasizes the need for refining biomechanical models to boost their accuracy and applicability, thus paving the way for future initiatives to tailor simulations for more accurate ocular diagnostics.

The oscillatory behavior of the eye is distinguished by variations in both amplitude and frequency, underscoring the intricate and complex interaction between the cornea and lens. As time progresses, the lens exhibits adaptive resilience, allowing it to rebound from the initial negative displacement and establish a dynamic equilibrium. This resilience observed in the eye signifies its extraordinary capacity to uphold its structural integrity and functionality even in the face of external disturbances arising from rotation. The experimental runs were effectively replicated

TABLE 5 Comparison of the averaged wobbling motion parameters estimated from *in vivo* experiment and obtained by means of biomechanical simulations.

	Frequency [Hz]	Q-factor	Damping factor	Time constant [s]
In vivo (average data)	20	1.86	0.27	0.11
Simulations	19.3	2.17	0.23	0.15
Relative discrepancy	3.5%	16%	15%	36%

by the simulation model, thereby showcasing its ability to accurately capture the oscillatory behavior of the eye. This alignment significantly enhances the usefulness of the model in predicting the dynamics of the eye during rotational motions. The agreement in Q-factor and damping factors between the simulation and experimental data further validates the model's precision in representing the mechanical response of the eye. This consistency greatly contributes to the reliability of the simulation in simulating real-world conditions.

The influence of mechanical parameters on the wobbling and overshooting behavior has been previously examined on an example of *ex-vivo* porcine eye model (Salimibani et al., 2024). The findings of this study indicate that while the effects of structures not in close proximity to the crystalline lens are minimal, changes in the mechanical characteristics of the zonular fibers play a crucial role. These results are likely applicable to the *in vivo* human eye model. However, the presence of additional anatomical features, such as the capsular bag and intricate lens components, adds a layer of complexity. This underscores the necessity for a thorough sensitivity analysis in future research to improve model customization.

The rationale for utilizing a 2D numerical model is based on its proficiency in accurately depicting the primary horizontal and vertical saccadic motions observed in controlled experimental environments. Nonetheless, we have to clearly acknowledge the assumption of planar eye rotation as a limitation, realizing that real-world saccades may present minor deviations from perfect planarity, which could result in discrepancies between the predictions of the model and the experimental findings.

The strong agreement between the simulated frequencies and the mean frequencies measured experimentally for a group of healthy volunteers demonstrates high reliability of the simulation in accurate reproducing of the oscillatory patterns observed in the eye, as presented in Table 5. Although the simulation quite closely approximates the frequencies, some slight deviations are observed. Taking into account the inherent variability in biological systems (Seely and Macklem, 2004), the discrepancies are considered to be within a reasonable range. The agreement in Q-factor and damping factors between the simulation and experimental runs, as shown in Table 5, is particularly noteworthy. The comparable levels of energy dissipation and stability further support the accuracy of the simulation in capturing the mechanical response of the eye.

A system characterized by consistent damping factors demonstrates its robustness in effectively attenuating oscillations. This resilience greatly contributes to the functional stability of the eye during rotations, accentuating its remarkable adaptability and ability to maintain equilibrium. The consistency in time durations suggests a predictable temporal response in the dynamics of the eye. The deviations observed in individual sequences prompt the need for personalized approaches in ocular biomechanics.

In each sequence, the Q-factors varied, indicating different dissipations of energy. We can gain a deeper understanding of rotational energy dynamics by investigating factors that influence Q-factor variations. As a result, the damping factors exhibited consistency, suggesting that the eye dampens oscillations on a stable basis. Furthermore, the results of this study indicate that the damping factor still exists, albeit with a smoother and altered function. This further supports the idea of the viscoelastic behavior of eye zonulas, as the presence of the damping factor in the results strengthens this concept (Dahaghin et al., 2023).

The presence of consistent damping factors indicates the existence of a robust system that effectively dissipates energy, thereby contributing to the functional stability of the eye during rotations. This discovery holds immense significance in understanding the eye's ability to withstand perturbations. The uniformity observed in the time constants further suggests a predictable temporal response exhibited by the eye's dynamics during rotations. When these time constants are understood, it becomes possible to improve predictive models for ocular biomechanics and potentially apply this knowledge in clinical scenarios.

Frequencies showed consistent oscillatory behavior, indicating stable oscillations. However, individual sequences showed variability. On the basis of the stable mean frequencies, it appears that the eye oscillates during rotation fundamentally. As a result of observed variability, personalized approaches in ocular biomechanics are necessary (Navarro et al., 2006). Consequently, comparing the *in vivo* cases with the simulation results shows differences in errors, which means that these parameters can be subjective and vary from one individual to the other. From a certain point of view, everybody has eyes with different geometrical and mechanical properties, as well as different experimental environments that can cause different results compared to simulations.

Personalizing biomechanical models to match individual characteristics can potentially improve the precision of diagnostic assessments and provide valuable guidance for interventions, especially in situations where the biomechanics of the eye are pivotal. The discussion highlights the complex dynamics of ocular biomechanics during specific rotations. The eye's response

is characterized by stable mean frequencies, varying Q-factors, consistent damping factors, and uniform time constants, collectively contributing to the intricate nature of its behavior. The 2D model illustrated in this study effectively demonstrates the *in vivo* outcomes, however, it fails to capture the complexities of the eye behavior in three-dimensional space. This simplification overlooks crucial elements such as torsional eye movements and depth perception, resulting in less accurate predictions. Additionally, the model lacks a detailed representation of the viscoelastic and hyperelastic properties of the tissues, including the cornea, sclera, and ocular muscles. This deficiency impedes the accurate simulation of parameters like frequency, Q-factor, damping factor, and time constant, limiting the relevance of the model to real-world scenarios. Furthermore, while the study assumes the sclera is non-deformable, this may influence the observed lens behavior following eye rotation. Future research should explore the potential impact of scleral deformability on our findings to provide a more comprehensive understanding of ocular dynamics. Moreover, to achieve a more precise and comprehensive analysis, transitioning to a 3D model that incorporates these biomechanical properties is necessary.

5 Conclusion

The research highlights the complex interplay between simulation data and experimental observations, with a particular focus on the ongoing refinement of the models. To ensure the accurate simulation of observed dynamics and the validation of experimental outcomes across diverse conditions, advanced biomechanical models have been developed. The proposed methodology has proven its capability to reproduce complex oscillation phenomena using a sophisticated model. A comprehensive understanding of the temporal dynamics involved in lens displacement plays a crucial role in advancing vision science and refining ocular biomechanical models.

As a methodical approach, integrating the biomechanics of the ocular system, has been implemented to address inconsistencies in Q-factors, damping factors, and time constants. Through the replication of experimental outcomes via simulation, we are empowered to explore ocular dynamics in scenarios that may present challenges when attempting to replicate them in a laboratory setting.

Despite the positive results, it is essential to acknowledge specific limitations. A simplification of the model to two dimensions, variations in experimental conditions, subject-specific factors (such as the ability to immediately fixate and maintain gaze on the target, the ability for accommodation, and the extent of accommodative effort), and the potential influence of measurement techniques may introduce uncertainties. Future investigations could prioritize enhancing the simulation model to incorporate additional biomechanical complexities. The customization of biomechanical models to suit individual characteristics holds the potential to greatly benefit personalized medicine and clinical interventions, leading to significant implications in the field.

Data availability statement

The original contributions presented in the study are included in the article/Supplementary Material, further inquiries can be directed to the corresponding author.

Ethics statement

The studies involving humans were approved by Informed consent was obtained from the *in vivo* subjects, and the study protocol was in accordance with the guidelines of the Declaration of Helsinki. It was approved by the Bioethics Committee of Wrocław Medical University (application No: 2021/0131). The studies were conducted in accordance with the local legislation and institutional requirements. The participants provided their written informed consent to participate in this study.

Author contributions

AD: Investigation, Methodology, Writing — original draft, Writing — review and editing. MS: Investigation, Methodology, Supervision, Writing—original draft, Writing—review and editing. AB: Conceptualization, Investigation, Resources, Software, Validation, Writing—original draft, Writing—review and editing. AJ: Investigation, Validation, Writing—original draft, Writing—review and editing. JG: Supervision, Writing—original draft, Writing—review and editing. JP-D: Investigation, Resources, Writing—original draft, Writing—review and editing. DS: Conceptualization, Funding acquisition, Investigation, Project administration, Resources, Supervision, Validation, Writing—original draft, Writing—review and editing.

Funding

The author(s) declare that financial support was received for the research, authorship, and/or publication of this article. AD is an ESR in the OBERON project funded within the framework of the European Union's Horizon 2020 research and innovation programme under the Marie Skłodowska-Curie grant agreement No. 956720. MS, AB, AJ, JP-D and DS: grant number 2019/35/B/ST7/03998 (National Science Center, Poland). FEM simulations have been carried out using resources provided by Wroclaw Center for Networking and Supercomputing (http://wcss.pl), grant No. 556.

Acknowledgments

Authors would like to acknowledge **Grzegorz Jóźwik** for construction of the illuminator and target and programming their operating scripts; and **Jacek Lisowski** for his relentless mental support in conducting the *in vivo* experiment.

Conflict of interest

The authors declare that the research was conducted in the absence of any commercial or financial relationships that could be construed as a potential conflict of interest.

Generative AI statement

The author(s) declare that no Generative AI was used in the creation of this manuscript.

Publisher's note

All claims expressed in this article are solely those of the authors and do not necessarily represent those of their affiliated organizations, or those of the publisher, the editors and the reviewers. Any product that may be evaluated in this article, or claim that may be made by its manufacturer, is not guaranteed or endorsed by the publisher.

Supplementary material

The Supplementary Material for this article can be found online at: https://www.frontiersin.org/articles/10.3389/fbioe.2025.1504769/full#supplementary-material

SUPPLEMENTARY VIDEO S1
Purkinje video sequences (nose to center).

SUPPLEMENTARY VIDEO S2
Purkinje video sequences (temple to center).

SUPPLEMENTARY VIDEO S3
Crystalline Lens Oscillations animation.

References

Behling, A. V., Giandolini, M., von Tscharner, V., and Nigg, B. M. (2021). Soft-tissue vibration and damping response to footwear changes across a wide range of anthropometrics in running. *PLoS One* 16, e0256296. doi:10.1371/journal.pone.0256296

Bocskai, Z., and Bojtár, J. (2013). Biomechanical modelling of the accommodation problem of human eye. *Period. Polytech. Civ. Eng.* 57, 3–9. doi:10.3311/PPci.2136

Boszczyk, A., Dębowy, F., Jóźwik, A., Dahaghin, A., and Siedlecki, D. (2023). Complexity of crystalline lens wobbling investigated by means of combined mechanical and optical simulations. *Biomed. Opt. Express* 14, 2465–2477. doi:10.1364/BOE.488176

Cabeza-Gil, I., Grasa, J., and Calvo, B. (2021). A validated finite element model to reproduce Helmholtz's theory of accommodation: a powerful tool to investigate presbyopia. *Ophthalmic Physiol. Opt.* 41, 1241–1253. doi:10.1111/opo.12876

Collewijn, H., Erkelens, C. J., and Steinman, R. M. (1988). Binocular co-ordination of human horizontal saccadic eye movements. *J. Physiol.* 404, 157–182. doi:10.1113/jphysiol.1988.sp017284

Dahaghin, A., Salimibani, M., Boszczyk, A., Jozwik, A., and Siedlecki, D. (2023). "Investigation of the crystalline lens inertial overshooting: *ex vivo* and simulation results," in Abstract retrieved from Proceedings of the COMSOL Conference 2023 Munich, Munich, Germany, 25–27 October, 2023.

Dahaghin, A., Salimibani, M., Boszczyk, A., Jóźwik, A., Skrok, M., Grasa, J., et al. (2024). Investigation of crystalline lens overshooting: *ex vivo* experiment and optomechanical simulation results. *Front. Bioeng. Biotechnol.* 12, 1348774. doi:10.3389/fbioe.2024.1348774

Dai, P., Zhao, Y., Sheng, H., Li, L., Wu, J., and Han, H. (2017). Simulating the effects of elevated intraocular pressure on ocular structures using a global finite element model of the human eye. *J. Mech. Med. Biol.* 17, 1750038. doi:10.1142/S0219519417500385

Deubel, H., and Bridgeman, B. (1995). Fourth Purkinje image signals reveal eye-lens deviations and retinal image distortions during saccades. *Vis. Res.* 35, 529–538. doi:10.1016/0042-6989(94)00146-D

Etminan, A., Salimibani, M., Dahaghin, A., Haghpanahi, M., and Maleki, A. (2023). FEM thermal assessment of a 3-D irregular tumor with capillaries in magnetic nanoparticle hyperthermia via dissimilar injection points. *Comput. Biol. Med.* 157, 106771. doi:10.1016/j.compbiomed.2023.106771

Issarti, I., Koppen, C., and Rozema, J. J. (2021). Influence of the eye globe design on biomechanical analysis. *Comput. Biol. Med.* 135, 104612. doi:10.1016/j.compbiomed.2021.104612

Lanchares, E., Navarro, R., and Calvo, B. (2012). Hyperelastic modelling of the crystalline lens: accommodation and presbyopia. *J. Optom.* 5, 110–120. doi:10.1016/j.optom.2012.05.006

Llapashtica, E., Sun, T., Grattan, K. T. V., and Barbur, J. L. (2024). Effects of post-saccadic oscillations on visual processing times. *PLoS One* 19, e0302459. doi:10.1371/journal.pone.0302459

Mardanbegi, D., Wilcockson, T. D. W., Killick, R., Xia, B., Gellersen, H., Sawyer, P., et al. (2020). A comparison of post-saccadic oscillations in European-born and China-born British university undergraduates. *PLoS One* 15, e0229177. doi:10.1371/journal.pone.0229177

Martin, H., Bahlke, U., Guthoff, R., Rheinschmitt, L., and Schmitz, K. P. (2009). "Determination of inertia forces at an intraocular lens implant during saccades," in World Congress on Medical Physics and Biomedical Engineering, IFMBE Proceedings, Munich, Germany, September 7-12, 2009. Editors O. Dössel and W. C. Schlegel (Berlin, Heidelberg: Springer), 100–103. doi:10.1007/978-3-642-03891-4_2725/11

Navarro, R., González, L., and Hernández-Matamoros, J. L. (2006). On the prediction of optical aberrations by personalized eye models. *Optom. Vis. Sci.* 83, 371–381. doi:10.1097/01.opx.0000221399.50864.c7

Nyström, M., Andersson, R., Magnusson, M., Pansell, T., and Hooge, I. (2015). The influence of crystalline lens accommodation on post-saccadic oscillations in pupil-based eye trackers. *Vis. Res.* 107, 1–14. doi:10.1016/j.visres.2014.10.037

Osmers, J., Kaiser, N., Sorg, M., and Fischer, A. (2021). Adaptive finite element eye model for the compensation of biometric influences on acoustic tonometry. *Comput. Methods Programs Biomed.* 200, 105930. doi:10.1016/j.cmpb.2021.105930

Pan, Y., Liu, Z., and Zhang, H. (2023). Research progress of lens zonules. *Adv. Ophthalmol. Pract. Res.* 3, 80–85. doi:10.1016/j.aopr.2023.02.002

Salimibani, M., Dahaghin, A., Boszczyk, A., Grasa, J., and Siedlecki, D. (2024). Assessment of material properties in key components of the porcine crystalline lens during overshooting. *Acta Bioeng. Biomech.* 26. doi:10.37190/ABB-02463-2024-03

Sarmiento, D. M. M., Montaño, Ó. L. R., Castiblanco, J. D. A., and Rodríguez, C. J. C. (2023). The impact of horizontal eye movements versus intraocular pressure on optic nerve head biomechanics: a tridimensional finite element analysis study. *Heliyon* 9, e13634. doi:10.1016/j.heliyon.2023.e13634

Seely, A. J., and Macklem, P. T. (2004). Complex systems and the technology of variability analysis. *Crit. Care.* 8, R367–R384. doi:10.1186/cc2948

Silva, A. F., Pimenta, F., Alves, M. A., and Oliveira, M. S. (2020). Flow dynamics of vitreous humour during saccadic eye movements. *J. Mech. Behav. Biomed. Mater.* 110, 103860. doi:10.1016/j.jmbbm.2020.103860

Singh, D., Firouzbakhsh, K., and Ahmadian, M. T. (2017). Human intraocular thermal field in action with different boundary conditions considering aqueous humor and vitreous humor fluid flow. *Int. J. Mech. Mechatron. Eng.* 11, 717–725.

Tabernero, J., and Artal, P. (2014). Lens oscillations in the human eye. Implications for post-saccadic suppression of vision. *PLoS One* 9, e95764. doi:10.1371/journal.pone.0095764

Tabernero, J., Chirre, E., Hervella, L., Prieto, P., and Artal, P. (2016). The accommodative ciliary muscle function is preserved in older humans. *Sci. Rep.* 6, 25551. doi:10.1038/srep25551/

Wang, K., and Pierscionek, B. K. (2019). Biomechanics of the human lens and accommodative system: functional relevance to physiological states. *Prog. Retin. Eye Res.* 71, 114–131. doi:10.1016/j.preteyeres.2018.11.004

Yamagishi, S., Yoneya, M., and Furukawa, S. (2020). Relationship of postsaccadic oscillation with the state of the pupil inside the iris and with cognitive processing. *J. Neurophysiol.* 123, 484–495. doi:10.1152/jn.00205.2019

Zapata-Díaz, J. F., Radhakrishnan, H., Charman, W. N., and López-Gil, N. (2019). Accommodation and age-dependent eye model based on *in vivo* measurements. *J. Optom.* 12, 3–13. doi:10.1016/j.optom.2018.01.003

Zemax (2024). OpticStudio, version 22.1.1.

frontiers | Frontiers in Bioengineering and Biotechnology

TYPE Original Research
PUBLISHED 28 April 2025
DOI 10.3389/fbioe.2025.1574231

OPEN ACCESS

EDITED BY
Sabine Kling,
University of Bern, Switzerland

REVIEWED BY
Sunho Park,
Pusan National University, Republic of Korea
Pan Long,
General Hospital of Western Theater Command, China
Brian Vohnsen,
University College Dublin, Ireland

*CORRESPONDENCE
Xiuqing Qian,
qianxq@ccmu.edu.cn

†These authors share first authorship

RECEIVED 10 February 2025
ACCEPTED 16 April 2025
PUBLISHED 28 April 2025

CITATION
Ma B, Liu L, Liu Y, Ren J and Qian X (2025) Mechanical property changes of glial LC and RGC axons in response to high intraocular pressure.
Front. Bioeng. Biotechnol. 13:1574231.
doi: 10.3389/fbioe.2025.1574231

Mechanical property changes of glial LC and RGC axons in response to high intraocular pressure

Bochao Ma[1†], Liu Liu[1,2†], Yushu Liu[1,3], Jifeng Ren[1,4] and Xiuqing Qian[1,4*]

[1]School of Biomedical Engineering, Capital Medical University, Beijing, China, [2]Department of Medical Engineering, Peking University Third Hospital, Beijing, China, [3]School of Special Education and Rehabilitation, Binzhou Medical University, Yantai, Shandong, China, [4]Beijing Key Laboratory of Fundamental Research on Biomechanics in Clinical Application, School of Biomedical Engineering, Capital Medical University, Beijing, China

Introduction: Pathological high intraocular pressure (IOP) is an important risk factor for glaucoma. The lamina cribrosa (LC) area in the optic nerve head is the initial site of optic nerve injury for glaucoma. LC deformation caused by elevated IOP will compress the retinal ganglion cells (RGC) axons passing through it, thereby leading to the damage of the RGC axons. The deformation of LC is highly correlated with its mechanical properties. Therefore, changes in mechanical properties of LC with the duration of high IOP is of great significance.

Methods: To investigate the impact of chronic high IOP on the mechanical properties of the LC, rat models were established by cauterizing the superior scleral vein and injecting 5-fluorouracil (5-FU) under the conjunctiva to maintain elevated IOP. The linear elastic properties of the glial LC and RGC axons in affected eyes were measured using atomic force microscopy (AFM) combined with image segmentation techniques. Morphological alterations of the glial LC were assessed using hematoxylin-eosin staining, immunofluorescence staining, and transmission electron microscopy (TEM).

Results: Compared to the control group, the Young's modulus of the glial LC decreased by 35.5%, 74.2%, and 80.6% at 4, 8, and 12 weeks of elevated IOP, respectively. Similarly, the Young's modulus of RGC axons decreased by 45.6%, 70.9%, and 75.9% over the same time points. These findings demonstrate a time-dependent reduction in the mechanical stiffness of both glial LC and RGC axons under chronic high IOP conditions.

Discussion: The progressive decrease in Young's modulus indicated that prolonged high IOP compromises the structural integrity and mechanical properties of the LC and RGC axons. This mechanical weakening likely contributes to the pathophysiological process of optic nerve injury in glaucoma. The present study offers important insights into the biomechanical mechanisms underlying glaucomatous damage, which may guide future research and therapeutic strategies.

KEYWORDS

high intraocular pressure, lamina cribrosa, morphology, mechanical properties, RGC axons

1 Introduction

Glaucoma is a serious, irreversible blinding eye disease and the second leading cause of blindness in the world (Tham et al., 2014). The pathogenesis of glaucoma is still unclear, but the pathological increase of intraocular pressure (IOP) is an important factor. The lamina cribrosa (LC), a connective tissue structure in the optic nerve head (ONH), supports the retinal ganglion cells (RGC) axons as they pass through the eyeball (Quigley and Addicks, 1980; Midgett et al., 2020). Elevated IOP can lead to LC deformation and further compression of the optic nerve (ON), resulting in the damage of RGC axons (Yan et al., 1994; Midgett et al., 2020; Korneva et al., 2023). The deformation of LC is associated with its mechanical properties (Karimi et al., 2021), and elevated IOP will alter the mechanical properties of LC (Jia et al., 2022). Therefore, studies of mechanical properties change of LC and RGC axons will provide information to analyze the LC deformation more accurately and provide a fundament for the mechanisms of optic nerve damage in glaucoma.

Previous research has shown that optic nerve damage occurs initially in the LC area and is related to the LC morphology of glaucoma patients (Ivers et al., 2015; Lozano et al., 2019; Ling et al., 2020; Wang et al., 2020). For rodents with chronically elevated intraocular pressure, morphological changes were identified in LC tissues (Dai et al., 2012; Pang and Clark, 2020; Zhang et al., 2022). Changes in the microstructure of tissues will affect their mechanical properties. Liu et al. found that the nonlinear mechanical behavior of the cornea is closely related to the curled morphology of collagen fibrils (Liu et al., 2014). Therefore, mechanical properties of LC may change with the duration of elevated IOP.

It has been found that the Young's modulus of LC in patients with pseudoexfoliation glaucoma decreases by 40% compared to normal eyes (Braunsmann et al., 2012). Jia et al. found that mechanical properties of peripapillary sclera and LC in monkeys varied with high IOP lasting 40 days (Jia et al., 2022). Recent research also found strains of mouse astrocytic LC in an *ex vivo* inflation test was greater than the control in the central astrocytic LC after 3 days of *in vivo* elevated IOP (Korneva et al., 2023). However, changes in mechanical properties of the LC and RGC axons with the duration of elevated IOP remain unclear.

To study changes in mechanical properties of the LC and RGC axons with the duration of elevated IOP, an animal model with chronic high IOP was established. The rat chronic high IOP animal model could be induced by injection of microbeads, laser photocoagulation, or episcleral vein cauterization (Ueda et al., 1998; Blanco et al., 2019; Pang and Clark, 2020; Rodrigo et al., 2021; Korneva et al., 2023). Our previous studies have induced the model by cauterizing episcleral veins with 5-Fluorouracil (5-Fu) subconjunctival injection, which may elevate the episcleral venous pressure and then obstruct the outflow of aqueous humor (Li et al., 2018; Peng et al., 2019; Ma et al., 2025). This model is reproducible and the high IOP of the model could be sustained for 3 months (Zhang et al., 2022). We called the rat LC tissue "glial LC" because the fortified astrocytes are the main component of the LC tissue (Liu et al., 2022). Additionally, we should verify whether 5-Fu affects the morphology and mechanical properties of the LC tissue in this paper.

It is difficult to measure the mechanical properties of LC using traditional mechanical methods because it is a multi-layered network structure with many pores (Quigley et al., 1981; Downs and Girkin, 2017). Braunsmann et al. measured the Young's modulus of the LC beams of normal human eyes and pseudo-exfoliated eyes by atomic force microscope (AFM), which is an effective tool for investigating the mechanical properties of small biological samples (Ziebarth et al., 2007; Last et al., 2009, 2011; Grant et al., 2011; Braunsmann et al., 2012). To analyze the influence of high IOP on the LC deformation more accurately and improve the prediction performance for optic nerve damage, we have proposed a method combining AFM with the Otsu image segmentation method to distinguish mechanical properties of glial LC and RGC axons in the glial LC area of rats (Liu et al., 2022).

This study established a chronic high IOP animal model by cauterizing episcleral veins with 5-FU subconjunctival injection and studied the effect of 5-FU on the morphology and mechanical properties of the LC tissue. Then we quantitatively evaluated the mechanical properties of glial LC and RGC axons, at different times with duration of high IOP, which might provide an important basis for in-depth study of the pathogenesis of optic nerve damage and early diagnosis of glaucoma.

2 Materials and methods

2.1 Animals

Male adult Sprague-Dawley rats (7–8 weeks, 270–300 g weight) were obtained from the Experimental Animal Department of the Capital Medical University. They were housed libitum and maintained in an air-conditioned room in a 12-h light/12-h dark cycle. Animal experiments conformed to the principles of animal treatment described in the Statement for Use of Animals in Ophthalmic and Vision Research of the Association for Research in Vision and Ophthalmology.

A total of 67 rats were involved in this experiment. According to different duration of high IOP, they were divided into four groups, including a blank control group, 4th, 8th, and 12th week after high IOP induction, denoted by Gw0, Gw4, Gw8, and Gw12, respectively. The right eye served as the experimental eye, while the left eye functioned as the contralateral control eye in the Gw4, Gw8, and Gw12 groups. To verify the feasibility of the model induction related to the injury of the posterior tissue of the eyeball, we established a 5-FU drug control group, named Gw0-5Fu. Table 1 shows the number of rats in each group prepared for hematoxylin-eosin (HE) staining, immunofluorescence staining, transmission electron microscopy testing, and AFM testing.

2.2 Model induction and IOP measurements

The rat model with chronic high IOP was established by cauterizing the episcleral venous in combination with subconjunctival injection of 5-Fu (Haipu Pharmaceutical Co., Shanghai, China), which was described in detail in previous studies (Li et al., 2018; Peng et al., 2019; Liu et al., 2022). Rats were anesthetized intraperitoneally with 1% sodium pentobarbital at a dose of 0.4 ml per 100 g weight. The surface anesthesia was performed on the cornea and periocular tissues by adding oxybuprocaine hydrochloride eye drops (Santen Pharmaceutical, Osaka, Japan) to the experimental eye. The experimental eye was cauterized with a high-temperature electrocoagulation pen on 3-4 upper scleral vein trunks. A 29G needle was used to administer a 100 μL subconjunctival injection of 5-Fu at a concentration of 2.5% (w/v) into the eyes to suppress neovascularization. Then a

TABLE 1 The number of rats in each group rat prepared for HE staining, immunofluorescence staining, transmission electron microscopy testing, and AFM testing.

Group	Gw0	Gw4		Gw8		Gw12		Gw0-5Fu
	Right	Right	Left	Right	Left	Right	Left	Right
HE staining	3	3	0	3	0	3	0	3
Immunofluorescence staining	3	3	0	3	0	3	0	3
Transmission electron microscopy testing	1	0	0	0	0	1	0	1
AFM testing	10	6	6	6	6	6	6	6

Note: Gw0 denotes blank control group; Gw4 denotes the experimental group with high IOP, for 4 weeks; Gw8 denotes the experimental group with high IOP, for 8 weeks; Gw12 denotes the experimental group with high IOP, for 12 weeks; GW0-5Fu denotes 5-FU, drug control group, which means the right eyes of rats were injected 5-Fu alone. Gw0, Gw4, Gw8, Gw12, and Gw0-5Fu used a total of 17, 12, 12, 13, and 13 rats, respectively.

subconjunctival injection of 100 μL of 5-Fu with a concentration of 2.5% (w/v) was performed by a 29G needle on the eyes to inhibit neovascularization. Levofloxacin eye drops were added to the ocular surface to prevent inflammation.

IOP was measured using a TonoLab Rebound Tonometer (Icare, Vantaa, Finland) every 3 days after induction. To avoid the effects of circadian rhythms, IOP measurements in awake rats were scheduled between 10 am and 12 am. If IOP was lower than 30 mmHg, cauterization was performed again. Otherwise, only 5-Fu was injected. For the 5-Fu drug control group, Gw0-5Fu, only 5-Fu was injected subconjunctivally to prevent the formation of new blood vessels.

2.3 HE staining

Histological changes in the ONH were assessed through HE staining in conjunction with optical microscopy. Three rats were selected randomly from every group to obtain coronal and sagittal sections of the ONH. Following ONH fixation, dehydration was carried out progressively using different ethanol concentrations (Macklin, Shanghai, China), followed by transparency using xylene (Solarbio, Beijing, China). After thorough infiltration with wax, the tissue was embedded. The ONH was sliced into 4 μm-thick sections using a paraffin slicing machine (Leica, Wetzlar, Germany). Paraffin sections were rinsed three times in PBS and then incubated with 3% hydrogen peroxide. Subsequently, the sections were immersed in hematoxylin (Push, Chengdu, China) and differentiated in 1% hydrochloric acid alcohol. After staining with eosin (Push, Chengdu, China), the slides were dehydrated using progressively concentrated ethanol and clarified with xylene. Neutral resin adhesive was employed to seal the slides.

2.4 Immunofluorescence staining

The tissues in the LC region of the rat are primarily composed of astrocytes and the RGC axons. To investigate morphology changes in the ONH, immunofluorescence staining of glial fibrillary acidic protein (GFAP) was performed on coronal plane sections of the ONH. A series of 10 μm cryo-sections were sliced. These cryo-sections were rinsed three times in PBS, sealed in 5% bovine serum albumin (BSA; Sigma, Saint Louis, USA) in PBS with 0.3% Triton X-100, and transferred to a primary antibody solution consisting of rat anti-glial fibrillary acidic protein (Abcam, Cambridge, UK) diluted with PBS (1:500). The sections were then incubated with the primary antibodies overnight at 4°C in a humidified box. Following the primary incubation, the sections were rinsed and incubated with species-specific secondary antibodies conjugated with Alexa-488 (1:500) (Abcam, Cambridge, UK) at 37°C for 2 h. Fluorescent images of the labeled tissues were visualized and captured using confocal laser scanning microscopy (CLSM; Leica, Wetzlar, Germany). Images of the eyes in every group were acquired under the same settings and conditions.

2.5 Transmission electron microscopy

To visualize the microstructure of the ONH, we used a transmission electron microscope (TEM, HT7700, HITACHI, Japan) to observe images of the ONH using three rats selected from the Gw0 group, the Gw12 group, and the Gw0-5Fu group, respectively. The tissue was prepared following TEM specifications, where it was fixed in 2.5% glutaraldehyde for 4–6 h and washed three times with PBS. Subsequently, the ONHs were fixed with 1% osmium acid. Following elution with gradient ethanol, the ONH was immersed in acetone, embedded, and solidified using Epon618 (Sigma, Saint Louis, USA). After determining the position, the tissue was sliced into approximately 50 nm-thick ultra-thin sections. These ultra-thin sections were then stained with lead citrate.

2.6 Mechanical properties measurement of glial LC and RGC axons

The mechanical properties of glial LC and RGC axons were obtained using an Atomic Force Microscope (AFM, Bioscope Resolve, Bruker, America) and image processing method based on our previous research (Liu et al., 2022). We chose a quadrangular pyramid probe (MLCT-A, Bruker, America) with a soft silicon nitride triangular cantilever whose spring constant is 0.07 N/m. The indentation velocity was set as 29.6 μm/s. We selected a soft silicon nitride triangular cantilever with a spring constant of 0.07 N/m and a four-sided pyramidal probe with a height of 2.5–8.0 μm (MLCT-A, Bruker, USA). It is worth noting that while the probe is tapered, its tip has a curvature radius of 20 nm to prevent stress concentration. The predefined maximum

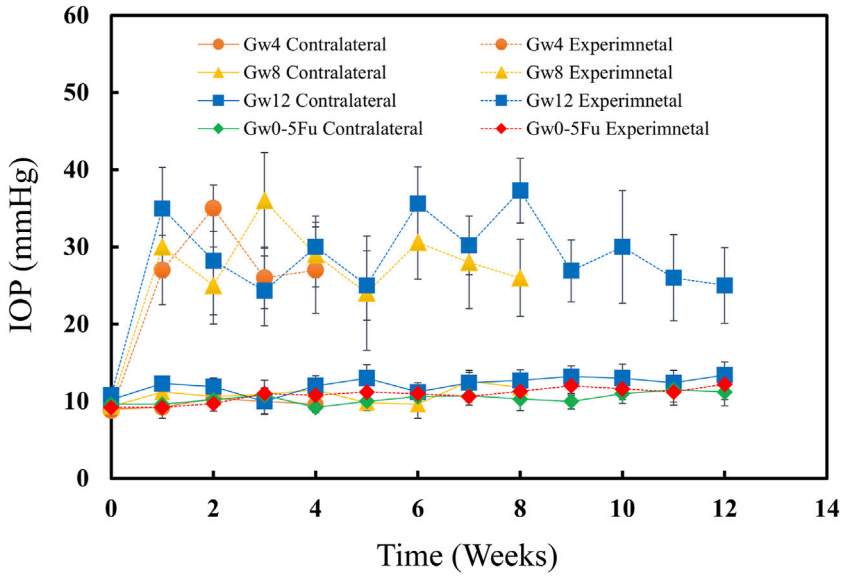

FIGURE 1
IOPs of both eyes in the 5-Fu group and experimental groups (n = 13). The IOPs of experimental eyes increased significantly after model induction ($P < 0.05$) and the IOPs of contralateral control eyes remained at normal level ($P > 0.05$). The IOPs of 5-Fu eyes showed no significant change after model induction ($P > 0.05$). Error bars represent the standard deviation (SD).

force for each indentation (trigger force) was set at 2.5 nN, and the indentation speed was 29.6 μm/s. In the force volume (FV) mode of AFM, the probe on the tip of the cantilever performed a two-dimensional scan of the sample within a region of interest (ROI) and acquired indentation curves (F-δ curve). Then, a Young's modulus image, each pixel value representing a local Young's modulus, is obtained by fitting the corresponding F-δ curve. In this experiment, an ROI with the size of 20 × 20 μm^2 was selected and indentations were performed on 128 × 128 points. The Young's modulus of glial LC and RGC axons were segmented using the Otsu thresholding segmentation method based on the Young's modulus image. The mechanical properties of glial LC and RGC axons were determined according to the respective Young's modulus extracted using statistical analysis.

2.7 Statistical analyses

A one-way analysis of variance (ANOVA) was conducted to compare data across multiple groups, with statistical significance set at $P < 0.05$. Post hoc pairwise comparisons were performed using the least significant difference (LSD) test, with a threshold of $P < 0.05$ indicating statistical significance.The correlation between the mechanical properties of glial LC or RGC axons and the duration time of high IOP was tested by using Spearman correlation with SPSS 26.0 (IBM Corporation, Armonk, United States).

3 Results

IOPs of eyes were measured when the rats were awake before the experiment. IOPs had no significant change between Gw0-5Fu contralateral eyes and Gw0-5Fu experimental eyes until 12 weeks, indicating that injection of 5-Fu did not affect IOP (Figure 1). IOPs of experimental eyes increased after inducing chronic high IOP model and sustained high IOP level for 12w. The contralateral eyes maintained normal IOP, indicating that the method of inducing the model did not affect the IOP level of the contralateral eyes in this study (Figure 1).

By following similar procedures, the results of HE staining presented a kidney-like shape in the cross-sectional view of the rat LC (Figure 2), which consists of glial LC and RGC axons (Dai et al., 2012; Peng et al., 2019). The circular or elliptical structures in blue-purple represent cell nuclei, and the cell types mainly included astrocytes, a small number of small glial cells, and vascular endothelial cells (Williams et al., 2017; Lopez et al., 2020; Strickland et al., 2022). The pink region mainly consists of elongated astrocytic protrusions. The morphology of the LC tissue in the Gw0-5Fu group exhibited no significant differences compared to the Gw0 group. Similarly, regular radial glial fiber processes were observed in the Gw0-5Fu group, along with a similar distribution of cell nuclei. The morphological structure of LC tissues has changed significantly with the duration of high IOP. Apart from the central region of LC tissue, the peripheral areas present a large number of cell nuclei, indicating the activation of cell proliferation and the increase of cell population. A large number of white voids appeared in the LC area, indicating that the structure of LC tissue had undergone remodeling, and the RGC axons might also be greatly affected (Figure 2).

To observe morphological changes in the glial LC intuitively, we applied immunofluorescent staining to label the GFAP protein of glial LC and observe the morphological changes through a laser confocal microscope. There were no significant differences in the distribution and arrangement of the glial LC beam between the Gw0-5Fu group and the Gw0 group. The astrocyte protrusions extended radially from the ventral side to the dorsal side, forming a

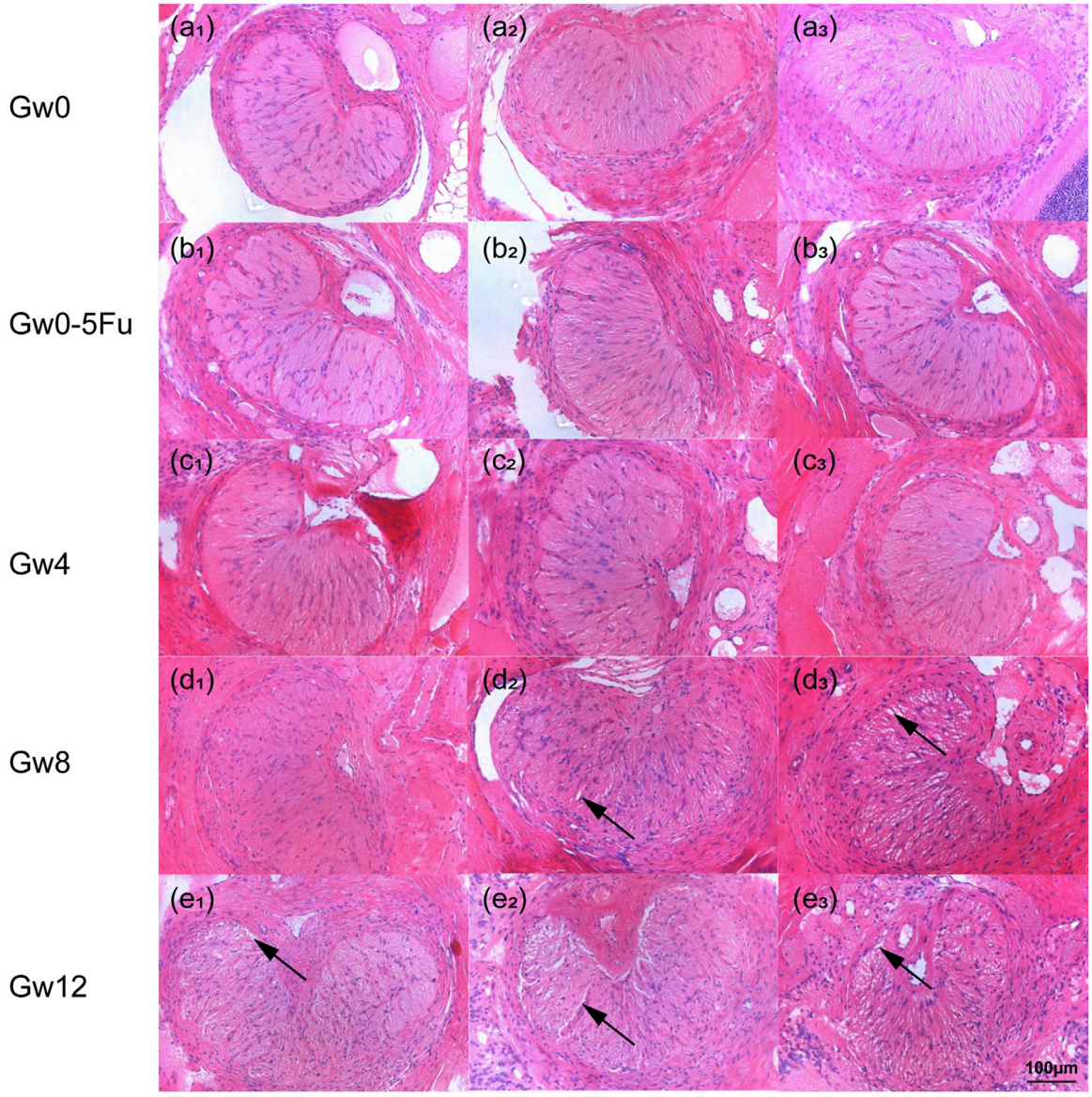

FIGURE 2
The HE staining images of cross sections in the LC tissues in all groups (n = 3). **(a1-3)** represents the Gw0 group, **(b1-3)** is the Gw0-5Fu group, while **(c1-3)**, **(d1-3)**, and **(e1-3)** correspond to the high IOP experimental groups at 4 weeks, 8 weeks, and 12 weeks, respectively. In the figure, the blue-purple color represents cell nuclei, the pink region is mainly composed of the elongated axons of astrocytes, and the white arrows indicate the gaps appearing in the LC.

reticular pattern with a relatively uniform and distinct hierarchical structure. With the duration of high IOP, the radial arrangement structure was destroyed and the staining was blurred. While high IOP lasted for 12 weeks, voids and gaps appeared after a large number of fibers were lost, and the original support structure of the glial LC was destroyed (Figure 3).

To further insight into the microstructural changes of RGC axons and astrocytes, we conducted more detailed observations using TEM on the cross-section of the ventral, central, and dorsal areas of the LC tissues in the Gw0, Gw0-5Fu, and Gw12 groups. The ventral area of the LC tissues in the Gw0 group revealed a dense and sturdy "root" of astrocytes, extending dorsally with the organized arrangement. The protrusions of astrocytes were relatively robust (marked as "p" in Figures 4a1,a4), with a single bundle diameter of 0.3–0.6 μm. The diameter of bundled protrusions (indicated by white arrows in Figures 4a1,a4) was 3–5 μm. Additionally, there were fine cell protrusions closely surrounding the bundles of RGC axons (indicated by black arrows in Figures 4a1,a4). Numerous RGC axons (marked as "n" in Figures 4a1,a4) shuttled in a circular bundle within the spindle-shaped gaps of astrocytic protrusions. Most RGC axons passed perpendicularly through the glial LC, whose diameter varied from 0.2 μm to 2 μm in cross-section. In the central area of glial LC, astrocytic protrusions continuously

10.3389/fbioe.2025.1574231

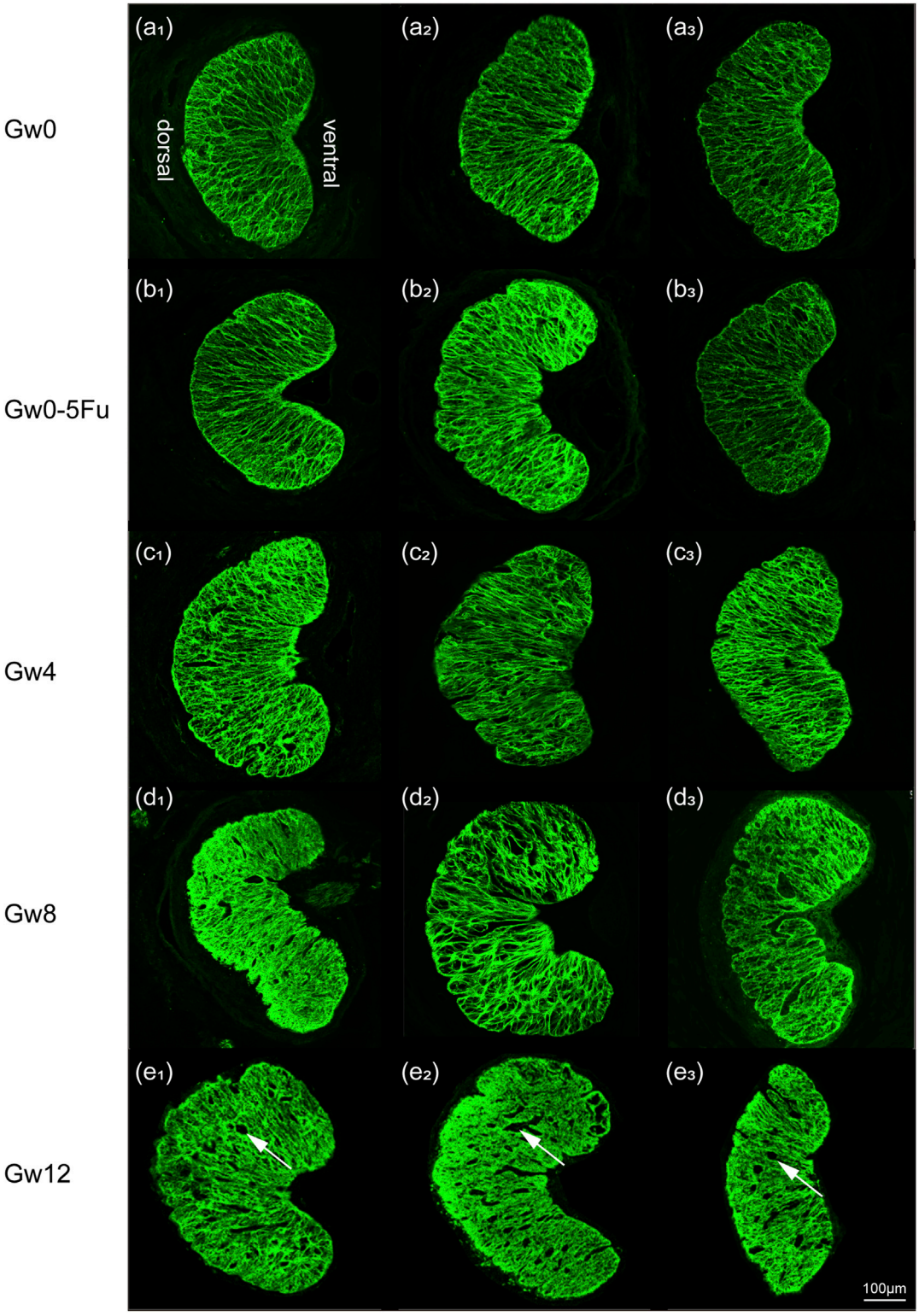

FIGURE 3
The fluorescent images of cross sections in the LC tissues in all groups (n = 3). Overall images in all groups show the variation of meshwork of astrocytes (green). Images **(a1-3)** represent the Gw0 group, **(b1-3)** is the Gw0-5Fu group, while **(c1-3)**, **(d1-3)**, and **(e1-3)** correspond to the high IOP experimental groups at 4 weeks, 8 weeks, and 12 weeks, respectively. In the figure, white arrows represent the voids and gaps that appeared in the LC.

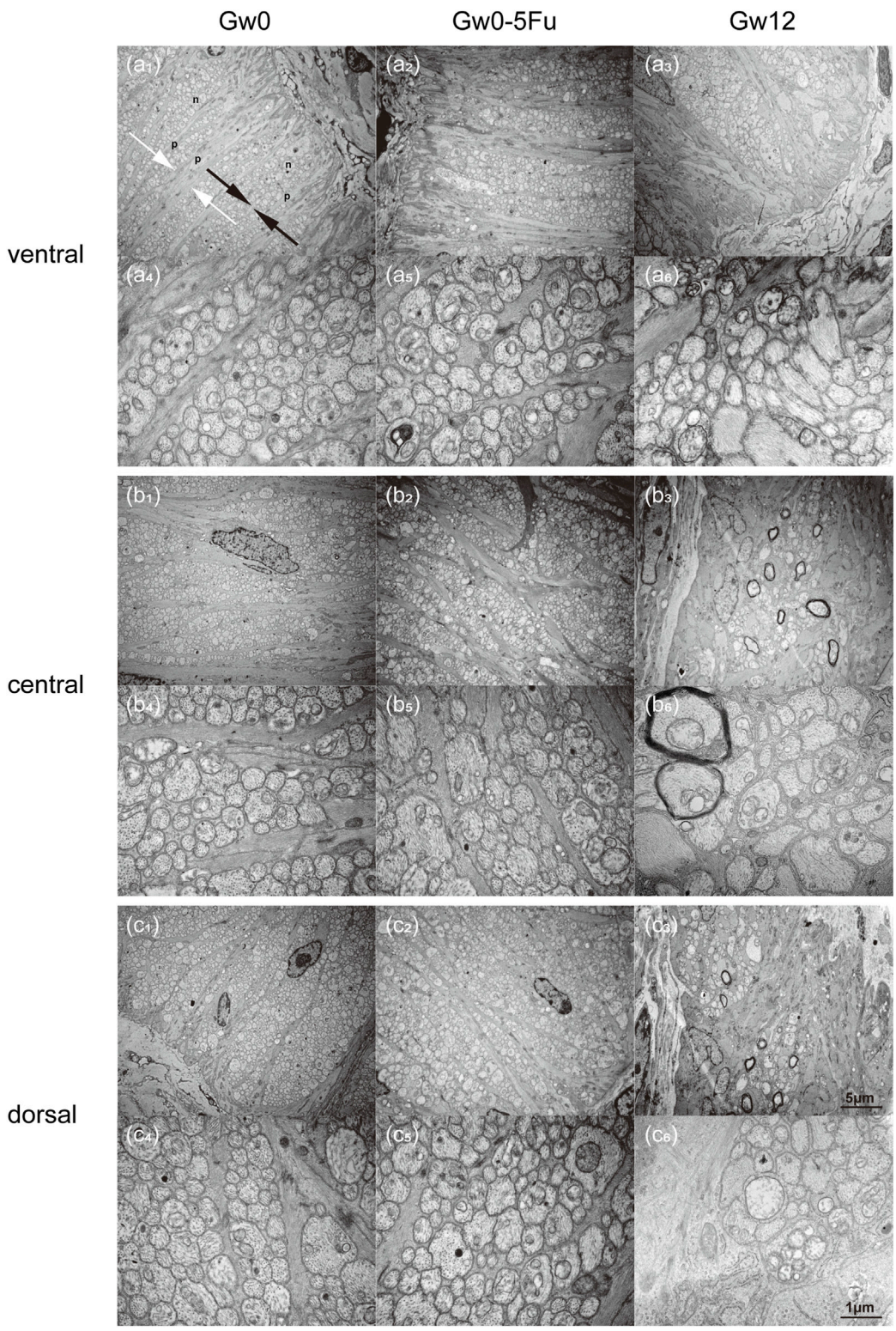

FIGURE 4
Transmission electron microscopy images of the glial LC in the experimental eyes in the Gw0, Gw0-5Fu, and Gw12 groups. Images **(a1-6)**, **(b1-6)**, and **(c1-6)** depict the ventral, central, and dorsal regions, respectively. Images **(a1-3)**, **(b1-3)**, and **(c1-3)** are magnified at 6,000 times, while images **(a4-6)**, **(b4-6)**, and **(c4-6)** show local regions at a magnification of 30,000 times. In the figure, 'p' represents the protrusions of astrocytes; 'n' represents RGC axons; white arrows represent bundles composed of protrusions of astrocytes; black arrows represent bundles of RGC axons.

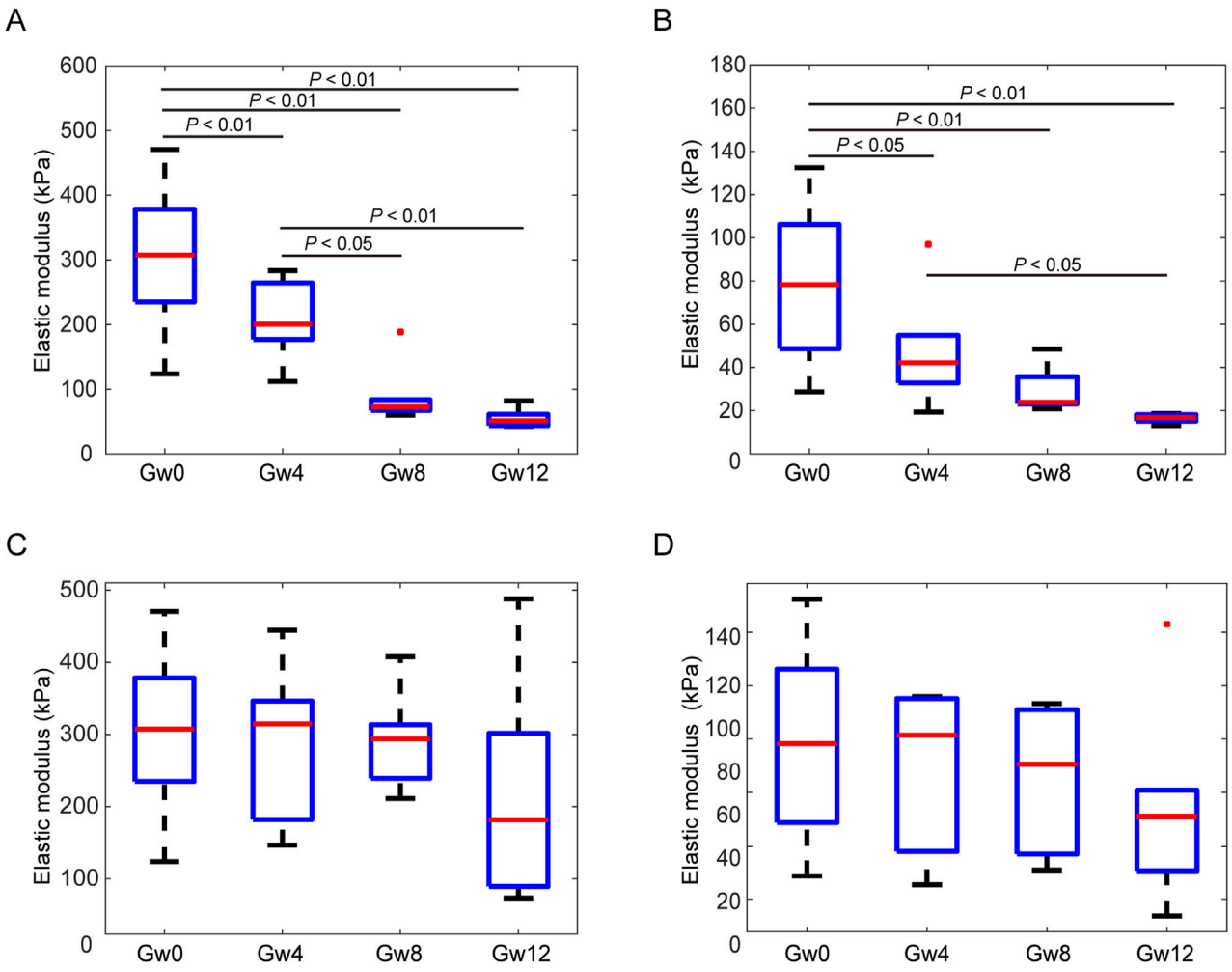

FIGURE 5
Comparison of the Young's modulus between experimental eyes at 4 weeks, 8 weeks, and 12 weeks and contralateral control eyes in the glial LC and RGC axons. **(A)**. The Young's modulus of the glial LC in the experimental eyes in the Gw0, Gw4, Gw8, and Gw12 groups. **(B)**. The Young's modulus of the RGC axons in the experimental eyes in the Gw0, Gw4, Gw8, and Gw12 groups. **(C)**. The Young's modulus of the glial LC in the contralateral control eyes in Gw0, Gw4, Gw8, and Gw12 groups. **(D)**. The Young's modulus of the RGC axons in the contralateral control eyes in Gw0, Gw4, Gw8, and Gw12 groups.

dispersed into finer bundles as they radiate from the ventral to the dorsal area, resembling branching tree structures. In the dorsal area of glial LC, astrocytic protrusions were finer and more sparsely distributed compared to the ventral area (Figures 4b1,b4). In contrast, RGC axons were denser in the dorsal area compared to the ventral area (Figures 4c1,4c4). The distribution of astrocytic protrusions in the Gw0-5Fu group resembled that of the Gw0 group. The outer sheath structure of RGC axons in the Gw0-5Fu group remained intact, with no loss of axons, and its distribution density was similar to that of the Gw0 group. It was indicated that 5-Fu did not cause significant changes in the morphology of RGC axons (Figures 4a2,a5,b2,b5,c2,c5). Compared to the Gw0 group, the Gw12 group exhibited a disrupted radial structure of astrocytic protrusions in the central and dorsal areas (Figures 4a3,b3,c3). The results show that both thickness and density of astrocytic protrusions are increased, which could compress and encroach upon the space of RGC axons. The sectional shape of part of RGC axons varied from ellipse to irregular shapes (Figures 4a6,b6,c6).

Next, we obtained the changes of Young's modulus of glial LC and RGC axons with the duration of high IOP (Figures 5A,B). The values of Young's modulus were taken as the typical Young's modulus, which is the peak of the fitted frequency distribution histogram of Young's modulus (Liu et al., 2022). With the sustained elevation of IOP, the Young's modulus of the experimental group of both glial LC and RGC axons significantly decreased (Figures 5A,B). The Young's modulus of glial LC are greater than those of RGC axons. The difference in Young's modulus of glial LC between the experimental group and control group is statistically significant ($P' < 0.01$). The variation of Young's modulus of glial LC with duration time of high IOP was similar to that of glial LC. There was no significant difference in the Young's modulus between the Gw8 group and the Gw12 group whether it was for the glial LC or RGC axons.

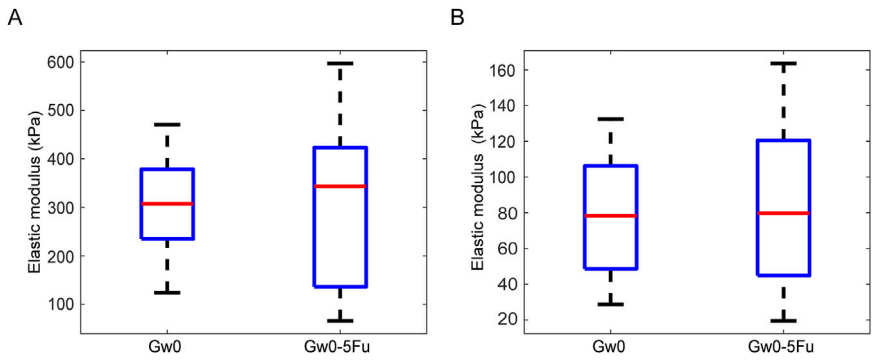

FIGURE 6
Comparison of the Young's modulus between the blank control group and 5-FU control group in the glial LC and RGC axons. **(A)**. The Young's modulus of the glial LC in the experimental eyes in the Gw0 and Gw0-5Fu groups. **(B)**. The Young's modulus of the RGC axons in the contralateral control eyes in the Gw0 and Gw0-5Fu groups.

TABLE 2 Correlation analysis of Young's modulus of glial LC and RGC axon with duration time of high IOP.

Group	*r*	P
Glial LC of experimental eyes	−0.795	**
RGC axon of experimental eyes	−0.773	**
Glial LC of contralateral eyes	−0.226	
RGC axon of contralateral eyes	−0.239	

Note the Spearman correlation coefficients had statistically significant ($P < 0.05$, **$P < 0.01$).

The Young's modulus showed no significant differences for different duration of IOP in either the glial LC or RGC axons in the contralateral eyes (Figures 5C,D). Additionally, both the glial LC and RGC axons showed no significant differences in Young's modulus between the Gw0 group and the Gw0-5Fu group, indicating that 5-FU had no obvious influence on the mechanical of the glial LC and RGC axons (Figures 6A,B).

The correlations between the Young's modulus of the tissues and the duration time of high IOP were further analyzed by Spearman correlation analysis for the experimental group and the control group. The results are shown in Table 2. The Young's modulus of the glial LC and RGC axons in the experimental group are negatively correlated with the duration time of high IOP, and the correlation is statistically significant ($P < 0.01$). There is no correlation between the Young's modulus of glial LC and RGC axons in the contralateral eye and the duration of high IOP.

4 Discussion

In this study, a rat model with chronic high IOP was established by cauterizing the superior scleral vein combined with subconjunctival injection of 5-FU, and the reliability of the modeling method was verified by combining HE staining, immunofluorescence staining, and TEM. With the duration of high IOP, the morphological structure of LC tissues has undergone significant changes. We used AFM combined with image segmentation methods to study the linear elastic mechanical properties of the glial LC and RGC axons in normal eyes and experimental eyes with different durations of high IOP. The results showed that the Young's modulus of glial LC and RGC axons decreased significantly with the duration of high IOP.

The IOP of the experimental eyes in the Gw0-5Fu group was not significantly different from that in the Gw0 group. Following the injection of the 5-Fu drug, there was no observable bleeding or edema around the bulbi conjunctiva, similar to normal eyes. Results from HE staining and GFAP immunofluorescence staining experiments indicate that the LC tissues in the Gw0-5Fu group are not different from those in the Gw0 group. Results of TEM reveal that in different regions of the LC tissue, there was no apparent loss of optic nerve fibers in the RGC axon bundles in the Gw0-5Fu group. Based on these findings, it can be inferred that 5-FU does not cause significant damage to RGC axons. Studies have shown that the efficacy of 5-FU occurs only when it is converted into active nucleoside metabolites in various tumor lesions (Sethy and Kundu, 2021; Alzahrani et al., 2023). If there are no lesions, they will quickly penetrate the blood-brain barrier and enter the brain tissue after being injected into the body, followed by 10%–30% of the prototype drug being excreted in the urine through the kidneys, and about 60%–80% was inactivated in the liver and decomposed into carbon dioxide and urea, which are excreted through the respiratory tract and urethra respectively (Matuo et al., 2009; Sethy and Kundu, 2021). 5-FU is a chemotherapeutic agent primarily employed in the treatment of various cancers, including colorectal, gastric, and breast cancers (Sommadossi et al., 1982; Petrelli et al., 1987; Kim et al., 1993; Prado et al., 2007). As a cell cycle-specific agent, 5-Fu primarily targets cells with high mitotic activity, like retinal epithelial cells. Astrocytes, which make up the rat glial LC, do not undergo proliferation during the development of glaucoma (Inman and Horner, 2007). Therefore, 5-Fu has no effect on cell proliferation within the LC tissue. Furthermore, it takes an injection of 60 mg/kg to trigger a noticeable inflammatory reaction in rats (Kırcadere et al., 2024). Since we injected only 2.5 mg of 5-Fu per mouse, we believe that the 5-Fu used in this study is unlikely to cause inflammation in the glial LC and RGC axons. In order to study the 5-Fu impact on the results, we design the 5-Fu control group.

A method for estimating mechanical properties of ONH tissues from parameters measurable using optical coherence tomography showed the average Young's modulus was 0.24 MPa for human LC (Sigal et al., 2014). The results showed that the Young's modulus of the LC tissues decreased with the duration of chronic elevated IOP, which was consistent with the Young's modulus of the LC tissues observed in patients with pseudoexfoliation glaucoma clinically (Braunsmann et al., 2012). The changes in mechanical properties of the LC tissues may be related to morphological alterations. The pore area fraction of the lamina cribrosa (LC) was significantly correlated with pressure-induced strains. Specifically, all strain measures increased with higher pore area fraction. This suggests that regions with a larger pore area fraction, indicating a less dense collagen network, are associated with greater susceptibility to deformation under elevated intraocular pressure, potentially contributing to glaucomatous damage (Ling et al., 2019). Our study revealed that with the duration of chronic elevated IOP, there is an increase in the expression of GFAP, disruption of the radial arrangement structure, and severe loss of RGC axons. The previous research also suggested that the glial LC was damaged with the duration of chronic elevated IOP (Guan et al., 2022; Zhang et al., 2022). Several researches indicated a correlation between changes in microstructure and mechanical properties. The nonlinear mechanical behavior of the cornea was closely correlated with the crimping morphology of collagen fibrils (Liu et al., 2014). Studies have shown that changes in the mechanical properties of the sclera in myopic eyes are closely related to alterations in its microstructure (Boote et al., 2020; Hoerig et al., 2022). Moreover, studies have shown that elevated IOP is significantly associated with ECM changes in the ONH. In the glaucomatous rat model with elevated IOP, deposition of TGF-β2 and collagen I in the ONH was significantly increased ($P < 0.01$), while collagen IV and MMP-1 showed no significant changes (Guo et al., 2005; Kim and Lim, 2022). These findings suggest that IOP-induced ECM remodeling may play an important role in ONH damage in glaucoma. Therefore, the underlying mechanisms of changes in the mechanical properties of LC and RGC axons, particularly extracellular matrix remodeling or alterations in the cytoskeleton, require further exploration.

Similar to human LC tissues, the structures of rat LC tissues exhibit significant differences in both cross-sections and longitudinal cross-sections (Morrison et al., 1995; Guan et al., 2022; Czerpak et al., 2023). Therefore, we investigated the anisotropy of the mechanical properties of rat LC tissues. Statistical analysis results indicate that there are no significant differences in Young's modulus in longitudinal cross-sections and cross-sections for glial LC or RGC axons (Supplementary Figure 1). The possible reason could be that the contact radius of indentation is 20–150 nm, which is related to the half of angle of the quadrangular pyramid probe depth (about 17°) depth (Liu et al., 2022). The maximum diameter of astrocyte protrusions (glial LC) could reach 0.3–0.6 μm, and the maximum short axis of the RGC axon bundle could reach 0.2–2 μm. Therefore, we believe that each indentation of the probe used in AFM measurement might press on the single astrocyte protrusions or RGC axon bundle of the glial LC or RGC axon. Therefore, there is no significant difference between the mechanical properties of tissues obtained from the longitudinal section or cross-section.

There are some differences between the induced elevated IOP in this study and the naturally occurring elevated IOP in glaucoma. Induced elevated IOP is usually limited to ocular pathological research and cannot reflect the complex effects of systemic metabolic abnormalities or the neuroendocrine axis on IOP regulation (McDermott et al., 2024). In contrast, elevated IOP in glaucoma is significantly associated with systemic diseases such as hypertension and diabetes (Umetsu et al., 2024). Additionally, compared to the induced elevated IOP, the elevated IOP in glaucoma lasts longer and is influenced by age-related factors. Moreover, there are also some differences between the LC in humans and rats. In primates, the LC primarily consists of collagen, with a dense population of astrocytes on its surface and LC cells within the LC (Hernandez et al., 2008). In contrast, the equivalent structure in rodents, known as the glial LC, is composed almost entirely of astrocytes and lacks collagen (Howell et al., 2007). We found that the mechanical properties of LC tissues in rats decreased with the duration of high IOP, which was consistent with the results of Braunsmann et al. (Braunsmann et al., 2012). Their results indicated that the Young's modulus of LC tissues in Pseudoexfoliation (PEX) eyes had a significant decrease compared with normal eyes.

There are some limitations in our study. First, the minimum duration of chronic elevated IOP in rats is 4 weeks, making it insufficient to observe alterations in morphology and mechanical properties of LC tissues within a shorter time. Second, we investigated the linear mechanical properties of LC tissues under chronic elevated IOP due to small indentation. Nonlinear and viscoelastic mechanical properties need to be further investigated with bigger indentation depth or other methods.

In summary, we found that mechanical properties of LC tissues in rats have changed significantly under long-term effects of high IOP. Compared with the control group, the Young's modulus of the glial LC decreased by 35.5%, 74.2%, and 80.6% after 4, 8, and 12 weeks of elevated IOP, respectively; the Young's modulus of RGC axons decreased by 45.6%, 70.9%, and 75.9% after 4, 8, and 12 weeks of elevated IOP, respectively. In addition to the supporting structures, RGC axons may also have been severely damaged. In the future study, we will set up more intensive time points of high IOP to further study the physiological changes of astrocytes and RGC axons under the effect of high IOP to provide the basis for further understanding the mechanism of the injury of the glaucoma optic nerve.

Data availability statement

The original contributions presented in the study are included in the article/Supplementary Material, further inquiries can be directed to the corresponding author/s.

Ethics statement

The animal study was approved by Institutional Animal Care and Use Committee of the Capital Medical University. The study was conducted in accordance with the local legislation and institutional requirements.

Author contributions

BM: Formal Analysis, Software, Writing – original draft. LL: Formal Analysis, Investigation, Methodology, Writing – review and editing. YL: Investigation, Writing – review and editing. JR: Writing – review and editing. XQ: Conceptualization, Funding acquisition, Resources, Visualization, Writing – review and editing.

Funding

The author(s) declare that financial support was received for the research and/or publication of this article. This research was funded by the National Natural Science Foundation of China, grant numbers 12472309 and 12072210.

Conflict of interest

The authors declare that the research was conducted in the absence of any commercial or financial relationships that could be construed as a potential conflict of interest.

Generative AI statement

The author(s) declare that no Generative AI was used in the creation of this manuscript.

Publisher's note

Supplementary material

The Supplementary Material for this article can be found online at: https://www.frontiersin.org/articles/10.3389/fbioe.2025.1574231/full#supplementary-material

References

Alzahrani, S. M., Al Doghaither, H. A., Al-Ghafari, A. B., and Pushparaj, P. N. (2023). 5-Fluorouracil and capecitabine therapies for the treatment of colorectal cancer. *Oncol. Rep.* 50, 175. doi:10.3892/or.2023.8612

Blanco, R., Martinez-Navarrete, G., Pérez-Rico, C., Valiente-Soriano, F. J., Avilés-Trigueros, M., Vicente, J., et al. (2019). A chronic ocular-hypertensive rat model induced by injection of the sclerosant agent polidocanol in the aqueous humor outflow pathway. *IJMS* 20, 3209. doi:10.3390/ijms20133209

Boote, C., Sigal, I. A., Grytz, R., Hua, Y., Nguyen, T. D., and Girard, M. J. A. (2020). Scleral structure and biomechanics. *Prog. Retin. Eye Res.* 74, 100773. doi:10.1016/j.preteyeres.2019.100773

Braunsmann, C., Hammer, C. M., Rheinlaender, J., Kruse, F. E., Schäffer, T. E., and Schlötzer-Schrehardt, U. (2012). Evaluation of lamina cribrosa and peripapillary sclera stiffness in pseudoexfoliation and normal eyes by atomic force microscopy. *Investigative Ophthalmol. & Vis. Sci.* 53, 2960–2967. doi:10.1167/iovs.11-8409

Czerpak, C. A., Ling, Y. T. T., Jefferys, J. L., Quigley, H. A., and Nguyen, T. D. (2023). The curvature, collagen network structure, and their relationship to the pressure-induced strain response of the human lamina cribrosa in normal and glaucoma eyes. *J. Biomech. Eng.* 145, 101005. doi:10.1115/1.4062846

Dai, C., Khaw, P. T., Yin, Z. Q., Li, D., Raisman, G., and Li, Y. (2012). Structural basis of glaucoma: the fortified astrocytes of the optic nerve head are the target of raised intraocular pressure. *Glia* 60, 13–28. doi:10.1002/glia.21242

Downs, J. C., and Girkin, C. A. (2017). Lamina cribrosa in glaucoma. *Curr. Opin. Ophthalmol.* 28, 113–119. doi:10.1097/ICU.0000000000000354

Grant, C. A., Thomson, N. H., Savage, M. D., Woon, H. W., and Greig, D. (2011). Surface characterisation and biomechanical analysis of the sclera by atomic force microscopy. *J. Mech. Behav. Biomed. Mater.* 4, 535–540. doi:10.1016/j.jmbbm.2010.12.011

Guan, C., Pease, M. E., Quillen, S., Ling, Y. T. T., Li, X., Kimball, E., et al. (2022). Quantitative microstructural analysis of cellular and tissue remodeling in human glaucoma optic nerve head. *Invest. Ophthalmol. Vis. Sci.* 63, 18. doi:10.1167/iovs.63.11.18

Guo, L., Moss, S. E., Alexander, R. A., Ali, R. R., Fitzke, F. W., and Cordeiro, M. F. (2005). Retinal ganglion cell apoptosis in glaucoma is related to intraocular pressure and IOP-induced effects on extracellular matrix. *Investigative Ophthalmol. & Vis. Sci.* 46, 175–182. doi:10.1167/iovs.04-0832

Hernandez, M. R., Miao, H., and Lukas, T. (2008). Astrocytes in glaucomatous optic neuropathy. *Prog. brain Res.* 173, 353–373. doi:10.1016/S0079-6123(08)01125-4

Hoerig, C., McFadden, S., Hoang, Q. V., and Mamou, J. (2022). Biomechanical changes in myopic sclera correlate with underlying changes in microstructure. *Exp. Eye Res.* 224, 109165. doi:10.1016/j.exer.2022.109165

Howell, G. R., Libby, R. T., Jakobs, T. C., Smith, R. S., Phalan, F. C., Barter, J. W., et al. (2007). Axons of retinal ganglion cells are insulted in the optic nerve early in DBA/2J glaucoma. *J. Cell Biol.* 179, 1523–1537. doi:10.1083/jcb.200706181

Inman, D. M., and Horner, P. J. (2007). Reactive nonproliferative gliosis predominates in a chronic mouse model of glaucoma. *Glia* 55, 942–953. doi:10.1002/glia.20516

Ivers, K. M., Sredar, N., Patel, N. B., Rajagopalan, L., Queener, H. M., Twa, M. D., et al. (2015). *In vivo* changes in lamina cribrosa microarchitecture and optic nerve head structure in early experimental glaucoma. *PLoS ONE* 10, 0134223. doi:10.1371/journal.pone.0134223

Jia, X., Zhang, F., Cao, M., Pan, Z., Liu, K., Zhou, D., et al. (2022). Elevated IOP alters the material properties of sclera and lamina cribrosa in monkeys. *Dis. Markers* 2022, 1–16. doi:10.1155/2022/5038847

Karimi, A., Rahmati, S. M., Grytz, R. G., Girkin, C. A., and Downs, J. C. (2021). Modeling the biomechanics of the lamina cribrosa microstructure in the human eye. *Acta Biomater.* 134, 357–378. doi:10.1016/j.actbio.2021.07.010

Kim, M. H., and Lim, S.-H. (2022). Matrix metalloproteinases and glaucoma. *Biomolecules* 12, 1368. doi:10.3390/biom12101368

Kim, N. K., Park, Y. S., Heo, D. S., Suh, C., Kim, S. Y., Park, K. C., et al. (1993). A phase III randomized study of 5-fluorouracil and cisplatin versus 5-fluorouracil, doxorubicin, and mitomycin C versus 5-fluorouracil alone in the treatment of advanced gastric cancer. *Cancer* 71, 3813–3818. doi:10.1002/1097-0142(19930615)71:12<3813::aid-cncr2820711205>3.0.co;2-5

Kırcadere, M., Harmancı, N., Eroğlu, E., Ünel, Ç. Ç., Şahin, E., and Yigitaslan, S. (2024). The potential effect of berberine on 5-fluorouracil induced gastrointestinal mucositis in rats. *Osman. Tıp Derg.* 46, 139–146. doi:10.20515/otd.1410189

Korneva, A., Kimball, E. C., Johnson, T. V., Quillen, S. E., Pease, M. E., Quigley, H. A., et al. (2023). Comparison of the biomechanics of the mouse astrocytic lamina cribrosa between glaucoma and optic nerve crush models. *Invest. Ophthalmol. Vis. Sci.* 64, 14. doi:10.1167/iovs.64.15.14

Last, J. A., Liliensiek, S. J., Nealey, P. F., and Murphy, C. J. (2009). Determining the mechanical properties of human corneal basement membranes with atomic force microscopy. *J. Struct. Biol.* 167, 19–24. doi:10.1016/j.jsb.2009.03.012

Last, J. A., Pan, T., Ding, Y., Reilly, C. M., Keller, K., Acott, T. S., et al. (2011). Elastic modulus determination of normal and glaucomatous human trabecular meshwork. *Invest. Ophthalmol. Vis. Sci.* 52, 2147–2152. doi:10.1167/iovs.10-6342

Li, T., Li, L., and Liu, Z. (2018). Time course changes of the mechanical properties of the iris pigment epithelium in a rat chronic ocular hypertension model. *BioMed Res. Int.* 2018, 1–10. doi:10.1155/2018/4862309

Ling, Y. T. T., Pease, M. E., Jefferys, J. L., Kimball, E. C., Quigley, H. A., and Nguyen, T. D. (2020). Pressure-Induced changes in astrocyte GFAP, Actin, and nuclear morphology in mouse optic nerve. *Invest. Ophthalmol. Vis. Sci.* 61, 14. doi:10.1167/iovs.61.11.14

Ling, Y. T. T., Shi, R., Midgett, D. E., Jefferys, J. L., Quigley, H. A., and Nguyen, T. D. (2019). Characterizing the collagen network structure and pressure-induced strains of the human lamina cribrosa. *Investigative Ophthalmol. & Vis. Sci.* 60, 2406–2422. doi:10.1167/iovs.18-25863

Liu, L., Liu, Y., Li, T., Li, L., Qian, X., and Liu, Z. (2022). A feasible method for independently evaluating the mechanical properties of glial LC and RGC axons by combining atomic force microscopy measurement with image segmentation. *J. Mech. Behav. Biomed. Mater.* 126, 105041. doi:10.1016/j.jmbbm.2021.105041

Liu, X., Wang, L., Ji, J., Yao, W., Wei, W., Fan, J., et al. (2014). A mechanical model of the cornea considering the crimping morphology of collagen fibrils. *Invest. Ophthalmol. Vis. Sci.* 55, 2739–2746. doi:10.1167/iovs.13-12633

Lopez, N. N., Clark, A. F., and Tovar-Vidales, T. (2020). Isolation and characterization of human optic nerve head astrocytes and lamina cribrosa cells. *Exp. Eye Res.* 197, 108103. doi:10.1016/j.exer.2020.108103

Lozano, D. C., Choe, T. E., Cepurna, W. O., Morrison, J. C., and Johnson, E. C. (2019). Early optic nerve head glial proliferation and jak-stat pathway activation in chronic experimental glaucoma. *Invest. Ophthalmol. Vis. Sci.* 60, 921–932. doi:10.1167/iovs.18-25700

Ma, B., Ren, J., and Qian, X. (2025). Study on the polarization of astrocytes in the optic nerve head of rats under high intraocular pressure: *in vitro*. *Bioengineering* 12, 104. doi:10.3390/bioengineering12020104

Matuo, R., Sousa, F. G., Escargueil, A. E., Grivicich, I., Garcia-Santos, D., Chies, J. A. B., et al. (2009). 5-Fluorouracil and its active metabolite FdUMP cause DNA damage in human SW620 colon adenocarcinoma cell line. *J Appl. Toxicol.* 29, 308–316. doi:10.1002/jat.1411

McDermott, C. E., Salowe, R. J., Di Rosa, I., and O'Brien, J. M. (2024). Stress, allostatic load, and neuroinflammation: implications for racial and socioeconomic health disparities in glaucoma. *Int. J. Mol. Sci.* 25, 1653. doi:10.3390/ijms25031653

Midgett, D. E., Jefferys, J. L., Quigley, H. A., and Nguyen, T. D. (2020). The inflation response of the human lamina cribrosa and sclera: analysis of deformation and interaction. *Acta Biomater.* 106, 225–241. doi:10.1016/j.actbio.2020.01.049

Morrison, J., Farrell, S., Johnson, E., Deppmeier, L., Moore, C. G., and Grossmann, E. (1995). Structure and composition of the rodent lamina cribrosa. *Exp. Eye Res.* 60, 127–135. doi:10.1016/s0014-4835(95)80002-6

Pang, I.-H., and Clark, A. F. (2020). Inducible rodent models of glaucoma. *Prog. Retin. Eye Res.* 75, 100799. doi:10.1016/j.preteyeres.2019.100799

Peng, F., Ma, L., Liu, L., Li, L., and Qian, X. (2019). Preliminary study on the blockade of axonal transport by activated astrocytes in optic nerve head under chronic ocular hypertension. *J. Mech. Med. Biol.* 19, 1940040. doi:10.1142/S0219519419400402

Petrelli, N., Herrera, L., Rustum, Y., Burke, P., Creaven, P., Stulc, J., et al. (1987). A prospective randomized trial of 5-fluorouracil versus 5-fluorouracil and high-dose leucovorin versus 5-fluorouracil and methotrexate in previously untreated patients with advanced colorectal carcinoma. *J. Clin. Oncol.* 5, 1559–1565. doi:10.1200/JCO.1987.5.10.1559

Prado, C. M., Baracos, V. E., McCargar, L. J., Mourtzakis, M., Mulder, K. E., Reiman, T., et al. (2007). Body composition as an independent determinant of 5-fluorouracil–based chemotherapy toxicity. *Clin. Cancer Res.* 13, 3264–3268. doi:10.1158/1078-0432.CCR-06-3067

Quigley, H. A., and Addicks, E. M. (1980). Chronic experimental glaucoma in primates. I. Production of elevated intraocular pressure by anterior chamber injection of autologous ghost red blood cells. *Invest. Ophthalmol. Vis. Sci.* 19, 126–136.

Quigley, H. A., Addicks, E. M., Green, W. R., and Maumenee, A. E. (1981). Optic nerve damage in human glaucoma: II. The site of injury and susceptibility to damage. *Archives Ophthalmol.* 99, 635–649. doi:10.1001/archopht.1981.03930010635009

Rodrigo, M. J., Garcia-Herranz, D., Subias, M., Martinez-Rincón, T., Mendez-Martínez, S., Bravo-Osuna, I., et al. (2021). Chronic glaucoma using biodegradable microspheres to induce intraocular pressure elevation. *Biomedicines* 9, 682. doi:10.3390/biomedicines9060682

Sethy, C., and Kundu, C. N. (2021). 5-Fluorouracil (5-FU) resistance and the new strategy to enhance the sensitivity against cancer: implication of DNA repair inhibition. *Biomed. & Pharmacother.* 137, 111285. doi:10.1016/j.biopha.2021.111285

Sigal, I. A., Grimm, J. L., Schuman, J. S., Kagemann, L., Ishikawa, H., and Wollstein, G. (2014). A method to estimate biomechanics and mechanical properties of optic nerve head tissues from parameters measurable using optical coherence tomography. *IEEE Trans. Med. Imaging* 33, 1381–1389. doi:10.1109/TMI.2014.2312133

Sommadossi, J., Gewirtz, D., Diasio, R., Aubert, C., Cano, J., and Goldman, I. (1982). Rapid catabolism of 5-fluorouracil in freshly isolated rat hepatocytes as analyzed by high performance liquid chromatography. *J. Biol. Chem.* 257, 8171–8176.

Strickland, R. G., Garner, M. A., Gross, A. K., and Girkin, C. A. (2022). Remodeling of the lamina cribrosa: mechanisms and potential therapeutic approaches for glaucoma. *Int. J. Mol. Sci.* 23, 8068. doi:10.3390/ijms23158068

Tham, Y.-C., Li, X., Wong, T. Y., Quigley, H. A., Aung, T., and Cheng, C.-Y. (2014). Global prevalence of glaucoma and projections of glaucoma burden through 2040: a systematic review and meta-analysis. *Ophthalmology* 121, 2081–2090. doi:10.1016/j.ophtha.2014.05.013

Ueda, J., Sawaguchi, S., Hanyu, T., Yaoeda, K., Fukuchi, T., Abe, H., et al. (1998). Experimental glaucoma model in the rat induced by laser trabecular photocoagulation after an intracameral injection of India ink. *Jpn. J. Ophthalmol.* 42, 337–344. doi:10.1016/s0021-5155(98)00026-4

Umetsu, A., Tanaka, M., Sato, T., Akiyama, Y., Endo, K., Mori, K., et al. (2024). High intraocular pressure is independently associated with new-onset systemic hypertension over a 10-year period. *Circulation J.* 88, 1689–1696. doi:10.1253/circj.CJ-24-0241

Wang, Y. X., Zhang, Q., Yang, H., Chen, J. D., Wang, N., and Jonas, J. B. (2020). Lamina cribrosa pore movement during acute intraocular pressure rise. *Br. J. Ophthalmol.* 104, 800–806. doi:10.1136/bjophthalmol-2019-314016

Williams, P. A., Marsh-Armstrong, N., and Howell, G. R. (2017). Neuroinflammation in glaucoma: a new opportunity. *Exp. Eye Res.* 157, 20–27. doi:10.1016/j.exer.2017.02.014

Yan, D. B., Coloma, F. M., Metheetrairut, A., Trope, G. E., Heathcote, J. G., and Ethier, C. R. (1994). Deformation of the lamina cribrosa by elevated intraocular pressure. *Br. J. Ophthalmol.* 78, 643–648. doi:10.1136/bjo.78.8.643

Zhang, J., Liu, Y., Liu, L., Li, L., and Qian, X. (2022). Morphological changes of glial lamina cribrosa of rats suffering from chronic high intraocular pressure. *Bioengineering* 9, 741. doi:10.3390/bioengineering9120741

Ziebarth, N. M., Wojcikiewicz, E. P., Manns, F., Moy, V. T., and Parel, J.-M. (2007). Atomic force microscopy measurements of lens elasticity in monkey eyes. *Mol. Vis.* 13, 504–510.

frontiers | Frontiers in Medicine

TYPE Original Research
PUBLISHED 30 May 2025
DOI 10.3389/fmed.2025.1518889

OPEN ACCESS

EDITED BY
Jos J. Rozema,
University of Antwerp, Belgium

REVIEWED BY
Pan Long,
General Hospital of Western Theater Command, China
Mohammed Alharthi,
Taif University, Saudi Arabia

*CORRESPONDENCE
Yanning Yang
✉ fy3554@hbuas.edu.cn
Jian Zhu
✉ zhujian0827@sina.com

†These authors share first authorship

RECEIVED 29 October 2024
ACCEPTED 13 May 2025
PUBLISHED 30 May 2025

CITATION
Zhang S, Yan Y, Shen Z, Liu L, Wang P, Zhu J and Yang Y (2025) Development of risk prediction model for small incision lenticule extraction. *Front. Med.* 12:1518889. doi: 10.3389/fmed.2025.1518889

Development of risk prediction model for small incision lenticule extraction

Shaowei Zhang[1†], Yulin Yan[1†], Zhengwei Shen[2], Lei Liu[3], Pengqi Wang[4], Jian Zhu[1*] and Yanning Yang[1*]

[1]Renmin Hospital of Wuhan University, Wuhan, China, [2]Wuhan Bright Eye Hospital, Wuhan, China, [3]Tongji Hospital Affiliated to Huazhong University of Science and Technology, Wuhan, China, [4]Xiangyang Central Hospital, Affiliated Hospital to Hubei University of Arts and Science, Xiangyang, China

Purpose: This study aimed to identify risk factors associated with small-incision lenticule extraction (SMILE) surgery and develop a risk prediction model to aid in determining patient suitability for SMILE.

Methods: This retrospective study included myopia patients from four medical centers in China, enrolled between January 2021 and December 2023. The data were randomly divided into training and test cohorts at an 8:2 ratio. A random forest (RF) model was developed and optimized using three-fold cross-validation, with feature importance assessed.

Results: The study included a total of 2,667 patients, with 2,134 patients in the training cohort and 533 patients in the test cohort. Significant statistical differences were observed in the Belin/Ambrosio Enhanced Ectasia Display and the total deviation value (BAD-D), Corvis Biomechanical Index (CBI), Tomographic and Biomechanical Index (TBI), and spherical equivalent between patients suitable for SMILE and those not suitable, in both the training and test cohorts. The univariate analysis identified ten key features relevant to SMILE. The RF model developed from the training data demonstrated high performance, with an accuracy of 96.0% in the validation set and 95.7% in the test set, an F1 score of 0.967, and an area under the curve (AUC) of 0.976 (95% CI: 0.962–0.990).

Conclusion: SMILE is not appropriate for all patients with myopia. The RF model, based on clinical characteristics, showed excellent performance in predicting SMILE suitability and has potential as a valuable tool for clinical decision-making in the future.

KEYWORDS

myopia, small-incision lenticule extraction, risk prediction, random forest, retrospective study

Background

Myopia is a common refractive disorder in which the eye is too long or the refractive power of the eye's optical system is too great (usually due to corneal protrusion resulting in excessive corneal curvature), causing images to focus in front of the retina, resulting in blurred vision at a distance (1). Epidemiological studies have shown that the global prevalence of myopia is increasing worldwide (2), and the estimated prevalence would reach 50% in 2050 if no effective intervention was performed (3). In the United States, the prevalence of myopia in

people aged 12 to 54 years nearly doubled from 1971–1972 to 1999–2004 (25 to 42%) (4). The prevalence of myopia also varies by race and ethnicity. Chiang et al. (5) showed that the prevalence of myopia in other races, Hispanic, Mexican American, non-Hispanic Black, and non-Hispanic White were 42.77, 38.43, 34.23, 32.26, and 31.06%, respectively. And the worldwide prevalence of myopia is particularly high in Asians (6). Treatment of myopia depends on individuals' symptoms and needs (7). The overall goals of treatment are to improve visual acuity, visual comfort (e.g., visual distortion, polymyalgia, decreased stereopsis), and other visual functions (e.g., color discrimination, motion detection, peripheral vision). First-line treatment includes corrective lenses, such as spectacles and contact lenses, or refractive surgery (8).

Small incision intrastromal lenticule extraction (SMILE) is one kind of refractive surgery performed using a femtosecond laser, and its early results were first reported in 2011 (9). SMILE became available in 2012, and the U.S. Food and Drug Administration (FDA) approved its use in the United States in September 2016. In a review of outcomes of SMILE patients, Song concluded that SMILE provided effective and predictable results and generally had equivalent outcomes with another refractive surgery option named laser-assisted stromal *in situ* keratomileusis (LASIK) (10). The long-term refractive regression was 0.48 diopters 5 years after surgery compared with 6 months after surgery, and there was no decrease in corrected distance visual acuity by two or more lines over the 5 years (11). Therefore, SMILE is now considered a safe and effective alternative to LASIK and photorefractive keratectomy (PRK) (12).

There are systemic and ocular contraindications to refractive surgery. Autoimmune diseases, collagen vascular diseases, and immunodeficiency disorders can impair corneal healing (13). Pregnant or lactating women can experience fluctuations in vision due to changes in corneal hydration causing refractive changes in the eye (14). Patients with scar tissue who have abnormal wound healing (e.g., keloids or abnormal scar formation) may experience abnormal corneal healing (15). Systemic medications such as oral isotretinoin can exacerbate dry eye symptoms, and amiodarone can leave transient corneal epithelial deposits (16). Although the U.S. FDA labeling contains a warning against laser refractive surgery in patients with diabetes, a literature review found that LASIK and PRK can be performed without complications in patients with well-controlled diabetes who do not have cataracts, diabetic retinopathy, or systemic complications of diabetes (17).

In summary, preoperative evaluation is crucial for decision-making in refractive surgery. This study focused on myopic patients seeking SMILE surgery to identify key factors influencing surgical suitability based on initial clinical examinations and medical history. By developing a machine learning model, we aimed to assist clinicians in determining the appropriateness of SMILE surgery for individual patients.

Methods

Study design and participants

This study included myopic patients who visited to Xiangyang Central Hospital, Affiliated Hospital to Hubei University of Arts and Science, Renmin Hospital of Wuhan University, Wuhan Bright eye hospital, and Tongji Hospital affiliated with Tongji Medical College of Huazhong University of Science and Technology from January 2021 to December 2023. The inclusion criteria were: (1) Myopic patients who intend to receive SMILE surgery; (2) Aged over 18 years or older; (3) Patients with relatively stable diopters, with recommended parameters: spherical equivalent within −0.75 to −10D, simple sphere from −0.5 to −10D, and astigmatism less than 5D. The exclusion criteria were: (1) Patients using systemic glucocorticoids or immunosuppressants, etc.; (2) Patients with diabetes, history of tumors, autoimmune diseases (including systemic lupus erythematosus, rheumatoid arthritis, multiple sclerosis, Hashimoto's thyroid disease), scar constitution, mental illness; (3) Pregnant or lactating women. This study was approved by the Ethics Committee of Xiangyang Central Hospital, and informed consent was waived due to the retrospective nature of the study.

Data collection and definitions

Baseline data were obtained from the medical history system and included the following variables: age, gender, occupation, and history of local eye diseases. Ophthalmological examination data collected comprised uncorrected visual acuity (UCVA), best corrected distance visual acuity (BCDVA), astigmatism, intraocular pressure (IOP), spherical, cylinder, axis, funduscopy evaluation, corneal thickness and diameter, corneal ectasia or other corneal degeneration, dry eye evaluation, slit lamp examination, dark pupil diameter (refers to the pupil diameter of patients in dark rooms), corneal topography data, and the tendency of keratoconus.

Patients were categorized into two groups: those suitable for SMILE surgery and those not suitable. Experienced ophthalmologists made a comprehensive assessment based on ocular examinations, which included corneal topography and biomechanics, degree of myopia, and corneal thickness.

Model development and validation

The entire cohort was randomly divided into a training set and a test set at an 8:2 ratio. A Random Forest (RF) model was utilized, with hyperparameter optimization performed using three-fold cross-validation. The final model was trained on the entire training cohort with the optimized parameters, and feature importance was assessed. The model's performance was evaluated on the test set, with predictions compared against actual outcomes. The Receiver Operating Characteristic (ROC) curve was plotted, and the Area Under the Curve (AUC) was used as the primary evaluation metric.

Statistical analysis

All statistical analyses in this study were performed using R software (version 4.2.3). Continuous variables were expressed as mean ± SD or median (IQR). Categorical variables were expressed as frequency and percentage *n* (%). Continuous variables were first tested for normality. If they were normally distributed, the *t*-test was used for

comparison between the two groups. If they were not normally distributed, the Wilcoxon-Mann-Whitney test was used for comparison between the two groups. Categorical variables were analyzed using the chi-square test or Fisher's exact value method. Factors with a miss rate > 20% were directly removed for further analysis, for data with a miss rate < 20%, the multiple imputation by chained equations (MICE) algorithm was conducted with the following parameters: five imputed datasets ($m = 5$) were generated through five iterations (maxit = 5) using the predictive mean matching (PMM) method. Following imputation, the convergence and consistency across the imputed datasets was assessed and one complete dataset with optimal stability was selected for subsequent analyses. The univariate analysis was used to explore the risk factors for the SMILE surgery. A logistic regression model was further built on the entire training set using the glm method and selected factors. Following that, bidirectional stepwise regression was performed based on the initial model, with the optimal bidirectional stepwise regression model selected as the final model according to the Akaike Information Criterion (AIC). The trained model was applied to the test set, the F1-score and area under the curve (AUC) were used for the evaluation of the developed prediction model. In this study, a $p < 0.05$ indicated a statistical significance.

Results

Patients' characteristics

A total of 2,667 patients were included in the analysis. The results revealed that patients not suitable for SMILE surgery had higher uncorrected visual acuity (UCVA) (0.06 vs. 0.04, $p < 0.001$), higher intraocular pressure (IOP) (18.00 vs. 17.25, $p < 0.001$), and a higher spherical equivalent (−5.28 vs. −4.75, $p < 0.001$), as well as lower K1, K2, and Km values. In terms of corneal characteristics, the non-SMILE group exhibited a larger radius of curvature, higher BAD-D (2.38 vs. 1.17, $p < 0.001$), higher CBI (0.62 vs. 0.02, $p < 0.001$), higher TBI (0.86 vs. 0.13, $p < 0.001$), and a larger dark pupil diameter (6.59 vs. 6.37, $p < 0.001$) (Table 1).

After splitting the data, the training cohort comprised 2,134 patients, while the test cohort had 533 patients. Despite the random split, the characteristics of patients in the training and test cohorts were similar to those of the overall cohort. Significant differences remained for BAD-D (training: 1.17 vs. 2.37; test: 1.19 vs. 2.48, both $p < 0.001$), CBI (training: 0.02 vs. 0.61; test: 0.04 vs. 0.66, both $p < 0.001$), TBI (training: 0.13 vs. 0.86; test: 0.14 vs. 0.88, both $p < 0.001$), and spherical equivalent (training: −5.50 vs. −4.75; test:

TABLE 1 Clinical characteristics for all participants.

Variables	Not suitable for SMILE (n = 975)	Suitable for SMIL (n = 1,692)	p-value
UCVA	0.06 (0.04, 0.10)	0.04 (0.02, 0.10)	<0.001
BSCVA	1.00 (1.00, 1.00)	1.00 (1.00, 1.00)	<0.001
IOP	18.00 (15.85, 20.00)	17.25 (15.00, 19.30)	<0.001
Spherical	-4.75 (−7.50, −3.50)	−4.50 (−5.50, −3.50)	<0.001
Cylinder	−0.50 (−0.75, 0.00)	−0.50 (−1.00, −0.25)	0.013
Axis	75.00 (0.00, 170.00)	80.00 (5.00, 170.00)	0.122
Spherical equivalent	−5.38 (−8.50, −4.00)	−4.75 (−5.88, −3.75)	<0.001
K1	42.70 (41.60, 44.10)	43.10 (42.20, 43.80)	<0.001
Axial K1	98.90 (8.00, 172.00)	98.80 (8.00, 171.70)	0.950
K2	43.90 (42.70, 45.20)	44.20 (43.20, 45.00)	0.006
Axial K2	89.70 (81.95, 97.65)	89.80 (81.50, 97.90)	0.855
Km	43.25 (42.17, 44.62)	43.60 (42.65, 44.40)	0.002
Mean radius of curvature	7.81 (7.57, 8.01)	7.74 (7.60, 7.91)	0.002
WTW	11.60 (11.30, 11.90)	11.60 (11.40, 11.90)	0.004
Preoperative Corneal thickness, μm	538.00 (508.00, 559.00)	547.00 (528.00, 564.00)	<0.001
BAD-D	2.38 (1.40, 2.97)	1.17 (0.96, 1.42)	<0.001
CBI	0.62 (0.23, 0.82)	0.02 (0.00, 0.13)	<0.001
TBI	0.86 (0.36, 1.00)	0.13 (0.04, 0.25)	<0.001
Dark pupil diameter, mm	6.59 (6.12, 7.16)	6.37 (5.95, 6.73)	<0.001
Schirmer's tear test, mm	14.00 (12.00, 16.00)	14.00 (12.00, 15.00)	0.201
Dominant eye, n (%)			0.145
Left	745 (76.41)	1,334 (78.84)	
Right	230 (23.59)	358 (21.16)	
Astigmatism, n (%)	783 (80.31)	1,382 (81.68)	0.383

BAD-D, Belin/Ambrosio Enhanced Ectasia Display and the total deviation value; CBI, Corvis Biomechanical Index; IOP, Intraocular pressure; TBI, Tomographic and Biomechanical Index; UCVA, uncorrected visual acuity, BSCVA, best spectacle-corrected visual acuity.

TABLE 2 Clinical characteristics for participants in the training cohort.

Variables	Not suitable for SMILE (n = 780)	Suitable for SMILE (n = 1,354)	p-value
UCVA	0.06 (0.03, 0.10)	0.04 (0.02, 0.10)	0.001
BSCVA	1.00 (1.00, 1.00)	1.00 (1.00, 1.00)	<0.001
IOP	18.00 (15.88, 20.00)	17.40 (15.20, 19.40)	0.001
S	−4.75 (−7.75, −3.50)	−4.50 (−5.50, −3.50)	<0.001
C	−0.50 (−0.75, 0.00)	−0.50 (−1.00, −0.25)	0.052
A	72.50 (0.00, 170.00)	80.00 (5.00, 170.00)	0.277
Spherical equivalent	−5.50 (−8.50, −4.00)	−4.75 (−5.88, −3.75)	<0.001
K1	42.70 (41.60, 44.20)	43.10 (42.20, 43.88)	0.006
Axial K1	111.55 (7.77, 172.62)	92.80 (8.30, 171.57)	0.579
K2	43.90 (42.70, 45.20)	44.20 (43.20, 45.00)	0.027
Axial K2	89.30 (82.00, 97.23)	89.90 (81.53, 98.30)	0.352
Km	43.30 (42.14, 44.65)	43.60 (42.65, 44.45)	0.012
Mean radius of curvature	7.81 (7.59, 8.02)	7.74 (7.61, 7.91)	0.001
WTW	11.60 (11.30, 11.90)	11.60 (11.40, 11.90)	0.003
Preoperative Corneal thickness, μm	538.00 (508.00, 559.00)	547.00 (529.00, 564.00)	<0.001
BAD-D	2.37 (1.39, 2.97)	1.17 (0.94, 1.42)	<0.001
CBI	0.61 (0.21, 0.81)	0.02 (0.00, 0.12)	<0.001
TBI	0.86 (0.35, 1.00)	0.13 (0.04, 0.25)	<0.001
dark pupil diameter, mm	6.61 (6.13, 7.18)	6.36 (5.93, 6.73)	<0.001
Schirmer's tear test, mm	14.00 (12.00, 15.00)	14.00 (12.00, 15.75)	0.089
Dominant eye, n (%)			0.389
Left	602 (77.2)	1,068 (78.9)	
Right	178 (22.8)	286 (21.1)	
Astigmatism, n (%)	626 (80.36)	1,106 (81.68)	0.428

BAD-D, Belin/Ambrosio Enhanced Ectasia Display and the total deviation value; CBI, Corvis Biomechanical Index; IOP, Intraocular pressure; TBI, Tomographic and Biomechanical Index; UCVA, uncorrected visual acuity, BSCVA, best spectacle-corrected visual acuity.

−5.12 vs. −5.00, both $p < 0.001$). Detailed information is provided in Tables 2, 3.

Univariate analysis for SMILE surgery

The univariate analysis identified ten factors associated with suitability for SMILE surgery, including BSCVA (OR: 18.96, 95%CI: 9.48 ~ 37.93, $p < 0.001$), IOP (OR: 0.95, 95%CI: 0.93 ~ 0.97, $p < 0.001$), S (OR: 1.15, 95%CI: 1.12 ~ 1.19, $p < 0.001$), spherical equivalent (OR: 1.15, 95%CI: 1.22 ~ 1.31, $p < 0.001$), WTW (OR:1.37, 95%CI: 1.12 ~ 1.68, $p = 0.002$), preoperative corneal thickness (OR:1.02, 95%CI: 1.01 ~ 1.02, $p < 0.001$), BAD-D (OR: 0.11, 95%CI: 0.09 ~ 0.13, $p < 0.001$), CBI (OR: 0.00, 95%CI: 0.00 ~ 0.00, $p < 0.001$), TBI (OR: 0.00, 95%CI: 0.00 ~ 0.00, $p < 0.001$), dark pupil diameter (OR: 0.57, 95%CI: 0.50 ~ 0.64, $p < 0.001$), and Schirmer's tear test (OR: 1.04, 95%CI: 1.02 ~ 1.06, $p < 0.001$) (Table 4).

Model performance

An RF model was developed and fine-tuned. The analysis identified the top five features that most significantly reduced the Gini coefficient: TBI, BAD-D, CBI, spherical equivalent, and spherical (Figure 1). This finding supports our previous analysis of the differing characteristics between the non-SMILE and SMILE groups. Cross-validation results indicated an accuracy of 96.0%, while the test results showed an accuracy of 95.7%. The F1 score was 0.967, and the AUC was 0.976 (Figure 2). The confusion matrix is provided in Figure 3.

The comparison of the two models showed that the RF model outperformed the logistic regression model in both the training and testing datasets, with AUC values of 1.000 versus 0.985 for the training set and 0.997 versus 0.968 for the testing set (Figure 4).

Discussion

This study identified BSCVA, IOP, S, spherical equivalent, preoperative corneal thickness, BAD-D, CBI, TBI, dark pupil diameter, and Schirmer's tear test as important factors for determining SMILE surgery suitability. Using these factors, a RF model was developed for predicting non-SMILE cases. The model achieved an AUC of 0.976, with an accuracy of 97.4% and an F1 score of 97.7%. These results suggest that machine learning methods could be a valuable tool for future surgical decision-making.

SMILE is an "all-in-one" surgical method for refractive correction that has been widely adopted worldwide. However, several risk factors have been associated with SMILE surgery and its prognosis. Lee et al. (18) found that steep corneal curvature is linked to a higher risk of significant postoperative residual astigmatism after SMILE surgery, Yang et al. (19) reported that steep corneal curvature, thin cap thickness, and high preoperative spherical equivalent are potential risk factors for the formation of an opaque bubble layer during SMILE surgery. Zhao et al. (20) demonstrated that the spherical equivalent is

TABLE 3 Clinical characteristics for participants in the test cohort.

Variables	Not suitable for SMILE (*n* = 195)	Suitable for SMILE (*n* = 338)	*p*-value
UCVA	0.04 (0.04, 0.11)	0.04 (0.02, 0.10)	0.129
BSCVA	1.00 (1.00, 1.00)	1.00 (1.00, 1.00)	0.037
IOP	18.00 (15.90, 19.00)	17.00 (15.00, 19.08)	0.195
S	−4.75 (−6.88, −3.50)	−4.75 (−5.50, −3.50)	0.056
C	−0.50 (−0.75, 0.00)	−0.50 (−1.00, −0.25)	0.098
A	75.00 (0.00, 167.50)	90.00 (5.50, 170.00)	0.179
Spherical equivalent	−5.12 (−7.62, −4.00)	−5.00 (−6.00, −3.75)	<0.001
K1	42.70 (41.75, 43.80)	43.20 (42.30, 43.80)	0.014
Axial K1	59.50 (8.55, 168.45)	112.40 (7.62, 172.40)	0.223
K2	43.80 (42.80, 44.90)	44.20 (43.30, 44.90)	0.067
Axial K2	91.80 (81.45, 98.90)	89.50 (81.50, 96.80)	0.141
Km	43.10 (42.38, 44.23)	43.65 (42.71, 44.30)	0.037
Mean radius of curvature	7.80 (7.52, 8.00)	7.71 (7.59, 7.88)	0.293
WTW	11.60 (11.30, 11.90)	11.60 (11.40, 11.80)	0.528
Preoperative Corneal thickness, μm	537.00 (506.00, 562.00)	544.00 (527.00, 560.75)	0.001
BAD-D	2.48 (1.48, 2.98)	1.19 (0.98, 1.39)	<0.001
CBI	0.66 (0.25, 0.86)	0.04 (0.00, 0.15)	<0.001
TBI	0.88 (0.45, 1.00)	0.14 (0.04, 0.25)	<0.001
dark pupil diameter, mm	6.53 (5.96, 7.04)	6.39 (6.00, 6.81)	0.016
Schirmer's tear test, mm	14.00 (12.00, 17.00)	14.00 (12.00, 15.00)	0.596
Dominant eye, *n* (%)			0.192
Left	143 (73.3)	266 (78.7)	
Right	52 (26.7)	72 (21.3)	
Astigmatism, *n* (%)	157 (80.51)	276 (81.66)	0.657

BAD-D, Belin/Ambrosio Enhanced Ectasia Display and the total deviation value; CBI, Corvis Biomechanical Index; IOP, Intraocular pressure; TBI, Tomographic and Biomechanical Index; UCVA, uncorrected visual acuity, BSCVA, best spectacle-corrected visual acuity.

TABLE 4 Univariate analysis for surgery decision.

Variables	*p*-value	OR (95%CI)
UCVA	0.236	0.62 (0.28 ~ 1.37)
BSCVA	<0.001	18.96 (9.48 ~ 37.93)
IOP	<0.001	0.95 (0.93 ~ 0.97)
S	<0.001	1.15 (1.12 ~ 1.19)
C	0.094	0.89 (0.77 ~ 1.02)
A	0.245	1.00 (1.00 ~ 1.00)
Spherical equivalent	<0.001	1.27 (1.22 ~ 1.31)
K1	0.439	1.02 (0.97 ~ 1.07)
Axial K1	0.923	1.00 (1.00 ~ 1.00)
K2	0.540	0.99 (0.94 ~ 1.03)
Axial K2	0.369	1.00 (1.00 ~ 1.00)
Km	0.977	1.00 (0.95 ~ 1.05)
The mean radius of curvature	0.516	0.91 (0.68 ~ 1.21)
WTW	0.002	1.37 (1.12 ~ 1.68)
Preoperative Corneal thickness, μm	<0.001	1.02 (1.01 ~ 1.02)
BAD-D	<0.001	0.11 (0.09 ~ 0.13)
CBI	<0.001	0.00 (0.00 ~ 0.00)
TBI	<0.001	0.00 (0.00 ~ 0.00)
Dark pupil diameter, mm	<0.001	0.57 (0.50 ~ 0.64)
Schirmer's tear test, mm	<0.001	1.04 (1.02 ~ 1.06)
Dominant eye (right)	0.145	0.87 (0.72 ~ 1.05)
Presence of astigmatism	0.383	1.09 (0.89 ~ 1.34)

BAD-D, Belin/Ambrosio Enhanced Ectasia Display and the total deviation value; CBI, Corvis Biomechanical Index; IOP, Intraocular pressure; TBI, Tomographic and Biomechanical Index; UCVA, uncorrected visual acuity, BSCVA, best spectacle-corrected visual acuity.

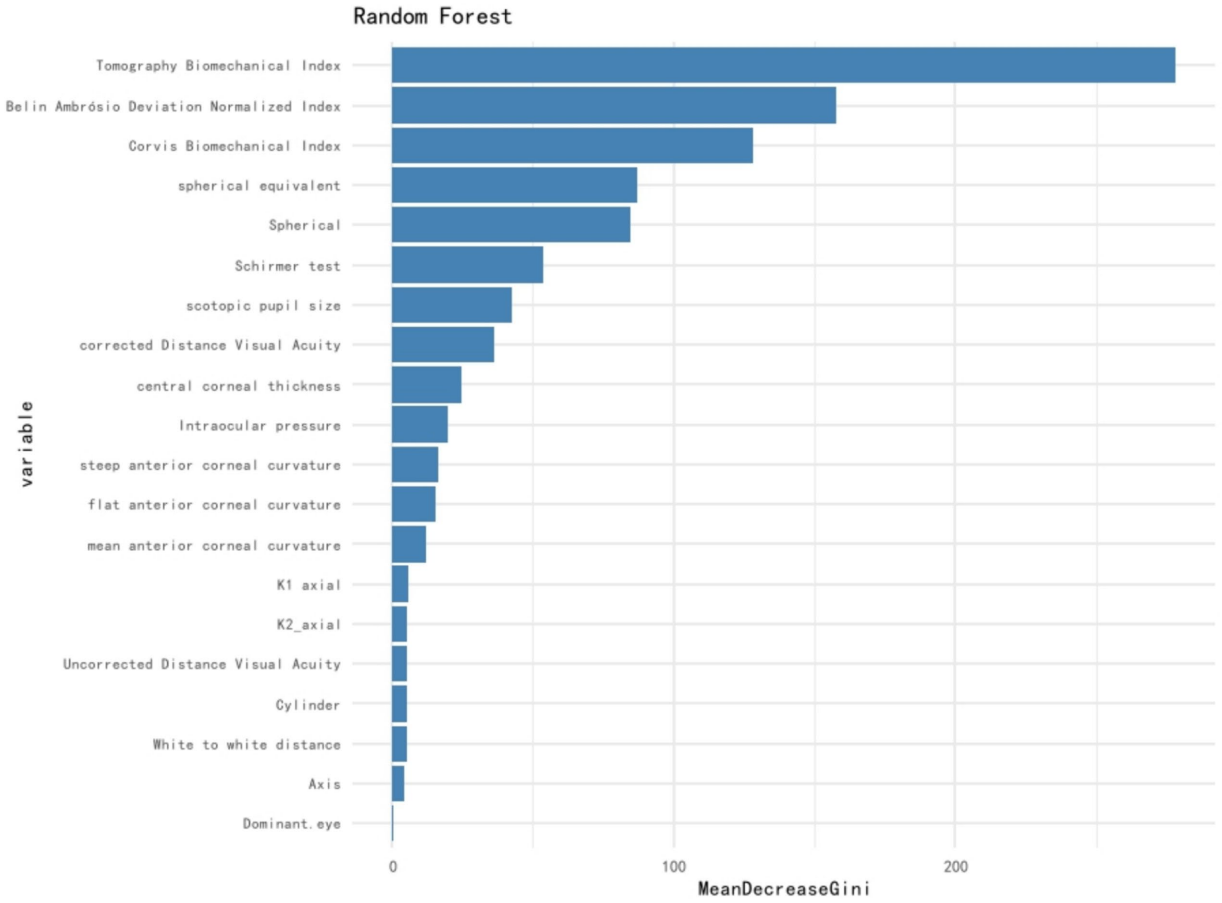

FIGURE 1
Feature importance for the random forest model.

correlated with surgical complications. Consistent with these studies, our results indicated that the spherical equivalent differed significantly between patients suitable for SMILE and those not suitable, even after data splitting, with a p value < 0.001. Furthermore, the spherical equivalent was identified as a risk factor for SMILE surgery, with an OR of 1.27 (95% CI: 1.22–1.31, $p < 0.001$).

CBI, TBI, and BAD-D are biomechanical features widely used for evaluating myopia, SMILE surgery, and other ocular diseases. Zarei-Ghanavati et al. (21) conducted a study where participants received a 110-μm cap thickness in one eye and a 145-μm cap thickness in the fellow eye. Three months post-surgery, researchers found a significant difference in the CBI (21). Vinviguerra et al. (22) suggested that CBI-related techniques could be useful for managing patients who underwent keratectomy. Corral et al. explored the changes in CBI and TBI in patients who successfully underwent orthokeratology (23). Additionally, Zhang et al. (24) used BAD-D, CBI, and TBI in combination as early predictive indicators for myopia patients with keratoconus before refractive surgery, showing that TBI, CBI, and BAD-D had excellent diagnostic efficiency. In our study, aside from the spherical equivalent, CBI, TBI, and BAD-D were consistently significant ($p < 0.001$) in both the training and test cohorts. The univariate analysis for these three factors also indicated their potential as useful features for SMILE surgery decision-making.

RF is a well-established machine learning algorithm with extensive applications across medical science. From the perspectives of myopia and SMILE surgery, several studies have demonstrated its efficacy. Xu et al. (25) employed the RF model to explore changes in pupil diameter among myopic preschoolers. Wang et al. (26) developed various machine learning models and found that the RF model performed best in estimating lenticule thickness in SMILE surgery. Additionally, Li et al. (27) created an RF-based model for selecting refractive surgery based on clinical data, which showed a strong agreement with ophthalmologists, with a performance metric of 0.8775. Given that RF is a validated and robust model across diverse datasets, the current study did not compare RF with other models and we will incorporate other machine learning models in future analysis. Nonetheless, the RF model demonstrated excellent performance in terms of both AUC and accuracy in this study. The development of this prediction model had great clinical potential, for patients who consider the SMILE operation, the model could provide a personalized prediction, although the prognostic of SMILE was not included in the present study, the model correlation well with the opinion of experienced ophthalmologists, which was of ultimate importance for medical centers with limited medical resources.

Except for the features selected, there were many other reasons that could affect the execution of SMILE surgery, including patients' willingness, financial status, and occupation requirement; all these factors were not included for the analysis; therefore, more detailed inclusion and exclusion criteria should be made for future studies. Moreover, to exclude potential confounding factors,

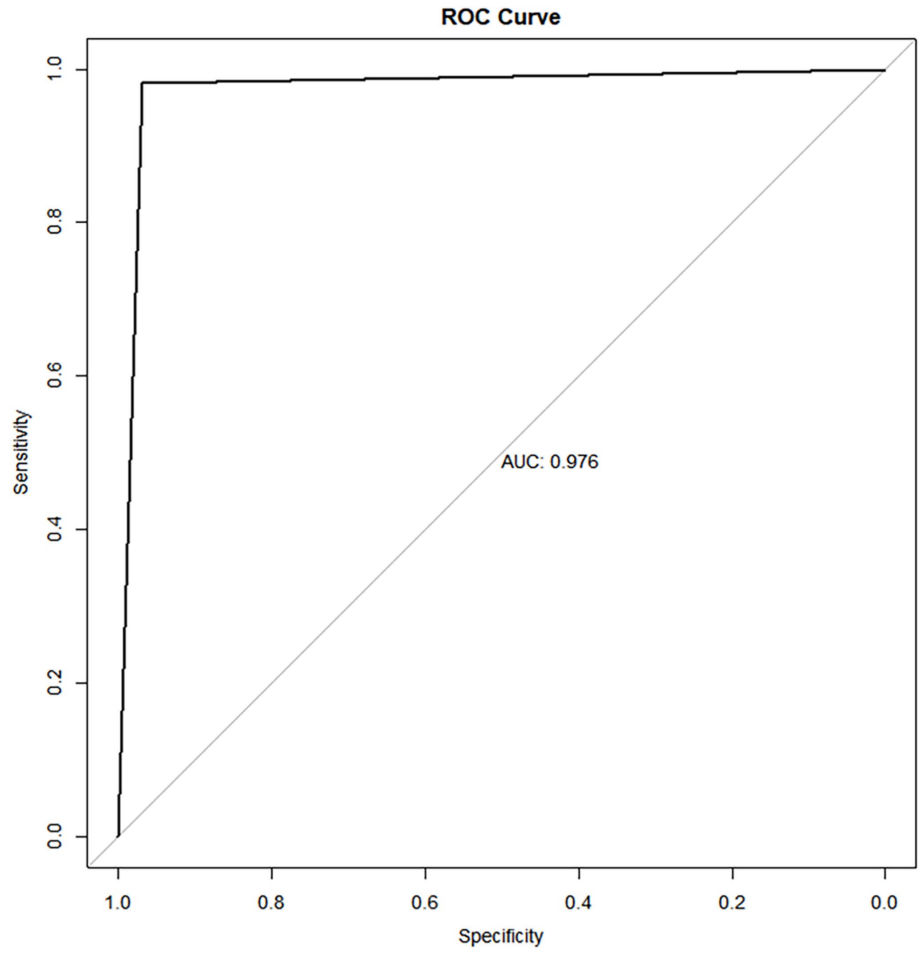

FIGURE 2
ROC curve of the random forest model for surgery decision prediction, the AUC was 0.976 (95%CI:0.962–0.990).

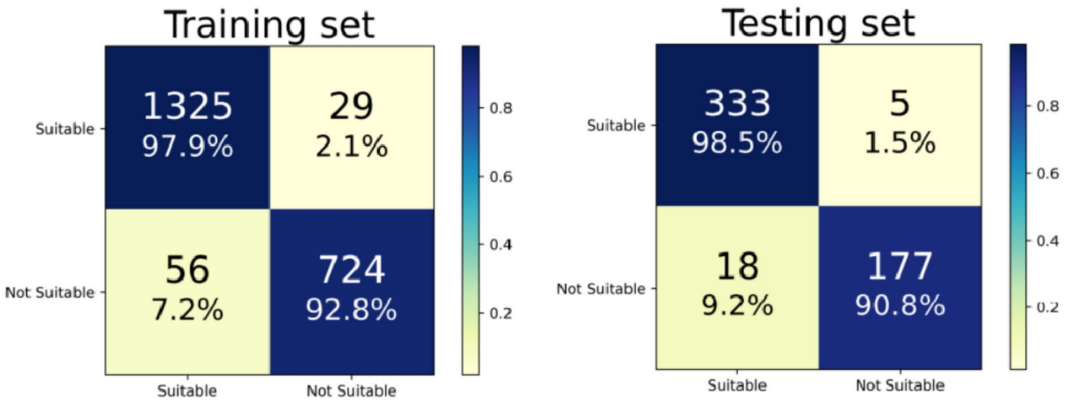

FIGURE 3
Confusion matrices of the training set and testing set.

mediation analysis should also be considered in future analyses. Consejo et al. (28) found that age is significantly correlated with both corneal tilt and corneal densitometry, and the interaction between corneal tilt and corneal densitometry is strongly influenced by age, in the present study, many parameters were included, and the mediation analysis could help filter features with greater importance.

However, this study has several limitations. Firstly, despite including patients from multiple medical centers, the retrospective nature of the study introduces selection bias, also, to improve the model performance, we did not select some data or further include data from other medical centers as an independent external validation set, which could limit the generalization ability of the present study. Secondly, the

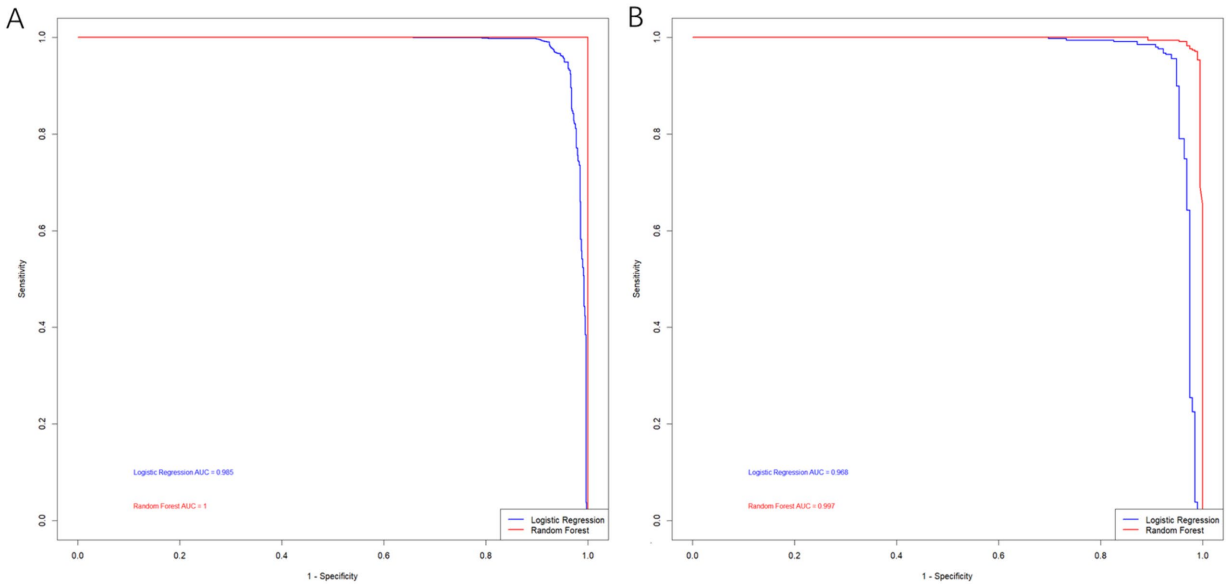

FIGURE 4
ROC curve of the random forest model and logistic regression model. **(A)** Training set; **(B)** Testing set.

determination of suitability for SMILE surgery was made by experienced ophthalmologists, making the results heavily reliant on their clinical judgment and expertise. Thirdly, due to time constraints, we were unable to perform a prognosis-related analysis. Investigating the risk factors associated with SMILE surgery outcomes would be highly valuable for future research.

Conclusion

This study showed that factors such as BSCVA, IOP, S, spherical equivalent, preoperative corneal thickness, BAD-D, CBI, TBI, dark pupil diameter, and the Schirmer's tear test are crucial in determining suitability for SMILE surgery. Additionally, the RF model was found to be an effective tool for aiding surgical decision-making. However, the retrospective design of this study limits its clinical applicability, highlighting the need for a larger prospective study to validate these findings.

Data availability statement

The original contributions presented in the study are included in the article/supplementary material, further inquiries can be directed to the corresponding authors.

Ethics statement

All procedures were performed in accordance with the ethical standards laid down in the 1964 Declaration of Helsinki and its later amendments. It was approved by the Ethics Committee of Xiangyang Central Hospital. The requirement for individual Informed consent was waived by Ethics Committee of Xiangyang Central Hospital because of the retrospective nature of the study. The study was carried out in accordance with the applicable guidelines and regulations.

Author contributions

SZ: Conceptualization, Investigation, Methodology, Writing – original draft, Writing – review & editing. YuY: Funding acquisition, Methodology, Software, Writing – original draft, Writing – review & editing. ZS: Investigation, Resources, Software, Writing – original draft, Writing – review & editing. LL: Methodology, Resources, Validation, Writing – original draft, Writing – review & editing. PW: Investigation, Software, Validation, Writing – original draft, Writing – review & editing. JZ: Formal analysis, Methodology, Software, Writing – original draft, Writing – review & editing. YaY: Conceptualization, Methodology, Project administration, Writing – original draft, Writing – review & editing.

Funding

The author(s) declare that no financial support was received for the research and/or publication of this article.

Conflict of interest

The authors declare that the research was conducted in the absence of any commercial or financial relationships that could be construed as a potential conflict of interest.

Generative AI statement

The authors declare that no Gen AI was used in the creation of this manuscript.

Publisher's note

References

1. Jackson D, Moosajee M. The genetic determinants of axial length: from Microphthalmia to high myopia in childhood. *Annu Rev Genomics Hum Genet*. (2023) 24:177–202. doi: 10.1146/annurev-genom-102722-090617

2. Bullimore MA, Ritchey ER, Shah S, Leveziel N, Bourne RRA, Flitcroft DI. The risks and benefits of myopia control. *Ophthalmology*. (2021) 128:1561–79. doi: 10.1016/j.ophtha.2021.04.032

3. Holden BA, Fricke TR, Wilson DA, Jong M, Naidoo KS, Sankaridurg P, et al. Global prevalence of myopia and high myopia and temporal trends from 2000 through 2050. *Ophthalmology*. (2016) 123:1036–42. doi: 10.1016/j.ophtha.2016.01.006

4. Vitale S, Sperduto RD, Ferris FL 3rd. Increased prevalence of myopia in the United States between 1971-1972 and 1999-2004. *Arch Ophthalmol*. (2009) 127:1632–9. doi: 10.1001/archophthalmol.2009.303

5. Chiang SY, Weng TH, Lin CM, Lin SM. Ethnic disparity in prevalence and associated risk factors of myopia in adolescents. *J Formos Med Assoc*. (2020) 119:134–43. doi: 10.1016/j.jfma.2019.03.004

6. Wong YL, Saw SM. Epidemiology of pathologic myopia in Asia and worldwide. *Asia Pac J Ophthalmol*. (2016) 5:394–402. doi: 10.1097/APO.0000000000000234

7. Singh H, Singh H, Latief U, Tung GK, Shahtaghi NR, Sahajpal NS, et al. Myopia, its prevalence, current therapeutic strategy and recent developments: a review. *Indian J Ophthalmol*. (2022) 70:2788–99. doi: 10.4103/ijo.IJO_2415_21

8. Gwiazda J. Treatment options for myopia. *Optom Vis Sci*. (2009) 86:624–8. doi: 10.1097/OPX.0b013e3181a6a225

9. Shah R, Shah S, Sengupta S. Results of small incision lenticule extraction: all-in-one femtosecond laser refractive surgery. *J Cataract Refract Surg*. (2011) 37:127–37. doi: 10.1016/j.jcrs.2010.07.033

10. Song J, Cao H, Chen X, Zhao X, Zhang J, Wu G, et al. Small incision Lenticule extraction (SMILE) versus laser assisted stromal in situ Keratomileusis (LASIK) for astigmatism corrections: a systematic review and meta-analysis. *Am J Ophthalmol*. (2023) 247:181–99. doi: 10.1016/j.ajo.2022.11.013

11. Blum M, Täubig K, Gruhn C, Sekundo W, Kunert KS. Five-year results of small incision lenticule extraction (ReLEx SMILE). *Br J Ophthalmol*. (2016) 100:1192–5. doi: 10.1136/bjophthalmol-2015-306822

12. Moshirfar M, Tukan AN, Bundogji N, Liu HY, McCabe SE, Ronquillo YC, et al. Ectasia after corneal refractive surgery: a systematic review. *Ophthalmol Ther*. (2021) 10:753–76. doi: 10.1007/s40123-021-00383-w

13. AlKharashi M, Bower KS, Stark WJ, Daoud YJ. Refractive surgery in systemic and autoimmune disease. *Middle East Afr J Ophthalmol*. (2014) 21:18–24. doi: 10.4103/0974-9233.124082

14. Anton N, Doroftei B, Ilie OD, Ciuntu RE, Bogdănici CM, Nechita-Dumitriu I. A narrative review of the complex relationship between pregnancy and eye changes. *Diagnostics (Basel)*. (2021) 11:1329. doi: 10.3390/diagnostics11081329

15. Fioretto BS, Rosa I, Andreucci E, Mencucci R, Marini M, Romano E, et al. Pharmacological stimulation of soluble guanylate cyclase counteracts the Profibrotic activation of human conjunctival fibroblasts. *Cells*. (2024) 13:360. doi: 10.3390/cells13040360

16. Ruiz-Lozano RE, Hernández-Camarena JC, Garza-Garza LA, Bustamante-Arias A, Colorado-Zavala MF, Cardenas-de la Garza JA. Isotretinoin and the eye: a review for the dermatologist. *Dermatol Ther*. (2020) 33:e14029. doi: 10.1111/dth.14029

17. Choi W, Bae HW, Shin HJ, Kim EW, Kim CY, Kim M, et al. Predicting the safety zone for steroid-induced ocular hypertension induced by intravitreal dexamethasone implantation. *Br J Ophthalmol*. (2022) 106:1150–6. doi: 10.1136/bjophthalmol-2020-318401

18. Lee CY, Shen JH, Chao CC, Lian IB, Huang JY, Yang SF, et al. Topographic and surgical risk factors for high postoperative residual astigmatism after small incision lenticule extraction in patients with different degrees of myopia: a retrospective cohort study. *BMC Ophthalmol*. (2024) 24:45. doi: 10.1186/s12886-024-03296-x

19. Yang S, Wang H, Chen Z, Li Y, Chen Y, Long Q. Possible risk factors of opaque bubble layer and its effect on high-order aberrations after small incision lenticule extraction. *Front Med (Lausanne)*. (2023) 10:1156677. doi: 10.3389/fmed.2023.1156677

20. Zhao J, Li Y, Yu T, Wang W, Emmanuel MT, Gong Q, et al. Anterior segment inflammation and its association with dry eye parameters following myopic SMILE and FS-LASIK. *Ann Med*. (2023) 55:689–95. doi: 10.1080/07853890.2023.2181388

21. Zarei-Ghanavati S, Jafarzadeh SV, Es'haghi A, Kiarudi MY, Hassanzadeh S, Ziaei M. Comparison of 110- and 145-μm small-incision Lenticule extraction cap thickness: a randomized contralateral eye study. *Cornea*. (2024) 43:154–8. doi: 10.1097/ICO.0000000000003294

22. Vinciguerra R, Cancian G, Ambrósio R Jr, Elsheikh A, Eliasy A, Lopes B, et al. Assessment of the specificity of corvis biomechanical index-laser vision correction (CBI-LVC) in stable corneas after phototherapeutic keratectomy. *Int Ophthalmol*. (2023) 43:4289–95. doi: 10.1007/s10792-023-02840-w

23. Pérez-Corral J, Cardona G, Piñero DP, Barroso D, Armadans L. Short- and mid-term changes in CORVIS ST parameters in successful, adult orthokeratology patients. *Clin Exp Optom*. (2023) 106:726–33. doi: 10.1080/08164622.2022.2140031

24. Zhang M, Zhang F, Li Y, Song Y, Wang Z. Early diagnosis of Keratoconus in Chinese myopic eyes by combining Corvis ST with Pentacam. *Curr Eye Res*. (2020) 45:118–23. doi: 10.1080/02713683.2019.1658787

25. Xu S, Li L, Han W, Zhu Y, Hu Y, Li Z, et al. Association between myopia and pupil diameter in preschoolers: evidence from a machine learning approach based on a real-world large-scale dataset. *Ophthalmol Ther*. (2024) 13:2009–22. doi: 10.1007/s40123-024-00972-5

26. Wang H, Zheng S, Tang S, Zhang X, Chen Y, Zhu Y. Investigation of accuracy and influence factors of predicting lenticule thickness in small incision lenticule extraction by machine learning models. *J Pers Med*. (2023) 13:256. doi: 10.3390/jpm13020256

27. Li J, Dai Y, Mu Z, Wang Z, Meng J, Meng T, et al. Choice of refractive surgery types for myopia assisted by machine learning based on doctors' surgical selection data. *BMC Med Inform Decis Mak*. (2024) 24:41. doi: 10.1186/s12911-024-02451-0

28. Consejo A, Jiménez-García M, Rozema JJ, Abass A. Influence of eye tilt on corneal densitometry. *Ophthalmic Physiol Opt*. (2022) 42:1032–7. doi: 10.1111/opo.13020

frontiers | Frontiers in Bioengineering and Biotechnology

TYPE Original Research
PUBLISHED 24 June 2025
DOI 10.3389/fbioe.2025.1576809

OPEN ACCESS

EDITED BY
Sabine Kling,
University of Bern, Switzerland

REVIEWED BY
Karim Makdoumi,
Örebro University, Sweden
Alexander Heisterkamp,
Leibniz University Hannover, Germany

*CORRESPONDENCE
Jan Rix,
jan.rix@tu-dresden.de

†These authors have contributed equally to this work and share first authorship

RECEIVED 14 February 2025
ACCEPTED 11 June 2025
PUBLISHED 24 June 2025

CITATION
Rix J, Steuer S, Golde J, Husein F, Lochmann F, Melcher S, Steiner G, Galli R, Walther J, Raiskup F, Khoramnia R and Herber R (2025) Investigation of corneal hydration and the impact of cross-linking therapy on water retention using Brillouin spectroscopy, Raman spectroscopy and polarization-sensitive optical coherence tomography.
Front. Bioeng. Biotechnol. 13:1576809.
doi: 10.3389/fbioe.2025.1576809

Investigation of corneal hydration and the impact of cross-linking therapy on water retention using Brillouin spectroscopy, Raman spectroscopy and polarization-sensitive optical coherence tomography

Jan Rix[1*†], Svea Steuer[2†], Jonas Golde[1,2,3], Fadi Husein[4], Felix Lochmann[4], Steven Melcher[2], Gerald Steiner[2], Roberta Galli[1], Julia Walther[1], Frederik Raiskup[4], Ramin Khoramnia[4] and Robert Herber[4]

[1]TU Dresden, Faculty of Medicine Carl Gustav Carus, Medical Physics and Biomedical Engineering, Dresden, Germany, [2]TU Dresden, Faculty of Medicine Carl Gustav Carus, Department of Anesthesiology and Intensive Care Medicine, Clinical Sensoring and Monitoring, Dresden, Germany, [3]Fraunhofer Institute for Material and Beam Technology IWS, Dresden, Germany, [4]Department of Ophthalmology, Faculty of Medicine and University Hospital Carl Gustav Carus, TU Dresden, Dresden, Germany

Recently, Brillouin spectroscopy has been proposed as a promising non-invasive tool to evaluate corneal biomechanics, e.g., during corneal cross-linking (CXL) treatment. However, the impact of corneal hydration on the Brillouin shift hampers straightforward interpretation of the measurements, especially when judging on the success of the CXL procedure. Therefore, in this work, we first quantify the effect of corneal (de)hydration on the Brillouin shift revealing that reliable measurements are only possible under constant hydration conditions, which was subsequently achieved by immersing porcine eyes in solution and waiting until an equilibrium state was reached. Investigations showed that Brillouin spectroscopy evaluates the CXL effect mainly indirectly via reduced water uptake, while polarization-sensitive optical coherence tomography evaluates the CXL effect directly via changes in collagen fiber alignment and is therefore insensitive to corneal hydration. Raman spectroscopy is not indicating any alterations in the molecular structure revealing that new cross-links are not created due to the CXL procedure. Compared to large water retention in balanced salt solution, the missing water uptake in dextran-based (16%) solution hampers the evaluation of the CXL effect by Brillouin spectroscopy.

KEYWORDS

cornea, corneal cross-linking, Brillouin, Raman, PS-OCT, hydration

1 Introduction

Keratoconus is an eye disease in which the cornea becomes thinner and cone-shaped (Rabinowitz, 1998). This unnatural corneal curvature results in astigmatism and a loss of visual acuity, which cannot be corrected by eyeglasses (Zadnik et al., 1996). While the underlying causes for this pathology are still subject of current research (Galvis et al., 2015; Karolak and Gajecka, 2017; Sugar and Macsai, 2012), corneal cross-linking (CXL) has been established as the standard treating method during the last 20 years, as it slows down or even stops corneal weakening (Raiskup et al., 2024; McGhee, Kim, and Wilson, 2015). In CXL, the corneas are soaked with the photosensitizer riboflavin and then irradiated with UV-A light to strengthen the collagen fibers and thus restore the original tensile strength of the cornea. Although CXL is routinely performed in clinics, the underlying molecular mechanisms are still subject of research (Hayes et al., 2013; McCall et al., 2010; O'Brart and David, 2014).

The most commonly used technique to evaluate the cross-linking effect is stress-strain extensiometry (Elsheikh and Anderson, 2005). Previous stress-strain investigations on porcine corneas have shown that CXL leads to a corneal stiffening by a factor of about 1.3 (Schumacher et al., 2011; Hammer et al., 2014). Consequently, corneal stiffening stabilizes the clinical progression of keratoconus in about 90% of cases (Koller et al., 2009; Caporossi et al., 2011). However, stress-strain measurements come along with an inherent shortcoming, as they are not performable *in vivo*. For this purpose, other techniques such as Scheimpflug-based air-puff tonometry (Vinciguerra et al., 2017) are currently being investigated whether they allow for *in vivo* assessment of CXL. Several *in vivo* studies have demonstrated a stiffening effect after CXL, particularly 1 month after treatment, using specific parameters of the device (Herber et al., 2023a; Herber et al., 2023b; Vinciguerra et al., 2019). In addition to these methods based on mechanical deformation, which might be unpleasant or painful for the patients and provide only general information about the cornea and not local changes, also full-optical Brillouin spectroscopy (BS) was proposed for the evaluation of CXL (Scarcelli et al., 2012; Scarcelli et al., 2013). Hereby, laser light is inelastically scattered by thermally excited sound waves in the tissue (Palombo and Fioretto, 2019). The occurring Brillouin frequency shift ν_B in the gigahertz range is related to the biomechanical properties via the speed of sound v_s at which the sound wave propagates in tissue (Equation 1):

$$M' = \rho v_s^2 = \frac{\rho \lambda^2 \nu_B^2}{4 n^2 \sin^2(\theta/2)} \quad (1)$$

where M' is the real part of the longitudinal modulus, ρ the mass density, λ the laser excitation wavelength, n the refractive index at the excitation wavelength and θ the scattering angle (Scarcelli et al., 2015). It should be emphasized that the Brillouin shift is related to the longitudinal modulus, whereas e.g., stress-strain measurements give access to the Young's modulus. Although these both measures are not identical and describe slightly different measuring situations, they are correlated with each other (Seiler et al., 2018; Webb et al., 2017; Scarcelli et al., 2011).

In the past 15 years, BS was used in several studies addressing corneal biomechanics (Scarcelli et al., 2012; Scarcelli et al., 2013; Seiler et al., 2018; Webb et al., 2017; Scarcelli et al., 2011; Scarcelli et al., 2014; Shao et al., 2019; 2018; Lepert et al., 2016; Lopes and Ahmed, 2023; Eltony et al., 2022; Webb et al., 2020; Seiler et al., 2019). Key results are that BS is able to differentiate between normal and various pathological biomechanical properties as well as artificially induced alterations, e.g., due to CXL. During this wide and promising application of BS in cornea research, it was noticed that the Brillouin frequency shift is also affected by corneal hydration, which might hamper straightforward *ex vivo* measurements (Seiler et al., 2018; Shao et al., 2018; Antonacci et al., 2020). Wu et al. even questioned whether hydration instead of stiffness is measured in highly hydrated media (Wu et al., 2018). The hydration aspect is also known from other biomedical applications (Wu et al., 2019; Jannasch et al., 2021) or rather made use of e.g., by changing the osmotic conditions in order to regulate the water balance (Scarcelli et al., 2015; Zhang et al., 2023). For protecting the cornea from dehydration (especially after de-epithelization), a moist chamber was used in several *ex vivo* studies (Scarcelli et al., 2012; Scarcelli et al., 2014). However, it remains unclear on what time scale dehydration and rehydration processes take place. Thus, it is for example, questionable, whether the dehydration during sample preparation can be compensated by short-time rehydration. Since a non-equilibrium hydration comes along with Brillouin shift measurements, hydration should in any case be accounted for in order to investigate weak mechanical effects like CXL reliably.

Brillouin spectroscopy can be combined with Raman spectroscopy. Raman scattering is also excited using a laser. Variations in the polarizability of molecular bonds lead to a vibration of the atoms and the generation of Raman scattering. The Raman spectrum provides a high amount of information about the molecular structure and is therefore sometimes referred to as a molecular fingerprint.

A recent study by our group, in which Surface Enhanced Raman Spectroscopy (SERS) was used to examine the CXL, showed only minimal variations of the molecular structure (Melcher et al., 2023). The observed changes were assigned to side chains. However, they alone do not explain the mechanical stiffening of the cornea. In any case, SERS can only be used to examine areas on the surface that are only a few nanometers thick.

Optical coherence tomography (OCT) is a well-established imaging technique in ophthalmology e.g., to investigate age-related macular degeneration, retinal detachment and diabetic retinopathy (Al-Mujaini et al., 2013). Recently, it was shown that anterior segment OCT is able to detect the stromal demarcation line being an indicator for the effective CXL depth (Doors et al., 2009; Kymionis et al., 2016). However, the visibility of the demarcation line from the OCT intensity images is quite challenging and subjective. Using the tissue-induced alterations of polarized light as an additional contrast, it was recently demonstrated that polarization-sensitive OCT (PS-OCT) is able to reveal the CXL effect by analyzing the degree of polarization (DOP) (Ju and Tang, 2015). After CXL, the DOP is increased in the upper part of the cornea, wherefore it can be used for validation of the CXL effect, too. The authors explain the increased DOP by a denser and more compact packaging of the collagen fiber network. However, the connection to the underlying biochemical changes due to CXL treatment is still missing as well as the connection to mechanical stiffening and the hydration dependency of the DOP.

The aim of this study is threefold: i) to investigate the impact of corneal hydration on the Brillouin shift measurements ii) to find conditions at which the hydration is in an equilibrium state and iii) to evaluate the detectability of CXL by means of BS. RS and PS-OCT were used to better understand the molecular and microscopic mechanisms underlying CXL and to verify whether the CXL was successful. The overall aim of this study is to improve the understanding of CXL's underlying molecular and microscopic mechanisms, which are responsible for corneal stiffening. This knowledge is on the one hand important to further optimize the CXL procedure, e.g., in terms of treatment time, UV light dose and treatment frequency. On the other hand, this study will support the development of future *in vivo* diagnostic approaches for CXL monitoring.

In a first part, this paper describes the time-dependence of corneal dehydration in order to show that reliable Brillouin shift measurements are only possible at constant hydration. This is in particular important for subsequent measurements of the CXL effect, which might otherwise be obscured. In a second part, the time-dependence of corneal hydration is studied in order to find the time after which an equilibrium hydration state is reached. This information is then used in the CXL measurements, where joint depth-dependent Brillouin spectroscopy, Raman spectroscopy and PS-OCT measurements are performed.

2 Materials and methods

2.1 Sample preparation

Porcine eyes were obtained from a local slaughterhouse. It should be emphasized that the animals were not killed for the purpose of this study, rather than the eyes were used as waste-products from meat industry. All eyes were measured within 12 h *postmortem*. For dehydration and hydration measurements, paired eyes, i.e., from the same animal, were used. After careful de-epithelization with a hockey knife, one eye was measured with BS, while the other one was examined with OCT. All measurements were carried out in an air-conditioned laboratory having about 50% relative humidity.

Paired eyes were also used for measurements of the CXL effect. After de-epithelization, one of the paired eyes was treated with a CXL protocol, i.e. 15 min riboflavin soaking followed by UV-A light (λ = 365 nm) irradiation. Here, the eyes were divided into two groups. Eyes of the first group were irradiated for 10 min with 9 mW/cm^2 (5.4 J/cm^2), whereas eyes of the second group were irradiated for 12 min with 15 mW/cm^2 (10.8 J/cm^2). The second of the paired eyes was only exposed to riboflavin, but not irradiated with UV-A light, and thus served as control sample. Instead of irradiation, it was rested for the same time. Afterwards, all eyes were placed for 15 min in balanced salt solution (BSS, Eye-lotion Balanced salt solution, Serumwerk Bernburg AG, Bernburg, Germany) to generate an equilibrium hydration state. All eyes were analyzed by combined Brillouin and Raman spectroscopy via a water-dipping objective and afterwards with PS-OCT. In a further experiment, paired eyes were placed in 16% Dextran solution (Dextran 500, Carl Roth GmbH, Karlsruhe, Germany) instead of BSS and treated with the 9 mW/cm^2 protocol only. Since the 16% Dextran solution possesses a mass density close to or even a bit higher than that of the porcine eyes they tend to lift and swim in the solution hampering accurate measurements. Therefore, a metal ring was placed on the eyes as an additional weight in order to compensate for buoyancy while maintaining optical access to the cornea.

2.2 Combined Brillouin and Raman spectroscopy

The combined Brillouin-Raman system is described in detail elsewhere (Rix et al., 2022). Briefly, it consists of a 780 nm wavelength excitation, coupled into an up-right WITec 300R microscope equipped with a ×10 objective (Zeiss Epiplan-Neofluar ×10/0.25NA) used for dehydration and hydration measurements and a ×40 water-dipping objective (Zeiss N-Achroplan ×40/0.75NA) used for CXL measurements (see Figure 1). The laser power on the sample was 25 mW. The Brillouin spectrometer consisted of a two-stage virtually imaged phased array setup (Berghaus et al., 2015). Axial scans consisting of 25 individual measuring points (with 1 s integration time and three repetitions per point) were performed in the center of the eye by elevating the stage up to 300 µm in z-direction. Note that the effective measuring depth is slightly greater (311 µm), because of the cornea's refractive index being about 1.377 in the visible range (Scarcelli et al., 2012; Webb et al., 2020) resulting in an elevation of the image. However, this effect is small, because a water-dipping objective was used, which is manufactured for a refractive index of 1.33. Therefore, this mismatch is in the range of the axial resolution and thus neglected. Brillouin spectra were analyzed by custom-written (Rix et al., 2022) Matlab scripts (Matlab 2024a; MathWorks Inc., Natick, MA) based on Lorentzian function fitting in order to obtain the Brillouin frequency shift.

Additionally, confocal single point Raman measurements were performed in 50 µm depth, where the CXL effect is predominantly expected (Melcher et al., 2023; Ju and Tang, 2015). The acquisition parameters were set to 30 s integration time and 10 repetitions in order to obtain high quality (signal-to-noise ratio >28) Raman spectra, which is crucial for evaluating the subtle CXL effect. Raman spectra were subjected to baseline correction and normalized using Matlab's *msbackadj* and *msnorm* functions.

2.3 Polarization-sensitive optical coherence tomography

Thorlabs' Telesto® system (TEL220PSC2, Thorlabs GmbH, Germany) was used for PS-OCT measurements, which is described in detail elsewhere (Golde et al., 2021). It was operated at 28 kHz scanning rate and equipped with an LSM04 objective, on which a custom 3D-printed structure with integrated coverslip was mounted allowing for measurements in solution (see Figure 2). 3D volume scans were acquired in the center position of the corneas with a lateral scanning field of 2 mm in each direction and axial imaging depth of 3.5 mm (in air). The axial resolution was approximately 5 µm in stroma, assuming a refractive index of n = 1.376 for a wavelength of 1,300 nm according to (Tan et al., 2019). A custom-written segmentation algorithm was used to find

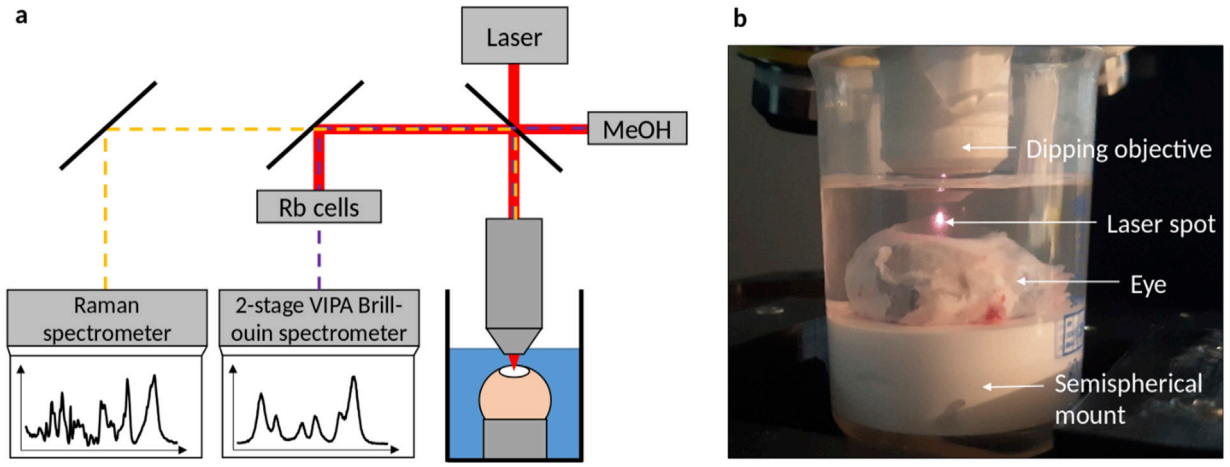

FIGURE 1
(a) Brillouin/Raman microscope setup with eyes being measured in solution via a dipping objective. While laser light (red) is filtered out by Rubidium cells, Brillouin scattered light (purple dashed) of the sample and the methanol reference signal is analyzed by a 2-stage VIPA spectrometer and Raman scattered light (orange dashed) is analyzed with a commercial grating-based spectrometer. **(b)** Picture of the setup, where the eye is totally immersed in solution.

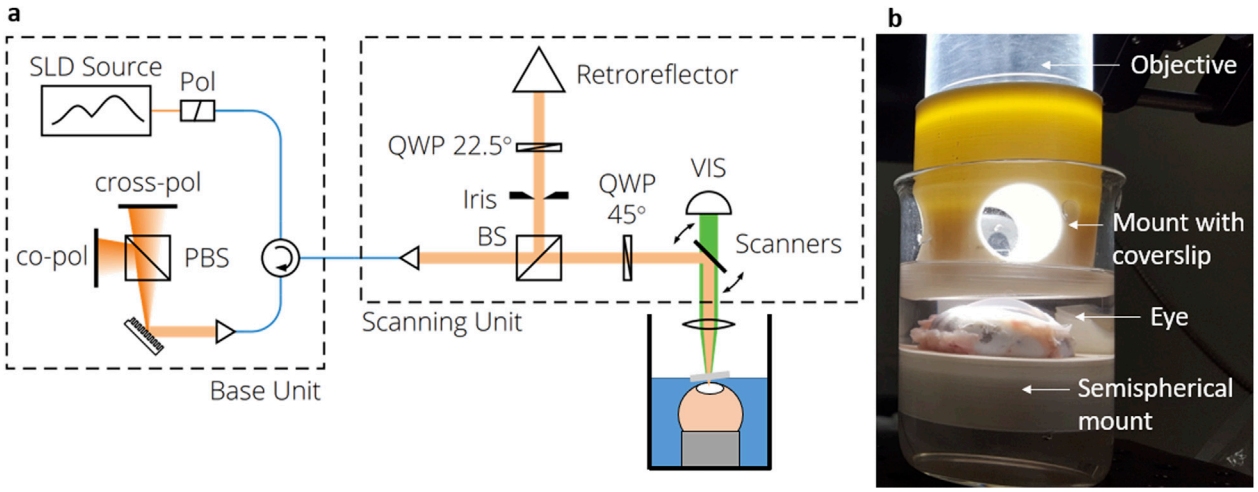

FIGURE 2
(a) PS-OCT setup consisting of the base unit, the beam scanning system and the scan lens kit. **(b)** Picture of the eye being placed in solution and measured through a cover slip added to the objective.

the top and bottom edges of the cornea in order to calculate the central corneal thickness (CCT) considering the refractive index as well. Details on the segmentation algorithm applied to the OCT intensity images can be found in Supplementary Material. For the CXL measurements, the DOP weighted by taking the SNR into account was calculated from the PS-OCT data as described elsewhere (Baumann et al., 2018). For further analysis, a mean DOP was calculated by averaging over 50 subsequent, central A-scans in both lateral directions. Throughout this manuscript, it is referred to OCT when only the intensity information is considered, which might be collected also with a standard OCT device, while PS-OCT is mentioned in relation to polarization-specific interpretations. However, all evaluations are based on the same data collected with a PS-OCT device.

2.4 Statistical analysis

To account for the biological variance in the experimental data, the interquartile range (IQR) was calculated and illustrated as shaded area or error bar in the figures. Non-parametric Mann-Whitney U tests were performed with Origin (Origin 2024b; OriginLab Corp., Northampton, MA) to compare the groups. Differences were considered significant if $p < 0.05$.

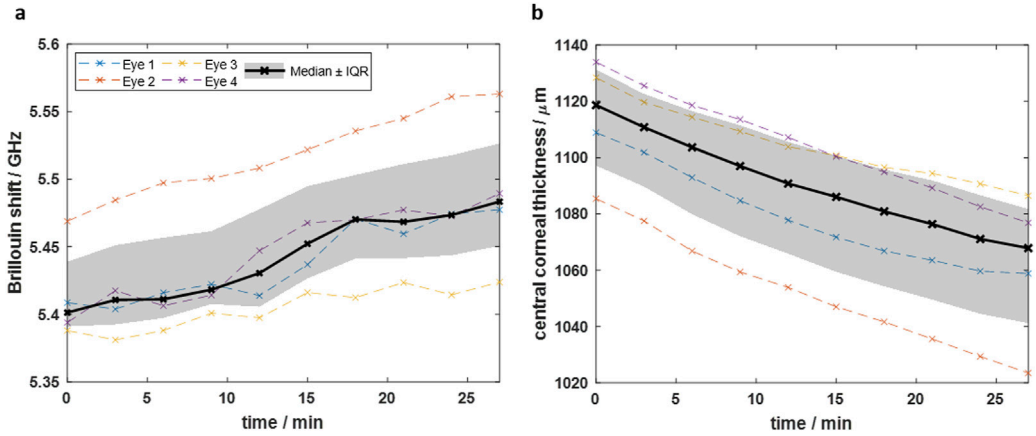

FIGURE 3
Time-dependence of dehydration process after de-epithelization showing that **(a)** the Brillouin shift increases and **(b)** the central corneal thickness decreases due to evaporation. Dashed colored curves are for individual eyes, whereas black solid curve is the median curve and the grey area the interquartile range, respectively.

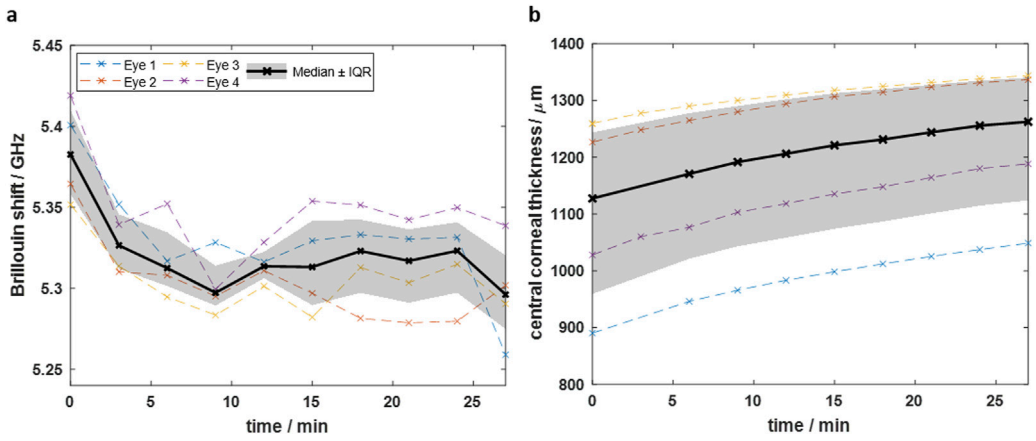

FIGURE 4
Time-dependent measurements after immersing eyes in BSS showing that **(a)** the Brillouin shift decreases and **(b)** the CCT increases over time. The Brillouin shift reaches an equilibrium, whereas the CCT still increases after 27 min. Dashed colored curves are for individual eyes, whereas black solid curve is the median curve and the grey area the interquartile range, respectively.

3 Results

3.1 Dehydration measurements

For time-dependent dehydration investigations, BS and OCT measurements were performed every 3 min in a time range of 27 min on n = 4 eyes, respectively. On the one hand, axial BS scans were performed, whereof the Brillouin shift in 48 µm depth was extracted. This is in the same depth region where the single point RS measurements were performed later on in the CXL experiments. On the other hand, the CCT was evaluated using the OCT images. Both measures plotted as a function of the time after de-epithelization are shown in Figure 3.

Starting from a median value of 5.40 GHz (IQR: 5.39–5.44 GHz), the Brillouin shift increases over time predominantly linearly. The CCT follows an inverse behavior, i.e., starting from a median value of 1,119 µm (IQR: 1,097–1,131 µm) and decreasing almost linearly. The linear behavior indicates that after 27 min the dehydration process is still in full progress and the cornea is far away from an equilibrium state. It should be emphasized that already 5 minutes after de-epithelization, the Brillouin shift increases by 0.014 GHz while the CCT decreases by 12 µm, indicating the need for hydration stabilization for reliable measurements of biomechanical properties.

3.2 Equilibrium hydration

To achieve a balanced hydration state *ex vivo*, the eyes were placed in BSS. BS and OCT measurements were performed on n = 4 eyes each to assess the time required to reach a state of equilibrium. Figure 4a shows the Brillouin shift within 27 min after immersion of the eyes in BSS. The CCT within the same time is plotted in

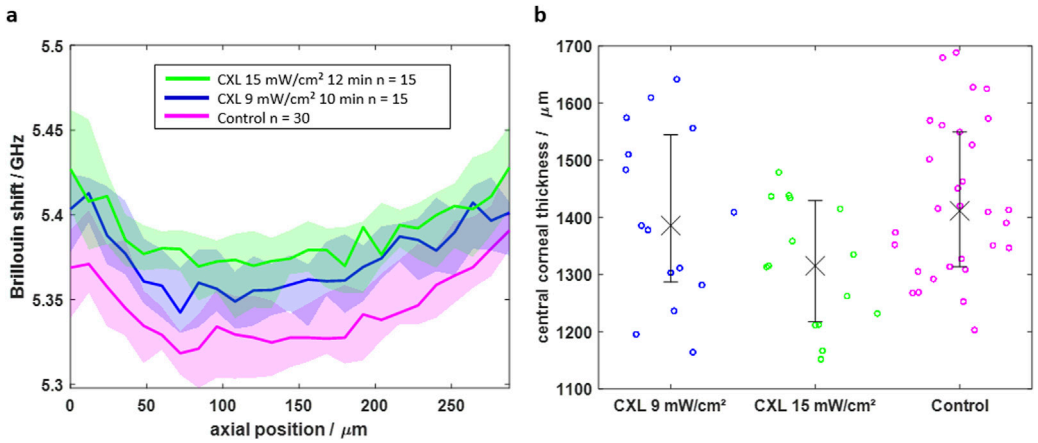

FIGURE 5
(a) Axial BS scans of CXL-treated (blue and green) and control (magenta) eyes indicating that CXL results in a higher Brillouin shift in the first 264 μm. **(b)** The central corneal thickness shows lower values for CXL-treated eyes, which is attributed to a mitigated water uptake. Solid line/crosses and shaded area/error bars are indicating the median value and interquartile range, respectively.

Figure 4b. The median data in Figure 4a shows that the Brillouin shift in 48 μm depth decreases exponentially shortly after immersion and reaches an equilibrium state at about 5.32 GHz (IQR: 5.29–5.34 GHz). Conversely, the CCT (Figure 4b) increases from 1,127 μm (IQR: 959–1,243 μm) to 1,262 μm (IQR: 1,124–1,340 μm) during 27 min soaking time, but converges to an equilibrium state, which is however not reached.

The results indicate that reliable Brillouin shift measurements with equilibrium hydration are possible, when immersing the eyes at least for 12 min in BSS. The fact, that the CCT is still increasing after 27 min might be due to the swelling of deeper tissue layers, where the water needs more time to reach. This is in accordance with the Brillouin shift in deeper layers (see Supplementary Material), which is still decreasing there and has not yet reached an equilibrium state after 12 min. However, as the CXL effect is mainly taking place in the upper part of the cornea, we chose hereinafter a soaking time of 15 min. This is sufficient to obtain a reliable Brillouin shift value for judging on the CXL effect, because an equilibrium state is already reached in the upper part of the cornea.

3.3 CXL measurements in BSS

The finding that an equilibrium hydration state is reached at least in the upper corneal layer was transferred into practice for the measurements of the CXL effect. First BS/RS and afterwards PS-OCT measurements were conducted on the same eyes immersed in BSS. Fifteen paired eyes were treated with the 9 mW/cm^2 protocol and another 15 paired eyes with the 15 mW/cm^2 protocol, with one eye of each pair serving as control. All control samples were exposed to riboflavin, too. The two different protocols were used in order to evaluate whether a higher energy dose leads to an improved CXL effect. The Brillouin shifts of the axial scans are shown in Figure 5a.

For both CXL protocols, the Brillouin shift is significantly (Mann-Whitney U test, $p < 0.05$) higher for the CXL groups (blue and green) in the first 264 μm compared to the control group (magenta). In deeper tissue layers, the median Brillouin shifts of the groups approximate each other. Moreover, the 15 mW/cm^2 protocol has a slightly stronger CXL effect, which gets mainly visible in a depth of 125 μm, where the Brillouin shift values are higher compared to those of the 9 mW/cm^2 protocol.

The CXL shows an effect on the CCT (Figure 5b), too. It is lower for the CXL groups than for the control group (1,411 μm, IQR: 1,313–1,549 μm). Again, this effect is larger for the 15 mW/cm^2 protocol (1,315 μm, IQR: 1,217–1,429 μm) than for the 9 mW/cm^2 protocol (1,386 μm, IQR: 1,287–1,545 μm). Considering the hydration results from above, it is concluded that CXL alters the hydration conditions of the cornea influencing both, the Brillouin shift and the CCT.

In contrast, the Raman spectrum shows changes in molecular structure, making the method a promising tool for evaluating the CXL effect independently of the hydration conditions. The mean Raman spectra of each group are shown in Figure 6. The overall spectral signature of the Raman mean spectra is similar within the three groups, which indicates that there is no change in the molecular structure of the cornea, i.e., the collagen backbone. The major bands at 863 cm^{-1}, 942 cm^{-1}, 1,009 cm^{-1}, 1,250 cm^{-1}, 1,272 cm^{-1}, 1,455 cm^{-1} and 1,667 cm^{-1} show no clear changes. An assignment to functional groups is summarized in Table 1.

Although the BS reveals the CXL effect, the measurement times are much longer compared to OCT. Moreover, the additional feature of polarization-sensitive detection in PS-OCT allows for the evaluation of the CXL effect via the DOP. The DOP was determined on the same eyes and shown as a function of the depth in Figure 7a. To enable a comparison between corneas of different thicknesses, the DOP of each group is plotted against the relative depth. In the upper region between relative thicknesses of 0 and 0.15, the DOP is remarkably increased for the CXL-treated eyes ranging between 0.87 and 0.98, whereas the control eyes have DOP values down to 0.82. Thus, the CXL results in microstructural changes, so that the back-scattered light experiences a decreased depolarization compared to the control eyes. Again, the 15 mW/cm^2 protocol (green) results in a stronger effect than the 9 mW/cm^2 protocol (blue). In greater depths, the DOP is not distinguishable between the groups. In relative depths greater than

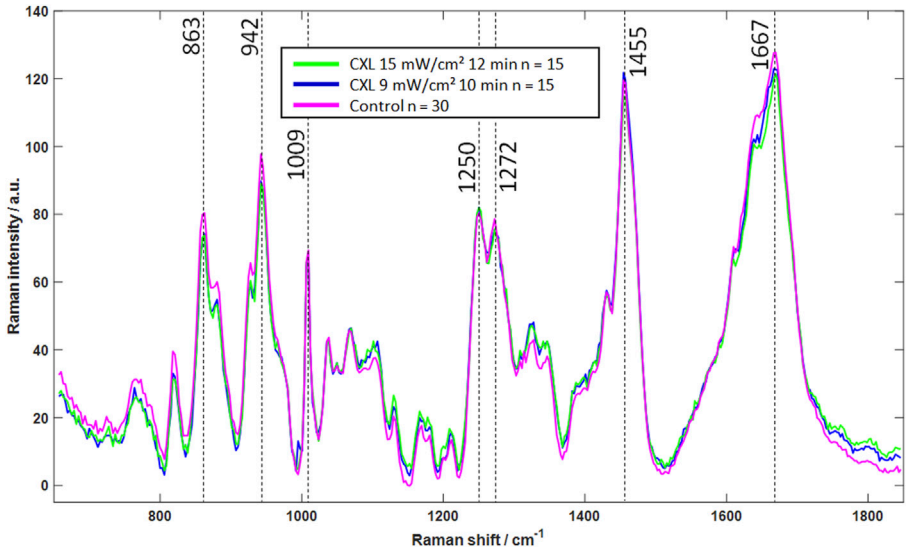

FIGURE 6
Mean Raman spectra of CXL-treated (blue and green) and control eyes (magenta), indicating that CXL does not lead to significant changes in Raman spectra. In particular, the strong signals (dashed lines) show no noticeable changes, which is an indicator of an unchanged molecular structure.

TABLE 1 Assignment of the Raman bands to functional groups.

Raman shift/cm^{-1}	Assignment to	Reference
863	ν(C-C) hydroxyproline	Frank et al. (1995)
942	ν(C-C) of polysaccharides	Z. Yan et al. (2024)
1,009	Ring breathing of phenylalanine	Naumann, (1998)
1,250	Amide III	Frank et al. (1995)
1,272	ρ(CH_2)	Schulz and Baranska, (2007)
1,455	δ(CH_2)	Lau et al. (2003)
1,667	Amide I	Cheng et al. (2005)

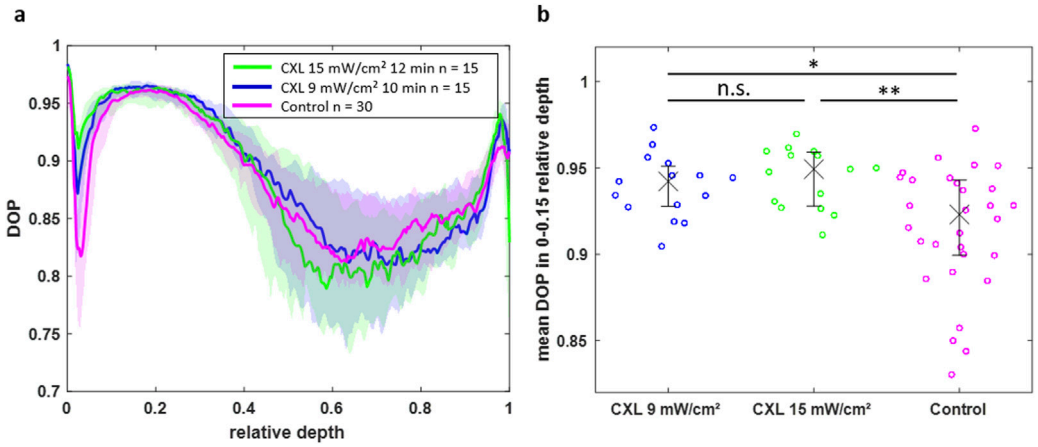

FIGURE 7
(a) DOP over the normalized depth showing that CXL-treated eyes have an increased DOP in the region of 0–0.15 relative depth. **(b)** Scatter plot of the mean DOP values in this region for all individual eyes indicating the statistical significance of the CXL effect on the DOP (*$p < 0.05$, **$p < 0.01$).

0.5 the high biological variability hampers a straightforward evaluation of the DOP.

For further statistical analysis, only the upper part of the corneas (relative depths between 0 and 0.15) was used, where the CXL effect is mainly occurring. For verification purposes, the mean DOP values of all eyes are visualized for the upper part (0–0.15 relative depth) in Figure 7b and for the lower part (0.15–1 relative depth) in Supplementary Material. The CXL-treated groups have a significant increased DOP in the upper cornea part compared to the control group ($p = 0.0174$ and $p = 0.0022$ for 9 mW/cm^2 and 15 mW/cm^2 protocol, respectively). However, the DOP is not significantly different between both CXL protocols. Moreover, the DOP is not significantly different within all groups in the lower part of the cornea.

3.4 CXL measurements in 16% dextran

All aforementioned measurements took place in BSS in order to guarantee an equilibrium hydration state. However, this does not reflect the *in vivo* conditions of human eyes during the CXL procedure, because there the eyes are in natural hydration state rather than in BSS. Therefore, further CXL measurements were performed in 16% Dextran solution, which fits the intrinsic hydration of porcine cornea (Fischinger et al., 2021). Again, first BS/RS and afterwards PS-OCT measurements were conducted on the same paired eyes. N = 12 eyes were treated with the 9 mW/cm^2 protocol. The 15 mW/cm^2 protocol was omitted here, as it showed only a slightly stronger CXL effect in previous measurements.

The axial Brillouin scans are shown in Supplementary Material. It is striking that the Brillouin shift values are about 0.35 GHz higher compared to the measurements in BSS (compare with Figure 5a), which agrees well with previous study of spheroids in Dextran (G. Yan et al., 2022). One factor that contributes to this increase is the refractive index n, which is directly proportional to the Brillouin shift and increasing by 1.72% when switching from pure BSS to pure 16% Dextran solution (Supplementary Material). However, this optical parameter is not explaining the full increase of the Brillouin shift (4.79%). Therefore, the mechanical properties of the cornea are assumed to be the main factor of the increase.

Moreover, there is no clear difference visible between the Brillouin shift of the CXL-treated (cyan) and the control (red) eyes. The two curves are overlapping especially when taking the interquartile range (shaded area) into account. Also, in the aforementioned region of 125 µm, where the CXL effect was maximal for BSS measurements, there is no striking effect visible for Dextran solution. There is only a slight tendency recognizable that the CXL-treated eyes have a tiny higher shift than the control eyes. The missing gap might be related to the mitigated/absent water uptake in the Dextran experiments compared to BSS experiments. The lower water uptake gets visible by evaluating the central corneal thicknesses.

In Dextran solution, the CCT (Supplementary Material) is only about 800 µm, which agrees well with the natural thickness of the cornea (HEICHEL et al., 2016). It is slightly less for the CXL group (783 µm, IQR: 752–830 µm) compared to the control group (810 µm, IQR: 786–844 µm).

The interpretation of the Raman spectra of measurements in dextran solution is somewhat complicated by the superposition of the dextran signals. Therefore, a factor analysis was first performed to separate the Raman signals from the dextran (further details are provided in the Supplementary Material). After subtraction of the Dextran contribution, the mean Raman spectra (Supplementary Material) show again that CXL treatment is not resulting in alterations of the molecular structure.

The DOP value in the upper part of the cornea is again higher for CXL-treated eyes compared to control eyes (Figure 8a). Interestingly, in 16% Dextran solution the difference is observable up to a relative depth of 0.28, whereas it was only present up to a relative depth of 0.15 in BSS. This might be related to the absolute thickness, which is in BSS almost two times larger, whereas the CXL effect is limited to a fixed depth of approximately 250 µm. Statistical analysis revealed that the CXL effect on the DOP in the upper part (0–0.28 relative depth) of the cornea is again significant (Figure 8b, $p = 0.0499$).

4 Discussion

Brillouin microscopy as a novel full-optical technique has access to the biomechanics of tissue and is therefore a promising tool for *in vivo* evaluation of the CXL effect. However, its measure–the Brillouin frequency shift–is highly affected by the hydration state of the tissue (Wu et al., 2018; 2019; Jannasch et al., 2021). This impact was also observed in the present study. While evaporation after de-epithelization resulted in a dehydrated cornea, soaking in BSS rehydrated the cornea. In the first case, the Brillouin shift increased, whereas it decreased in the latter. This observation is explainable by the water retention of the cornea. The cornea constantly aims to be in a thermodynamic equilibrium with its environment. Therefore, water evaporates from the cornea into the surrounding air. De-epithelization even fosters this process (Çınar et al., 2014), whereas a moist-chamber attenuates it (Bao et al., 2018). On the other hand, positioning the eyes in water results in soaking (Meek, 2009). As a result, the cornea is either shrinking or swelling, when it does not fit the hydration conditions of the environment. This is in line with our findings from the OCT thickness measurements. Indeed, the CCT is decreasing due to dehydration and increasing due to rehydration.

For understanding the impact of the hydration state on the Brillouin shift, the morphological structure of the cornea has to be considered. It consists mainly of a collagen fiber network, where the fibers are predominantly aligned in-plane of the cornea and less perpendicular to it (out-of-plane) (Eltony et al., 2022; Abass et al., 2015). This leads to a layered structure, which is also visible in the OCT images (see Figure 1 in Supplementary Material). The multi-layered fiber network allows water to be trapped like in a sponge. Therefore, the cornea has to be treated as a composite consisting of collagen as a "solid" material and water as a surrounding fluid (Shao et al., 2018).

This composite model can be used to explain the observed behavior of the Brillouin frequency shift. During the dehydration and hydration experiments, only the fluid component changed, while the collagen component remained unchanged. As pure water and pure collagen have Brillouin shifts of 5.09 GHz (Berghaus et al., 2015) and 5.93 GHz (Palombo et al., 2014), respectively, dehydration results in a decreased water content and therefore in an increased Brillouin shift. In hydration experiments, the high water content leads to a decreased Brillouin shift.

On the contrary, the CXL procedure strengthens the "solid" collagen phase. As a secondary effect, this reduces the water

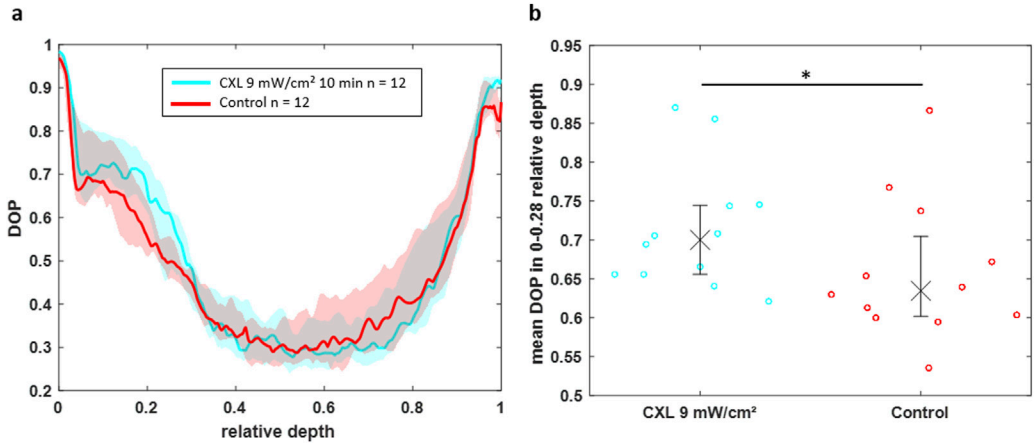

FIGURE 8
(a) DOP over the normalized depth showing that CXL-treated eyes (cyan) in 16% Dextran solution have an increased DOP in the region of 0–0.28 relative depth compared to control eyes (red). **(b)** Scatter plot of the mean DOP values in this region for individual eyes indicating the statistical significance of the CXL effect on the DOP (*$p < 0.05$).

retention potential. Therefore, less water can be trapped in the fiber network, wherefore the Brillouin shift is increased in the CXL-treated groups compared to the control group (Figure 5a).

By using 16% Dextran solution as soaking medium instead of BSS, the cornea is already close to or even at the thermodynamic equilibrium state and (almost) no additional water is stored in it. Therefore, corneas in 16% Dextran solution have a significantly lower thickness compared to soaking in BSS. In CXL experiments, the strengthened collagen fibers might again reduce the water retention potential. However, as the water uptake is only minimal, the Brillouin shift values between the CXL-treated and the control group are almost indistinguishable and the CCT is only slightly, but not significantly, decreased. Thus, BS gives mainly only indirect information on the CXL effect via the water storage potential rather than directly indicating a mechanical strengthening. This finding that the CXL effect is more difficult to detect with BS in medium-hydrated corneas compared to high-hydrated corneas is in line with previous study (Webb et al., 2020).

Whether in BSS or in 16% Dextran solution, registered Raman spectra revealed that CXL treatment is not altering the molecular structure of the cornea. Thus, new covalent bonds in form of cross-links between collagen fibers are not the reason for mechanical stiffening (Melcher et al., 2023). Therefore, it is instead assumed that the stiffening is achieved by polar-polar or hydrophobic-hydrophobic interactions between the collagen fibers. After CXL treatment, the amide I band shows a marginal broadening towards lower wavenumbers. This indicates new polar interactions of the amine group and supports the hypothesis that the stiffening of the cornea after CXL therapy is mainly due to new polar-polar interactions. Furthermore, it is assumed that these weak intermolecular forces are connected with the hydration of the cornea. This hypothesis is in line with the effects observed with BS, i.e., less water is stored in the fiber network after eyes are treated with riboflavin and UV light resulting in an increased Brillouin shift and an increased mechanical stiffness. However, the mechanism by which CXL treatment leads to a decrease in hydration remains unclear.

Moreover, PS-OCT was used in this study to verify, whether the CXL procedure was successful or not. As expected, the CXL-treated eyes show an increased DOP compared to the control eyes, being in accordance to previous literature (Ju and Tang, 2015). The DOP is mainly influenced by the collagen fiber structure and density (Ju and Tang, 2015). Two concurrent effects should be considered when interpreting these depolarizing properties of the cornea: On the one hand, collagen fibers are birefringent. Thus, randomly oriented fibers induce locally varying polarization states of the back-scattered light, which is observed as partially polarized or depolarized light. Accordingly, high DOP values are caused by highly oriented fibers, whereas lower DOP values are originating from more randomly oriented fibers. On the other hand, depolarization is also related to multiple scattering. Strong refractive index changes in the tissue cause this effect. While other tissues, e.g., demineralized tooth enamel with an increased pore volume, have shown similar relations between structure change and depolarization based on birefringence and multiple scattering (Grundmann et al., 2024), further investigations are required to better understand this interplay. However, these findings underline the hypothesis that after CXL treatment fibers are more densely aligned to build intermolecular forces resulting in a stiffening.

The advantage of BS and PS-OCT over classical stress-strain extensiometry is the depth information, which allows for an evaluation of the penetration depth of the CXL procedure. In our study, BS and PS-OCT revealed that CXL is limited to the upper part of the cornea, which agrees with previous literature (Ju and Tang, 2015; Kohlhaas et al., 2006). Both, BS and PS-OCT revealed a CXL penetration depth of about 250 µm.

The great benefit of all three optical methods over stress-strain extensiometry is the *in vivo* applicability. Although this study was performed *ex vivo*, important aspects for *in vivo* measurements can be derived. First, the corneal hydration has an effect on the Brillouin frequency shift. Although the cornea is normally almost constantly hydrated due to blinking (Shao et al., 2018), the eyes might dehydrate during long CXL-treating and measuring times. Second, Raman spectra revealed that not covalent bonds are the

major reason for mechanical stiffening, wherefore weak intermolecular forces, which are highly affected by corneal hydration, are assumed to play a key role. This once again underlines the importance of a constant hydration state for any mechanical *in vivo* measurements. Third, PS-OCT is able to detect a significant CXL effect, is insensitive to corneal hydration and has a fast acquisition time. Moreover, OCT is already an established tool in eye clinics and PS-OCT requires only minor upgrades, thus making it a promising technique for future *in vivo* application.

5 Conclusion

Non-invasive Brillouin microscopy is a promising technique to assess the corneal biomechanics, for example, during the CXL procedure. However, it turned out that reliable measurements are only possible, when keeping the hydration state constant. Time series showed that evaporation in air immediately leads to increased Brillouin shift values, whereas soaking in balanced salt solution results in decreased Brillouin shift values coming along with corneal shrinking and swelling, respectively. After 12 min, the corneas are approaching a new equilibrium state, where reliable measurements are again possible.

CXL measurements of eyes immersed in BSS and 16% Dextran solution revealed that the effect of CXL on the Brillouin shift is more dominant in high-hydrated corneas compared to medium-hydrated corneas. This leads to the conclusion that BS is mainly only indirectly accessing the CXL effect by means of the water uptake, which is hampered in CXL-treated corneas. This suggests that weak intermolecular interactions are playing a main role in mechanical stiffening, which are difficult to detect with RS. In contrast, PS-OCT directly assesses the CXL effect via the fiber alignment of collagen and therefore being independent of the corneal hydration. Nevertheless, Brillouin microscopy remains a promising method for *in vivo* applications where hydration is kept constant by blinking.

Data availability statement

The datasets for this study can be found here: https://doi.org/10.25532/OPARA-750.

Ethics statement

Ethical approval was not required for the studies involving animals in accordance with the local legislation and institutional requirements because the animals were not killed for the purpose of this study, rather than the eyes were used as waste-products from meat industry. Written informed consent was not obtained from the owners for the participation of their animals in this study because the eyes were used as waste-products from meat industry.

Author contributions

Jan Rix: Conceptualization, Formal Analysis, Investigation, Visualization, Writing – original draft. Svea Steuer: Formal Analysis, Investigation, Visualization, Writing – original draft. JG: Conceptualization, Investigation, Supervision, Visualization, Writing – review and editing. FH: Investigation, Writing – review and editing. FL: Investigation, Writing – review and editing. SM: Conceptualization, Writing – review and editing. GS: Conceptualization, Supervision, Writing – review and editing. RG: Resources, Supervision, Writing – review and editing. JW: Resources, Writing – review and editing. FR: Resources, Supervision, Writing – review and editing. RK: Resources, Writing – review and editing. RH: Conceptualization, Investigation, Project administration, Writing – review and editing.

Funding

The author(s) declare that financial support was received for the research and/or publication of this article. We would like to acknowledge the National Center for Tumor Diseases (NCT), Partner Site Dresden, for financial support regarding the experimental Brillouin-Raman set-up. Moreover, we would like to acknowledge the department of neurosurgery at the University Hospital Carl Gustav Carus Dresden for access to the system. Robert Herber and Jan Rix gratefully thank the Faculty of Medicine Carl Gustav Carus for the young scientist MeDDrive funding. We acknowledge support from the Open Access Publication Funds of the SLUB/TU Dresden.

Conflict of interest

RH and RK received lecture fees from Oculus Optikgeraete GmbH (Wetzlar, Germany) and Heidelberg Engineering GmbH (Heidelberg, Germany).

The remaining authors declare that the research was conducted in the absence of any commercial or financial relationships that could be construed as a potential conflict of interest.

Generative AI statement

The author(s) declare that no Generative AI was used in the creation of this manuscript.

Publisher's note

Supplementary material

The Supplementary Material for this article can be found online at: https://www.frontiersin.org/articles/10.3389/fbioe.2025.1576809/full#supplementary-material

References

Abass, A., Hayes, S., White, N., Sorensen, T., and Meek, K. M. (2015). Transverse depth-dependent changes in corneal collagen lamellar orientation and distribution. *J. R. Soc. Interface* 12 (104), 20140717. doi:10.1098/rsif.2014.0717

Al-Mujaini, A., Wali, U. K., and Azeem, S. (2013). Optical coherence tomography: clinical applications in medical practice. *Oman Med. J.* 28 (2), 86–91. doi:10.5001/omj.2013.24

Antonacci, G., Beck, T., Bilenca, A., Czarske, J., Elsayad, K., Guck, J., et al. (2020). Recent progress and current opinions in Brillouin microscopy for life science applications. *Biophys. Rev.* 12 (3), 615–624. doi:10.1007/s12551-020-00701-9

Bao, Q., Newman, B., Wang, Y., Choi, S., and Burgess, D. J. (2018). *In vitro* and *ex vivo* correlation of drug release from ophthalmic ointments. *J. Control. Release* 276 (April), 93–101. doi:10.1016/j.jconrel.2018.03.003

Baumann, B., Augustin, M., Lichtenegger, A., Harper, D. J., Muck, M., Eugui, P., et al. (2018). Polarization-sensitive optical coherence tomography imaging of the anterior mouse eye. *J. Biomed. Opt.* 23 (8), 1. doi:10.1117/1.JBO.23.8.086005

Berghaus, K. V., Yun, S. H., and Scarcelli, G. (2015). High speed sub-GHz spectrometer for Brillouin scattering analysis. *JoVE J. Vis. Exp.* 106 (December), e53468. doi:10.3791/53468

Caporossi, A., Mazzotta, C., Baiocchi, S., Caporossi, T., and Denaro, R. (2011). Age-related long-term functional results after riboflavin UV A corneal cross-linking. *J. Ophthalmol.* 2011, 608041–608046. doi:10.1155/2011/608041

Cheng, W.-T., Liu, M.-T., Liu, H.-N., and Lin, S.-Y. (2005). Micro-Raman spectroscopy used to identify and grade human skin pilomatrixoma. *Microsc. Res. Tech.* 68 (2), 75–79. doi:10.1002/jemt.20229

Çınar, Y., Cingü, A. K., Şahin, A., Türkcü, F. M., Yüksel, H., and Caca, I. (2014). Intraoperative corneal thickness measurements during corneal collagen cross-linking with isotonic riboflavin solution without dextran in corneal ectasia. *Cutan. Ocular Toxicol.* 33 (1), 28–31. doi:10.3109/15569527.2013.793700

Doors, M., Tahzib, N. G., Eggink, F. A., Berendschot, T. T. J. M., Webers, C. A. B., and Nuijts, R. M. M. A. (2009). Use of anterior segment optical coherence tomography to study corneal changes after collagen cross-linking. *Am. J. Ophthalmol.* 148 (6), 844–851.e2. doi:10.1016/j.ajo.2009.06.031

Elsheikh, A., and Anderson, K. (2005). Comparative study of corneal strip extensometry and inflation tests. *J. R. Soc. Interface* 2 (3), 177–185. doi:10.1098/rsif.2005.0034

Eltony, A. M., Peng, S., and Yun, S.-H. (2022). Measuring mechanical anisotropy of the cornea with Brillouin microscopy. *Nat. Commun.* 13 (1), 1354. doi:10.1038/s41467-022-29038-5

Fischinger, I., Seiler, T. G., Wendelstein, J., Tetz, K., Fuchs, B., and Bolz, M. (2021). Biomechanical response after corneal cross-linking with riboflavin dissolved in dextran solution versus hydroxypropyl methylcellulose. *J. Refract. Surg.* 37 (9), 631–635. doi:10.3928/1081597X-20210610-04

Frank, C. J., McCreery, R. L., and Redd, D. C. (1995). Raman spectroscopy of normal and diseased human breast tissues. *Anal. Chem.* 67 (5), 777–783. doi:10.1021/ac00101a001

Galvis, V., Sherwin, T., Tello, A., Merayo, J., Barrera, R., and Acera, A. (2015). Keratoconus: an inflammatory disorder? *Eye* 29 (7), 843–859. doi:10.1038/eye.2015.63

Golde, J., Rüsing, M., Rix, J., Eng, L. M., and Koch, E. (2021). Quantifying the refractive index of ferroelectric domain walls in periodically poled $LiNbO_3$ single crystals by polarization-sensitive optical coherence tomography. *Opt. Express* 29 (21), 33615–33631. doi:10.1364/OE.432810

Grundmann, J., Golde, J., Steuer, S., Tetschke, F., Kirsten, L., Walther, J., et al. (2024). Visualization of carious lesions with polarized and depolarized light microscopy. *Biomed. Opt. Express* 15 (5), 3018–3036. doi:10.1364/BOE.514904

Hammer, A., Richoz, O., Arba Mosquera, S., Tabibian, D., Hoogewoud, F., and Hafezi, F. (2014). Corneal biomechanical properties at different corneal cross-linking (CXL) irradiances. *Investigative Ophthalmol. and Vis. Sci.* 55 (5), 2881–2884. doi:10.1167/iovs.13-13748

Hayes, S., Kamma-Lorger, C. S., Craig, B., Young, R. D., Quantock, A. J., Rost, A., et al. (2013). The effect of riboflavin/UVA collagen cross-linking therapy on the structure and hydrodynamic behaviour of the ungulate and rabbit corneal stroma. *PLOS ONE* 8 (1), e52860. doi:10.1371/journal.pone.0052860

Heichel, J., Wilhelm, F., Kunert, K. S., and Hammer, T. (2016). Topographic findings of the porcine cornea. *Med. Hypothesis, Discov. Innovation Ophthalmol.* 5 (4), 125–131.

Herber, R., Francis, M., Spoerl, E., Pillunat, L. E., Raiskup, F., and Roy, A. S. (2023a). Evaluation of biomechanical changes after accelerated cross-linking in progressive keratoconus: a prospective follow-up study. *Cornea* 42 (11), 1365–1376. doi:10.1097/ICO.0000000000003219

Herber, R., Vinciguerra, R., Tredici, C., Legrottaglie, E. F., Pillunat, L. E., Raiskup, F., et al. (2023b). Repeatability of corneal deformation response parameters by dynamic ultra–high-speed Scheimpflug imaging before and after corneal crosslinking. *J. Cataract and Refract. Surg.* 49 (5), 518–524. doi:10.1097/j.jcrs.0000000000001136

Jannasch, A., Rix, J., Welzel, C., Schackert, G., Kirsch, M., König, U., et al. (2021). Brillouin confocal microscopy to determine biomechanical properties of SULEEI-treated bovine pericardium for application in cardiac surgery. *Clin. Hemorheol. Microcirc.* 79 (1), 179–192. doi:10.3233/CH-219119

Ju, M. J., and Tang, S. (2015). Usage of polarization-sensitive optical coherence tomography for investigation of collagen cross-linking. *J. Biomed. Opt.* 20 (4), 046001. doi:10.1117/1.JBO.20.4.046001

Karolak, J. A., and Gajecka, M. (2017). Genomic strategies to understand causes of keratoconus. *Mol. Genet. Genomics* 292 (2), 251–269. doi:10.1007/s00438-016-1283-z

Kohlhaas, M., Spoerl, E., Schilde, T., Unger, G., Wittig, C., and Pillunat, L. E. (2006). Biomechanical evidence of the distribution of cross-links in corneastreated with riboflavin and ultraviolet A light. *J. Cataract and Refract. Surg.* 32 (2), 279–283. doi:10.1016/j.jcrs.2005.12.092

Koller, T., Mrochen, M., and Seiler, T. (2009). Complication and failure rates after corneal crosslinking. *J. Cataract Refract. Surg.* 35 (8), 1358–1362. doi:10.1016/j.jcrs.2009.03.035

Kymionis, G. D., Tsoulnaras, K. I., Liakopoulos, D. A., Skatharoudi, C. A., Grentzelos, M. A., and Tsakalis, N. G. (2016). Corneal stromal demarcation line depth following standard and a modified high intensity corneal cross-linking protocol. *J. Refract. Surg.* 32 (4), 218–222. doi:10.3928/1081597X-20160216-01

Lau, D. P., Huang, Z., Lui, H., Man, C. S., Berean, K., Morrison, M. D., et al. (2003). Raman spectroscopy for optical diagnosis in normal and cancerous tissue of the nasopharynx—preliminary findings. *Lasers Surg. Med.* 32 (3), 210–214. doi:10.1002/lsm.10084

Lepert, G., Gouveia, R. M., Connon, C. J., and Paterson, C. (2016). Assessing corneal biomechanics with Brillouin spectro-microscopy. *Faraday Discuss.* 187 (0), 415–428. doi:10.1039/C5FD00152H

Lopes, B. T., and Ahmed, E. (2023). *In vivo* corneal stiffness mapping by the stress-strain index maps and Brillouin microscopy. *Curr. Eye Res.* 48 (2), 114–120. doi:10.1080/02713683.2022.2081979

McCall, S. A., Kraft, S., Edelhauser, H. F., Kidder, G. W., Lundquist, R. R., Bradshaw, H. E., et al. (2010). Mechanisms of corneal tissue cross-linking in response to treatment with topical riboflavin and long-wavelength ultraviolet radiation (UVA). *Investigative Ophthalmol. and Vis. Sci.* 51 (1), 129–138. doi:10.1167/iovs.09-3738

McGhee, C. N. J., Kim, B. Z., and Wilson, P. J. (2015). Contemporary treatment paradigms in keratoconus. *Cornea* 34 (October), S16–S23. doi:10.1097/ICO.0000000000000504

Meek, K. M. (2009). Corneal collagen—its role in maintaining corneal shape and transparency. *Biophys. Rev.* 1 (2), 83–93. doi:10.1007/s12551-009-0011-x

Melcher, S., Zimmerer, C., Galli, R., Golde, J., Herber, R., Raiskup, F., et al. (2023). Analysis of riboflavin/ultraviolet a corneal cross-linking by molecular spectroscopy. *Heliyon* 9 (2), e13206. doi:10.1016/j.heliyon.2023.e13206

Naumann, D. (1998). "Infrared and NIR Raman spectroscopy in medical microbiology,", 3257. SPIE, 245–257. doi:10.1117/12.306089*Infrared Spectrosc. New Tool Med.*

O'Brart, and David, P. S. (2014). Corneal collagen cross-linking: a review. *J. Optometry* 7 (3), 113–124. doi:10.1016/j.optom.2013.12.001

Palombo, F., and Fioretto, D. (2019). Brillouin light scattering: applications in biomedical sciences. *Chem. Rev.* 119 (13), 7833–7847. doi:10.1021/acs.chemrev.9b00019

Palombo, F., Peter Winlove, C., Edginton, R. S., Green, E., Stone, N., Caponi, S., et al. (2014). Biomechanics of fibrous proteins of the extracellular matrix studied by Brillouin scattering. *J. R. Soc. Interface* 11 (101), 20140739. doi:10.1098/rsif.2014.0739

Rabinowitz, Y. S. (1998). Keratoconus. *Surv. Ophthalmol.* 42 (4), 297–319. doi:10.1016/s0039-6257(97)00119-7

Raiskup, F., Herber, R., Lenk, J., Pillunat, L. E., and Spoerl, E. (2024). Crosslinking with UV-A and riboflavin in progressive keratoconus: from laboratory to clinical practice – developments over 25 years. *Prog. Retin. Eye Res.* 102 (September), 101276. doi:10.1016/j.preteyeres.2024.101276

Rix, J., Uckermann, O., Kirsche, K., Schackert, G., Koch, E., Kirsch, M., et al. (2022). Correlation of biomechanics and cancer cell phenotype by combined Brillouin and Raman spectroscopy of U87-MG glioblastoma cells. *bioRxiv* 19. doi:10.1098/rsif.2022.0209

Scarcelli, G., Besner, S., Pineda, R., and Yun, S. H. (2014). Biomechanical characterization of keratoconus corneas *ex vivo* with Brillouin microscopy. *Investigative Ophthalmol. and Vis. Sci.* 55 (7), 4490–4495. doi:10.1167/iovs.14-14450

Scarcelli, G., Kim, P., and Yun, S. H. (2011). *In vivo* measurement of age-related stiffening in the crystalline lens by Brillouin optical microscopy. *Biophysical J.* 101 (6), 1539–1545. doi:10.1016/j.bpj.2011.08.008

Scarcelli, G., Kling, S., Quijano, E., Pineda, R., Marcos, S., and Yun, S. H. (2013). Brillouin microscopy of collagen crosslinking: noncontact depth-dependent analysis of corneal elastic modulus. *Investigative Ophthalmol. and Vis. Sci.* 54 (2), 1418–1425. doi:10.1167/iovs.12-11387

Scarcelli, G., Pineda, R., and Yun, S. H. (2012). Brillouin optical microscopy for corneal biomechanics. *Investigative Ophthalmol. and Vis. Sci.* 53 (1), 185–190. doi:10.1167/iovs.11-8281

Scarcelli, G., Polacheck, W. J., Nia, H. T., Patel, K., Grodzinsky, A. J., Kamm, R. D., et al. (2015). Noncontact three-dimensional mapping of intracellular hydromechanical properties by Brillouin microscopy. *Nat. Methods* 12 (12), 1132–1134. doi:10.1038/nmeth.3616

Schulz, H., and Baranska, M. (2007). Identification and quantification of valuable plant substances by IR and Raman spectroscopy. Vib. Spectrosc. *Vib. Spectrosc.* 43 (1), 13–25. doi:10.1016/j.vibspec.2006.06.001

Schumacher, S., Oeftiger, L., and Mrochen, M. (2011). Equivalence of biomechanical changes induced by rapid and standard corneal cross-linking, using riboflavin and ultraviolet radiation. *Investigative Ophthalmol. and Vis. Sci.* 52 (12), 9048–9052. doi:10.1167/iovs.11-7818

Seiler, T. G., Peng, S., Eltony, A., Seiler, T., and Yun, S.-H. (2019). Brillouin spectroscopy of normal and keratoconus corneas. *Am. J. Ophthalmol.* 202 (June), 118–125. doi:10.1016/j.ajo.2019.02.010

Seiler, T. G., Peng, S., Frueh, B. E., Yun, S.-H., and Seiler, T. (2018). The influence of hydration on different mechanical moduli of the cornea. *Graefe's Archive Clin. Exp. Ophthalmol.* 256 (9), 1653–1660. doi:10.1007/s00417-018-4069-7

Shao, P., Eltony, A. M., Seiler, T. G., Tavakol, B., Pineda, R., Koller, T., et al. (2019). Spatially-resolved Brillouin spectroscopy reveals biomechanical abnormalities in mild to advanced keratoconus *in vivo*. *Sci. Rep.* 9 (1), 7467. doi:10.1038/s41598-019-43811-5

Shao, P., Seiler, T. G., Eltony, A. M., Ramier, A., Kwok, S. J. J., Scarcelli, G., et al. (2018). Effects of corneal hydration on Brillouin microscopy *in vivo*. *Investigative Ophthalmol. and Vis. Sci.* 59 (7), 3020–3027. doi:10.1167/iovs.18-24228

Sugar, J., and Macsai, M. S. (2012). What causes keratoconus? *Cornea* 31 (6), 716–719. doi:10.1097/ICO.0b013e31823f8c72

Tan, X., Agrawal, A., Hammer, D. X., and Ilev, I. (2019). Application of optical coherence tomography and optical path length method for monitoring corneal thickness and refractive index change during corneal cross-linking. *Appl. Opt.* 58 (17), 4616–4621. doi:10.1364/AO.58.004616

Vinciguerra, R., Romano, V., Arbabi, E. M., Brunner, M., Willoughby, C. E., Batterbury, M., et al. (2017). "Vivo early corneal biomechanical changes after corneal cross-linking in patients with progressive keratoconus,". Thorofare, N.J: Journal of Refractive Surgery, 840–846. doi:10.3928/1081597X-20170922-02

Vinciguerra, R., Tzamalis, A., Romano, V., Arbabi, E. M., Batterbury, M., and Kaye, S. B. (2019). Assessment of the association between *in vivo* corneal biomechanical changes after corneal cross-linking and depth of demarcation line. *J. Refract. Surg.* 35 (3), 202–206. doi:10.3928/1081597X-20190124-01

Webb, J. N., Su, J. P., and Scarcelli, G. (2017). Mechanical outcome of accelerated corneal crosslinking evaluated by Brillouin microscopy. *J. Cataract Refract. Surg.* 43 (11), 1458–1463. doi:10.1016/j.jcrs.2017.07.037

Webb, J. N., Zhang, H., Roy, A. S., Randleman, J. B., and Scarcelli, G. (2020). Detecting mechanical anisotropy of the cornea using Brillouin microscopy. *Transl. Vis. Sci. and Technol.* 9 (7), 26. doi:10.1167/tvst.9.7.26

Wu, P.-J., Kabakova, I. V., Ruberti, J. W., Sherwood, J. M., Dunlop, I. E., Paterson, C., et al. (2018). Water content, not stiffness, dominates Brillouin spectroscopy measurements in hydrated materials. *Nat. Methods* 15 (8), 561–562. doi:10.1038/s41592-018-0076-1

Wu, P.-J., Masouleh, M. I., Dini, D., Paterson, C., Török, P., Overby, D. R., et al. (2019). Detection of proteoglycan loss from articular cartilage using Brillouin microscopy, with applications to osteoarthritis. *Biomed. Opt. Express* 10 (5), 2457–2466. doi:10.1364/BOE.10.002457

Yan, G., Monnier, S., Mouelhi, M., and Thomas, D. (2022). Probing molecular crowding in compressed tissues with Brillouin light scattering. *Proc. Natl. Acad. Sci.* 119 (4), e2113614119. doi:10.1073/pnas.2113614119

Yan, Z., Chang, C., Kang, Z., Chen, C., Lv, X., and Chen, C. (2024). Application of one-dimensional hierarchical network assisted screening for cervical cancer based on Raman spectroscopy combined with attention mechanism. *Photodiagnosis Photodyn. Ther.* 46 (April), 104086. doi:10.1016/j.pdpdt.2024.104086

Zadnik, K., Barr, J. T., Gordon, M. O., and Edrington, T. B. (1996). Biomicroscopic signs and disease severity in keratoconus. *Cornea* 15 (2), 139–146. doi:10.1097/00003226-199603000-00006

Zhang, J., Nikolic, M., Tanner, K., and Scarcelli, G. (2023). Rapid biomechanical imaging at low irradiation level via dual line-scanning Brillouin microscopy. *Nat. Methods* 20 (5), 677–681. doi:10.1038/s41592-023-01816-z

frontiers | Frontiers in Bioengineering and Biotechnology

TYPE Original Research
PUBLISHED 24 September 2025
DOI 10.3389/fbioe.2025.1603679

OPEN ACCESS

EDITED BY
Sabine Kling,
University of Bern, Switzerland

REVIEWED BY
Abhishek Appaji,
BMS College of Engineering, India
Giuseppe Lombardo,
National Research Council (CNR), Italy

*CORRESPONDENCE
J. S. Bell,
bellj10@cardiff.ac.uk

RECEIVED 31 March 2025
ACCEPTED 29 August 2025
PUBLISHED 24 September 2025

CITATION
Bell JS, Morgan SR, Shebanova O, Evans SL, Boote C, Terrill N, Meek KM and Hayes S (2025) Hierarchical biomechanical characterisation of riboflavin-UVA crosslinking and decorin treatment in the porcine cornea.
Front. Bioeng. Biotechnol. 13:1603679.
doi: 10.3389/fbioe.2025.1603679

Hierarchical biomechanical characterisation of riboflavin-UVA crosslinking and decorin treatment in the porcine cornea

J. S. Bell[1,2]*, S. R. Morgan[2], O. Shebanova[3], S. L. Evans[4], C. Boote[2], N. Terrill[3], K. M. Meek[2] and S. Hayes[2]

[1]School of Physics and Astronomy, Cardiff University, Cardiff, United Kingdom, [2]School of Optometry and Vision Sciences, Cardiff University, Cardiff, United Kingdom, [3]Diamond Light Source Ltd, Didcot, United Kingdom, [4]School of Engineering, Cardiff University, Cardiff, United Kingdom

Introduction: The mechanisms underpinning the stiffening and stabilising effect of riboflavin/UVA crosslinking on the corneal stroma are not well understood. We report the findings of a biomechanics and synchrotron X-ray scattering study aimed at quantifying hierarchical strain mechanisms in treated and untreated porcine corneas. We applied the same approach to specimens treated with human recombinant decorin core protein, in isolation and in conjunction with riboflavin/UVA.
Methods: Tensile testing was carried out in conjunction with simultaneous synchrotron X-ray scattering. Diffraction peaks associated with the interfibrillar spacing and D-period of collagen were fit to bespoke models to quantify fibril elongation and reorientation under load.
Results: Riboflavin/UVA crosslinking stiffened corneas by approximately 60% while decorin treatment did not significantly affect the mechanical properties. Correlations between fibril elongation caused by applied tensile strain and bulk stiffness were used to approximate fibril stiffness, values for which were relatively similar for control and treatment groups, compared with the magnitude of difference in the bulk stiffness alone.
Discussion: The results imply the bulk stiffening caused by crosslinking was not primarily due to increases in fibril stiffness. Instead, trends in bulk fibril reorientation and straightening/uncrimping imply the stiffening is attributable to enhanced interconnectivity of the fibrillar stroma, leading to greater fibril recruitment fraction. The techniques reported here are applicable to a wide range of tissues for the evaluation of new, existing and adjuvant therapies.

KEYWORDS

riboflavin/UVA crosslinking, decorin, cornea, biomechanics, synchrotron X-ray scattering, collagen, crimp

Introduction

The human cornea is the primary lens of the eye and thus has to fulfil the criteria of being transparent, precisely curved and sufficiently tough to protect the eye from insult. It achieves these criteria primarily through the precise hierarchical arrangement of fibrillar collagen. Keratoconus is a degenerative disease of the cornea that disrupts the organisation of collagen (Koster et al., 2013), causing weakening and changes in macroscopic curvature,

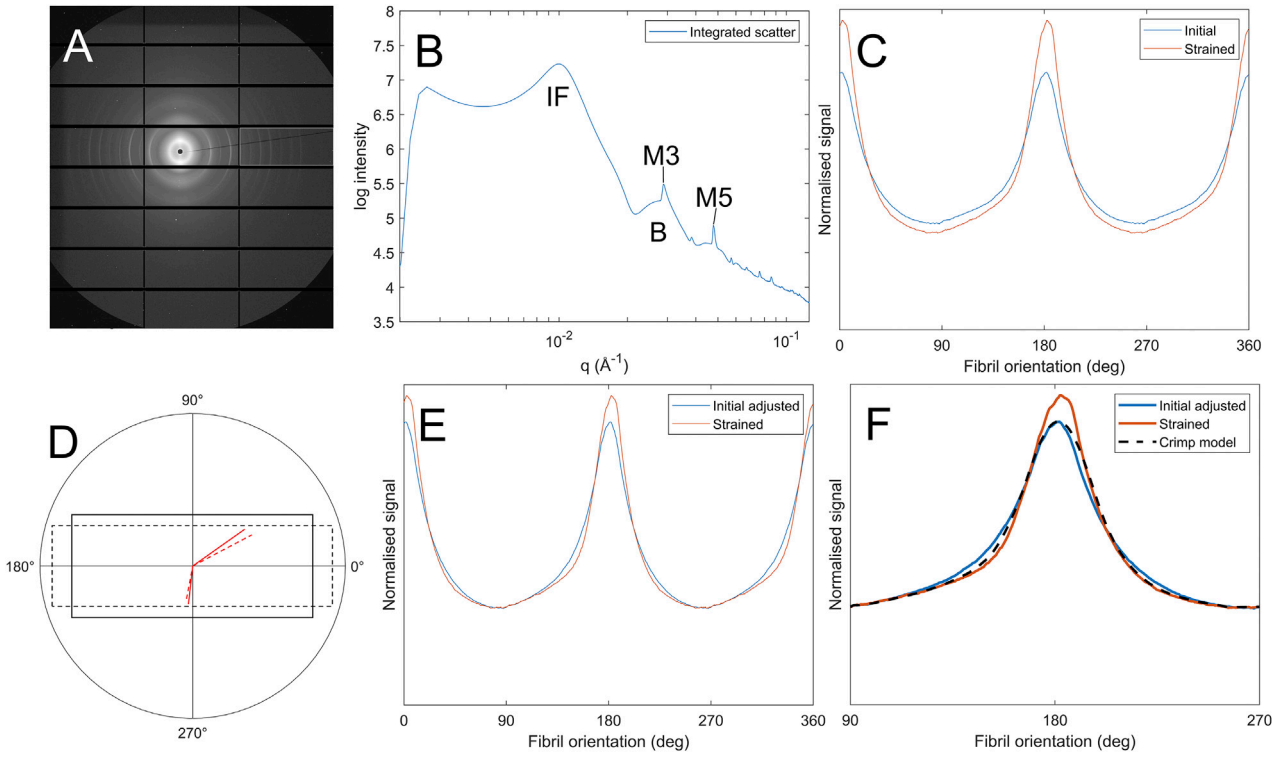

FIGURE 1
Process of calculating fibril crimp. **(A)** SAXS pattern of corneal collagen. **(B)** Azimuthal integration showing peaks corresponding to the interfibrillar spacing (IF), meridional D-spacing (M3, M5) and the Bessel-shaped cylinder transform (B) **(C)** Polar dependence of interfibrillar diffraction peak, $F(\chi)$, for a sample in its initial state and when subjected to tensile strain. **(D)** Illustration of how affine deformations affect fibril orientation (solid lines are the initial geometry, dashed lines are the deformed geometry). **(E)** Polar data from panel C with the initial distribution adjusted to compensate for the affine deformation of the strained state, this distribution is referred to as $F_c(\chi)$. **(F)** The same polar data as in panel E with the crimp model overlaid, which calculates the crimping required to map the strained dataset to the initial adjusted dataset.

which has a severely detrimental impact on patient quality of life and can cause blindness (Kymes et al., 2008).

Riboflavin/UVA cross-linking therapy, commonly referred to as "CXL", was first introduced in the early 2000s as a corneal stiffening therapy for halting keratoconus progression (Wollensak et al., 2003a). Since then, the long-term effectiveness of the treatment for stabilising the cornea has been demonstrated in numerous clinical trials, with follow-ups of up to 10 years (Raiskup et al., 2015) CXL therapy involves soaking the cornea with a photosensitiser, riboflavin (vitamin B2) and subsequently exposing it to UVA light (365 nm) with a radiant exposure of 5.4 mJ/cm. The resulting photochemical process leads to the production of oxygen radicals within the corneal stroma and the creation of covalent connections between amino acids, referred to as "crosslinks". Ultrastructural and biochemical analyses have indicated that the crosslinks formed during CXL therapy, which increase the stiffness (Wollensak et al., 2003b; Hammer et al., 2014) and enzymatic resistance (Aldahlawi et al., 2015; Spoerl et al., 2004) of the cornea, likely occur between collagen molecules at the surface of the fibrils and within the proteoglycan-rich coating surrounding them (Hayes et al., 2013; Zhang et al., 2011). However, the fundamental mechanisms underpinning the enhancement of the cornea's biomechanical properties remain elusive, and so the potential for manipulating tissue stiffening effects for adjuvant therapies remains unknown.

Interestingly, it has been reported that a 60 s application of human recombinant decorin core protein to de-epithelialised *ex vivo* corneas leads to an immediate tissue stiffening effect that is comparable in magnitude to that achieved with CXL (Pappa et al., 2021; Metzler et al., 2016). Decorin is a well characterised, small leucine rich proteoglycan that is naturally expressed in relatively high levels throughout the corneal stroma at all stages of development (Zhang et al., 2009). Its 40 kDa core protein is a horseshoe-shaped protein (Scott, 1996) that binds to Type I collagen fibrils at specific sites, namely, the 'd' and 'e' bands, with its associated covalently bound glycosaminoglycan side chains spanning the interfibrillar spaces (Scott and Haigh, 1988; Meek et al., 1986). Molecular modelling suggests that each horseshoe-shaped decorin core protein monomer binds to the collagen fibril surface through interactions with at least four separate collagen molecules from four individual collagen microfibrils, thereby forming bridges that help to stabilise the fibrils (Orgel et al., 2009). We postulate that application of exogenous human recombinant decorin core protein to the cornea, in conjunction with CXL, could lead to an enhanced crosslinking procedure with greater achievable tissue stiffening as their combined actions may further stabilise corneal collagen fibrils and the proteoglycan-rich coating surrounding them.

Fibrillar collagen is known for its remarkable tensile stiffness and strength, which is often compared with that of steel, however

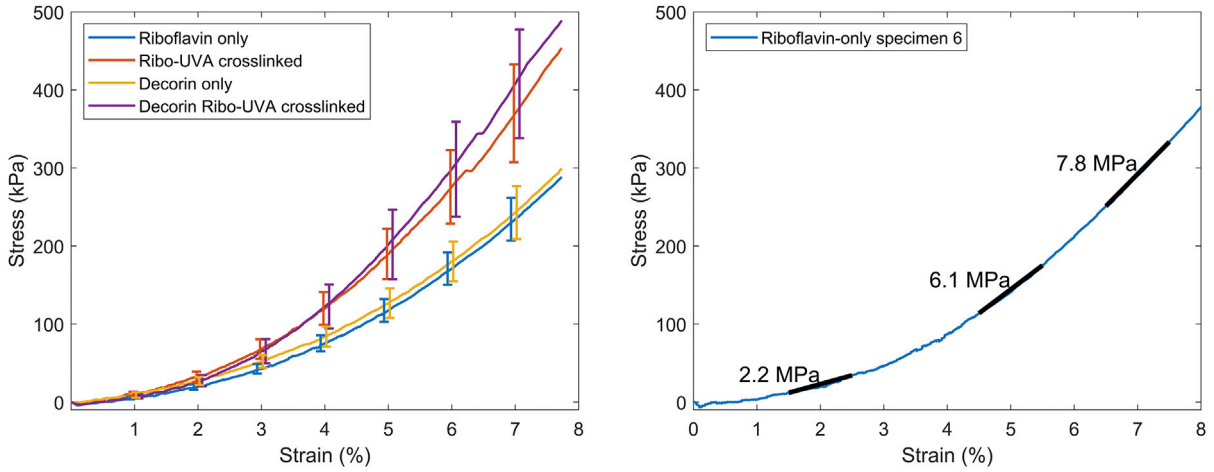

FIGURE 2
Left. Averaged stress-strain plots for each group (bars SEM). Right. Representative stress-strain plot from a riboflavin-only treated corneal strip with the tangent moduli overlaid.

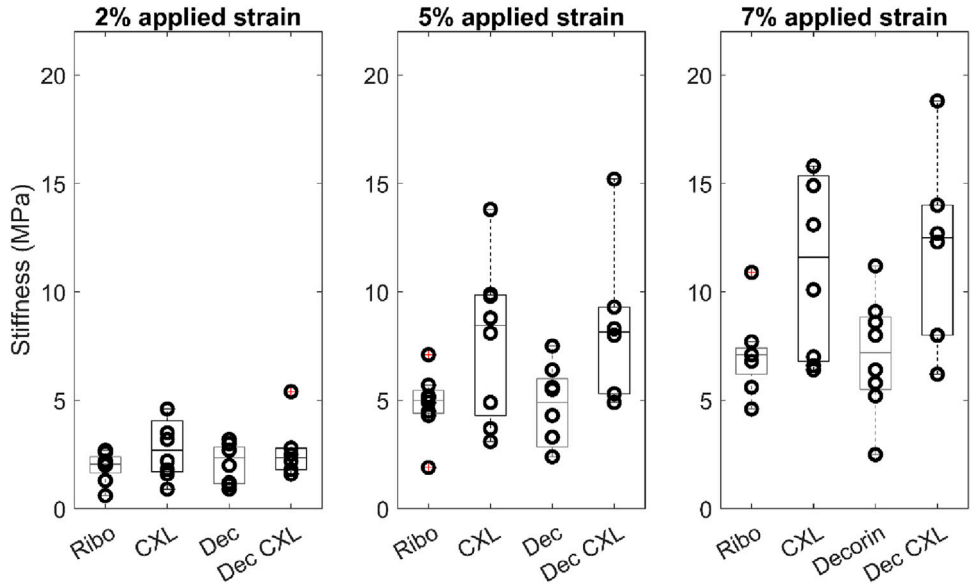

FIGURE 3
Tangent moduli for each group at 2%, 5% and 7% applied strain. Boxes show interquartile range and mean.

this belies its behaviour in non-weightbearing tissues such as the cornea, where its compliance is equally remarkable. Corneal collagen differs from that of tendon and other high load-absorbing tissues by exhibiting a significant supramolecular twist (Reale et al., 1981; Ottani et al., 2002; Ottani et al., 2001; Holmes et al., 2001), meaning tropocollagen molecules are coiled within their constituent fibrils. This architecture endows corneal collagen fibrils (and that of other non-loadbearing tissues such as skin) with the "spring-like" ability to elongate under very small loads–loads of physiological magnitude in the cornea (Bell et al., 2022; Bell et al., 2018). The hierarchical mechanisms by which corneal collagen accommodates strain can be quantified using X-ray scattering (Aghamohammadzadeh et al., 2004; Worthington and Inouye, 1985), due to the quasi-crystalline arrangement of fibrils. Tissue-scale strains in the physiological range, such as those caused by blinking, eye movement or intraocular pressure fluctuations, are typically attributed to straightening of fibril crimp (Grytz and Meschke, 2009) and, more recently, fibril elongation (Bell et al., 2022) (crimp is the wavy arrangement of fibrils that can be straightened under load. The extent to which a crimped fibril can be extended by fully straightening it without stretching is usually referred to as its

TABLE 1 Average tangent stiffness (in MPa) of each group as a function of applied strain.

Applied strain	2%	5%	7%
Ribo	1.8 ± 0.3	4.6 ± 0.5	6.7 ± 0.7
CXL	2.8 ± 0.5	7.8 ± 1.3	11.2 ± 1.5
Dec	2.1 ± 0.3	4.7 ± 0.7	7.1 ± 1.0
Dec + CXL	2.7 ± 0.6	8.5 ± 1.5	12.0 ± 1.8

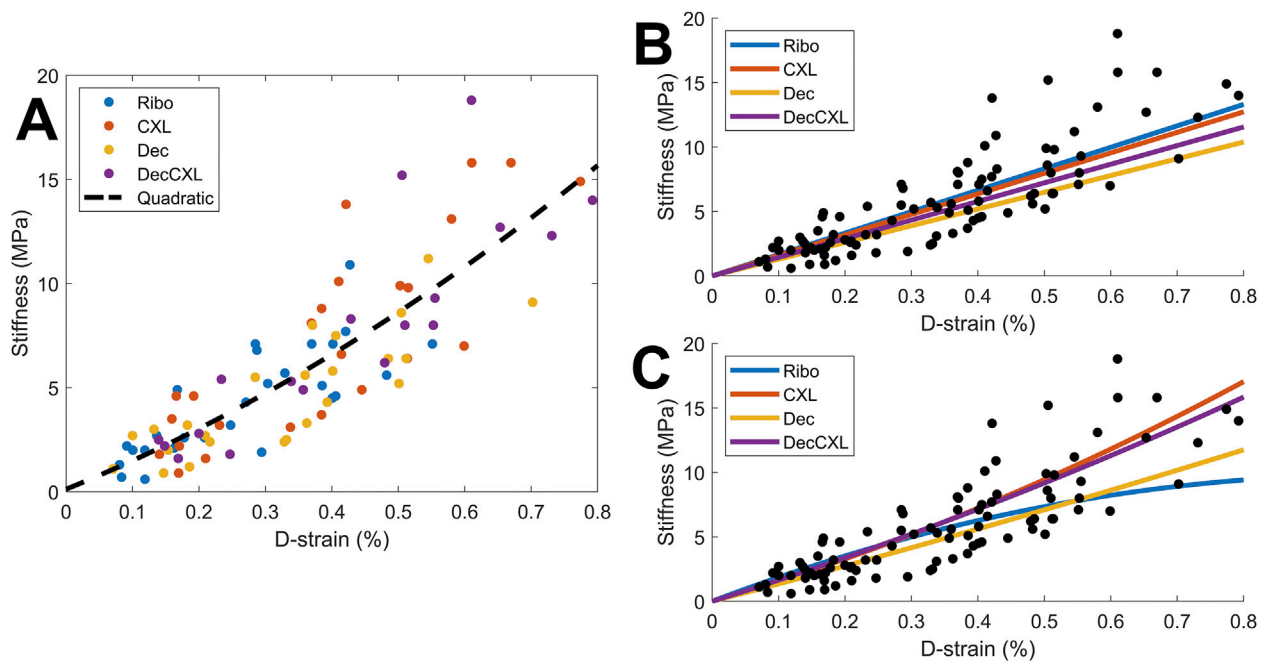

FIGURE 4
Comparison of D-strain and associated tangent stiffness for all samples at 2%, 5% and 7% applied strain. The distribution appeared nonlinear, so different fits were tested (see text for details). **(A)** Comparison of individual values with an overall average quadratic fit. **(B)** Linear fits for each group based on data up to D-strain of 0.4%. **(C)** Quadratic fits for each group.

tortuosity). It is worth noting that a significant proportion of corneal collagen remains crimped at physiological intraocular pressure (Jan et al., 2018). Changes in the macroscopic mechanical properties of the cornea, such as those caused by CXL treatment, should therefore manifest as some change in either or both of these strain mechanisms.

In this study we aim to develop a mechanistic understanding of CXL and decorin treatment by using synchronized biomechanical testing and X-ray scattering to quantify changes in corneal collagen architecture in response to tensile load. This approach allows stiffness to be directly correlated with variations in hierarchical strain mechanisms, allowing a picture to be built of how crosslinking may stiffen the cornea and halt the progression of keratoconus. In addition to this, we explore the tissue stiffening effects of exogenous human recombinant Decorin core protein when applied in isolation and in combination with CXL to assess the therapeutic potential of these treatments.

Methods

Specimen preparation

46 porcine eyes were obtained and transported on ice from a local DEFRA licensed abattoir within 6 h of euthanasia and divided into the treatment groups described below. In all cases, the corneal epithelium was removed prior to treatment. In Groups 1 and 2 (Decorin; n = 10 and Dec + CXL; n = 7), an 11-mm diameter corneal well was used to apply 300 μL human recombinant decorin core protein (Galacorin®) in a phosphate buffered saline solution (5 mg/mL Galacorin® at pH 7.2 supplied by Phoenicis Therapeutics, Massachusetts, USA). After 60s the corneal well was removed, and the solution was gently wiped away from the corneal surface. In the Dec + CXL group, the decorin treatment was immediately followed by riboflavin/UVA cross-linking, involving a 16-min application of 0.1% riboflavin/1.1% HPMC solution (Mediocross

TABLE 2 Structural metrics and their change with applied strain.

	D-strain (%)		D-strain uniformity (a.u.)		Fibril reorientation (%)		Fibril uncrimping (a.u.)	
Applied strain	2%	7%	2%	7%	2%	7%	2%	7%
Ribo	0.12 ± 0.03	0.40 ± 0.09	6.53 ± 0.43	6.46 ± 0.46	0.4 ± 0.5	1.3 ± 1.7	6.9 ± 7.3	0.4 ± 5.7
CXL	0.18 ± 0.03	0.57 ± 0.12	6.85 ± 0.50	6.97 ± 0.37	1.4 ± 0.8	4.1 ± 1.6	12.4 ± 9.9	7.4 ± 2.5
Dec	0.15 ± 0.05	0.48 ± 0.12	7.14 ± 0.70	7.14 ± 0.70	0.9 ± 0.9	2.2 ± 1.3	5.5 ± 5.0	−3.1 ± 2.5
Dec + CXL	0.19 ± 0.04	0.63 ± 0.12	7.52 ± 0.91	7.53 ± 0.91	1.4 ± 0.9	4.2 ± 2.6	15.5 ± 6.2	9.8 ± 2.1

M) to the stromal surface followed by UVA exposure (365 nm UVA light with a fluence of 9 mW/cm^2, exposure time of 10 min and an 11-mm beam diameter). In Group 3 (CXL, n = 10), eyes underwent the riboflavin/UVA cross-linking procedure without a decorin pre-treatment. The remaining eyes served as either riboflavin-only controls (Ribo, n = 10), receiving a 20-min application of 0.1% riboflavin/1.1% HPMC solution (Mediocross M) to the stromal surface without UVA exposure, or as untreated controls (n = 9). The central corneal thickness of each eye was measured using a SP-100 portable pachymeter (Tomey GmbH Technology and Vision, Nurnberg, Germany) before and after each treatment. All samples were wrapped in plastic film (to maintain tissue hydration) and stored at 4 °C overnight until required for data collection.

Untreated specimens were used solely for the purpose of testing equipment and internal controls. The non-irradiated, riboflavin-soaked corneas were used as controls for the treatment groups to minimise the effect of hydration differences on the biomechanical and structural data. Mechanical and equipment failure meant full datasets were not acquired from every specimen. 9 Ribo, 8 CXL, 8 Dec and 6 Dec + CXL datasets were obtained in total.

Mechanical testing

Specimens were tested approximately 24 h following treatment. Central corneal thickness was measured and then a strip approximately 3.5 mm in width was excised using a custom-designed punch comprising two precisely aligned parallel razor blades. In all cases, the strip was obtained in the superior-inferior direction.

A custom-built tensile tester comprising a piezo linear stage (Q-545-240, PI, driven by PIShift E−871 controller) and 4.9 N tension/compression load cell (Model 31, RDP) was used to apply loads to the tensile strips. Specimens were attached to micromanipulator arms using cyanoacrylate glue and a tare load was applied to straighten them. This straightened state was used as the reference configuration for each specimen and subsequent measurements and analyses were based on this consistent baseline, ensuring internal validity across specimens. During preparation and while waiting for the glue to cure, the specimens were sprayed periodically with distilled water using a perfume mister, taking care not to wet the glue. Distilled water was used to replace water lost due to air drying in the low-humidity environment of the synchrotron (in this instance PBS or similar osmotically-balanced solutions are inappropriate as they add additional solute, which can affect hierarchical structure and mechanics (Huang and Meek, 1999)). The specimens were then strained to 8% at a constant rate over 3 min, during which time X-ray scatter patterns were acquired from the centre. Strains of interest were 2% (IOP-induced hoop stress induces strains of approximately 2%), 5% and 8% (for comparison with other tensile studies of cornea (Hatami-Marbini and Jayaram, 2018; Hatami-Marbini and Rahimi, 2015; Boyce et al., 2007)). Note that gross strains were only used for quantification and comparison of gross mechanical stiffness.

Specimens were then relaxed and carefully removed from the arms using a razor blade and their central corneal thickness was measured again using a pachymeter.

X-ray scattering

Small-angle X-ray scattering (SAXS) were carried out on beamline I22 at Diamond Light Source, the United Kingdom synchrotron (Smith et al., 2021). The beam wavelength was 1 Å, with an elliptical profile approximately 250 μm by 150 μm with major axis parallel to the direction of load. A Pilatus P3-2M photodetector (Dectris, Switzerland) collected scattered light at a distance of 5.95 m from the specimen. This arrangement allowed visualisation of scattering features corresponding to fibril-scale architecture (10 nm–100 nm). The 58.38 Å peak associated with the [001] crystal plane reflection of powdered silver behenate was used to centre and calibrate the SAXS images.

SAXS images were acquired from a region approximately 1.5 mm × 1.5 mm about the centre of each specimen by controlling the beamline stage in conjunction with the tensile tester. This avoided sample edges and associated cutting artefacts (Bell et al., 2022), ensured strains were largely uniaxial, and minimized intraspecimen variability in fibril structure (it has been shown elsewhere the porcine central cornea fibril arrangement is largely invariant with lateral position (Hayes et al., 2007)). An example SAXS pattern from the centre of a pig cornea is shown in Figure 1A. Analysis of scatter patterns to quantify the hierarchical structure of corneal collagen has been described elsewhere (Bell et al., 2018). Briefly, a data reduction process (Pauw et al., 2017) was run to remove beamline artefacts from the data, such as dead pixels, panel edges, beam flux fluctuations, etc., and then a circumferential integration was carried out to produce an intensity (I) vs. wavevector (Q) dataset. The Porod background, which takes the form $I(Q) \sim Q^{-4}$, was removed from peaks of interest through an automated, iterative process whereby a linear polynomial was fitted to a plot of log(I) vs. log(q) (Figure 1B) such that the area under the fit was minimised. Features of interest in this study are labelled in Figure 1B. The interfibrillar Bragg peak (IF) allows measure of the lateral spacing of fibrils, the meridional peaks

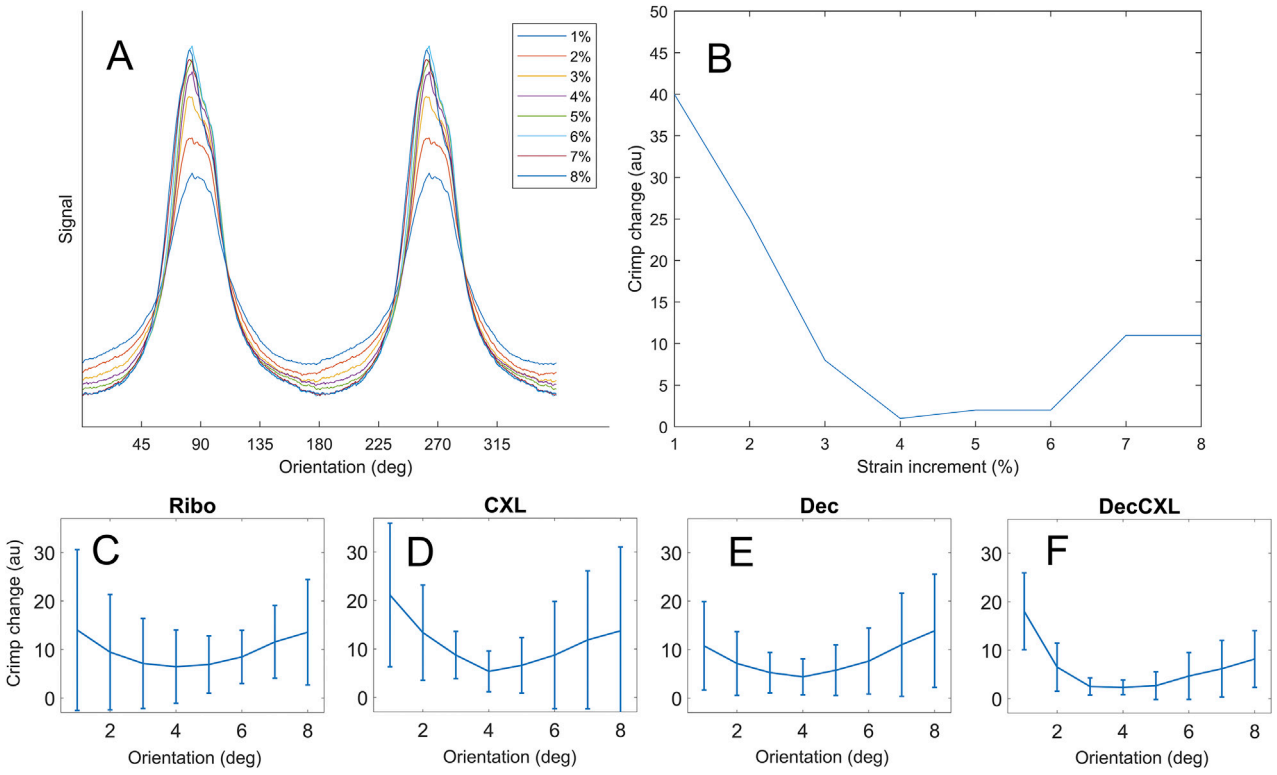

FIGURE 5
Crimp data. **(A)** Polar arrangement of fibrils for a representative specimen at each strain increment. **(B)** Extent of crimp at each strain increment relative to the least crimped state. **(C–F)** Averaged crimp extents for each group (bars mean ± SD).

(M3, M5) are diffractive orders of the D-period and the Bessel-shaped cylinder transform peaks (B) provide a measure of the fibril diameter. The azimuthal dependence (commonly referred to as χ) of the IF peak was used as a measure of the fibril orientation distribution, such as in Figures 1C,E.

Hydration was approximated through measures of specimen thickness and observation of interfibrillar spacing, trends in which have been investigated previously (Hayes et al., 2017). Measures of specimen thickness were made before and after imaging using a pachymeter, although this is quite imprecise on tensile strips (variability of ~5%). It was not possible to use weight as a measure of hydration, as the use of cyanoacrylate glue precluded like-for-like weighing before and after imaging. Exclusion criteria were: (i) Interfibrillar spacing outside of range shown in (Hayes et al., 2017) (at H ratios of 2.9–3.4, IFS^2 range is approximately 500 mm^2, so using the fit parameters provided this equates to an IFS range of approximately ±6 nm about the mean); (ii) Measured thickness drop in excess of 10%. No samples in this study dried to the extent that data needed to be excluded and measurements pertaining to hydration are included as a supplement.

Hierarchical strain characterisation

The reorientation of fibrous structures under external load is a nonlinear process that is dependent on several factors, including changes in gross geometry of the tissue, extracellular matrix interconnectivity, fibril waviness/crimp and the ability of the crimp to straighten. To approximate and separate the different strain mechanisms, the analysis was split into three stages.

Fibril elongation

Fibrils can elongate via several mechanisms, but under small loads we have shown previously that the dominant mechanism is the *spring-like* straightening of supramolecular twist (Bell et al., 2022). The straightening of "tropocollagen springs" gives rise to a change in D-period (referred to as "D-strain"), so precise measurement of the relative changes in the M3 peak provides a measure of fibril elongation that is separate from other strain mechanisms. In contrast to most approaches to SAXS analysis, the mean peak value was chosen as opposed to the peak (statistical mode) to provide a measure of mean fibril elongation, i.e.

$$\varepsilon_{n,fibril} = \frac{D_{n,mean}}{D_{0,mean}}$$

where $\varepsilon_{n,fibril}$ is the fibril-scale strain at the nth data point, $D_{0,mean}$ is the mean value of the D-period before load and $D_{n,mean}$ is the mean value of the D-period for the nth data point. The mean was used in preference to the mode in order to make meaningful statistical comparisons between groups and strain values.

Affine deformation

Assuming sinusoidal crimp (Jan et al., 2018), the orientation distribution of fibrils $F(\chi)$, obtained from the azimuthal dependence

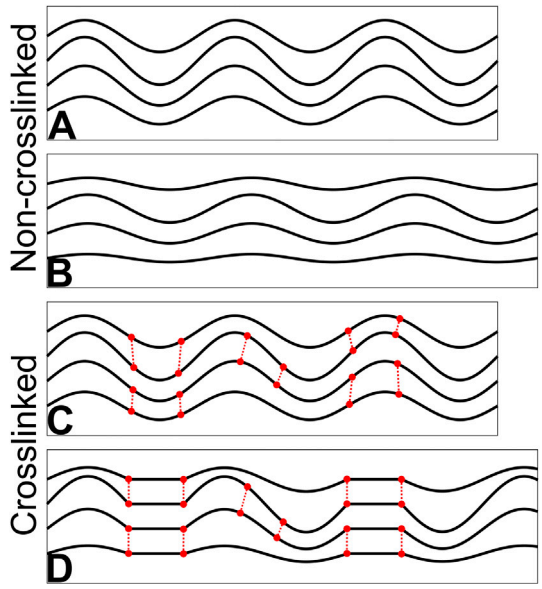

FIGURE 6
Illustration of uncrimping and the effect of crosslinking. **(A)** Crimped fibrils in an unstrained state. **(B)** When strained, some fibrils straighten and recruit before others; here the top and bottom fibrils are contributing more to specimen stiffness than the middle two. **(C)** The same arrangement as A with crosslinks between fibrils. **(D)** When strained, the top and bottom fibrils recruit along with the connected regions of the middle fibrils. A greater proportion of fibrillar collagen resists the tensile load in D than B, making it stiffer.

of the IF peak is a convolution of the sinusoid describing the crimp and the orientation distribution of the crimped fibrils (see Bell et al. (Bell et al., 2022) for a detailed explanation). In the absence of a separate imaging technique such as digital image correlation to quantify the local strain, the fibril orientation density (the number of fibrils aligned within a particular orientation range) around the direction orthogonal to the applied strain can be used to approximate affine sample deformations (in this case, the amount of stretch parallel to the applied load, and the amount of contraction perpendicular to it, close to where the data is collected). This relies on the assumption that changes in fibril orientation associated with strain-induced uncrimping only affect fibrils aligned within some angular range of the applied load (fibrils aligned outside of this range will not be under tension and not be uncrimping). Figure 1C shows typical fibril orientation data for a specimen in a strained and unstrained state, with a clear reduction in the amount of collagen aligned orthogonally to the applied load (load direction 0° and 180°). Affine changes are schematically illustrated in Figure 1D–assuming the strain is invariant with position, the solid lines represent the unstrained geometry and the dashed lines represent the strained geometry. The affine strain causes a reorientation in the angled lines. This reorientation is calculated for each 0.5° increment that the initial fibril orientation was sampled over, for a range of plausible affine deformations (strains parallel and perpendicular to the applied load that the corneal strip could be expected to experience) until a fit is reached with the strained data. The reason the number of fibrils in the orthogonal direction decreases with an affine deformation is because, for a given range of initial orientations, the reorientated range is wider–e.g., a fibril aligned at 90° will stay at 90°, while a fibril at 91° will reorientate to approximately 91.1°. Hence, fibrils initially aligned between 90° and 91° now occupy a range of 90°–91.1° and the fibril orientation density reduces. This effect is reversed close to the direction of applied load. The resulting affine-compensated distribution $F_c(\chi)$ is shown in Figure 1E, and with affine effects accounted for the remaining difference between the initial adjusted distribution and the strained distribution is assumed to be associated with uncrimping.

Uncrimping

Calculating directly the effect of uncrimping on an orientation distribution is a challenging problem, however the inverse problem (applying crimp to a dataset) simply involves convolving the distribution with that of a sinusoid (see (Bell et al., 2022) for more details). Firstly, the orientation distribution F_c(χ) with least crimp was assumed to be that with the largest slenderness ratio (the ratio of height to width of the orientation peak). The difference in crimp states between the least crimped distribution and another distribution can then be approximated by convolving the strained dataset with sinusoids of the form $y = A\sin\theta$ where A is iterated until the best fit with the unstrained data is found. This is computationally quick, so a brute force approach to find A is feasible. The value of A that maps the least crimped distribution to each other distribution (see Figure 1F) for a given specimen is then taken as the crimp state. Note that this is a measure of *relative* crimp, as it is not possible to know how crimped the least crimped state was to obtain an absolute value. This also means that the ability to compare specimens is limited as the least crimped states for two individual specimens are unlikely to be the same. We therefore limit comparisons of crimp data to averages between treatment groups.

Statistics

This study explores the effect of CXL and decorin treatment (as individual treatments and as a combined treatment) on biomechanical and structural metrics. To quantify the effect of CXL we compared groups CXL and Dec + CXL with Ribo and Dec, whereas to quantify the effects of decorin application we compared Dec and Dec + CXL groups with Ribo and CXL. T-tests were used to assess significance with the null-hypothesis rejected at the 0.05 confidence level.

To quantify correlations between metrics, the Spearman's Rho correlation was used with the null-hypothesis rejected at the 0.05 confidence level.

Results

Tensile stiffness

Figure 2 shows averaged stress-strain plots for each treatment group alongside representative data from a single riboflavin-only treated specimen with tangent moduli calculations at 2%, 5% and 7% applied strains. The calculated tangent moduli for each treatment group at 2%, 5% and 7% applied strain are shown in Figure 3 and Table 1.

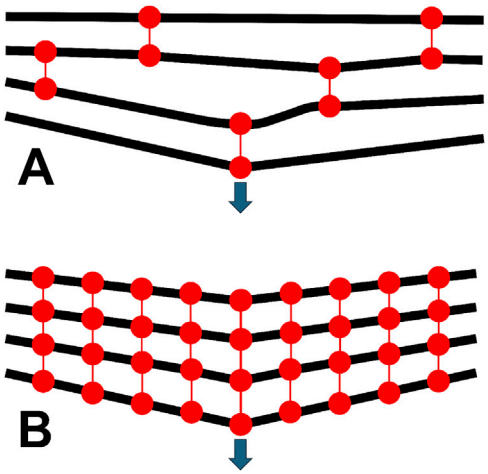

FIGURE 7
Illustration of the reorientation behaviour of collagen fibrils (black lines) in **(A)** untreated tissue and **(B)** crosslinked tissue. The resting configuration of the fibrils is horizontal and equally spaced. The crosslinked tissue exhibits more total fibril-scale reorientation when a point strain is applied (arrow).

CXL, and Dec + CXL, groups were significantly stiffer than Ribo and Dec groups, respectively at applied strains of 2% ($p < 0.05$), 5% ($p < 0.01$) and 7% ($p < 0.01$). Decorin applied in isolation or with CXL, did not affect stiffness significantly.

Fibril elongation/D-strain

D-strain was found to correlate with stiffness when all specimens were combined (2%: $p < 0.05$, 5% and 7%: $p < 0.0001$). To assess whether either CXL or decorin treatment stiffens fibrils individually, we explored the relationship between D-strain and tangent stiffness, and a scatter plot comparing the values between each group is shown in Figure 4A. The overall trend is approximately linear for all groups up to 0.4% D-strain, and for D-strains higher than this (data for which is dominated by the CXL and Dec + CXL groups) the stiffness increases more nonlinearly. To make quantitative comparisons of fibril stiffness between treatment groups, a reference trendline needed to be established. Linear fits through the origin for data up to a D-strain of 0.4% are shown in Figure 4B (gradients: Ribo: 1.66 GPa, CXL: 1.59 GPa, Dec: 1.30 GPa, Dec + CXL: 1.44 GPa), however these were particularly sensitive to noisy low-strain data and it has been suggested previously that the relationship between D-strain and fibril stiffness is nonlinear (Leighton et al., 2021). By comparing the average fractional difference between each group's datapoints and the quadratic trendline in Figure 4A, we can approximate the fibril stiffness relative to the average over all groups (Ribo: +4%, CXL: +8%, Dec -11% Dec + CXL: +2%). This showed that fibrils in the decorin treated group were significantly less stiff than those of the other three groups ($p < 0.05$). While the quadratic trendline belies what is likely a much more complex relationship between D-strain and stiffness, it provides a measure of differences between groups, which are small compared to their differences in stiffnesses. This implies that fibril stiffening is a relatively minor contributor to the overall tissue stiffening effect associated with CXL. Due to the relatively small group size and large inter-sample variability, quadratic fits for each group (Figure 4C) were not a useful comparison.

The uniformity of D-strain was investigated by quantifying the slenderness of M5 and its change with strain for fibrils aligned close to parallel to the applied load. This effectively measures the range of strains being experienced by fibrils, with a higher uniformity meaning a smaller range of strains. Slenderness was quantified by measuring the height of the peak and dividing it by the full width at half maximum (FWHM), which effectively measures the variance of fibril D-period within the scanned volume. Decorin treated datasets (Dec and Dec + CXL) were significantly more uniform than Ribo and CXL at 2% and 7% applied strain ($p < 0.01$) (Table 2).

Fibril reorientation

The fibril orientation distribution, $F(\chi)$, (an example of which is shown in Figure 1C), can be integrated to determine the relative orientation density between different angular ranges. The amount of collagen aligned within ±45° of the direction of applied load was compared with that aligned within ±45° of the perpendicular direction. At rest the ratio of these values:

$$\frac{\int_{-45}^{45} F(\chi)}{\int_{45}^{135} F(\chi)}$$

was approximately 60:40 in favour of the parallel orientation range for all samples. The ratio generally increased as strain increased, however the increase was significantly higher for the Ribo/UVA crosslinked specimens than non-crosslinked specimens (see Table 2; confidences: 2%: $p < 0.01$, 7%: $p < 0.001$). It was found that the extent of parallel:perpendicular reorientation correlated strongly with D-strain and stiffness when all groups were combined (2%: $p < 0.01$, 7%: $p < 0.001$).

Crimp

Fibril crimp was estimated by obtaining the affine-compensated orientation distribution $F_c(\chi)$ when fibrils were estimated to be straightest under applied load (chosen as the distribution with largest slenderness ratio–the ratio of height to width of the peak). This distribution was convolved with sinusoids of varying tortuosity, adjusted by varying their amplitude A, until a fit with $F_c(\chi)$ at other strains was found. A was taken as a relative measure of crimp with strain for each sample. CXL groups exhibited significantly different uncrimping trends to non-CXL groups at 2% ($p < 0.05$) but not at 7% (Table 2). It was found that the modelled crimp for most samples initially trended down before increasing again at higher strains (see Figure 5). The upward turn in crimp for each sample corresponded with a reduction in slenderness of the polar distribution of fibrils, a change in the trend of movement of the mean orientation and often the appearance of a shoulder in the distribution. This suggests that the assumption that fibril reorientation is simply a convolution of affine deformation and uncrimping breaks down somewhere between 2% and 7% applied strain, with nonlinear effects

becoming significant. Given these nonlinear effects, while we report the results of the crimp model for all strains to illustrate the more complex rearrangements of corneal collagen, we suggest that the model only isolates uncrimping behaviour at the 2% data point. At this datapoint, D-strain and crimp correlated ($p < 0.05$) when all groups were combined.

Discussion

The primary aim of this study was to characterise the structural changes that occur in riboflavin/UVA crosslinking (CXL) that give rise to enhanced biomechanical properties. We also investigated the structural and biomechanical impact of applying human recombinant decorin core protein to the corneal stroma, in isolation and in combination with CXL. CXL resulted in a significant increase in the tangent stiffness of corneal strips at all applied strains (2%–7%). The increase in tangent tensile stiffness caused by CXL was approximately 60%, which falls between values reported in the literature (Hammer et al., 2014; Wollensak and Spoerl, 2004; Chang et al., 2018). However, contrary to previous reports (Pappa et al., 2021), we found that a 60 s application of decorin core protein to the de-epithelialised corneal stroma did not significantly increase the stiffness of the cornea. Similarly, when decorin core protein application was combined with CXL (Dec + CXL), the tissue stiffening effect did not extend beyond that achieved with CXL alone.

To elucidate the mechanism underpinning CXL stiffening, X-ray scattering was employed to probe the microstructural mechanical environment. Our attention focused on fibrillar collagen, as the most abundant loadbearing structure in the cornea, specifically how fibrils elongate and reorientate. We quantified fibril elongation through close inspection of meridional diffraction peaks associated with the D-staggered structure of the collagen fibril. The increase in D-period associated with the application of tensile strain was found to correlate very significantly with tissue stiffness when all treatment groups were pooled together. Furthermore, factoring in the nonlinear relationship between D-strain and specimen stiffness, our data suggests that stiffening of individual fibrils is likely only a minor contributor to the overall increase in tissue stiffness following CXL. This finding is not entirely surprising, based on our previous studies which have indicated that intra-fibrillar cross-linking may be limited to just the collagen molecules at the surface of the fibrils. However, it should be noted that whilst CXL is limited to the anterior 300 microns of the cornea, the X-ray scatter patterns represent average measurements of collagen parameters throughout the entire thickness of the cornea. As such, detected changes in collagen parameters reported in this study should be viewed as conservative estimates of treatment effects.

Assuming minimal stiffening occurs within individual collagen fibrils then the origin of CXL stiffening must be a change in larger-scale strain mechanisms, and the data overall shows clearly that stiffer specimens experience more fibril reorientation. This could be explained by a greater fraction of fibrils being recruited (recruitment meaning fibrils being pulled to an extent that they contribute to the tissue stiffness), and/or a reduction in the strain required to recruit fibrils, and this would effectively stiffen the tissue. These effects could be achieved by the induced cross-links providing stronger and more plentiful links between extracellular matrix proteins, resulting in a form of interfibrillar bracing (linking together of fibrils such that they share loads more evenly). The patterns in fibril reorientation support this hypothesis, as there was significantly more in CXL specimens than non-CXL specimens. The patterns in strain uniformity also somewhat support this hypothesis–decorin treated samples exhibited significantly greater strain uniformity (i.e., reduced variance in D-strain) than non-treated samples, although CXL samples did not (mean strain uniformity increased but not significantly, $p = 0.1$). It is possible that this is a real effect in CXL that is masked by only treating approximately half of the tissue thickness (Caporossi et al., 2006) while SAXS data is averaged through the full thickness of the specimen. A clear answer to this will require greater statistical power or the analysis of entirely treated tissue. It is not currently known how deep decorin solution penetrates into the tissue. It should be noted here that riboflavin/UVA-induced crosslinks cannot themselves bridge between and brace fibrils, but they can reinforce structures that do, as we discuss later.

When fibrils are braced together more, their ability to straighten is likely to be impacted. This is because the periodicity of crimp in corneal collagen is in excess of 10 μm (Jan et al., 2018) while the periodicity of binding sites for crosslinks to form must be at most 67 nm (the length of a D-repeat). The complex, multidirectional movement involved in uncrimping will therefore tug at other fibrils, forcing them to move in unison. Our modelling of crimp revealed that CXL specimens exhibited significantly more uncrimping than non-crosslinked specimens, supporting the hypothesis that more fibrils are engaged in treated tissues. This conclusion is derived from the fact that fibrils require more force to straighten as they become less crimped, meaning the output of the model for a small fraction of fibrils straightening due to a fixed load will be less than a larger fraction of fibrils straightening under the same load. This was, however, limited to the 2% datapoint as at greater applied strains the modelling was complicated by changes in the shape of the orientation distribution. It was noted qualitatively that CXL specimens deviated more from the typical smooth bimodal distribution (Figure 5A) under strain than non-CXL specimens (such as through the formation of shoulders and additional mini-peaks).

While fibrils are probably too interconnected to uncrimp independently even without exogenous crosslinking, any added interconnectivity is likely to have two effects. Firstly, load will be distributed more evenly across fibrils in the tissue. Where in the untreated state the mechanical response is dictated by the rate of fibril recruitment, the interconnected nature of treated specimens means more tortuous (wavy) fibrils will have a greater contribution. This is supported by the increase in D-strain in CXL specimens. An illustration of this is shown in Figure 6. This is somewhat analogous to how tight-woven fabrics are stiffer than those with a loose weave; a tight weave means load is shared over more material with less ability for strands to straighten or slip independently. The second effect relates to fibril reorientation, which will be more sensitive to strain as the shorter lengths between braces will require smaller deflections to achieve the same reorientation. As the number of braces between fibrils increases in density, the response to

exogenous strain will approach that of a continuum (illustrated in Figure 7). Continuing with the woven fabric analogy, this is similar to adding extra stitches to a loose weave, holding strands in close conformity so pulling or pushing of a region of the fabric causes all the strands in the vicinity to reorientate, not just the ones directly loaded.

Corneal collagen structure is mediated by a network of interconnected glycosaminoglycans (GAGs), which bind to adjacent collagen fibrils via decorin and lumican proteoglycan core proteins (Scott and Haigh, 1988; Meek et al., 1986). It has been shown that CXL forms crosslinks between fibrillar collagen and decorin (Zhang et al., 2011), which envelopes tropocollagen molecules in a horseshoe-shaped structure and enhances the stiffness of type 1 collagen gels (Reese et al., 2013). However, the binding force between collagen amino acids and decorin core proteins has been modelled as being greater than the ultimate strength of GAG chains, suggesting enhanced collagen-proteoglycan binding may not contribute significantly to extracellular matrix stiffness (Vesentini et al., 2005). The creation of reactive oxygen species during the CXL process is likely to alter the chemistry of some GAGs, although it has been noted that sulphation has an insulating effect on GAG depolymerisation *in vitro* (Moseley et al., 1995). The mediating effect of minor collagens, which are abundant in cornea (Zimmermann et al., 1986), and their potential to act as braces themselves, has yet to be explored.

There were several notable challenges and limitations associated with this study. Firstly, due to the techniques employed and the quantity of tissue required, it was necessary for the study to be performed using post-mortem porcine eyes. Post-mortem corneas are subject to posthumous swelling, and changes in tissue hydration are well known to affect the ultrastructure (Hayes et al., 2017) and biomechanical properties of the tissue (Elliott and Hodson, 1998). To minimise the impact of such changes, tissue was obtained and treated within 6 h of death and corneal thickness measurements, made at regular intervals throughout the treatments and prior to data collection, were used to monitor levels of tissue hydration. Furthermore, the order of treatment and data collection (alternating eyes from each group) and the use of a non-irradiated, riboflavin-only control group (in preference to untreated corneas) helped ensure that there was no significant difference in corneal thickness/hydration between the groups. Comparisons of absolute tensile stiffness values to others in the literature should be made with caution, as the slenderness ratio (ratio of length to width) of specimens in this study was approximately 3:1. While this meets the minimum standard for testing polymer matrix composite materials (ASTM Standard, 2008) it does not meet the recommended values (which need to be especially strict for anisotropic materials (Legerlotz et al., 2010)), meaning the stress environment in the strip will comprise both uniaxial and planar components. This is an unavoidable issue associated with the size of the cornea and the need to mitigate the effects of cut edges and explains in part the variation in stiffness results across studies in the literature. It should also be noted that the nature of the test and the necessary straightening of corneal curvature perturbs specimens from their physiological state, meaning any direct physiological comparisons should be made with caution. The use of synchrotron X-ray scattering, which obtains data through the full thickness of specimens, means results are insensitive to depth-dependent variation. Follow-up studies using complementary techniques will be of particular value for evaluating changes associated with CXL, which only affects the anterior 300 μm of the tissue.

The results have some interesting implications for both the clinic and wider field of connective tissue research. Firstly, the findings of this study, which indicate that the stiffening effect in CXL treated corneas is primarily due to an increased interconnectivity of the fibrillar collagen network rather than a stiffening of the fibrils themselves, represent a major step forward in our understanding of the mechanism by which CXL therapy stops keratoconus progression, and has important ramifications for the accuracy with which computational models (based on structural data), may predict the outcome of surgical procedures. Furthermore, this is an extracellular example demonstrating how the interconnectivity of biopolymer networks can tune gross mechanical stiffness (Gardel et al., 2004; Head et al., 2003). The results highlight the need to further explore the role of proteoglycan and minor collagens in the crosslinking process, particularly whether their exogenous application or removal could allow for greater control over CXL treatment, and ultimately better outcomes for patients. The findings also provide a new dimension to explore in the mechanical modelling of cornea and soft tissue in general as we begin to incorporate fibril-scale architecture.

In conclusion, we have shown that Riboflavin/UVA crosslinking enhances the tensile stiffness of corneas by approximately 60%, while decorin treatment does not change the stiffness significantly. The stiffening effect appears to be associated with increased interconnectivity of the fibrillar collagen network as opposed to stiffening of the fibrils themselves, although a small increase in fibril stiffness was measured. While decorin treatment did not affect the macroscopic mechanical properties, it did enhance the interconnectivity of fibrillar collagen whilst also reducing fibril stiffness. Combining decorin treatment with Riboflavin/UVA crosslinking did not significantly enhance the stiffness over crosslinking alone, and as such is unlikely to be useful in the treatment of keratoconus. The methodology developed here can be adapted to a broad range of tissues and conditions for the evaluation of new and adjuvant therapies.

Data availability statement

All data supporting this study is openly available in Figshare data repository at 10.17035/cardiff.30122182.

Ethics statement

Ethical approval was not required for the study involving animals in accordance with the local legislation and institutional requirements because samples obtained were byproducts from animals slaughtered at abattoirs for the food industry.

Author contributions

JB: Conceptualization, Data curation, Formal Analysis, Funding acquisition, Investigation, Methodology, Project administration, Resources, Software, Validation, Visualization, Writing – original draft, Writing – review and editing. SM: Investigation, Methodology, Writing – original draft, Writing – review and editing. OS: Investigation, Software, Supervision, Writing – original draft, Writing – review and editing. SE: Data curation, Formal Analysis, Writing – original draft, Writing – review and editing. CB: Formal Analysis, Investigation, Methodology, Writing – original draft, Writing – review and editing. NT: Software, Writing – original draft, Writing – review and editing. KM: Conceptualization, Data curation, Formal Analysis, Funding acquisition, Methodology, Writing – original draft, Writing – review and editing. SH: Conceptualization, Data curation, Formal Analysis, Funding acquisition, Investigation, Methodology, Supervision, Writing – original draft, Writing – review and editing.

Funding

The author(s) declare that financial support was received for the research and/or publication of this article. This work was supported by the Medical Research Council (grant number MR/S037829/1).

Acknowledgments

The authors wish to thank Phoenicis Therapeutics for the supply of the decorin used in this study. We acknowledge Diamond Light Source for time on beamline I22 under proposal SM34903. For the purpose of open access, the author has applied a CC BY public copyright licence to any Author Accepted Manuscript version arising.

Conflict of interest

The authors declare that the research was conducted in the absence of any commercial or financial relationships that could be construed as a potential conflict of interest.

Generative AI statement

The author(s) declare that no Generative AI was used in the creation of this manuscript.

Any alternative text (alt text) provided alongside figures in this article has been generated by Frontiers with the support of artificial intelligence and reasonable efforts have been made to ensure accuracy, including review by the authors wherever possible. If you identify any issues, please contact us.

Publisher's note

Supplementary material

The Supplementary Material for this article can be found online at: https://www.frontiersin.org/articles/10.3389/fbioe.2025.1603679/full#supplementary-material

References

Aghamohammadzadeh, H., Newton, R. H., and Meek, K. M. (2004). X-ray scattering used to map the preferred collagen orientation in the human cornea and limbus. *Structure* 12, 249–256. doi:10.1016/s0969-2126(04)00004-8

Aldahlawi, N. H., Hayes, S., O'Brart, D. P. S., and Meek, K. M. (2015). Standard *versus* accelerated riboflavin–ultraviolet corneal collagen crosslinking: resistance against enzymatic digestion. *J. Cataract. Refract. Surg.* 41, 1989–1996. doi:10.1016/j.jcrs.2015.10.004

ASTM Standard D3039/D3039M - 07 standard test method for tensile properties of polymer matrix composite materials, (2008). doi:10.1520/C0033-03

Bell, J. S., Hayes, S., Whitford, C., Sanchez-Weatherby, J., Shebanova, O., Vergari, C., et al. (2018). The hierarchical response of human corneal collagen to load. *Acta Biomater.* 65, 216–225. doi:10.1016/j.actbio.2017.11.015

Bell, J. S., Hayes, S., Whitford, C., Sanchez-Weatherby, J., Shebanova, O., Terrill, N. J., et al. (2022). Tropocollagen springs allow collagen fibrils to stretch elastically. *Acta Biomater.* 142, 185–193. doi:10.1016/j.actbio.2022.01.041

Boyce, B. L., Jones, R. E., Nguyen, T. D., and Grazier, J. M. (2007). Stress-controlled viscoelastic tensile response of Bovine cornea. *J. Biomech.* 40, 2367–2376. doi:10.1016/j.jbiomech.2006.12.001

Caporossi, A., Baiocchi, S., Mazzotta, C., Traversi, C., and Caporossi, T. (2006). Parasurgical therapy for keratoconus by riboflavin–ultraviolet type A rays induced cross-linking of corneal collagen: preliminary refractive results in an Italian study. *J. Cataract. Refract. Surg.* 32, 837–845. doi:10.1016/j.jcrs.2006.01.091

Chang, S.-H., Eliasy, A., Chen, K.-J., Ji, Y.-R., Young, T.-H., Wang, T.-J., et al. (2018). The relationship between mechanical properties, ultrastructural changes, and intrafibrillar bond Formation in corneal UVA/Riboflavin cross-linking treatment for keratoconus. *Surgery* 34, 264–272. doi:10.3928/1081597x-20180220-01

Elliott, G. F., and Hodson, S. A. (1998). Cornea, and the swelling of polyelectrolyte gels of biological interest. *Rep. Prog. Phys.* 61, 1325–1365. doi:10.1088/0034-4885/61/10/001

Gardel, M. L., Shin, J. H., MacKintosh, F. C., Mahadevan, L., Matsudaira, P., and Weitz, D. A. (2004). Elastic behavior of cross-linked and bundled actin networks. *Sci. (80)* 304, 1301–1305. doi:10.1126/science.1095087

Grytz, R., and Meschke, G. (2009). Constitutive modeling of crimped collagen fibrils in soft tissues. *J. Mech. Behav. Biomed. Mat.* 2, 522–533. doi:10.1016/j.jmbbm.2008.12.009

Hammer, A., Richoz, O., Mosquera, S. A., Tabibian, D., Hoogewoud, F., and Hafezi, F. (2014). Corneal biomechanical properties at different corneal cross-linking (CXL) irradiances. *Invest. Ophthalmol. Vis. Sci.* 55, 2881–2884. doi:10.1167/iovs.13-13748

Hatami-Marbini, H., and Jayaram, S. M. (2018). Relationship between initial corneal hydration and stiffening effects of corneal crosslinking treatment. *J. Cataract. Refract. Surg.* 44, 756–764. doi:10.1016/j.jcrs.2018.01.036

Hatami-Marbini, H., and Rahimi, A. (2015). Collagen cross-linking treatment effects on corneal dynamic biomechanical properties. *Exp. Eye Res.* 135, 88–92. doi:10.1016/j.exer.2015.04.005

Hayes, S., Boote, C., Lewis, J., Sheppard, J., Abahussin, M., Quantock, A. J., et al. (2007). Comparative study of fibrillar collagen arrangement in the corneas of primates and other mammals. *Anat. Rec. Adv. Integr. Anat. Evol. Biol. Adv. Integr. Anat. Evol. Biol.* 290, 1542–1550. doi:10.1002/ar.20613

Hayes, S., Kamma-Lorger, C. S., Boote, C., Young, R. D., Quantock, A. J., Rost, A., et al. (2013). The effect of riboflavin/UVA collagen cross-linking therapy on the structure and hydrodynamic behaviour of the ungulate and rabbit corneal stroma. *PLoS One* 8, e52860. doi:10.1371/journal.pone.0052860

Hayes, S., White, T., Boote, C., Kamma-Lorger, C. S., Bell, J., Sorenson, T., et al. (2017). The structural response of the cornea to changes in stromal hydration. *J. R. Soc. Interface.* 14, 20170062. doi:10.1098/rsif.2017.0062

Head, D. A., Levine, A. J., and MacKintosh, F. C. (2003). Deformation of cross-linked semiflexible polymer networks. *Phys. Rev. Lett.* 91, 108102. doi:10.1103/PhysRevLett.91.108102

Holmes, D. F., Gilpin, C. J., Baldock, C., Ziese, U., Koster, A. J., and Kadler, K. E. (2001). Corneal collagen fibril structure in three dimensions: structural insights into fibril assembly, mechanical properties, and tissue organization. *Proc. Natl. Acad. Sci.* 98, 7307–7312. doi:10.1073/pnas.111150598

Huang, Y., and Meek, K. M. (1999). Swelling studies on the cornea and sclera: the effects of pH and ionic strength. *Biophys. J.* 77, 1655–1665. doi:10.1016/s0006-3495(99)77013-x

Jan, N.-J., Brazile, B. L., Hu, D., Grube, G., Wallace, J., Gogola, A., et al. (2018). Crimp around the globe; patterns of collagen crimp across the corneoscleral shell. *Exp. Eye Res.* 172, 159–170. doi:10.1016/j.exer.2018.04.003

Koster, M., Boote, C., Meek, K., Fowler, P., Girkin, C., Meschke, G., et al. (2013). Inter- and intra-lamellar slippage of collagen fibrils as a potential mechanism of keratoconus progression. *Invest. Ophthalmol. Vis. Sci.* 54, 1642.

Kymes, S. M., Walline, J. J., Zadnik, K., Sterling, J., Gordon, M. O., of, C. L. E., et al. (2008). Changes in the quality-of-life of people with keratoconus. *Am. J. Ophthalmol.* 145, 611–617.e1. doi:10.1016/j.ajo.2007.11.017

Legerlotz, K., Riley, G. P., and Screen, H. R. C. (2010). Specimen dimensions influence the measurement of material properties in tendon fascicles. *J. Biomech.* 43, 2274–2280. doi:10.1016/j.jbiomech.2010.04.040

Leighton, M. P., Rutenberg, A. D., and Kreplak, L. (2021). D-band strain underestimates fibril strain for twisted collagen fibrils at low strains. *J. Mech. Behav. Biomed. Mat.* 124, 104854. doi:10.1016/j.jmbbm.2021.104854

Meek, K. M., Elliott, G. F., and Nave, C. (1986). A synchrotron X-Ray diffraction Study of Bovine Cornea stained with cupromeronic blue. *Res.* 6, 203–218. doi:10.1016/s0174-173x(86)80026-7

Metzler, K. M., Roberts, C. J., Mahmoud, A. M., Agarwal, G., and Liu, J. (2016). *Ex vivo* transepithelial collagen cross-linking in porcine and human corneas using human decorin core protein. *J. Refract. Surg.* 32, 410–417. doi:10.3928/1081597x-20160428-08

Moseley, R., Waddington, R., Evans, P., Halliwell, B., and Embery, G. (1995). The chemical modification of glycosaminoglycan structure by oxygen-derived species *in vitro*. *Biochim. Biophys. Acta (BBA)-General Subj.* 1244, 245–252. doi:10.1016/0304-4165(95)00010-9

Orgel, J. P. R. O., Eid, A., Antipova, O., Bella, J., and Scott, J. E. (2009). Decorin core protein (decoron) shape complements collagen fibril surface structure and mediates its binding. *PLoS One* 4, e7028. doi:10.1371/journal.pone.0007028

Ottani, V., Raspanti, M., and Ruggeri, A. (2001). Collagen structure and functional implications. *Micron* 32, 251–260. %3CGo. doi:10.1016/s0968-4328(00)00042-1

Ottani, V., Martini, D., Franchi, M., Ruggeri, A., and Raspanti, M. (2002). Hierarchical structures in fibrillar collagens. *Micron* 33, 587–596. doi:10.1016/S0968-4328(02)00033-1

Pappa, C. S., Nguyen, B. A., Mahmoud, A. M., Agarwal, G., and Roberts, C. J. (2021). Effect of penetration enhancer with novel corneal cross-linking using recombinant human decoron in porcine eyes. *Exp. Eye Res.* 206, 108542. doi:10.1016/j.exer.2021.108542

Pauw, B. R., Smith, A. J., Snow, T., Terrill, N. J., and Thünemann, A. F. (2017). The modular small-angle X-ray scattering data correction sequence. *J. Appl. Crystallogr.* 50, 1800–1811. doi:10.1107/s1600576717015096

Raiskup, F., Theuring, A., Pillunat, L. E., and Spoerl, E. (2015). Corneal collagen crosslinking with riboflavin and ultraviolet-A light in progressive keratoconus: Ten-year results. *Surgery* 41, 41–46. doi:10.1016/j.jcrs.2014.09.033

Reale, E., Benazzo, F., and Ruggeri, A. (1981). Differences in the microfibrillar arrangement of collagen fibrils. Distribution and possible significance. *J. Submicrosc. Cytol.* 13, 135–143.

Reese, S. P., Underwood, C. J., and Weiss, J. A. (2013). Effects of decorin proteoglycan on fibrillogenesis, ultrastructure, and mechanics of type I collagen gels. *Matrix Biol.* 32, 414–423. doi:10.1016/j.matbio.2013.04.004

Scott, J. E. (1996). Proteodermatan and proteokeratan sulfate (decorin, lumican/fibromodulin) proteins are horseshoe shaped. Implications for their interactions with collagen. *Biochemistry* 35, 8795–8799. doi:10.1021/bi960773t

Scott, J. E., and Haigh, M. (1988). Identification of specific binding sites for keratan sulphate proteoglycans and chondroitin-dermatan sulphate proteoglycans on collagen fibrils in cornea by the use of cupromeronic blue in 'critical-electrolyte-concentration'techniques. *Biochem. J.* 253, 607–610. doi:10.1042/bj2530607

Smith, A. J., Alcock, S. G., Davidson, L. S., Emmins, J. H., Hiller Bardsley, J. C., Holloway, P., et al. (2021). I22: SAXS/WAXS beamline at Diamond Light Source–an overview of 10 years operation. *J. Synchrotron Radiat.* 28, 939–947. doi:10.1107/s1600577521002113

Spoerl, E., Wollensak, G., and Seiler, T. (2004). Increased resistance of crosslinked cornea against enzymatic digestion. *Curr. Eye Res.* 29, 35–40. doi:10.1080/02713680490513182

Vesentini, S., Redaelli, A., and Montevecchi, F. M. (2005). Estimation of the binding force of the collagen molecule-decorin core protein complex in collagen fibril. *J. Biomech.* 38, 433–443. doi:10.1016/j.jbiomech.2004.04.032

Wollensak, G., and Spoerl, E. (2004). Collagen crosslinking of human and porcine sclera. *J. Cataract. Refract. Surg.* 30, 689–695. doi:10.1016/j.jcrs.2003.11.032

Wollensak, G., Spoerl, E., and Seiler, T. (2003a). Riboflavin/ultraviolet-A–induced collagen crosslinking for the treatment of keratoconus. *Am. J. Ophthalmol.* 135, 620–627. doi:10.1016/s0002-9394(02)02220-1

Wollensak, G., Spoerl, E., and Seiler, T. (2003b). Stress-strain measurements of human and porcine corneas after riboflavin–ultraviolet-A-induced cross-linking. *J. Cataract. Refract. Surg.* 29, 1780–1785. doi:10.1016/s0886-3350(03)00407-3

Worthington, C. R., and Inouye, H. (1985). X-ray diffraction study of the cornea. *Int. J. Biol. Macromol.* 7, 2–8. doi:10.1016/0141-8130(85)90057-1

Zhang, G., Chen, S., Goldoni, S., Calder, B. W., Simpson, H. C., Owens, R. T., et al. (2009). Genetic evidence for the coordinated regulation of collagen fibrillogenesis in the cornea by decorin and biglycan. *J. Biol. Chem.* 284, 8888–8897. doi:10.1074/jbc.m806590200

Zhang, Y., Conrad, A. H., and Conrad, G. W. (2011). Effects of ultraviolet-A and riboflavin on the interaction of collagen and proteoglycans during corneal cross-linking. *J. Biol. Chem.* 286, 13011–13022. doi:10.1074/jbc.m110.169813

Zimmermann, D. R., Trüeb, B., Winterhalter, K. H., Witmer, R., and Fischer, R. W. (1986). Type VI collagen is a major component of the human cornea. *FEBS Lett.* 197, 55–58. doi:10.1016/0014-5793(86)80297-6

Frontiers in
Bioengineering and Biotechnology

Accelerates the development of therapies, devices, and technologies to improve our lives

A multidisciplinary journal that accelerates the development of biological therapies, devices, processes and technologies to improve our lives by bridging the gap between discoveries and their application.

Discover the latest Research Topics

See more →

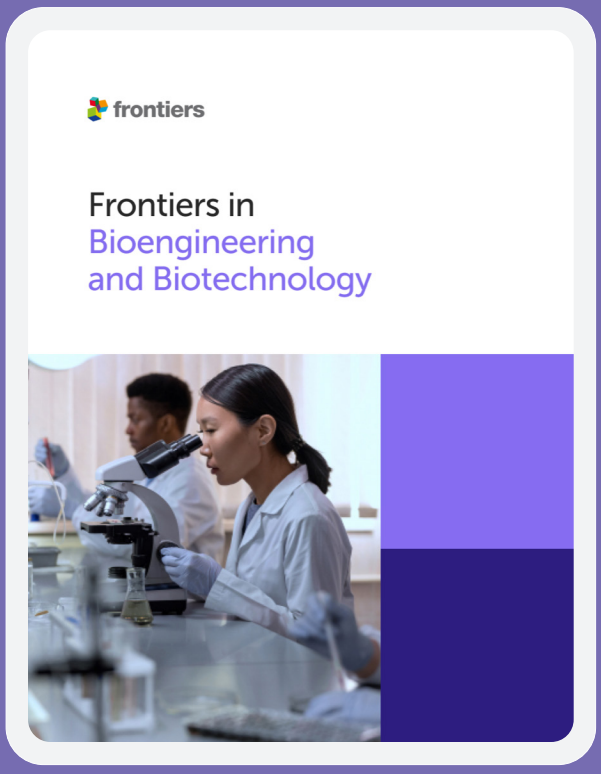

Frontiers

Avenue du Tribunal-Fédéral 34
1005 Lausanne, Switzerland
frontiersin.org

Contact us

+41 (0)21 510 17 00
frontiersin.org/about/contact